

# Investigating Covalency in Uranyl and its Complexes via Exploration of Electronic Excited States

Sapphire McNeil Armstrong



A thesis presented for the degree of

Doctor of Philosophy

2022

Lancaster University

Department of Chemistry

# Declaration

*I, Sapphire Armstrong confirm that the work presented in this thesis is my own work, and has not been submitted for the award of a higher degree elsewhere. Where information has been derived from other sources, I confirm that this has been indicated in the thesis.*

# Abstract

*Herein, computational calculation has been used to study the electronic structure and bonding of uranyl ( $[UO_2]^{2+}$ ) and its complexes at both the ground and electronically excited state geometries. The optically accessible  $\sigma_u \rightarrow \delta_u$  triplet excitation, allowed via spin-orbit coupling, was investigated throughout. Density Functional Theory (DFT) was used for obtaining optimised geometries and corresponding excitation energies for the transitions of interest. Application of the density based analytical tool, Quantum Theory of Atoms in Molecules (QTAIM) on the generated structures enabled rationalisation of the bonding interactions within the complexes. Here, QTAIM analysis was utilised for the first time to probe an excited state structure of an f-element complex. This became significantly important as although trends between the ground and excited state electronic structures were similar, investigation of the excited state resulted in additional findings which would not have been established by investigation of the ground state alone. Investigation of the covalency in uranyl via symmetry-preserving excited states resulted in trends between the type of covalency dependence and the orbitals involved in the excitation to be established. The covalency in the  $U-O_{yl}$  bond was found to decrease upon equatorial complexation, with charge being transferred onto the uranyl oxygen centres highlighting an increase in the ionic nature of the  $U-O_{yl}$  bond. Investigation into the electronic structure and bonding of bent uranyl complexes enabled the design of theoretical complexes, which although found to not be synthetically viable did have a significant O-U-O bend (O-U-O angle  $\sim 100^\circ$ ). Intramolecular proton transfers within uranyl hydroxide analogues were investigated as an alternative method for obtaining cis uranyl. The energy barrier was lowered in the electronic excited state for all complexes, again highlighting the significance of considering the excited state. Throughout this work, the importance of excited state investigation is established, and these results present a promising starting point for further actinide covalency investigations.*

---

*"The deepest solace lies in understanding, this ancient unseen stream. A shudder  
before the beautiful"*

To my husband Craig, for his endless love and support. This work closes a chapter of our lives as we get ready for our next great adventure.

# List of Publications

## Published

## Submitted

*A theoretical investigation of uranyl covalency via symmetry-preserving excited state structures*

S. Armstrong, T. Malcomson, A. Kerridge

*Phys. Chem. Chem. Phys.* **2022**,

## Work Not Included in this Thesis

*Structural, spectroscopic, and computational evaluations of cation–cation and halogen bonding interactions in heterometallic uranyl hybrid materials.*

K. P. Carter, M. Kalaj, S. McNeil, A. Kerridge, M. H. Schofield, J. A. Ridenour and C. L. Cahill

*Inorg. Chem. Front.*, **2021**, 8, 1128–1141

*Electrochemical Carbon Dioxide Reduction by a Homogeneous Iron Di-thiolene Catalyst*

C. Armstrong, T. Malcomson, R. Hogue, M. Potter, S. Armstrong, A. Kerridge, K. E. Toghil

*ChemElectroChem* **2022**, accepted

# Acknowledgements

Firstly, my biggest thank you goes to my supervisor Andy Kerridge for taking me under his wing after changing supervisors in my first year. You always treated me as your own student from day one and I am incredible grateful for your patience and support during those challenging times. Thank you for proposing such an interesting (and challenging!) project that incorporated the themes of my original PhD in such a short space of time. This research would not have been possible without your ideas, guidance and weekly meetings.

Thank you to all the staff within the Chemistry Department at Lancaster for an incredible 8 years of studying here, both undergraduate and postgraduate. Your enthusiasm for research was what inspired me to pursue a PhD. I am humbled by the many opportunities being part of the new chemistry department has given me over the years, it has been a truly amazing experience. Lancaster will always hold a special place in my heart; it was my home for 8 wonderful years, many long-lasting friendships and most incredibly I found and married my soulmate here.

I would also like to thank my fellow PhD colleagues and friends, its been a pleasure to share my PhD experience with you all. I am very grateful for your guidance, support and friendship throughout these years, not to mention the many lunch-time grumbles of research, it was nice to not feel so alone in my problems!

A big thank you must also go to my family, both McNeil's and Armstrong's, your unwavering support throughout the years. Thank you for the many trips to Lancaster and the countless memories we have had throughout my time here. To my fur baby Lilith, thank you for the many cat cuddles throughout working from home and your many contributions to this work by sitting on the keyboard - I blame any typo's in this document on you!

Finally, to my husband Craig, I am so incredibly grateful for your endless love, support and encouragement. I honestly do not think I could have done this without you. I am sorry for all the stressful, challenging times and the many hours of tears. Thank you for our many adventures in and around Lancaster, I really miss adventuring the North West with you. Onwards to the next chapter of our lives together and many more great adventures.

# Contents

<b>Abstract</b>	<b>ii</b>
<b>Dedication</b>	<b>iii</b>
<b>List of Publications</b>	<b>iv</b>
<b>Acknowledgements</b>	<b>v</b>
<b>Contents</b>	<b>vi</b>
<b>List of Figures</b>	<b>x</b>
<b>List of Tables</b>	<b>xvi</b>
<b>List of Abbreviations</b>	<b>xxi</b>
<b>1 Introduction</b>	<b>1</b>
1.1 Actinide Chemistry . . . . .	2
1.2 Problems with nuclear power . . . . .	4
1.3 Uranyl . . . . .	7
1.3.1 Structure and Bonding . . . . .	7
1.3.2 Optical Spectra . . . . .	9
1.4 Thesis Overview . . . . .	10
<b>2 Methodology</b>	<b>16</b>
2.1 Dirac Notation . . . . .	17
2.2 Schrödinger Equation . . . . .	17
2.3 The Variational Principle . . . . .	18
2.4 The Hamiltonian . . . . .	18
2.5 The Born–Oppenheimer Approximation . . . . .	18
2.6 The Orbital Approximation . . . . .	19
2.7 Linear Combinations of Atomic Orbitals . . . . .	20
2.8 Basis Sets . . . . .	20
2.8.1 Slater Type Orbitals . . . . .	21
2.8.2 Gaussian Type Orbitals . . . . .	21

2.8.3	Basis set quality . . . . .	23
2.8.3.1	Minimal basis set . . . . .	23
2.8.3.2	Double zeta basis sets . . . . .	23
2.8.3.3	Polarised Basis Sets . . . . .	24
2.8.3.4	Diffuse Basis Sets . . . . .	25
2.8.4	Specific Basis Sets . . . . .	26
2.8.4.1	Atomic Natural Orbital Basis Sets . . . . .	27
2.8.4.2	Correlation Consistent Basis Sets . . . . .	27
2.8.4.3	Effective Core Potentials . . . . .	27
2.9	Hartree–Fock Theory . . . . .	29
2.10	Electron Correlation . . . . .	32
2.11	Post Hartree–Fock Methods . . . . .	35
2.11.1	Configuration Interaction . . . . .	35
2.11.2	The Complete/Restricted Active Space, Self-Consistent Field Methods (CASSCF/RASSCF) . . . . .	38
2.11.3	Many-Body Perturbation Theory and CASPT2 . . . . .	41
2.12	Density Functional Theory . . . . .	43
2.12.1	Hohenberg-Kohn Theorems . . . . .	44
2.12.2	Kohn-Sham Equations . . . . .	45
2.12.3	Exchange–Correlation Functionals . . . . .	46
2.12.3.1	The Local Density Approximations . . . . .	47
2.12.3.2	Generalised-Gradient Approximation and meta- GGA xc-Functionals . . . . .	48
2.12.3.3	Hybrid xc-functionals . . . . .	48
2.12.3.4	Double Hybrids . . . . .	49
2.12.3.5	Range-Separated Hybrids . . . . .	50
2.12.4	Excited States . . . . .	50
2.12.4.1	TD-DFT . . . . .	51
2.12.4.2	Tamm–Dancoff Approximation . . . . .	53
2.13	Relativistic Effects . . . . .	54
2.13.1	Effects in Atoms . . . . .	54
2.13.2	Relativistic Hamiltonian . . . . .	55
2.13.3	Relativistic Pseudopotentials . . . . .	57
2.14	The Quantum Theory of Atoms in Molecules . . . . .	57
2.14.1	Topological Properties of the Electron Density . . . . .	60
2.14.2	Integrated Properties of the Electron Density . . . . .	60
<b>3</b>	<b>Investigation of uranyl covalency via symmetry-preserving excited state structures</b> . . . . .	<b>70</b>
3.1	Introduction . . . . .	71
3.2	Computational Details . . . . .	73

3.3	Results and Discussion . . . . .	74
3.3.1	Electronic Properties at the Ground State Geometry . . . . .	74
3.3.2	Symmetric Stretching of the U-O bond . . . . .	79
3.3.2.1	Symmetry decomposition of QTAIM metrics . . . . .	81
3.3.3	Electronic Properties at Excited State Geometries . . . . .	82
3.3.4	The Optically Active Excited State . . . . .	87
3.4	Conclusions and Outlook . . . . .	88
<b>4</b>	<b>Exploring covalency in uranyl complexes with a variety of equatorial ligands</b> . . . . .	<b>95</b>
4.1	Introduction . . . . .	96
4.2	Computational Details . . . . .	98
4.3	Results and Discussion . . . . .	98
4.3.1	Ground State Geometries . . . . .	99
4.3.2	Excited State Geometries . . . . .	116
4.4	Conclusions . . . . .	130
<b>5</b>	<b>Investigating the effect of bending the uranyl unit on electronic structure and bonding</b> . . . . .	<b>136</b>
5.1	Introduction . . . . .	137
5.2	Methodology . . . . .	139
5.2.1	Bending bare uranyl - Multiconfigurational study . . . . .	139
5.2.2	DFT Studies . . . . .	140
5.3	Results and discussion . . . . .	142
5.3.1	Bending bare uranyl . . . . .	142
5.3.2	Synthetically realised complexes . . . . .	147
5.3.2.1	Ground State Geometry . . . . .	147
5.3.2.2	Excited State Geometries . . . . .	151
5.3.3	Theoretical complexes . . . . .	154
5.3.3.1	Ground state geometries . . . . .	155
5.3.4	Excited state geometries . . . . .	166
5.4	Conclusions . . . . .	170
<b>6</b>	<b>Investigation of a <i>trans</i> - <i>cis</i> isomerism in uranyl hydroxide analogues via intramolecular proton transfer</b> . . . . .	<b>178</b>
6.1	Introduction . . . . .	179
6.2	Computational Details . . . . .	181
6.3	Results and Discussion . . . . .	182
6.3.1	Effect of overall charge . . . . .	185
6.3.2	Replacing hydroxide with a halogen . . . . .	189
6.3.3	Effect of bite angle: investigation of bidentate ligands . . . . .	195
6.3.4	Summary . . . . .	200

6.4 Conclusions and future work . . . . .	202
<b>7 Conclusions and Outlook</b>	<b>207</b>

# List of Figures

1.1	Schematic showing the scale from ionic→covalent bonding between different groups of the periodic table, in contrast to a purely ionic (bottom) and purely covalency (top) systems. . . . .	3
1.2	Illustrative radial distribution functions for 4f,5s, 5p, 5d, 5f, 6s, 6p, and 6d atomic orbitals, reproduced with permissions from [7] . . . . .	4
1.3	N-donor ligands proposed for the SANEX process: BTP, BTBP and BTPPhen from top to bottom, respectively. . . . .	5
1.4	Representation of the three steps in the SANEX process . . . . .	6
1.5	MO diagram showing the bonding in $[\text{UO}_2]^{2+}$ redrawn with inspiration from [50] . . . . .	7
1.6	Combination of the uranium 6d orbitals with oxygen 2p resulting in the $\sigma_g, \pi_g, \sigma_g^*, \pi_g^*$ bonding and antibonding MOs. . . . .	8
1.7	Combination of the uranium 5f orbitals with oxygen 2p resulting in the $\sigma_u, \pi_u, \sigma_u^*, \pi_u^*$ bonding and antibonding MOs. . . . .	9
2.1	A comparison of Slater and Gaussian type functions for a 1s orbital: $n = 1, l = 0, N = 1, Y_{l,m}=1, \zeta=1$ . . . . .	23
2.2	A double zeta basis allows for bonding in two different directions, example molecule HCN, recreated with inspiration from [3]. C/N $p_x$ and $p_y$ AOs are represented by orange/grey electron distribution which have a smaller exponent associated with their basis functions; while C $p_z$ AOs (yellow/blue) have a larger exponent on the corresponding basis function. . . . .	24
2.3	A graph comparing GTOs with and without diffuse functions $\zeta = 0.1$ and $\zeta = 1$ respectively. . . . .	25
2.4	A comparison of three different basis sets, taking the exponents from the $p$ -functions on a carbon atom presented in [18] . . . . .	26
2.5	A flow chart showing the SCF process in the context of HF theory . . . . .	31
2.6	A visual representation of dynamic correlation in a helium atom, left arrangement is more favourable and lower in energy than the right . . . . .	34
2.7	A visual representation of static correlation in the $\text{H}_2$ molecule, left arrangement is more favourable and lower in energy than the right which shows ionic nature . . . . .	35

2.8	Excitations from the HF Slater determinant showing an example of single, double, triple and quadruple excitations; replacing 1, 2, 3 and 4 occupied spin orbitals with virtual orbitals. . . . .	36
2.9	Representation of the partitioning in both CASSCF and RASSCF methods . . . . .	40
2.10	Schematic of ‘Jacob’s Ladder of Chemical Accuracy’ representing different types of exchange-correlation functional. Drawn with inspiration from [83] . . . . .	47
2.11	Cubane molecule with all the CPs labelled. The bond critical points are shown in red, nuclear critical points are grey (carbon) and white (hydrogen), the bond paths are the lines which link the NCPs and BCP. The ring critical points are located in the centre of each square face (blue) and the cage critical point is the green dot in the centre of the cube. . . . .	59
3.1	Simple Jablonski diagram depicting the variations discussed in the analysis of the QTAIM results . . . . .	74
3.2	$\sigma_g^*$ MO showing diffuse character with significant O contribution . . . . .	78
3.3	Potential energy surfaces of the 15 lowest lying excitations of $A_g$ symmetry. State labels are indicated by the ordering of the excitations at the ground state as given in Table 3.1 and the excitations of interest are given as solid lines. . . . .	79
3.4	Trends in the QTAIM metrics: (a) charge ( $q$ ), (b) localisation index ( $\lambda$ ) and (c) delocalisation index ( $\delta$ ) as the U-O bond is elongated . . . . .	80
3.5	Variation in the symmetry-decomposed $\delta$ metrics when the U-O bond is elongated . . . . .	81
3.6	Comparison of density differences at ground (left) and excited (right) state geometries. Orange/black represents positive/negative electron density . . . . .	83
3.7	Graphs showing how (a) $q_U$ and (b) $q_O$ QTAIM metrics at the excited state electronic structures at both the ground (orange) and excited state (grey) geometries vary from $q_U$ and $q_O$ at ground state electronic structure at the ground state geometry (line). . . . .	85
3.8	Graphs showing how (a) $\lambda_U$ and (b) $\lambda_O$ QTAIM metrics at the excited state electronic structures at both the ground (orange) and excited state (grey) geometries vary from $\lambda_U$ and $\lambda_O$ at ground state electronic structure at the ground state geometry (line). . . . .	86
3.9	Graphs showing how $\delta_{U-O}$ QTAIM metrics at the excited state electronic structures at both the ground (orange) and excited state (grey) geometries vary from $\delta_{U-O}$ at ground state electronic structure at the ground state geometry (line). . . . .	86

4.1	Uranyl complexes studied in this chapter . . . . .	96
4.2	A schematic of the 4 lowest-lying excitations in uranyl complexes. $\Delta E$ is the excitation energy, in this case for the $\sigma_u \rightarrow \delta_u$ excitation. $\Delta^{\text{ES}}$ compares the excited state electronic structure at the excited state geometry to the ground state electronic structure at the ground state geometry, this will be the comparison made in Section 4.3.2 . . . . .	100
4.3	Comparison of the MOs of free uranyl and complex <b>(1)</b> which are involed in excitations depicted in Figure 3.1. $\sigma_u^+$ and $\sigma_u^-$ represent the $\sigma_u$ MOs which are a result of either bonding or anti-bonding interactions between the uranium centre and the coordinating chloride ligands respectively. . . . .	101
4.4	The four lowest-lying virtual MOs of complex <b>(6)</b> ; MOs 76, 78 and 79 have mostly $\phi_u$ nature and MO 77 showing some $\delta_u$ nature. . . . .	102
4.5	MO 73 and 74 in complex <b>(4)</b> which are related by a $45^\circ$ rotation and both have some antibonding character between the uranium 6d and nitrate 2p orbitals . . . . .	103
4.6	Density difference plots (from two different perspectives) for both $\sigma_u \rightarrow \delta_u$ excitations in free uranyl. Orange indicated areas of positive electron density and black negative. . . . .	104
4.7	Density difference plots for free uranyl and uranyl complexes, with the lowest energy excitation on the left and the highest on the right. . . . .	105
4.8	Linear regression performed on data given in Table 4.3 for both U-O <sub>y1</sub> and U-L bonds. These plots show negative correlation between bond length and $\rho_{\text{BCP}}$ for U-O <sub>y1</sub> <b>(a)</b> and U-L <b>(b)</b> bonds, with <b>(a)</b> having better linear correlation. . . . .	107
4.9	Linear regression performed on data from Tables 4.3, 4.1 and 4.2 for U-L bonds. These plots show <b>(a)</b> negative correlation between U-L $\rho_{\text{BCP}}$ and $\Delta E$ and <b>(b)</b> postive correlation between U-L bond length and $\Delta E$ . Data points from <b>(2)</b> and the U-Cl bond in <b>(6)</b> are omitted from the linear regression but are given in the plots. . . . .	108
4.10	$\rho_{\text{BCP}}$ values of the U-O <sub>y1</sub> bond vs U-L bond, showing a reasonable dependency between the $\rho_{\text{BCP}}$ values of the uranyl bond and the equatorial ligands. . . . .	109
4.11	Graphs showing positive correlation between $\delta$ and $\rho_{\text{BCP}}$ for both <b>(a)</b> U-O <sub>y1</sub> and <b>(b)</b> U-L bonds. . . . .	113
4.12	$\delta$ values of U-O <sub>y1</sub> vs U-L bonds, showing positive correlation between $\delta_{\text{U-O}_{y1}}$ and $\delta_{\text{U-L}^-}$ , with complex <b>(7)</b> being an outlier and no correlation between $\delta_{\text{U-O}_{y1}}$ and $\delta_{\text{U-L}^+}$ . . . . .	114

4.13	Comparison of the total delocalisation on the uranyl unit ( $\delta_{\text{U-O}_2}$ ) against <b>(a)</b> total localisation on the uranyl unit ( $\lambda_{\text{UO}_2}$ ) and <b>(b)</b> total delocalisation between the uranium-equatorial ligands ( $\delta_{\text{U-L}}$ ) . . . . .	115
4.14	Comparison of the total delocalisation on the uranyl unit ( $\delta_{\text{U-O}_2}$ ) against the combined total of the uranyl localisation ( $\lambda_{\text{UO}_2}$ ) and the delocalisation indices between the uranium and equatorial ligands ( $\delta_{\text{U-L}}$ ). . . . .	116
4.15	Density difference plots for the uranyl complexes at the excited state geometry, the lowest energy excitation on the left and the higher on the right. . . . .	119
4.16	Graphs showing negative correlation between bond length and $\rho_{\text{BCP}}$ at the excited state electronic structures at the excited state geometries for U-O <sub>yl</sub> <b>(a)</b> and U-L <b>(b)</b> . The two different excitations for each complex are represented with filled and unfilled marker for the lower and higher energy excitations respectively. . . . .	123
4.17	Graphs showing <b>(a)</b> general negative correlation between $\rho_{\text{BCP}}$ U-L and excitation energy and <b>(b)</b> positive correlation between U-L bond length and excitation energy for each coordinating ligand type at the excited state electronic structures at the excited state geometries . . .	124
4.18	Graph showing general positive correlation between U-O <sub>yl</sub> $\rho_{\text{BCP}}$ and $\Delta E$ at the excited state electronic structures at the excited state geometries . . . . .	125
4.19	Correlation between U-O <sub>yl</sub> bond length and excitation energy, giving two curves for the higher and lower excited states at the excited state electronic structures at the excited state geometries . . . . .	126
4.20	Graph showing no correlation between U-O <sub>yl</sub> $\rho_{\text{BCP}}$ and U-L $\rho_{\text{BCP}}$ at the excited state electronic structures at the excited state geometries	126
4.21	Graph showing no correlation between U-O <sub>yl</sub> $\rho_{\text{BCP}}$ and $\delta_{\text{U-O}_{yl}}$ at the excited state electronic structures at the excited state geometries . . .	127
4.22	Graph showing positive correlation between U-L $\rho_{\text{BCP}}$ and $\delta_{\text{U-L}}$ of individual at the excited state electronic structures at the excited state geometries . . . . .	128
5.1	Bonding (top) antibonding (middle) and non-bonding (bottom) MOs of uranyl included in the active space. The irrep, in the $c_{2v}$ point group is noted in brackets and only one of the two degenerate MOs are shown for the $\pi_u$ , $\pi_g$ , $\delta_u$ and $\phi_u$ MOs. . . . .	140
5.2	Trends in the excitation energy of the singlet (top) and triplet (bottom) states as the uranyl unit deviates from linearity. . . . .	143
5.3	The effect of distorting the O-U-O angle on the hole and particle MOs investigated in this study. . . . .	145

5.4	Experimental complexes studied in this investigation, reference [16] for a review . . . . .	147
5.5	Complex (ii) MOs with $\sigma_u$ character; arranged left to right in order of energy where left is the lowest energy MO (145, 159 & 161) . . . .	148
5.6	Macrocycles studied: (A)-(C) denote the crown ethers while complexes (D) and (E) are the porphyrinoids (porphyrin [porph] and phthalocyanine [phthalo] respectively). . . . .	154
5.7	Inclusion vs side-on coordination of the uranyl unit to the porphyrin macrocycle . . . . .	155
5.8	(C) (18C6) side-on complex, showing the crown ether unit curving as if to encase the uranyl unit . . . . .	156
5.9	Fully coordinated complexes . . . . .	161
5.10	UO <sub>2</sub> (OH) <sub>2</sub> 8C4 complex ((a)) in its excited state geometry, showing that the uranyl unit bends towards the crown ether macrocycle. . . .	167
6.1	Concerted mechanism proposed by Clark <i>et. al</i> explaining the rapid ligand exchange between axial and equatorial oxygens. [1, 3] . . . . .	180
6.2	Energy profile for a proton transfer from an equatorial hydroxide ligand to a uranyl oxygen as proposed by Schreckenbach <i>et. al</i> [2] The activation energy for the forward reaction ( <i>trans</i> → <i>Transition State (TS)</i> ) and the reverse ( <i>cis</i> → <i>TS</i> ) are represented by E <sub>a</sub> T‡ and E <sub>a</sub> C‡ respectively, while the relative stabilisation of the <i>trans</i> isomer with respect to the <i>cis</i> is denoted $\Delta^{\text{TC}}$ . . . . .	180
6.3	Two possible orientations for the equatorial hydroxide ligand at the <i>TS</i> optimised geometries . . . . .	182
6.4	IRC reaction path for complex (b); the stages of the curve, from left to right, represent the <i>cis</i> isomer, the <i>TS</i> and then the <i>trans</i> isomer at the lowest energy . . . . .	183
6.5	MOs with $\sigma_u$ and $\delta_u$ nature for each conformer of [UO <sub>2</sub> (OH) <sub>4</sub> ] <sup>2-</sup> . . . .	184
6.6	Energy diagrams at both the ground and excited states of complex (b) . . . .	185
6.7	Optimised <i>TS</i> geometries for the neutral ligand (H <sub>2</sub> O and NH <sub>2</sub> Me) complexes investigated . . . . .	186
6.8	Energy diagrams for complexes (b) and (iii) at both the ground (GS) and excited states (ES). . . . .	189
6.9	Optimised <i>TS</i> geometries for the halogen ligands (F, Cl and Br) complexes investigated . . . . .	190
6.10	Ground state energy diagrams for the complexes which have two halogen ligands 180° to each other ((C), (F) and (I)). . . . .	192
6.11	Optimised <i>TS</i> geometries for the bidentate complexes . . . . .	195
6.12	Ground state energy diagrams for complexes (b), (3) and (1). . . . .	198

6.13 Energy diagrams comparing the best complex from every section to  
the benchmark complex . . . . . 202

# List of Tables

1.1	Electronic configurations of the actinide elements . . . . .	2
2.1	Number of configurations generated in an $[n,n]$ -CASSCF wavefunction	38
2.2	Bond angles in minima complexes . . . . .	59
3.1	Excitation energies ( $\Delta E$ ) and natures of the 15 lowest energy singlet excitations of $A_g$ symmetry . . . . .	75
3.2	Summary of electronic excitations between bonding and antibonding MOs of the same character at the ground state geometry . . . . .	76
3.3	Integrated QTAIM metrics: charge ( $q$ ), localisation ( $\lambda$ ) and delocalisation ( $\delta$ ) indices at the ground (GS) and excited state electronic structures. . . . .	76
3.4	Topological QTAIM metrics (a.u.) at the ground and excited state electronic structures at the ground state geometry . . . . .	79
3.5	Symmetry-decomposed $\delta$ evaluated at the ground state minimum and the minimum value for each state on the PES given in Figure 3.3	82
3.6	Characterisation of electronic excitations ( $\Delta E$ ) at the excited state geometries of uranyl, the Stokes shift when compared to the excitation energy at the ground state geometries and the elongation of the U-O bond compared to the ground state geometry ( $\Delta r$ ). . . . .	82
3.7	Charge ( $q$ ), localisation index ( $\lambda$ ) and delocalisation index ( $\delta$ ) at the excited state electronic structures at the excited state geometries of the states of interest . . . . .	84
3.8	Topological QTAIM (a.u.) parameters at the excited state electronic structures at the excited state geometries of the states of interest . . . . .	87
3.9	Comparison of the QTAIM metrics: charge ( $q$ ), localisation index ( $\lambda$ ), delocalisation index ( $\delta$ ), $\rho_{\text{BCP}}$ , $\nabla^2\rho_{\text{BCP}}$ and $H$ at the ground (GS) and excited (ES) state equilibrium geometries at the excited state electronic structure for the optically active $\sigma_u \rightarrow \delta_u$ excitation . . . . .	88
4.1	Uranyl Complex average bond lengths calculated in this study (DFT) vs the experimental literature (Exp) . . . . .	99

4.2	Uranyl Complex excitation energies ( $\Delta E$ ) for the excitation of interest; comparison of calculated DFT values to experimental absorption energies (Exp) . . . . .	101
4.3	Topological QTAIM properties of the coordinating atoms to uranium in the ground state electronic structure at the ground state geometries; U-O <sub>yl</sub> and U-L. L: O, Cl or S; for the complexes which have both O/S and Cl coordination the U-Cl metrics are given second. . .	106
4.4	Charge ( $q$ ) and localisation ( $\lambda$ ) indices associated with the uranyl unit in the ground state electronic structure at the ground state geometries.	110
4.5	Delocalisation ( $\delta$ ) indices associated with the U-O <sub>yl</sub> bond and the U-L bonds at ground state electronic structure at the ground state geometries . . . . .	111
4.6	Changes in charge on the uranium and oxygen centres in the complexes in comparison to free uranyl and the ratio of these differences .	112
4.7	Total values of all metrics used in Figures 4.13 and 4.14 . . . . .	114
4.8	Excitation energies of the $\sigma_u \rightarrow \delta_u$ excitation at both the ground (GS) and excited state (ES) geometries . . . . .	117
4.9	Bond elongation ( $\Delta r$ ) in excited state geometries . . . . .	117
4.10	Topological QTAIM properties of the coordinating atoms to uranium, in the excited state electronic structures at the excited state geometries; U-O <sub>yl</sub> and U-L. L:O, Cl or S; for the complexes which have both O/S and Cl coordination the U-Cl metrics are given on the second row.	120
4.11	Charge ( $q$ ) and localisation index ( $\lambda$ ) integrated QTAIM metrics associated with the uranyl unit in the excited state electronic structures at the excited state geometries) . . . . .	121
4.12	Delocalisation ( $\delta$ ) indices associated with the uranyl unit in the excited state electronic structures at the excited state geometries . . . .	122
4.13	Summary of the transfer of charge occurring at the excited state electronic structures at the excited state geometries . . . . .	129
5.1	Symmetry properties of the irreps which contribute to the six lowest excitations for each irrep. . . . .	141
5.2	Excitation energies ( $\Delta E$ ) of the optically allowed excitation of principally $\sigma_u \rightarrow \delta_u$ character calculated on a selection of complexes from Chapter 4 with both aug-cc-pVDZ and cc-pVDZ basis sets at both the ground and excited state geometries. . . . .	142
5.3	Spin orbit free (SOF) and Spin orbit coupled (SOC) excitation energy and oscillator strength for the $\sigma_u \rightarrow \delta_u$ triplet excitation . . . . .	146

5.4	Comparison of the average bond lengths between the uranium centre and ligands between this study (DFT) and the experimental literature [1, 10, 48] (Exp). $L_1$ are the neutral ligands and $L_2$ the negatively charged ligands. ( $L_1$ : N, N and O(THF) and $L_2$ : Cl, OTf and O(Phen) for complexes (i) - (iii) respectively.) . . . . .	147
5.5	Excitation energies ( $\Delta E$ ), and overall contribution of the $\sigma_u \rightarrow \delta_u$ excitation at the ground state geometry . . . . .	148
5.6	Topological QTAIM metrics: $\rho_{\text{BCP}}$ , $\nabla^2 \rho_{\text{BCP}}$ and $H_{\text{BCP}}$ at the ground state geometries. . . . .	149
5.7	Integrated QTAIM metrics: $q$ , $\lambda$ and $\delta$ at the ground state geometries.	150
5.8	Comparison of the O-U-O bond angle (Angle) and excitation energy ( $\Delta E$ ) for the $\sigma_u \rightarrow \delta_u$ triplet excitation at the ground and excited state geometries . . . . .	151
5.9	Geometric bond lengths ( $\text{\AA}$ ) at the excited state geometries. . . . .	152
5.10	QTAIM topological metrics at the excited state electronic structures at the excited state geometry . . . . .	152
5.11	QTAIM integrated metrics at the excited state electronic structures at the excited state geometry . . . . .	153
5.12	Comparing uranyl bond angle (O-U-O) and energy difference ( $\delta E$ ) between the inclusion and side-on binding in minima geometries . . . .	155
5.13	Important bond lengths ( $\text{\AA}$ ): uranium to macrocycle O/N (U-M), distance of the uranyl unit above the macrocycle plane ( $\text{UO}_2\text{-P}$ ) and the U-O bond length in the uranyl unit ( $\text{U-O}_{\text{yl}}$ ); in the side-on coordinated complexes. . . . .	157
5.14	Comparing the symmetric and asymmetric stretches ( $\text{cm}^{-1}$ ) of the uranyl unit in the complexes . . . . .	158
5.15	Topological properties at the important critical points: electron density ( $\rho$ ), laplacian of electron density ( $\nabla^2 \rho$ ) and energy density ( $H$ ) at the ground state electronic structure at the ground state geometries.	158
5.16	Integrated properties: charge ( $q$ ), localisation ( $\lambda$ ) and delocalisation ( $\delta$ ) indices for the ground state electronic structures at the ground state geometries. . . . .	159
5.17	Excitation energies ( $\Delta E$ ) for the triplet $\sigma_u \rightarrow \delta_u$ excitation for the complexes studied . . . . .	160
5.18	Uranyl bond angles at the ground state geometries of the complexes .	161
5.19	Important bond lengths ( $\text{\AA}$ ) in the fully coordinated complexes: uranium to macrocycle O/N (U-M), distance of the uranyl unit above the macrocycle plane ( $\text{UO}_2\text{-P}$ ), uranium to ligand ( $\text{U-O}_{\text{lig}}$ ) and the U-O bond length in uranyl ( $\text{U-O}_{\text{yl}}$ ) . . . . .	162

5.20	Comparing the symmetric and asymmetric stretches ( $\text{cm}^{-1}$ ) in the uranyl unit . . . . .	163
5.21	Electronic reaction energies (eV) for both the gas and solvent phases .	164
5.22	Excitation energies ( $\Delta E$ ), for the OH/ $\text{H}_2\text{O}$ ligand complexes and the smallest difference in energy ( $\delta$ ) to the bare complexes in Table 5.17, for the $\sigma_u \rightarrow \delta_u$ triplet excitation . . . . .	165
5.23	$\rho_{\text{BCP}}$ , $\nabla^2 \rho_{\text{BCP}}$ and $H_{\text{BCP}}$ QTAIM metrics at the uranium-oxygen (U- $\text{O}_{\text{yl}}$ ), uranium-ligand (U-L) and uranium-macrocycle (U-M) BCPs at the ground state electronic structures of the fully coordinated complexes at the ground state geometries. . . . .	165
5.24	$q$ , $\lambda$ and $\delta$ QTAIM metrics at the ground state electronic structures of the fully coordinated complexes at the ground state geometries. . .	166
5.25	Comparison of the O-U-O bond angle and excitation energy ( $\Delta E$ ) for the $\sigma_u \rightarrow \delta_u$ triplet excitation at the ground and excited state geometries	167
5.26	Important bond lengths ( $\text{\AA}$ ) in the excited state complexes: uranium to macrocycle O/N (U-M), distance of the uranyl unit above the macrocycle plane ( $\text{UO}_2\text{-P}$ ), uranium to ligand (U- $\text{O}_{\text{lig}}$ ) and the U-O bond length in uranyl (U- $\text{O}_{\text{yl}}$ ) . . . . .	168
5.27	$\rho_{\text{BCP}}$ , $\nabla^2 \rho_{\text{BCP}}$ and $H_{\text{BCP}}$ QTAIM metrics at the uranium-oxygen (U- $\text{O}_{\text{yl}}$ ), uranium-ligand (U-L) and uranium-macrocycle (U-M) BCPs at the excited state electronic structures of the fully coordinated complexes at the excited state geometries. . . . .	169
5.28	$q$ , $\lambda$ and $\delta$ QTAIM metrics at the uranium (U), uranyl oxygens ( $\text{O}_{\text{yl}}$ ), ligand (L) and macrocycle (M) critical points at the excited state electronic structures of the fully coordinated complexes at the excited state geometries. . . . .	169
6.1	Lowest energy $\sigma_u \rightarrow \delta_u$ excitation energy ( $\Delta E$ ) and overall contribution from the transition of interest for the conformers of $[\text{UO}_2(\text{OH})_4]^{2-}$ . .	184
6.2	Comparison of the activation energies for the forward and reverse reaction ( $E_{\text{a}}\text{T}\ddagger/E_{\text{a}}\text{C}\ddagger$ ) and the <i>trans</i> stabilisation ( $\Delta^{\text{TC}}$ ) energy for complexes (i) - (vi) at the optimised geometries. . . . .	186
6.3	Lowest energy $\sigma_u \rightarrow \delta_u$ excitation energy ( $\Delta E$ ) and overall contribution from the transition of interest for the minimum and <i>TS</i> geometries of complexes (i) - (vi) . . . . .	187
6.4	Comparison of the activation energies for the forward and reverse reaction ( $E_{\text{a}}\text{T}\ddagger/E_{\text{a}}\text{C}\ddagger$ ) and the <i>trans</i> stabilisation ( $\Delta^{\text{TC}}$ ) energy in the excited states of complexes (i) - (vi) . . . . .	188
6.5	Comparison of the activation energies for the forward and reverse reaction ( $E_{\text{a}}\text{T}\ddagger/E_{\text{a}}\text{C}\ddagger$ ) and the <i>trans</i> stabilisation ( $\Delta^{\text{TC}}$ ) energy of complexes (A) - (I). . . . .	191

6.6	Lowest energy $\sigma_u \rightarrow \delta_u$ excitation energies ( $\Delta E$ ) and overall contribution from the transition of interest for the optimised geometries of complexes <b>(A)</b> - <b>(I)</b> . . . . .	193
6.7	Comparison of the activation energies for the forward and reverse reaction ( $E_a T^\ddagger / E_a C^\ddagger$ ) and the <i>trans</i> stabilisation ( $\Delta^{TC}$ ) energy of complexes <b>(A)</b> - <b>(I)</b> in the excited state (ES). . . . .	194
6.8	Bite angles of the bidentate complexes shown in Figure 6.11. . . . .	196
6.9	Comparison of the activation energies for the forward and reverse reaction ( $E_a T^\ddagger / E_a C^\ddagger$ ) and the <i>trans</i> stabilisation ( $\Delta^{TC}$ ) energy of complexes <b>(1)</b> - <b>(5)</b> in the ground state. . . . .	197
6.10	Lowest energy $\sigma_u \rightarrow \delta_u$ excitation energy ( $\Delta E$ ) and overall contribution from the transition of interest for the optimised geometries for complexes <b>(1)</b> - <b>(5)</b> . . . . .	199
6.11	Comparison of the activation energies for the forward and reverse reaction ( $E_a T^\ddagger / E_a C^\ddagger$ ) and the <i>trans</i> stabilisation ( $\Delta^{TC}$ ) energy of complexes <b>(1)</b> - <b>(5)</b> in the excited state (ES). . . . .	200
6.12	Comparison of the activation energies [ $\text{kJ mol}^{-1}$ ] ( $E_a T^\ddagger / E_a C^\ddagger$ ) and the <i>trans</i> stabilisation energies ( $\Delta^{TC}$ ) [ $\text{kJ mol}^{-1}$ ] for all complexes studied in this chapter at both the ground (GS) and excited states (ES). . . . .	201

# List of Abbreviations

Abbreviation	Definition
ANO	Atomic Natural Orbital
AO	Atomic Orbital
BCP	Bond Critical Point
CASPT2	Complete Active Space with Second-order Perturbation Theory
CASSCF	Complete Active Space Self-Consistent Field
CC	Coupled Cluster
CGTO	Contracted Gaussian Orbital
CI	Configuration Interaction
CP	Critical Point
CT	Charge Transfer
DFT	Density Functional Theory
DOE	Department of Energy
ECP	Effective Core Potential
ES	Excited State
ESES	Excited State Electronic Structure
ESG	Excited State Geometry
FCI	Full Configuration Interaction
GGA	Generalised-Gradient Approximation
GS	Ground State
GSES	Ground State Electronic Structure
GSG	Ground State Geometry
GTO	Gaussian Type Orbital
HF	Hartree-Fock
HOMO	Highest Occupied Molecular Orbital
HP	Hartree Product
IPEA	Ionisation Potential Electron Affinities

IRC	Intrinsic Reaction Coordinate
LCAO	Linear Combination of Atomic Orbitals
LDA	Local Density Approximation
LUMO	Lowest Unoccupied Molecular Orbital
MO	Molecular Orbital
MP2	Second-order Moller-Plessett Perturbation Theory
PES	Potential Energy Surface
PGTO	Primitive Gaussian Orbital
PUREX	Plutonium and Uranium Reduction EXtraction
QTAIM	Quantum Theory of Atoms in Molecules
RASSCF	Restricted Active Space Self-Consistent Field
RASSI	Restricted Active Space State Interaction
RECP	Relativistic Effective Core Potential
SANEX	Selective ActiNide Extraction
SCF	Self-Consistent Field
SOC	Spin Orbit Coupling
SOF	Spin Orbit Free
STO	Slater Type Orbital
TALSPEAK	Trivalent Actinide Lanthanide Separation with Phosphorus-Reagent Extraction from Aqueous Komplexes
TD-DFT	Time-Dependent Density Functional Theory
TDA	Tamm-Dancoff Approximation
TS	Transition State

---

---

# Chapter 1

## Introduction

*In this chapter, the context of this research, along with some of the relevant literature is discussed, although further literature discussion is delayed until the introductions of each chapter. This chapter will start with an overview of: the relevant aspects of actinide chemistry, nuclear power and its problems, uranyl chemistry and the rest of the thesis.*

## 1.1 Actinide Chemistry

The actinides are comprised of elements 89→103, Ac→Lr all of which are radioactive, radiotoxic, paramagnetic and pyrophoric, which makes them hazardous to handle. [1–4] These properties highlight the significance of computational investigations in addition to experimental work in order to limit difficulties and expenses when handling such radioactive substances.

Upon traversing the actinide series the electronic configuration is not simply iterative *i.e.* [Rn]  $7s^2, 5f^n$ , where  $n$  takes values 1-14 in single integer steps. Instead, the subshells are filled in a similar way to the transition metals, which instead of a  $d^{4/9}$  configuration an electron is removed from the s subshell resulting in an  $s^1, d^{5/10}$  electronic configuration. In contrast to the transition metals, instead of removing an electron from the 7s shell, the ‘next’ electron is added/removed from the 6d shell, which occurs due to the 5f and 6d shells being close in energy. A generalised electronic configuration of actinides can be summarised as [Rn]  $5f^n, 6d^m, 7s^2$ ; where  $n$  takes values between 0-14 and  $m$ : 0-2. [1–4] Table 1.1 summarises the electronic configurations of the actinides. [3]

Table 1.1: Electronic configurations of the actinide elements

Elements	Ac→Th	Pa→Np	Pu→Am	Cm	Bk→No	Lr
Electronic Configuration [Rn]	$5f^0$ $6d^{1-2}$ $7s^2$	$5f^{2-4}$ $6d^1$ $7s^2$	$5f^{6-7}$ $6d^0$ $7s^2$	$5f^7$ $6d^1$ $7s^2$	$5f^{9-14}$ $6d^0$ $7s^2$	$5f^{14}$ $6d^1$ $7s^2$

In contrast to other groups, (*i.e.* transition metals and lanthanides), there is variation between the chemistry within the actinide group. In general, the actinides can be separated into; the early actinides: Ac→Am, which bear some similarities in the structure and bonding characteristics to the transition metals while the latter actinides: Cm→Lr are more similar to the lanthanides. The early actinides have multiple oxidation states, whereas, the latter actinides have increasing ionic character and a preference for the +3 oxidation state. Figure 1.1 gives a generalised overview of the bonding interactions present in the groups discussed above. In contrast to these trends, it is worth noting that covalency in Bk and Cf has been established by Albrecht-Schmitt and co-workers. [5, 6]

Scalar relativistic effects are more prominent in the actinides in comparison to the lanthanides and hence it is critical that they are accounted for in computational simulation. Scalar relativistic effects occur everywhere on the periodic table, with these effects becoming particularly prominent after Pt (78). [7] In short, objects moving at a substantial fraction of the speed of light increase in mass, therefore as

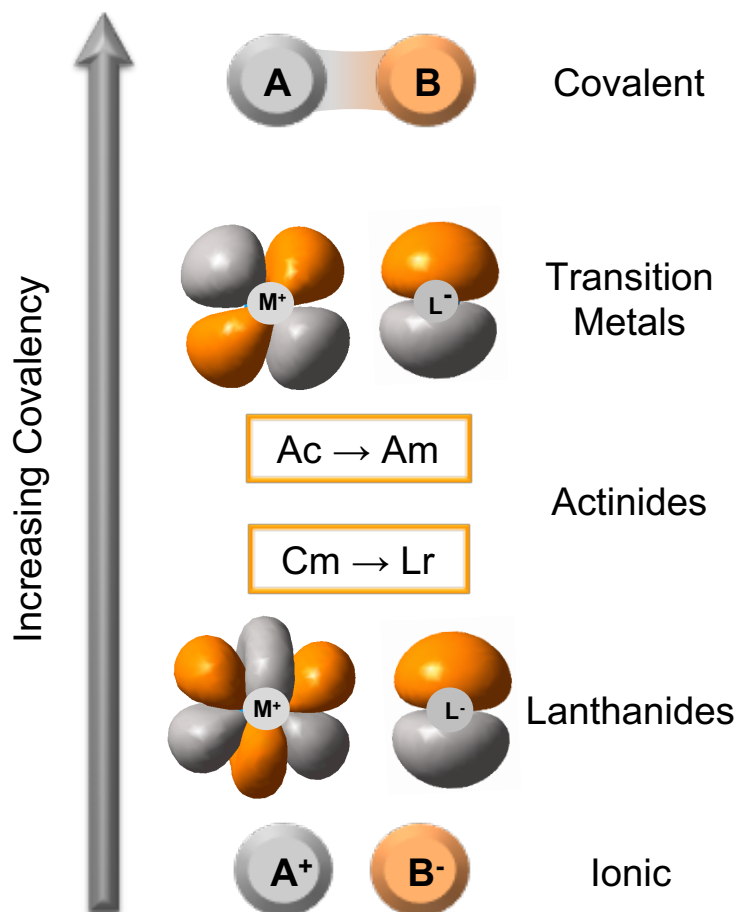


Figure 1.1: Schematic showing the scale from ionic→covalent bonding between different groups of the periodic table, in contrast to a purely ionic (bottom) and purely covalency (top) systems.

an electron travels a significant fraction of the speed of light the relativistic mass of the electron increases. This increase in mass causes the s and p orbitals to contract which results in the d and f orbitals becoming more shielded from the effective nuclear charge and become expanded. This contraction can be clearly seen in the radial distribution functions given in Figure 1.2, reproduced with permissions from reference [7].

Interestingly in actinides, the 5f and 6d orbitals are very close in energy and as a result, both can contribute to the bonding. As expected, this is most prevalent in the early actinides (as these behave more like transition metals) and highlighted in the electronic configuration of Th ( $6d^2, 7s^2$ ), [8] this indicates that the 6d orbitals are lower in energy than the 5f.

Hybridisation of the 5f and 6d orbitals, is seen in the early actinides, particularly in valence MOs in low symmetry complexes, as a result of the 5f and 6d orbitals being close in energy. Again this is highlighted in their electronic configurations (Table 1.1), where the first 5 actinides have 6d contributions in their ground state electronic configurations. In general, as the series is traversed the energy of the 5f orbitals decreases as they contract and become more core-like while the 6d increase;

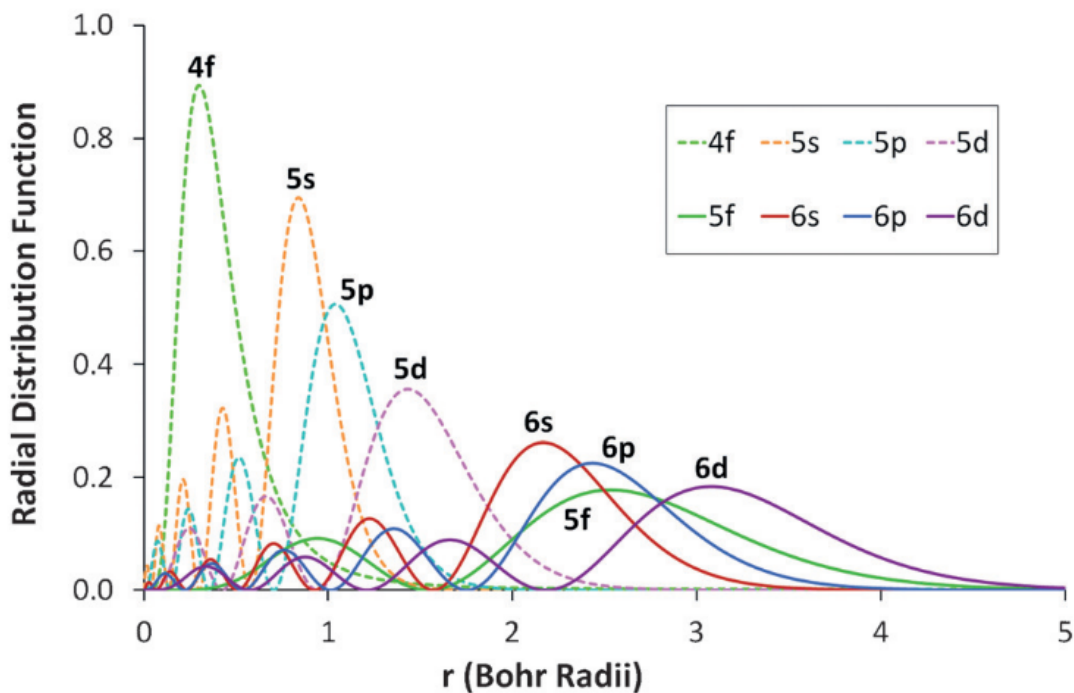


Figure 1.2: Illustrative radial distribution functions for 4f, 5s, 5p, 5d, 5f, 6s, 6p, and 6d atomic orbitals, reproduced with permissions from [7]

with the 5f and 6d orbital energies passing each other at uranium. [9–13]

The most obvious and well-known application of actinides is within the nuclear power industry in which uranium and plutonium decay upon absorption of a neutron generating heat and releasing more neutrons, resulting in a controlled chain reaction. Other applications of actinides include: smoke detectors (Am), [14] gas mantles (Th), [15] powering heart pacemakers (Pu), portable heat sources in NASA space missions (Pu) and as neutron and gamma sources in industry and medicine (Ac). [3]

## 1.2 Problems with nuclear power

As mentioned previously, the nuclear industry is the dominant application for actinide chemistry. Currently, nuclear power accounts for 15% of the world’s electricity, which is likely to increase based on the growing energy demands. [16] A major problem within the nuclear industry is managing and storing the long-lived and highly radiotoxic spent nuclear fuel. Typically, a nuclear reactor will generate 20 metric tons of spent fuel in a year [17] and with demand likely to increase, long-term storage of dangerous spent fuel is going to become a more prominent issue.

Spent nuclear fuel consists of radioactive: U, Pu, Np, Am, Cm, lanthanides, and other various fission products. Typically, spent nuclear fuel comprises roughly 96% U, 1% Pu and 3% fission products including the other actinides (Np, Am, Cm), which are termed ‘*minor actinides*’. It is these minor actinides which are responsible

for the long-term heat load, are highly radiotoxic and have very long lifetimes. [18] By use of the PUREX [19–21] (Plutonium and Uranium Reduction EXtraction) process, which is a liquid-liquid extraction ion-exchange process, U and Pu can be extracted for re-use. This leaves the minor actinides along with the fission products mentioned above.

As the minor actinides are responsible for the longevity of the post-PUREX nuclear waste (many thousands of years), methods of separating the minor actinides have grown over the years. The difficulty in separating the minor actinides from the rest of the post-PUREX waste stems from the fact that the minor actinides and lanthanides have similar chemistries, both of which are dominated by the +3 oxidation state. [22] Once separated, the minor actinides can for example, be transmuted in fast neutron reactors, resulting in shorter-lived and less hazardous isotopes. [23] This transmutation is not possible when lanthanides are present, due to their large neutron cross-section and hence separation [24, 25] of these from the minor actinides is vital for more cost-effective nuclear waste storage.

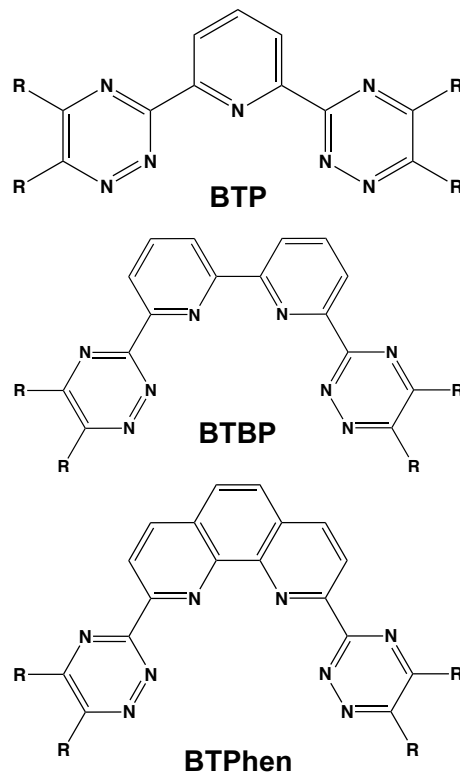


Figure 1.3: N-donor ligands proposed for the SANEX process: BTP, BTBP and BTPhen from top to bottom, respectively.

The SANEX (Selective ActiNide EXtraction) process utilises soft-donor N-ligands, such as bis-triazinyl-pyridines (BTPs), bis-triazinyl-bipyridines (BTBPs) and bis-triazinyl-phenanthrolines (BTPhens), Figure 1.3 which selectively complex the minor actinides over the lanthanides. [26–31] This process has three stages, which are shown in Figure 1.4. The first step mixes the post-PUREX waste with an organic solvent containing the N-donor ligands, this extracts the minor actinides

into the organic phase. Next, the aqueous phase is scrubbed with nitric acid, removing the lanthanides. Finally, the minor actinides are stripped from the N-donor ligands back into the aqueous phase. [20, 32]

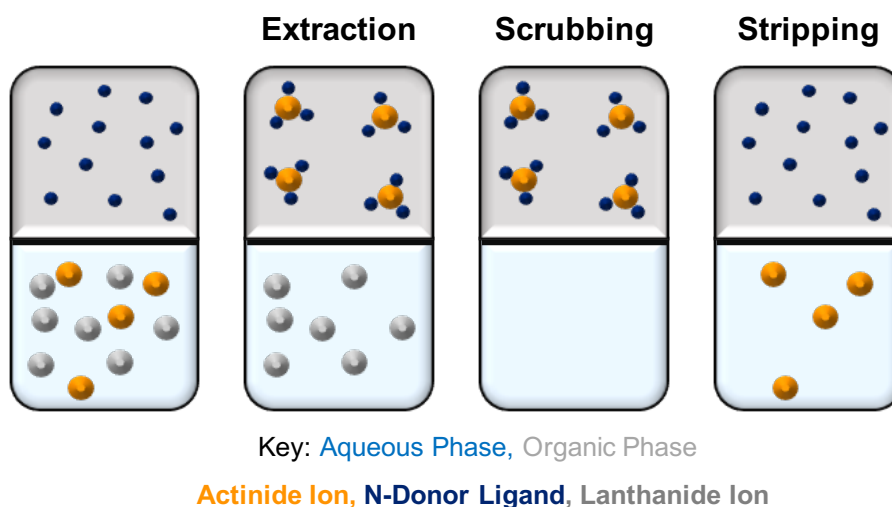


Figure 1.4: Representation of the three steps in the SANEX process

While the SANEX method has several advantages over other methods: low energy input and the ability to recycle the organic phase, design of the ligands is challenging due to them needing to withstand harsh acidic conditions and radioactivity. [29, 33, 34]

Another well documented method for the separation of 4f/5f elements is the TALSPEAK (Trivalent Actinide Lanthanide Separation with Phosphorus-reagent Extraction from Aqueous Komplexes) process. To summarise, this process utilises mixed O/N donor ligands and retains the actinides in the aqueous phase while the lanthanides are separated. [35] While TALSPEAK is efficient this method has two main disadvantages: requires a rigid narrow pH range and the phase transfer kinetics are often slower than ideal. [36]

It is important to enhance understanding of the bonding interactions within actinide complexes both from a fundamental and practical standpoint. Development and design of ligands which selectively complex actinides over lanthanides in the same oxidation state is of particular relevance to the nuclear waste problem. Computational investigations offer a great tool in the search for selectively complexing ligands. Using computational modelling rather than experimental work allows the exploration of properties which are hard to quantify experimentally, investigation of hypothetical/hard to synthesise complexes and many complexes can be studied simultaneously. [37] The fundamental nature of actinides however make them challenge to model computationally. [38–43] Actinide complexes have strong electron correlation, weak crystal fields and relativistic effects are significant. The challenges with computational modelling and actinides is further explored in Chapter 2. It is worth noting that there are numerous computational studies on actinide systems

with different methodologies throughout the literature. [39, 44–47]

## 1.3 Uranyl

Within the ever expanding field of actinide chemistry, uranium still remains the most extensively studied element. [7, 48, 49] Amongst the vast array of hexavalent uranium chemistry, the uranyl ion ( $[\text{UO}_2]^{2+}$ ) is the most ubiquitous fragment. Uranyl is a chemically robust species with two short, strong and collinear U-O triple bonds, which suppress the reactivity of the uranyl unit and result in equatorial ligation exclusively. [50–52]

### 1.3.1 Structure and Bonding

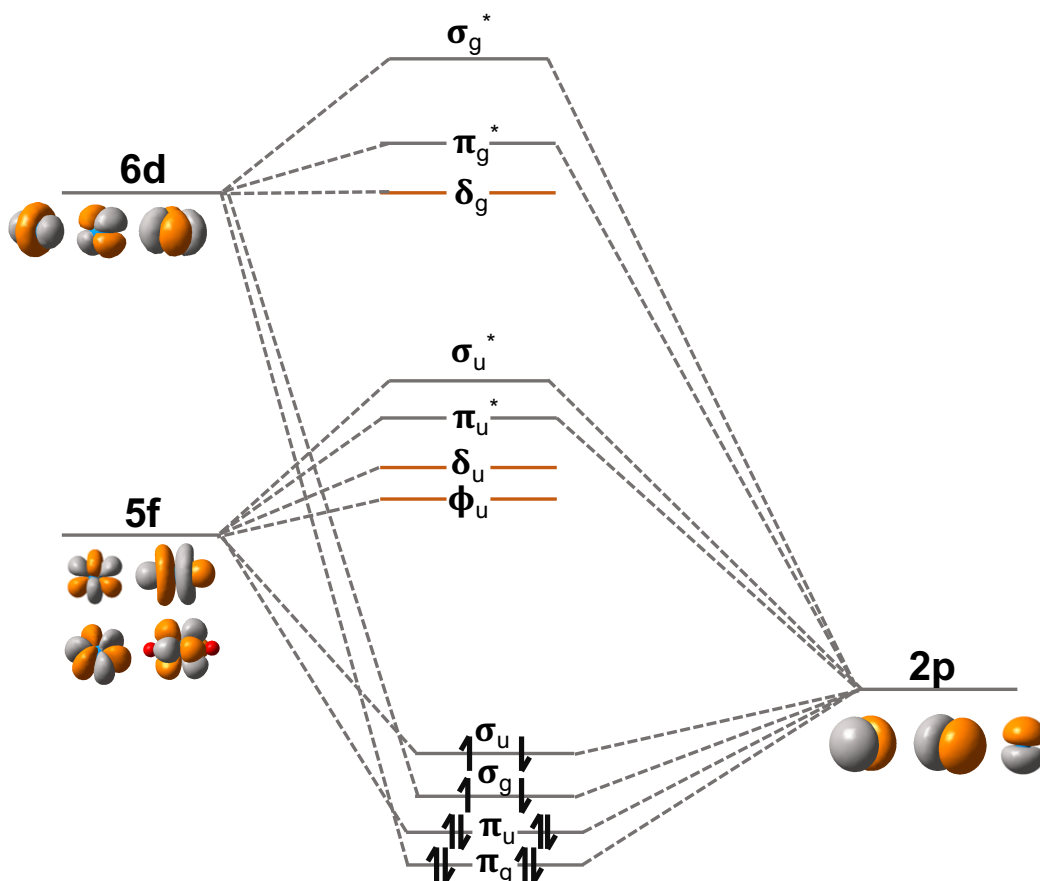


Figure 1.5: MO diagram showing the bonding in  $[\text{UO}_2]^{2+}$  redrawn with inspiration from [50]

In contrast to similar structures, seen in group VI transition metals species ( $\text{MoO}_2$ ,  $\text{RuO}_2$ ,  $\text{WO}_2$  *etc.*) the uranyl bond is linear. Thermodynamic studies have shown that the bond strength is also much greater than in the transition metal analogues, with the bond strength being comparable to  $\text{CO}_2$ . [53–55] As well as being thermodynamically robust, uranyl has also been found to be kinetically inert, with the rate of isotopic oxygen exchange between water and uranyl oxygens resulted in

an exchange half-life of over 40,000 hours. [55, 56] The chemical stability of uranyl accounts for the vast array of coordination chemistry which is exploited in many areas, an example of which is the solvent extraction PUREX process in the nuclear fuel cycle described in section 1.2. [20]

The molecular orbital (MO) diagram, replicated from reference [50] for uranyl is given in Figure 1.5. The lowest unoccupied molecular orbitals (LUMO) arise from the 5f orbitals which have  $\delta$  and  $\phi$  character, with respect to the U-O bond, as these cannot overlap with the oxygen 2p MOs. These MOs are comprised of the:  $5f_{z(x^2-y^2)}$  and  $5f_{xyz}$ ,  $\delta$  orbitals and  $5f_{y(3x^2-y^2)}$  and  $5f_{x(x^2-3y^2)}$   $\phi$  orbitals and are known as the non-bonding MOs in uranyl, labelled  $\delta_u$  and  $\phi_u$ , respectively. It is also worth noting that the MOs with  $\delta$  character from the 6d shell, labelled  $\delta_g$  are also non-bonding; these correspond to the  $6d_{xy}$  and  $6d_{x^2-y^2}$  orbitals. The rest of the 5f and 6d orbitals, those with  $\pi$  and  $\sigma$  nature combine with the 2p orbitals in oxygen to give the:  $\sigma_u$ ,  $\sigma_g$ ,  $\pi_u$  and  $\pi_g$  bonding MOs and  $\sigma_u^*$ ,  $\sigma_g^*$ ,  $\pi_u^*$  and  $\pi_g^*$  antibonding MOs. The 6d orbitals in uranium combine with the 2p in oxygen resulting in MOs with *gerade* symmetry, while the 5f and 2p orbitals combine to give MOs with *ungerade* symmetry. The combinations of  $U_{5f/6d}$  and  $O_{2p}$  are given in detail in Figures 1.6 and 1.7.

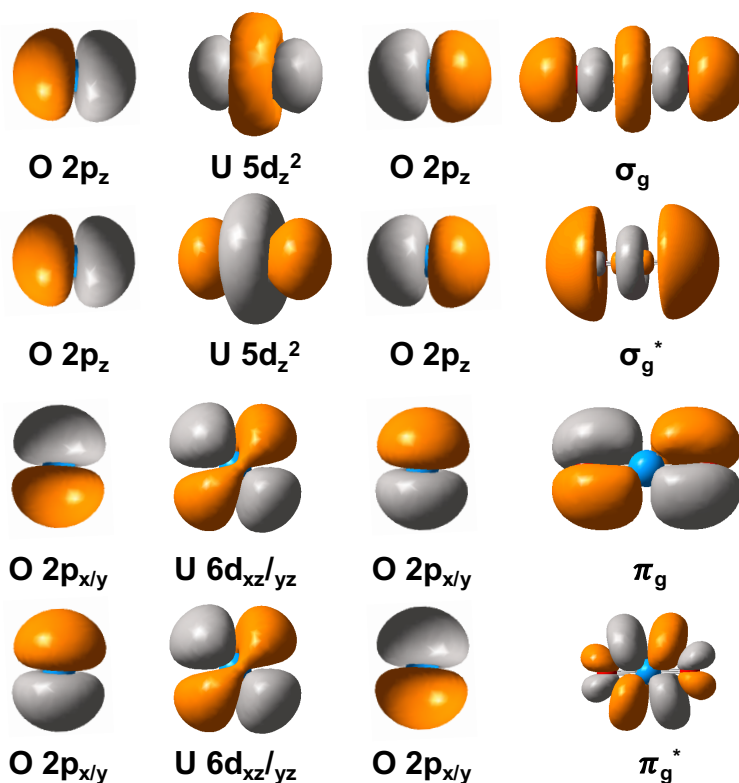


Figure 1.6: Combination of the uranium 6d orbitals with oxygen 2p resulting in the  $\sigma_g$ ,  $\pi_g$ ,  $\sigma_g^*$ ,  $\pi_g^*$  bonding and antibonding MOs.

In contrast to the other bonding MOs, it has been proven that the  $\sigma_u$  is higher in energy relative to the other five bonding MOs ( $2\pi_u$ ,  $2\pi_g$  &  $\sigma_g$ ). This has been explain via a ‘*pushing from below*’ mechanism which involves the pseudocore U6p orbitals which results in the destabilisation of the  $\sigma_u$  MO. [44, 46, 57–60]

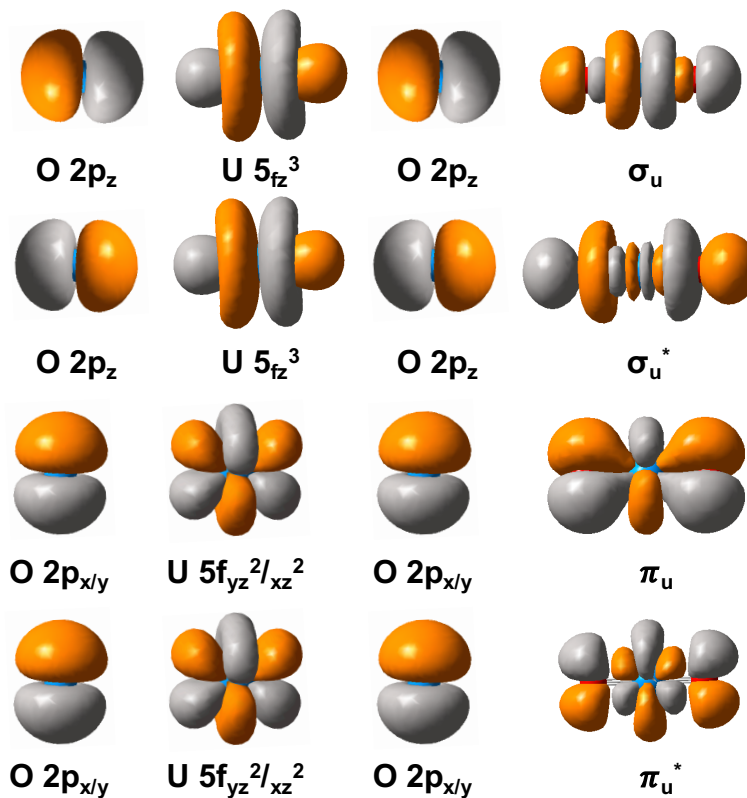


Figure 1.7: Combination of the uranium 5f orbitals with oxygen 2p resulting in the  $\sigma_u$ ,  $\pi_u$ ,  $\sigma_u^*$ ,  $\pi_u^*$  bonding and antibonding MOs.

### 1.3.2 Optical Spectra

The optical spectra of uranyl has intrigued scientists for decades, since Brewster [61] started investigating the green luminescence of uranium glass. This green luminescence (phosphorescence) occurs due to the relaxation from the lowest triplet excited state to the singlet ground state. [62] Given the MO diagram in Figure 1.5, this transition would correspond to relaxation from the non-bonding  $\phi_u/\delta_u$  MOs to the  $\sigma_u$  bonding MO. It is worth highlighting that this transition is formally forbidden according to the Laporte Rule; in which transitions between states of the same symmetry with respect to inversion are forbidden, [63] but allowed via spin-orbit coupling (SOC). [55]

The absorption and luminescent spectrum of uranyl has been studied extensively, both experimentally, [50, 55, 64–69] and computationally. [47, 70–75] Due to the destabilisation of the  $\sigma_u$  bonding MO transitions out of this into the non-bonding  $\delta_u/\phi_u$  MO are the lowest-lying excitations, with a typical spectrum having a range of 2.48 eV - 3.71 eV.

Detailed spectroscopic studies have been performed by Denning and co-workers [50, 55, 69] who studied crystalline uranyl chloride and uranyl nitride complexes (also studied in this thesis in Chapter 4). They concluded that the energy of the low-lying excited states is largely independent of the equatorial ligand. These findings were also concluded by Gorller-Walrand and Vanquickenborne [66, 67] who studied

a series of different uranyl complexes in solution.

Pierloot *et.al.* studied the low-lying excited states of free uranyl ( $[\text{UO}_2]^{2+}$ ) and uranyl chloride ( $[\text{UO}_2\text{Cl}_4]^{2-}$ ) with both Complete Active Space Self-Consistent Field (CASSCF)/Complete Active Space with Second-order Perturbation Theory (CASPT2) and Density Functional Theory (DFT). [46, 70] They concluded that the lowest-lying excitations are made up of transitions from the  $\sigma_u$  bonding MO to the  $\delta_u/\phi_u$  non-bonding MOs as predicted by experiment. Interestingly, allowing for spin-orbit coupling effects, they concluded that it is the  $\sigma_u \rightarrow \delta_u$  excitation, which is allowed via spin-orbit coupling. They also found reasonable agreement between both the CASPT2 and DFT studies and the experimental data, although the CASPT2 data was superior.

## 1.4 Thesis Overview

This chapter gave an overview of the chemistry and motivation behind the studies in this thesis. Throughout the introductory sections of each chapter the relevant literature and background information is provided in more detail.

This thesis has two main themes: covalency in the uranyl unit and how this is affected in the electronically excited state of the optically accessible  $\sigma_u \rightarrow \delta_u$  excitation. This excitation is one of the lowest-lying excitations in uranyl and its complexes and is allowed via spin-orbit coupling. [46, 47, 71, 72, 76]

Chapter 2 discusses the theory and methodology of electronic structure methods. A brief overview of quantum mechanics alongside the fundamentals of wavefunction theories, Density Functional Theory (DFT) and the Quantum Theory of Atoms in Molecules (QTAIM), a density-based analysis method is given.

The first results chapter (Chapter 3) explores the covalency of free uranyl in the ground and electronically excited states which maintain symmetry as well as the optically accessible  $\sigma_u \rightarrow \delta_u$  excitation. Using the findings of Chapter 3, the investigation is extended in Chapter 4 to simple uranyl complexes, where only the optically accessible  $\sigma_u \rightarrow \delta_u$  excitation is studied. Firstly, the changes in covalency of the uranyl unit upon equatorial ligation is studied followed by an exploration of the changes in structure and bonding at the electronically excited state geometries.

The first two result chapters cover the effects of excitation and equatorial coordination on covalency of the uranyl unit. Chapter 5 turns attention to bending of the uranyl unit. This chapter is split into three investigations. The first is a Complete Active Space Self-Consistent Field (CASSCF) and second order perturbation (CASPT2) study on gradually distorted free uranyl in order to investigate whether the optically accessible  $\sigma_u \rightarrow \delta_u$  excitation is still optically active when the uranyl unit is distorted. Secondly, the effects of bending on the covalency and whether this is enhanced by excitation into the  $\sigma_u \rightarrow \delta_u$  electronically excited state on experimentally realised complexes with bent O-U-O unit is investigated. Finally, using

the information obtained about the electronic structure in the synthetically realised complexes, theoretical complexes were designed and studied to initiate a smaller O-U-O angle.

The final results chapter (Chapter 6) explores a second way to bend the uranyl unit via a *trans*→*cis* isomerism, starting with the model uranyl tetrahydroxide complex studied by Schreckenbach *et. al.* [77] The energy profile for the *trans*→*cis* isomerism was investigated on variety of complexes by swapping one or two hydroxide ligands for different ligand types *i.e.* neutral ligands, more/less electronegative ligands, bidentate ligands in order to see if the *trans*→*Transition State (TS)* barrier would decrease and/or the *cis* isomer was stabilised. The effect of vertically exciting into  $\sigma_u \rightarrow \delta_u$  state on the barrier heights was also investigated. Although no excited state geometries were investigated in this study due to significant computational cost for obtaining an excited state *TS* geometry.

A summary of the findings and concluding remarks can be found in Chapter 7.

# References

- [1] T. Gray in *Elements: A Visual Exploration of Every Known Atom in the Universe*, Black Dog & Leventhal, **2012**, p. 240.
- [2] N. N. Greenwood, A. Earnshaw in *Chemistry of the Elements*, Butterworth-Heinemann, **1997**, p. 1264.
- [3] Chemistry LibreTexts, <https://chem.libretexts.org/Bookshelves/The-Actinides/1General-Properties-and-Reactions-of-The-Actinides>, Accessed: 2022-05-13.
- [4] L. Morss, L. B. Asprey, actinoid element. Encyclopedia Britannica. <https://www.britannica.com/science/actinoid-element>, Accessed: 2022-05-13, **2018**.
- [5] S. K. Cary, M. Vasiliu, R. E. Baumbach, J. T. Stritzinger, T. D. Green, K. Diefenbach, J. N. Cross, K. L. Knappenberger, G. Liu, M. A. Silver, A. E. DePrince, M. J. Polinski, S. M. Van Cleve, J. H. House, N. Kikugawa, A. Gallagher, A. A. Arico, D. A. Dixon, T. E. Albrecht-Schmitt, *Nat. Commun.* **2015**, 6827.
- [6] T. E. Albrecht-Schmitt, D. E. Hobart, D. Páez-Hernández, C. Celis-Barros, *Int. J. Quantum Chem.* **2020**, 26254.
- [7] S. T. Liddle, *Angew. Chem. Int. Ed.* **2015**, *54*, 8604–8641.
- [8] E. F. Worden, J. Blaise, M. Fred, N. Trautmann, J. F. Wyatt in *The Chemistry of the Actinide and Transactinide Elements*, (Eds.: L. Morss, N. M. Edelstein, J. Fuger), Springer, Berlin, **2006**, Chapter Vol 3, p. 1836.
- [9] J. Blaise, J. F. Wyatt, *International Tables of Selected Constants* **1992**, *20*.
- [10] W. J. Liu, W. Küchle, M. Dolg, *Phys. Rev. A.* **1998**, *58*, 1103.
- [11] X. Y. Cao, M. Dolg, *Mol. Phys.* **2003**, *101*, 961.
- [12] B. A. Palmer, R. Engleman, *J. Opt. Soc. Am.* **1984**, *1*, 609.
- [13] B. E. Bursten, L. F. Rhodes, R. J. Strittmatter, *J. Am. Chem. Soc.* **1989**, *111*, 2756.
- [14] N. N. Greenwood, A. Earnshaw in *Chemistry of the Elements*, Butterworth-Heinemann, **1997**, p. 1262.

- [15] N. N. Greenwood, A. Earnshaw in *Chemistry of the Elements*, Butterworth-Heinemann, **1997**, p. 1255.
- [16] H. H. Dam, D. N. Reinhoudt, W. Verboom, *Chem. Soc. Rev.* **2007**, *36*, 367–377.
- [17] Nuclear Energy Institute, <http://www.nei.org/Knowledge-Center/Nuclear-Statistics/World-Statistics>. Accessed: 2022-04-13.
- [18] J. Narbutt in *Liquid-Phase Extraction*, (Ed.: C. F. Poole), Elsevier, **2020**, pp. 725–744.
- [19] N. Kaltsoyannis, *Inorg. Chem.* **2013**, *52*, 3407–3413.
- [20] J. M. McKibben, *Radiochim. Acta.* **1984**, *36*, 3–5.
- [21] A. K. Wilson, T. Van Mourik, T. H. J. Dunning, *J. Mol. Struct.: THEOCHEM* **1996**, *388*, 339–349.
- [22] P. A. Baisden, G. R. Choppin in Nuclear waste management and the nuclear fuel cycle, **2007**.
- [23] L. Koch, *J. Less-Common Met.* **1986**, *122*, 371–382.
- [24] J. Alstad, T. Jahnsen, A. C. Pappas, *J. Inorg. Nucl. Chem.* **1967**, *29*, 2155–2160.
- [25] M. Salvatores, G. Palmiotti, *Prog. Part. Nucl. Phys.* **2011**, *66*, 144–166.
- [26] F. W. Lewis, L. M. Harwood, M. J. Hudson, M. G. B. Drew, A. Wilden, M. Sypula, G. Modolo, T. Vu, G. Vidick, N. Bouslimani, J. F. Desreux, *Procedia Chem.* **2012**, *7*, 231–238.
- [27] Z. Kolarik, *Solvent Extr. Ion Exch.* **2003**, *21*, 381–397.
- [28] M. G. B. Drew, M. R. S. J. Foreman, C. Hill, M. J. Hudson, C. Madic, *Inorg. Chem. Com.* **2005**, *8*, 239–241.
- [29] F. W. Lewis, M. J. Hudson, L. M. Harwood, *Synlett* **2011**, *18*, 2609–2632.
- [30] L. Petit, C. Adamo, P. Maldivi, *Inorg. Chem.* **2006**, *45*, 8517–8522.
- [31] T. Retegan, C. Ekberg, I. Dubois, A. Fermvik, G. Skarnemark, T. J. Wass, *Solvent Extr. Ion Exch.* **2007**, *25*, 417–431.
- [32] L. S. Natrajan, M. H. Paden, *F-block elements recovery, Vol. 58*, **2013**, pp. 140–184.
- [33] Z. Kolarik, *Chem. Rev.* **2008**, *108*, 4208–4252.
- [34] M. J. Hudson, L. M. Harwood, D. M. Laventine, F. W. Lewis, *Inorg. Chem.* **2013**, *52*, 3414–3428.
- [35] B. Weaver, F. A. Kappelmann, *J. Inorg. Nucl. Chem.* **1968**, *30*, 263–272.
- [36] K. L. Nash, *Solvent Extr. Ion Exch.* **2015**, *33*, 1–55.

- [37] Q. J. Pan, S. O. Odoh, G. Schreckenbach, P. L. Arnold, J. B. Love, *Dalton Trans.* **2012**, *41*, 8878–8885.
- [38] M. Seth, P. Schwerdtfeger, M. Dolg, P. Fulde, *J. Am. Chem. Soc.* **1995**, *117*, 6597–6598.
- [39] M. Dolg, *Encyclopedia of Computational Chemistry*, (Ed.: E. H. F. Schaefer), Wiley, Chichester, **2002**.
- [40] P. Söderlind, A. Gonis, *Phys. Rev. B.* **2010**, *82*, 1–4.
- [41] G. Schreckenbach, G. A. Shamov, *Acc. Chem. Res.* **2010**, *43*, 19–29.
- [42] D. Wang, W. F. van Gunsteren, Z. Chai, *Chem. Soc. Rev.* **2012**, *41*, 5836.
- [43] J. Dognon, *Coord. Chem. Rev.* **2014**, *266–267*, 110–122.
- [44] N. Kaltsoyannis, *Chem. Soc. Rev.* **2003**, *32*, 9–16.
- [45] P. Söderlind, G. Kotliar, K. Haule, P. M. Oppeneer, D. Guillaumont, *MRS Bull.* **2010**, *35*, 883–888.
- [46] K. Pierloot, E. Van Besien, E. Van Lenthe, E. J. Baerends, *J. Chem. Phys.* **2007**, *126*.
- [47] P. Tecmer, R. Bast, K. Ruud, L. Visscher, *J. Phys. Chem. A.* **2012**, *116*, 7397–7404.
- [48] S. Schöne, T. Radoske, J. März, T. Stumpf, M. Patzschke, A. Ikeda-Ohno, *Chem. Eur. J.* **2017**, *23*, 13574–13578.
- [49] M. B. Jones, A. J. Gaunt, *Chem. Rev.* **2013**, *113*, 1137–1198.
- [50] R. G. Denning, *J. Phys. Chem. A.* **2007**, *111*, 4125–4143.
- [51] E. A. Pedrick, J. W. Schultz, G. Wu, L. M. Mirica, T. W. Hayton, *Inorg. Chem.* **2016**, *55*, 5693–5701.
- [52] M. Gregson, E. Lu, D. P. Mills, F. Tuna, E. J. McInnes, C. Hennig, A. C. Scheinost, J. McMaster, W. Lewis, A. J. Blake, A. Kerridge, S. T. Liddle, *Nat. Commun.* **2017**, *8*, 14137.
- [53] R. G. Denning in *Gmelin's Handbook of Inorganic Chemistry*, (Eds.: K. C. Buschbeck, H. Bergmann, J. J. Füssel, H. Hartwig, H. Katscher, R. Keim, E. Koch, D. D. Koschel, U. Krüerke, P. Merlet, E. Schleitzer-Rust, F. A. Schröder, A. Slawisch, W. Topper), Springer-Verlag Berlin Heidelberg GmbH, **1989**, Chapter Uranium A6, p. 31.
- [54] C. Clidewell, *Inorg. Chim. Acta.* **1977**, *24*, 149.
- [55] R. G. Denning in *Electronic Structure and Bonding in Actinyl Ions*, **1992**, pp. 217–276.
- [56] G. Gordon, H. Taube, *J. Inorg. Nucl. Chem.* **1961**, *19*, 189.

- [57] K. Tatsumi, R. Hoffmann, *Inorg. Chem.* **1980**, *19*, 2656.
- [58] C. K. Jørgensen, R. Reisfeld, *Struct. Bond. Berlin.* **1982**, *50*, 121.
- [59] R. L. Dekock, E. J. Baerends, P. M. Boerrigter, J. G. Sniijders, *Chem. Phys. Lett.* **1984**, *105*, 308–316.
- [60] N. Kaltsoyannis, *Inorg. Chem.* **2000**, *39*, 6009–6017.
- [61] D. Brewster, *Trans. R Soc Ed.* **1849**, *16*, 111–121.
- [62] V. Balzani, V. Carassiti in *Photochemistry of Coordination Compounds*, (Ed.: F. Wasgestian), Academic Press, **1970**, p. 432.
- [63] O. Laporte, W. F. Meggers, *J. Opt. Soc. Am.* **1925**, *11*, 459–463.
- [64] E. Hashem, T. McCabe, C. Schulzke, R. J. Baker, *Dalton Trans.* **2014**, *43*, 1125–1131.
- [65] D. Meng, N. Pu, L. Mei, T. Sun, L. Xu, W. Shi, J. Chen, C. Xu, *J. Radioanal. Nucl. Chem.* **2018**, *317*, 121–129.
- [66] C. Görller-Walrand, L. G. Vanquickenborne, *J. Chem. Phys.* **1971**, *54*, 4178–4186.
- [67] C. Görller-Walrand, L. G. Vanquickenborne, *J. Chem. Phys.* **1972**, *57*, 1436–1440.
- [68] C. Görller-Walrand, S. De Houwer, L. Fluyt, K. Binnemans, *Phys. Chem. Chem. Phys.* **2004**, *6*, 3292–3298.
- [69] R. G. Denning, J. C. Green, T. E. Hutchings, C. Dallera, A. Tagliaferri, K. Giarda, N. B. Brookes, L. Braicovich, *J. Chem. Phys.* **2002**, *117*, 8008–8020.
- [70] K. Pierloot, E. Van Besien, *J. Chem. Phys.* **2005**, *123*.
- [71] P. Tecmer, A. S. P. Gomes, U. Ekström, L. Visscher, *Phys. Chem. Chem. Phys.* **2011**, *13*, 6249–6259.
- [72] P. Tecmer, N. Govind, K. Kowalski, W. A. De Jong, L. Visscher, *J. Chem. Phys.* **2013**, *139*.
- [73] S. Matsika, R. M. Pitzer, *J. Phys. Chem. A.* **2001**, *105*, 637–645.
- [74] J. Su, K. Zhang, W. H. Eugen Schwarz, J. Li, *Inorg. Chem.* **2011**, *50*, 2082–2093.
- [75] Z. Zhang, R. M. Pitzer, *J. Phys. Chem. A.* **1999**, *103*, 6880–6886.
- [76] L. Gagliardi, B. O. Roos, P.-Å. Malmqvist, J. M. Dyke, *J. Phys. Chem. A.* **2001**, *105*, 10602–10606.
- [77] G. Schreckenbach, P. J. Hay, R. L. Martin, *Inorg. Chem.* **1998**, *37*, 4442–4451.

# Chapter 2

## Methodology

*Throughout this work, a variety of different electronic structure methods and analysis techniques were utilised depending on the complexity of the investigation. Electronic structure methods are used in quantum chemistry to describe the intrinsic properties and behaviour of electrons in molecules; it is important to have a general understanding into the theoretical background of these methods. This chapter will start with a general overview of quantum chemistry followed by a discussion on basis sets. The next sections will cover Hartree–Fock theory (Section 2.9), electron correlation (Section 2.10), and Post-Hartree–Fock methods (Section 2.11). Density Functional Theory (Section 2.12) is then discussed as an alternative method to approximate solutions to the Schrödinger equation and methods of simulating the electronic excited state using density functional theory methods are also highlighted. The final section of the chapter discusses the diagnostic method, Quantum Theory of Atoms in Molecules (Section 2.14) which is the chosen method of analysis in this work.*

## 2.1 Dirac Notation

Dirac or ‘Bra-Ket’ notation will be primarily used throughout this chapter. Dirac notation is a powerful tool as it enables complex expressions for quantum states to be truncated. In this notation a wavefunction is represented by a ‘ket’, while the complex conjugate of a wavefunction is a ‘bra’.

$$\begin{aligned} f(\mathbf{r}) &= |f\rangle && \text{‘ket’} \\ f^*(\mathbf{r}) &= \langle f| && \text{‘bra’} \end{aligned} \quad (2.1)$$

Overlap of functions can be represented in Dirac notation as the combination of a ‘bra’ and a ‘ket’:

$$\int \Psi^*(\mathbf{r})\Psi(\mathbf{r})d\mathbf{r} = \langle\Psi|\Psi\rangle \quad (2.2)$$

Therefore, in Dirac notation, the normalisation and orthogonality conditions can be expressed as:

$$\begin{aligned} \langle i|i\rangle &= 1 && \text{(normalised)} \\ \langle i|j\rangle &= 0 && \text{(orthogonal)} \end{aligned} \quad (2.3)$$

In quantum mechanics, the expectation value of an observable represented by operator  $\hat{H}$  with respect to state  $|\Phi\rangle$  would be expressed as:

$$\int_{-\infty}^{\infty} \Phi^*(\mathbf{r})\hat{H}\Phi(\mathbf{r}) d\mathbf{r} \quad (2.4)$$

Which, in Dirac notation Equation 2.4 truncates to:

$$\langle\Phi|\hat{H}|\Phi\rangle \quad (2.5)$$

## 2.2 Schrödinger Equation

Obtaining approximate solutions to the Schrödinger equation forms the basis of all electronic structure methods; in its time-independent form:

$$\hat{H}\Psi = E\Psi \quad (2.6)$$

$E$  is the energy of the system,  $\hat{H}$  is the Hamiltonian operator and  $\Psi$  is the wavefunction. The Schrödinger equation is an eigenvalue equation; there are multiple eigenfunctions ( $\Psi$ ) of  $\hat{H}$  which each have their own eigenvalue  $E$ . The eigenfunction which results in the lowest energy is referred to as the ground state of the system ( $\Psi_0, E_0$ ), with all other eigenfunctions corresponding to excited states.

The Schrödinger equation can be solved for a one-electron system, however, an exact solution for a many-body system is generally unobtainable, due to the

complexity of the Hamiltonian when there is more than one electron. [1] There are a variety of different electronic structure methods which approximate the solution to the many-body Schrödinger equation and these will be discussed throughout this chapter.

## 2.3 The Variational Principle

The variational principle states that any trial wavefunction cannot be lower in energy than the exact wavefunction (with exact ground state energy  $E_0$ ). For a trial wavefunction ( $\Phi$ ), the energy of that system ( $E_\Phi$ ) can be represented as:

$$\frac{\langle \Phi | \hat{H} | \Phi \rangle}{\langle \Phi | \Phi \rangle} \geq E_0 \quad (2.7)$$

Hence, the variational principle can be used to systematically select the best wavefunction for any given system.

## 2.4 The Hamiltonian

The Hamiltonian ( $\hat{H}$ ) describes the kinetic and electrostatic energies of electrons ( $N$ ) and nuclei ( $P$ ) in a system. When expressed in atomic units, the Hamiltonian has the form:

$$\hat{H} = - \sum_{i=1}^N \frac{\nabla_i^2}{2} - \sum_{A=1}^P \frac{\nabla_A^2}{2M_A} - \sum_{A=1}^P \sum_{i=1}^N \frac{Z_A}{r_{iA}} + \sum_{j>i}^N \sum_{i=1}^N \frac{1}{r_{ij}} + \sum_{B>A}^P \sum_{A=1}^P \frac{Z_A Z_B}{r_{AB}} \quad (2.8)$$

$M_A$  is the ratio of the mass of nucleus  $A$  to the mass of an electron,  $Z_A$  is the charge of nucleus  $A$ ,  $r_{iA}$  and  $r_{AB}$  are the distances from electron  $i$  to nucleus  $A$  and from nucleus  $A$  to nucleus  $B$ , respectively. Finally, the Laplacian operator ( $\nabla^2$ ) involves the second differentiation with respect to the coordinates of the electron ( $i$ ) and nucleus ( $A$ ), and is mathematically defined in Equation 2.9. The first two terms, in Equation 2.8, corresponds the kinetic energy operators for the electrons and nuclei, respectively, the third term is the electron–nuclear attraction and the final two terms define the electron–electron and nuclear–nuclear repulsion.

$$\nabla_i^2 = \frac{\partial^2}{\partial^2 x_i} + \frac{\partial^2}{\partial^2 y_i} + \frac{\partial^2}{\partial^2 z_i} \quad (2.9)$$

## 2.5 The Born–Oppenheimer Approximation

The Hamiltonian can be simplified in cases where only the electronic properties are of interest with the application of the Born–Oppenheimer approximation. [2]. This is justified as, in comparison to the electrons, the nuclei are much heavier and

as a result move much slower. As a result of this the molecular wavefunction can be separated into electronic and nuclear components (i.e.  $\Psi = \Psi_{el}\Psi_{nuc}$ ). Thus solving the time independent schrödinger equation; for  $\Psi_{el}$  the electronic Hamiltonian ( $\hat{H}_{el}$ ) becomes:

$$\hat{H}_{el} = - \sum_{i=1}^N \frac{\nabla_i^2}{2} - \sum_{A=1}^P \sum_{i=1}^N \frac{Z_A}{r_{iA}} + \sum_{j>i}^N \sum_{i=1}^N \frac{1}{r_{ij}} \quad (2.10)$$

## 2.6 The Orbital Approximation

The electronic Hamiltonian only depends on the three spatial coordinates of an electron, however, in order to fully describe an electron, a fourth coordinate, the spin, must be specified. There are two spin functions:  $\alpha$  and  $\beta$ , spin up ( $\uparrow$ ) and spin down ( $\downarrow$ ), respectively. These functions follow the orthonormality conditions *i.e.* obey both normalised and orthogonal conditions, as defined in Equation 2.3. [3]

A many-electron wavefunction can be approximated using the orbital/Hartree approximation, which is constructed from the product of many ( $n$ ) one-electron orbitals, this is known as the Hartree product. [4]

$$\Psi^{\text{HP}}(\mathbf{x}_1, \mathbf{x}_2, \dots, \mathbf{x}_N) = \chi_i(\mathbf{x}_1)\chi_j(\mathbf{x}_2) \cdots \chi_k(\mathbf{x}_N) \quad (2.11)$$

Where  $\mathbf{x}_1$  represents the spin and spatial coordinates of electron 1 in spin orbital  $\chi_i$ . The spin orbitals ( $\chi_k$ ) are the product of a spatial orbital and a spin function:  $\chi_k(\mathbf{x}_N) = \psi_k(\mathbf{r}_n)\sigma(n)$ , where  $\mathbf{r}_n$  is the spatial coordinate of electron  $n$  and  $\sigma(n)$  is the spin function, which can be either  $\alpha$  or  $\beta$ .

The Hartree product describes as system on non-interacting particles as the probability of finding electron 1 with  $\mathbf{x}_1$  at position  $\mathbf{r}_i$  is independent on the coordinates of electron 2 with  $\mathbf{x}_2$ . Therefore, the Hartree product is not exact for a many-fermionic system as it fails to account for the indistinguishability of electrons and does not obey the antisymmetry principle, which states that; *‘a many-electron wavefunction must be antisymmetric with respect to the interchange of the coordinate  $\mathbf{x}$  of any two fermions’*.

$$\Psi(\mathbf{x}_1, \dots, \mathbf{x}_i, \dots, \mathbf{x}_j, \dots, \mathbf{x}_N) = -\Psi(\mathbf{x}_1, \dots, \mathbf{x}_j, \dots, \mathbf{x}_i, \dots, \mathbf{x}_N) \quad (2.12)$$

Therefore, in order to improve upon this approximation, the Hartree product needs to be antisymmetric. This can be achieved by taking linear combinations of Hartree products via a single Slater determinant (Equation 2.22), which is used to approximate an exact  $n$ -electron wavefunction. This will be discussed further in Section 2.9.

## 2.7 Linear Combinations of Atomic Orbitals

In a hydrogen molecule, as the 1s atomic orbitals (situated on an individual hydrogen atom) approach each other, molecular orbitals are formed via a linear combination of atomic orbitals (LCAO). The two localised atomic orbitals (AOs) ( $\phi_1(\mathbf{r})$  and  $\phi_2(\mathbf{r})$ ) form two delocalised molecular orbitals (MOs) ( $\psi_1(\mathbf{r})$  and  $\psi_2(\mathbf{r})$ ).  $\psi_1(\mathbf{r})$  and  $\psi_2(\mathbf{r})$  correspond to the bonding and anti-bonding molecular orbitals, respectively, and have *gerade* and *ungerade* symmetry with respect to inversion about the point centred between the nuclei. Equation 2.13 shows the mathematical formation of these orbitals;  $S_{12}$  represents the overlap between the two atomic orbitals and is distance dependent.

$$\begin{aligned}\psi_1(\mathbf{r}) &= [2(1 + S_{12})]^{-\frac{1}{2}}(\phi_1(\mathbf{r}) + \phi_2(\mathbf{r})) \\ \psi_2(\mathbf{r}) &= [2(1 - S_{12})]^{-\frac{1}{2}}(\phi_1(\mathbf{r}) - \phi_2(\mathbf{r}))\end{aligned}\tag{2.13}$$

The example given in Equation 2.13 is a specific example of expanding a set of spatial MOs in a set of known spatial AOs (spatial basis functions), which is given by the general expression.

$$\psi_i(\mathbf{r}) = \sum_{\mu=1}^K c_{\mu i} \phi_{\mu}(\mathbf{r})\tag{2.14}$$

Where  $\psi_i$  is a MO,  $c_{\mu i}$  is an expansion coefficient, which can be varied to minimise the energy of the system and  $\phi_{\mu}$  are the atomic orbitals which constitute the basis set. We can therefore consider a set of  $K$  atomic orbital functions as a basis set.

## 2.8 Basis Sets

In theoretical chemistry, basis sets are used to describe the MO of a system, which are built using the LCAO approach for a set of  $K$  AO functions (Equation 2.14). Typically, for molecular systems the AOs are described by atom-centred basis functions, however, for other applications such as condensed-phase calculations, plane wave basis sets are used. Generally, the more basis functions in a given basis set the better the description of the properties, however, additional basis functions corresponds to a higher computational expense, with the overall cost scaling as  $K^x$ , where  $K$  is the number of basis functions and  $x$  scales depending on which method used. [3]

When choosing a basis set, it is important to choose basis functions which are ‘necessary’ to provide a ‘reasonable’ description of the system. For example, a basis set with tight/compact core-like basis functions would provide a poor description of an anionic structure as key electrons are located in diffuse orbitals. Therefore, when choosing a basis set for a system, it is not only important to balance the expense and accuracy but to also consider the type of functions which accurately represent

the system.

In this section, the types of basis functions will be discussed, along with their advantages and disadvantages for modelling molecular systems.

### 2.8.1 Slater Type Orbitals

There are two main types of atom-centred basis functions; the first are *Slater Type Orbitals* (STO), [5] which have the general form.

$$\psi_{\zeta,n,l,m}(r, \theta, \phi) = NY_{l,m}(\theta, \phi)r^{n-1}e^{-\zeta r} \quad (2.15)$$

$N$  is a normalisation constant,  $Y_{l,m}$  are spherical harmonic functions,  $\zeta$  is the exponent which determines the rate of decay,  $n$ ,  $m$ ,  $l$  are quantum numbers and  $r$ ,  $\theta$  and  $\phi$  are the polar coordinates with  $r$  as the distance from the nucleus and  $\theta$  and  $\phi$  are angular coordinates. The exponent is always positive with its magnitude influencing the diffuseness of the function, a large exponent indicates small diffuseness while a small exponent represents large diffuseness., with the value of the exponent is always positive and non-zero.

These functions are good as they reflect known qualities of molecular orbitals, particularly at small and large  $r$  values. At large  $r$  values Slater functions decay exponentially, while at  $r = 0$ , (near the nucleus), the Slater function results in a finite slope, this represents a nuclear ‘cusp’.

$$\frac{\partial}{\partial r}(e^{-\zeta r}) = -\zeta(e^{-\zeta r}) \quad \text{when } r = 0 \quad \frac{\partial}{\partial r} = -\zeta \quad (2.16)$$

This behaviour of STOs corresponds to the exact orbitals in the hydrogen atom, however, it is worth noting that STOs do not have any radial nodes in the form given in Equation 2.15. In order to obtain radial nodes, linear combinations of STO’s need to be taken.

Although fairly straightforward for two Slater functions linear combinations of three- or more-centred two-electron integrals Slater functions cannot be performed analytically. [3, 6] Despite STOs being too expensive for use in large systems, they can be used in atomic and diatomic systems which require high accuracy and in semi-empirical methods which neglect all three- and four-centre integrals. [7] It is worth highlighting that despite their high computational expense, STOs are used for example in the popular ADF (Amsterdam Density Functional) code. [8]

### 2.8.2 Gaussian Type Orbitals

An alternative to STO’s was developed by Boys, [9] in which the exponential component is dependent on  $r^2$  instead of  $r$ , these are known as *Gaussian Type Orbitals*. Gaussian functions are much less computationally expensive to take linear combinations of; this is because the product of two Gaussian’s results in a third

Gaussian which is situated between the original two. Equation 2.17 gives the general form of a *Gaussian Type Orbitals* (GTO) [9] in terms of polar coordinates; GTOs have a similar form to STOs with the key difference being in the exponent, which is dependent on  $r^2$ .

$$\psi_{\zeta,n,l,m}(r, \theta, \phi) = NY_{l,m}(\theta, \phi)r^{2n-2-l}e^{-\zeta r^2} \quad (2.17)$$

It is worth noting that GTOs can also be expressed in terms of Cartesian coordinates with the form: [3]

$$\psi_{\zeta,l_x,l_y,l_z}(x, y, z) = Nx^{l_x}y^{l_y}z^{l_z}e^{-\zeta r^2} \quad (2.18)$$

Where the sum of  $l_x$ ,  $l_y$  and  $l_z$  determines the type of orbital (for example  $l_x + l_y + l_z = 2$  is a d-orbital). The difference between the polar and Cartesian GTOs is in the number of components to the functions generated; a f-type GTO written in spherical coordinates results in seven functions. In contrast, in Cartesian form, there are ten f-functions, which can then be transformed into seven spherical f-functions and one set (three) of p-functions. [3]

This dependence on  $r^2$  causes a few issues both near and far from the nucleus; at large  $r$  values the Gaussian functions do not decay exponentially and when  $r = 0$  there is no nuclear cusp.

$$\frac{\partial}{\partial r}(e^{-\zeta r^2}) = -2\zeta r e^{-\zeta r^2} \quad \text{when } r=0 \quad \frac{\partial}{\partial r} = 0 \quad (2.19)$$

This means that GTOs are particularly poor when modelling short and long range electronic behaviour, in comparison to STOs. Figure 2.1 compares the behaviour of both functions (STO and GTO) for a 1s orbital ( $n = 1, l = 0, N = 1, Y_{l,m}=1, \zeta=1$ ) as a function of distance ( $r$ ).

Due to the shortcomings of GTOs, a significant number of linear combinations of GTOs is required to achieve a sufficient level of accuracy when compared to STOs. However, a combination of several GTOs is still computationally less expensive in comparison to STOs due to the integrals in GTOs being much simpler to compute.

A single Gaussian function is known as a *primitive* Gaussian function, linear combinations of *primitive* Gaussians are referred to as a *contracted* Gaussian function. As an example of how a contraction can be expressed, consider the uranium atom in the ANO-RCC-VTZP basis set [10–13], which is utilised in Chapter 5. Such contraction can be denoted as: (26s, 23p, 17d, 13f, 5g, 3h)→[9s, 5p, 6d, 4f, 2g, 1h]; with the number of primitives included quoted in ( ), and the number of contracted functions in [ ].

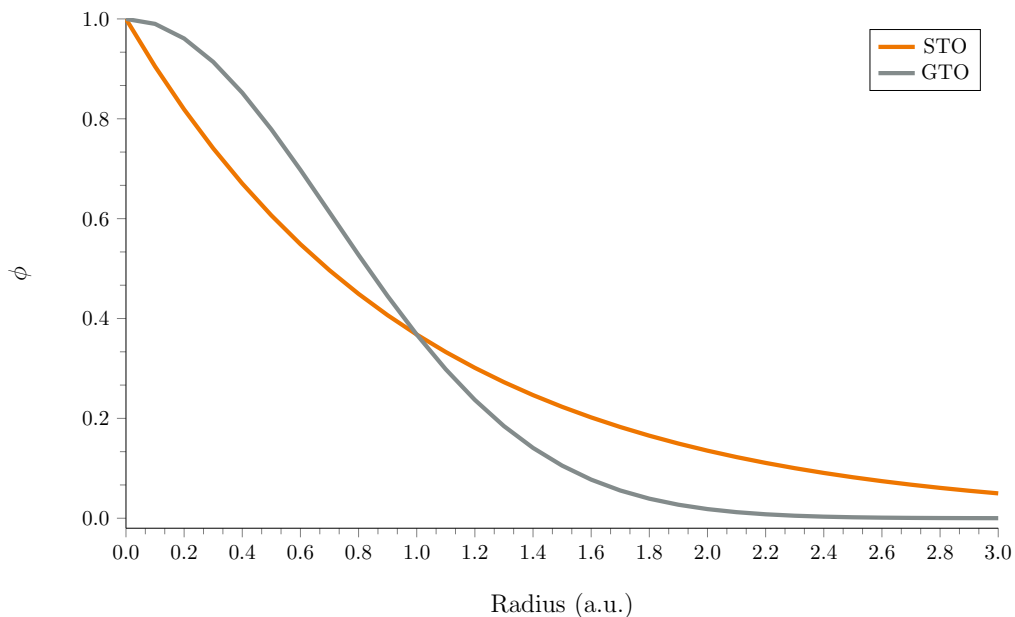


Figure 2.1: A comparison of Slater and Gaussian type functions for a 1s orbital:  $n = 1$ ,  $l = 0$ ,  $N = 1$ ,  $Y_{l,m}=1$ ,  $\zeta=1$

### 2.8.3 Basis set quality

Generally, the more basis functions in a given basis set, the more accurately the system is represented. In order to improve the basis set, different types of functions can be added, which can more accurately describe a given system. In this next section, different types of functions, which are typically found in basis sets will be described.

#### 2.8.3.1 Minimal basis set

A minimal or single- $\zeta$  (SZ) basis set comprises of the smallest number of basis functions to describe all the electrons in a system. For hydrogen and helium the minimal basis set would comprise of a single s-function. For first row periodic elements (Li→Ne), this would increase to two s-functions and three p-functions ( $p_x$ ,  $p_y$  and  $p_z$ ), when modelling third row elements (Na→Ar), this would increase to three s-functions and six p-functions and so on.

#### 2.8.3.2 Double zeta basis sets

In order to improve the flexibility and accuracy of a basis set, the number of basis functions used to describe an AO can be doubled, tripled, quadrupled *etc.*, this is known as double-, triple-, quadruple- $\zeta$  (DZ), (TZ), (QZ) basis sets, respectively. As mentioned previously, a single- $\zeta$  (SZ) basis set includes no additional basis functions, a double- $\zeta$  (DZ) basis set includes one extra basis function and so on. For a first row periodic element, a double- $\zeta$  basis set includes four  $s$  ( $1s$ ,  $1s'$ ,  $2s$ ,  $2s'$ ) and six  $p$

( $2p_x$ ,  $2p_y$ ,  $2p_z$ ,  $2p'_x$ ,  $2p'_y$  and  $2p'_z$ ) functions.

In a double- $\zeta$  basis set, each atomic orbital can be represented by two basis functions, with their own contractions. The addition of this second function makes it possible to change the size of the orbital. An example of where two different sized basis functions aids in the description of a molecule can be seen in HCN molecule (Figure 2.2). The two  $p$ -functions on the carbon allows for different electron distribution to be associated with each type of bond. The C-N  $\pi$ -bond (made with  $p_x$  and  $p_y$  AOs) is more diffuse than the  $\sigma$  C-H bond (H  $1s$  and C  $2p_z$  AOs), therefore, doubling the number of basis functions allows for the possibility that the electron distribution may be different in different directions.

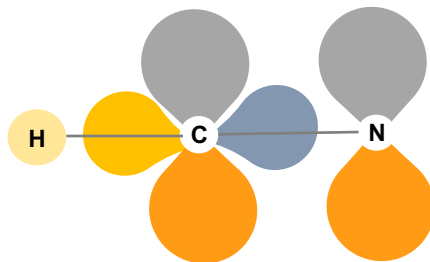


Figure 2.2: A double zeta basis allows for bonding in two different directions, example molecule HCN, recreated with inspiration from [3]. C/N  $p_x$  and  $p_y$  AOs are represented by orange/grey electron distribution which have a smaller exponent associated with their basis functions; while C  $p_z$  AOs (yellow/blue) have a larger exponent on the corresponding basis function.

As the number of basis functions increases, the accuracy of the model increases but with this comes additional computational expense. A way to minimise the cost is to only double basis functions for the valence orbitals (VDZ) as these are the orbitals which are most likely to be involved in bonding.

### 2.8.3.3 Polarised Basis Sets

While adding  $\zeta$ -functions gives more flexibility in the size of the orbital it does not change the shape. Basis sets which include a higher than minimal level of angular momentum have this ability and are known as polarised basis sets. Examples of these are adding  $p$  or higher functions to hydrogen and  $d$  or higher functions to carbon.

Considering the HCN molecule again; the H-C bond consists of the hydrogen  $s$ -orbital and the carbon  $p_z$  orbital. In a chemical world, the electron distribution parallel and perpendicular to the H-C bond differs, however, the  $s$ -orbital is spherical and hence electron distribution is even in all directions. Addition of a  $p$ -function to the hydrogen atom polarises the  $s$ -orbital and makes the electron distribution less uniform; in this scenario, the  $p$ -function would polarise the  $s$ -orbital to a more  $p_z$  like shape, but only a single lobe. This results in the electron density differing

parallel and perpendicular to the H-C bond. Hence polarisation functions are very important when describing molecules as the orbitals take a less symmetric shape than in atoms.

#### 2.8.3.4 Diffuse Basis Sets

Diffuse basis functions comprise of Gaussian functions with small exponents ( $\zeta$ ). Diffuse functions allow electrons to be far away from the nuclei due to their low rate of decay. This low rate of decay can be seen clearly in Figure 2.3, which plots the original GTO ( $\zeta = 1$ , shown in Figure 2.1) and another GTO with  $\zeta = 0.1$ .

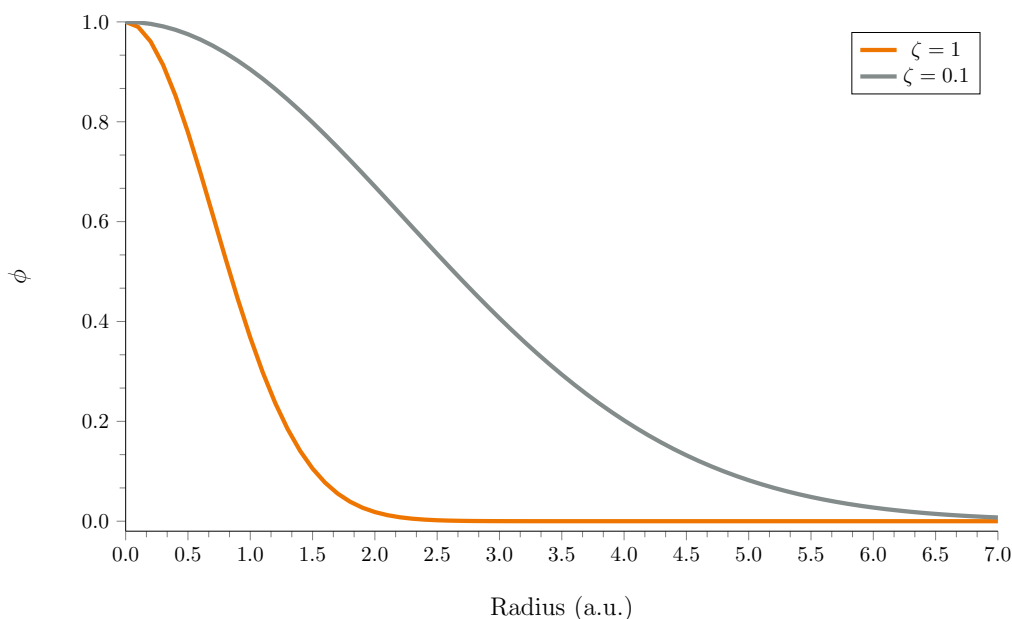


Figure 2.3: A graph comparing GTOs with and without diffuse functions  $\zeta = 0.1$  and  $\zeta = 1$  respectively.

Diffuse basis sets are of particular importance when modelling systems in which the electrons are loosely bound to the nucleus, specific examples include; anions, transition states, excited states and non-covalently bound systems. There are two approaches to adding diffuse functions to a basis set.

The first approach is to add standard diffuse  $s$  and  $p$ -functions (4 functions in total) to all non-hydrogen atoms, this is labelled as  $+$ . There is also a  $++$  option, which adds diffuse  $s$  and  $p$ -functions to non-hydrogen atoms and diffuse  $s$ -functions to H and He. [14] The most common of these is 6-31+G basis set of Pople and co-workers. [15]

The second approach is known as aug; where a diffuse function is added to every atom for every symmetry already present in the original basis set. [16] For a sulfur atom which has  $s$ ,  $p$ ,  $d$  and  $f$  basis functions present, the aug function would add 16 extra function in total from the addition of  $s$ ,  $p$ ,  $d$  and  $f$  diffuse functions (1, 3, 5 & 7 respectively). This results in basis sets which include aug functions to be much

larger and converge more rapidly than a basis sets which includes  $+ / ++$  functions. [17]

Truhlar and co-workers combined both types of diffuse functions with the cc-pVTZ basis set of Dunning and co-workers (see Section 2.8.4.2) and compared these labelled as: cc-pVTZ, cc-pVTZ+ and aug-cc-pVTZ. Figure 2.4 plots the GTO function and changes the  $\zeta$  value to those presented by Truhlar and co-workers [18] for the exponents of the  $p$ -functions on a carbon atom ( $n = 2, l = 1$  for quantum numbers).

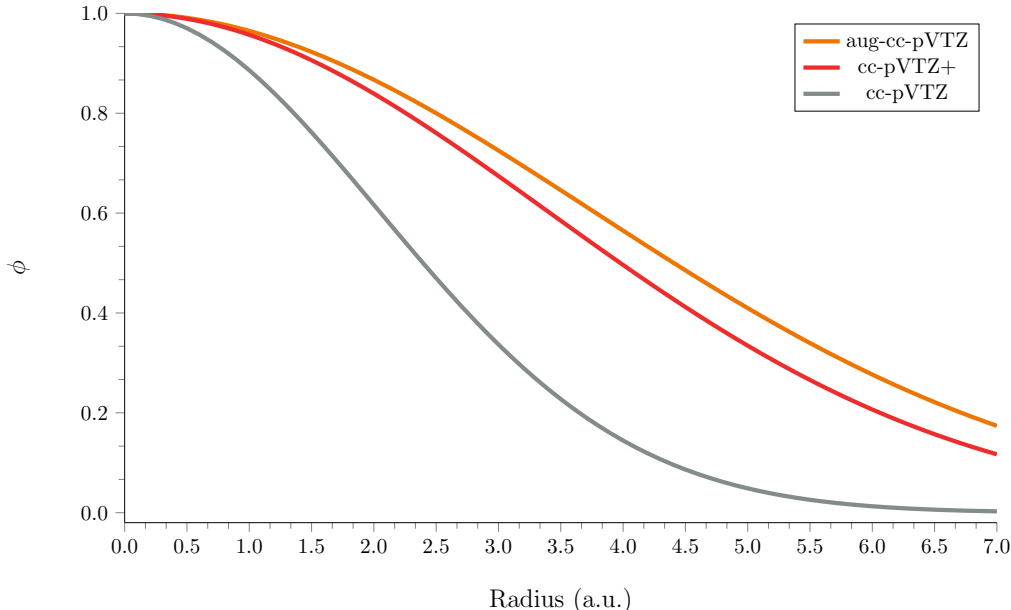


Figure 2.4: A comparison of three different basis sets, taking the exponents from the  $p$ -functions on a carbon atom presented in [18]

## 2.8.4 Specific Basis Sets

Now that the different types of basis functions have been defined, specific basis sets which are relevant to this research can be discussed.

There are two types of basis set contraction, segmented and general. Most basis sets utilise the segmented contraction, where each given primitive only appears in one contraction forming a disjointed set of primitive functions. In a segmented contraction, the contraction coefficients are evaluated by a variational optimisation of the Hartree–Fock energy, in which both the exponents and contraction coefficients are optimised simultaneously. [3, 19]

In contrast, general contraction allows all primitive functions to contribute to each contracted function. The optimised primitive set gives the basis function exponents and the contraction coefficients are calculated by atomic calculations. These calculated exponents and coefficients can be used to generate several different contracted basis sets. [3, 19]

#### 2.8.4.1 Atomic Natural Orbital Basis Sets

Atomic natural orbital (ANO) basis sets [20–22] utilise the general contraction method. ANO basis sets contract a large primitive Gaussian (PGTO) set into a small number of contracted Gaussian (CGTO) using a correlated wavefunction, usually at the CISD level (see Section 2.11.1). [21, 22] The correlated wavefunction generates a set of *natural orbitals* which are identified as those which diagonalise the density matrix, the eigenvalues of these natural orbitals denoted *orbital occupation numbers*. The orbital occupation number represents the number of electrons in the orbital and can have any value between 0 and 2 when a correlated wavefunction method is used.

#### 2.8.4.2 Correlation Consistent Basis Sets

Dunning and co-workers have developed correlation consistent basis sets, which contain a smaller set of primitive Gaussians than the ANO basis sets. [23, 24] These basis sets are designed so that functions which contribute similar amounts of correlation energy are grouped together at the same stages, regardless of the function type. Correlation consistent basis sets are attuned to recovering the correlation energy of valence electrons.

Dunning’s basis sets have the form cc-pVnZ, which can be broken down into the terms: correlation consistent (cc), polarised (p), valence (V), zeta (Z). N refers to the number of extra basis functions per angular function *i.e.* DZ (as seen in Section 2.8.3.2). This design allows for systematic increase in the basis set size, *i.e.* changing the basis set from cc-pVDZ to cc-pVTZ would increase each type of basis function by 1 and adds a new type of higher order polarisation function. The augmented (aug) diffuse functions, discussed in Section 2.8.3.4 can also be added to these basis sets; with the aug-cc-pVDZ basis set adding 4 diffuse functions on hydrogens and 9 on every non-hydrogenic atom.

A second variety of these basis sets is the cc-pCVnZ basis sets, which are augmented with tight functions, the idea of these functions is to recover core-core and core-valence electron correlation. [25] The cc-pCVDZ basis set adds 1 *s* and 3 *p* tight functions, and the TZ adding 2 *s*, 6 *p* 5 *d* tight functions.

#### 2.8.4.3 Effective Core Potentials

Moving down the periodic table, the number of core electrons increases and thus modelling becomes more computationally expensive. As discussed previously, these core electrons are unimportant for the majority of chemical processes, however, it is still necessary to use a significant number of basis functions in order for the valence orbitals to be described properly. Effective core potentials (ECP) or pseudopotential greatly reduce the computational expense by replacing the core electrons with an effective potential and the valence electrons can be also be treated explicitly. [26–28]

It is also worth noting that in the lower half of the periodic table, relativistic effects tend to be more prominent (see Section 2.13) and hence the pseudopotential may also include implicit treatment of relativistic effects, such pseudopotentials are referred to as relativistic ECPs (RECP). [29–34] Direct relativistic effects are more significant for the core electrons, the use of a RECP is favourable as it still allows for the valence electrons to be modelled by a non-relativistic Hamiltonian. [35, 36]

An ECP is generating by the following steps: [3]

1. Produce a good quality all-electron wavefunction for the atom. Calculated from Hartree–Fock (Section 2.9) or density functional calculation (Section 2.12) for non-relativistic ECP or relativistic Dirac-Hartree–Fock (Section 2.13) for a RECP.
2. Replace the valence orbitals with nodeless pseudo-orbitals, which lack nodal structure in the core region but behave correctly in the valence region.
3. Replace the core electrons with an appropriate potential.
4. Fit the parameters of the potential so that the pseudo-orbitals produced from solving the many-electron Schrödinger/Dirac equation (or similar) match the all-electron valence orbitals.

As discussed in Section 2.8, molecular systems are typically described by GTOs and therefore if GTOs are utilised for modelling the valence orbitals then they should also be used for generating the ECP. The quality of the ECP is determined by the number of electrons chosen for the ECP and hence this is a key consideration when designing/choosing an ECP. ‘Small-core’ ECPs treat all except the two outermost shells as core while ‘large-core’ ECP treat all except the outermost shell. [6] Using Ag with an electronic configuration:  $1s^2, 2s^2, 2p^6, 3s^2, 3p^6, 4s^2, 3d^{10}, 4p^6, 4d^{10}, 5s^1$  as an example: [3]

- Small-core ECP treat:  $1s^2, 2s^2, 2p^6, 3s^2, 3p^6, 3d^{10}$  as core
- Large-core ECP treat:  $1s^2, 2s^2, 2p^6, 3s^2, 3p^6, 4s^2, 3d^{10}, 4p^6$  as core

This makes small-core ECP more accurate than large-core ECP however they are more computationally expensive as there are more electrons to model explicitly.

There are numerous ECPs used throughout the literature, some of the most popular are: LANL (Los Alamos National Laboratory) developed by Hay and Wadt [37] and the Stuttgart–Dresden pseudopotentials developed by Dolg and co-workers. [38] In contrast to most other ECPs, in the Hay–Wadt ECPs parameters for elements Na→Kr are derived from non-relativistic Hartree–Fock calculations, while from Rb onwards relativistic Hartree–Fock calculations are used. [6] Throughout this thesis, the Stuttgart-RSC-1997 ECP for uranium treats 60 (out of 92) electrons as core

electrons and hence greatly reduces the number of electrons. [39–41] Dyllal developed a set of ECPs for the 4p, 5p and 6p elements, which are equivalent to the correlation-consistent basis sets of Dunning discussed previously (Section 2.8.4.2). [6, 42, 43]

## 2.9 Hartree–Fock Theory

The many-electron wavefunction in terms of a Hartree product was defined in Equation 2.11; it was noted that the indistinguishability of the electrons is not accounted for by this definition. Slater determinants are used to make Hartree products antisymmetric; [44] consider a pair of Hartree products which describe the same two-electron system.

$$\Psi_{12}^{\text{HP}}(\mathbf{x}_1, \mathbf{x}_2) = \chi_i(\mathbf{x}_1)\chi_j(\mathbf{x}_2) \quad (2.20)$$

$$\Psi_{21}^{\text{HP}}(\mathbf{x}_1, \mathbf{x}_2) = \chi_i(\mathbf{x}_2)\chi_j(\mathbf{x}_1)$$

In the first scenario ( $\Psi_{12}^{\text{HP}}$ ), spin orbitals  $\chi_i$  and  $\chi_j$  are occupied by electron 1 and electron 2, respectively; in contrast with the second scenario in which electrons 1 and 2 have swapped spin orbitals. Although these definitions distinguish between which electron is in which orbital, the wavefunction is not antisymmetric as there was no change in sign when the electrons changed position. To achieve an antisymmetric wavefunction, linear combination of Hartree products can be taken.

$$\Psi(\mathbf{x}_1, \mathbf{x}_2) = 2^{-\frac{1}{2}}(\chi_i(\mathbf{x}_1)\chi_j(\mathbf{x}_2) - \chi_j(\mathbf{x}_1)\chi_i(\mathbf{x}_2)) \quad (2.21)$$

The  $2^{-\frac{1}{2}}$  is a normalisation factor and the central minus sign ensures the wavefunction is antisymmetric. In this expression, if both electrons occupied the same spin orbital *i.e.*  $i = j$ , the wavefunction would vanish. This expression therefore satisfies the *Pauli exclusion principle* [45], which states that, ‘no two fermions can occupy the same quantum state’. Equation 2.21 can be expressed as a Slater determinant:

$$\Psi(\mathbf{x}_1, \mathbf{x}_2) = \frac{1}{\sqrt{2}} \begin{vmatrix} \chi_i(\mathbf{x}_1) & \chi_j(\mathbf{x}_1) \\ \chi_i(\mathbf{x}_2) & \chi_j(\mathbf{x}_2) \end{vmatrix} \quad (2.22)$$

In an  $N$ -electron system, the normalisation factor becomes:  $\frac{1}{\sqrt{N!}}$  and the Slater determinant is given in Equation 2.22 is expanded to give the general Slater determinant (Equation 2.23). Conventionally, the rows represent electrons and the columns the spin orbitals.

$$\Psi(\mathbf{x}_1, \mathbf{x}_2, \dots, \mathbf{x}_N) = \frac{1}{\sqrt{N!}} \begin{vmatrix} \chi_i(\mathbf{x}_1) & \chi_j(\mathbf{x}_1) & \dots & \chi_k(\mathbf{x}_1) \\ \chi_i(\mathbf{x}_2) & \chi_j(\mathbf{x}_2) & \dots & \chi_k(\mathbf{x}_2) \\ \vdots & \vdots & \ddots & \vdots \\ \chi_i(\mathbf{x}_N) & \chi_j(\mathbf{x}_N) & \dots & \chi_k(\mathbf{x}_N) \end{vmatrix} \quad (2.23)$$

This can also be written in a short-hand, where only diagonal matrix elements are included and implies the electron order  $\mathbf{x}_1, \mathbf{x}_2, \dots, \mathbf{x}_N$ .

$$\Psi(\mathbf{x}_1, \mathbf{x}_2, \dots, \mathbf{x}_N) = |\chi_i \chi_j \cdots \chi_k\rangle \quad (2.24)$$

By using a single Slater determinant to describe the ground state of an N-electron system coupled with the variational principle, the Hartree–Fock (HF) equations can be derived by minimising the energy via a choice of spin orbitals. The HF equation determines the optimal spin orbitals and has the form

$$f(i)\chi(\mathbf{x}_i) = \varepsilon\chi(\mathbf{x}_i) \quad (2.25)$$

in which  $f(i)$  is the 1-electron Fock operator.

$$f(i) = -\frac{1}{2}\nabla_i^2 - \sum_{A=1}^M \frac{Z_A}{r_{iA}} + \nu^{\text{HF}} \quad (2.26)$$

The first two terms in the Fock operator make up the 1-electron Hamiltonian and the final term is the HF potential. The HF potential ( $\nu^{\text{HF}}$ ) is defined as: *‘the average potential experienced by the  $i^{\text{th}}$  electron due to the presence of the other electrons.’* [46] The  $\nu^{\text{HF}}$  is comprised of the coulomb and exchange operators ( $\mathbf{J}$  and  $\mathbf{K}$ ).

The average local potential at a point  $\mathbf{x}_1$  due to the charge distribution from the electron in orbital  $\chi_j$  is given by the Coulomb operator.

$$\mathbf{J}_i(\mathbf{x}_1) = \int d\mathbf{x}_2 |\chi_j(\mathbf{x}_2)|^2 r_{12}^{-1} \quad (2.27)$$

The exchange operator arises from the antisymmetry requirement of the wavefunction, it switches the  $\chi_i$  and  $\chi_j$  spin orbitals. The exchange operator is defined based on its action on an arbitrary spin orbital,  $\chi_i$

$$\mathbf{K}_j(\mathbf{x}_1)\chi_i(\mathbf{x}_1) = \left[ \int d\mathbf{x}_2 \chi_j^*(\mathbf{x}_2) r_{12}^{-1} \chi_i(\mathbf{x}_2) \right] \chi_j(\mathbf{x}_1) \quad (2.28)$$

In the HF approximation the many-electron problem is replaced with a series of 1-electron problems in which electron–electron repulsion is averaged. As the HF equation is non-linear, due to the HF potential being dependent on the spin orbitals of other electrons, the HF equation has to be solved iteratively. This process is called the self-consistent field (SCF) method.

Figure 2.5 gives a flow diagram of the SCF process. Firstly, the spin orbitals  $\{\chi_k\}$  are guessed, these are then used to calculate the average field seen by each electron ( $\nu^{\text{HF}}$ ). Using the calculated HF potential the eigenvalue equations, Equation 2.25, can then be solved for a new set of spin orbitals. The process continues with each new set of  $\{\chi_k\}$  being used to generate  $\nu^{\text{HF}}$ , until the spin orbitals (and  $\nu^{\text{HF}}$ ) remain unchanged (within a threshold), *i.e.* self-consistency is reached.

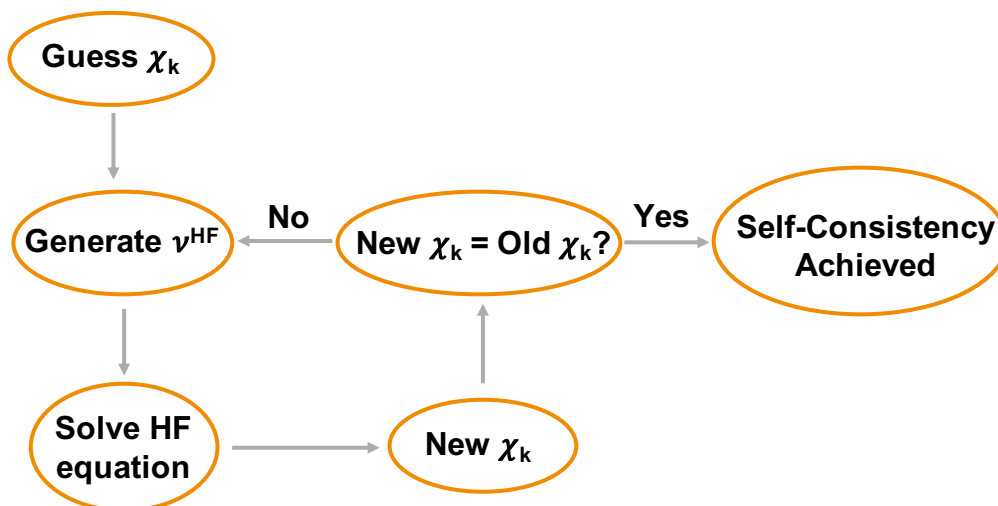


Figure 2.5: A flow chart showing the SCF process in the context of HF theory

This process generates a set of  $\{\chi_k\}$  orthonormal HF spin orbitals with orbital energies  $\{\epsilon_k\}$ . The spin orbitals with the lowest energy are termed occupied spin orbitals ( $\chi_a, \chi_b, \dots$ ), while the rest are termed virtual/unoccupied spin orbitals ( $\chi_s, \chi_r, \dots$ ). The Slater determinant which is formed from the occupied spin orbitals is the HF ground state wavefunction.

As there are an infinite number of solutions to the HF equations, there is an infinite number of virtual spin orbitals. In practice, when solving the HF equation, a finite set of spatial basis functions  $\{\phi_\mu(\mathbf{r}) | \mu = 1, 2, \dots, K\}$  are used. A basis set of  $K$  spatial functions  $\{\phi_\mu\}$  returns  $2K$  spin orbitals, with  $K$  amounts of  $\alpha$  and  $\beta$  spin.  $N$  occupied orbitals  $\{\chi_a\}$  and  $2K - N$  virtual spin orbitals  $\{\chi_r\}$  are also generated. The larger the basis set, the more flexibility there is in the expansion of the spin orbitals and hence the HF energy ( $E_0$ ) decreases, until a limit is reached. This is known as the HF limit.

## 2.10 Electron Correlation

Electron correlation occurs in every system with more than one electron and can be thought of as the instantaneous interactions between electrons in a system. HF theory accounts for exchange or Fermi-correlation; introduced by the Slater determinant, which allows the antisymmetry principle to be obeyed. Therefore, in HF theory electrons with the same spin are correlated as two electrons with the same spin cannot occupy the same space. In contrast, Coulomb correlation which accounts for the electrostatic repulsion between electrons is neglected in HF as the electron-electron repulsion is averaged instead of considering individual electronic repulsion and hence electrons with opposite spin are uncorrelated. A single determinant wavefunction is often referred to as uncorrelated as it does not account for Coulomb correlation. [46]

By considering a two electron Slater determinant, we can see how Fermi-correlation arises.

$$\Psi(\mathbf{x}_1, \mathbf{x}_2) = |\chi_i(\mathbf{x}_1)\chi_j(\mathbf{x}_2)\rangle \quad (2.29)$$

In a situation where the electrons have opposite spins,

$$\begin{aligned} \chi_i(\mathbf{x}_1) &= \psi_i(\mathbf{r}_1)\alpha(1) \\ \chi_j(\mathbf{x}_2) &= \psi_j(\mathbf{r}_2)\beta(2) \end{aligned} \quad (2.30)$$

expanding the determinant for a two electron wavefunction, results in:

$$\Psi(\mathbf{x}_1, \mathbf{x}_2) = \chi_i(\mathbf{x}_1)\chi_j(\mathbf{x}_2) - \chi_j(\mathbf{x}_1)\chi_i(\mathbf{x}_2) \quad (2.31)$$

The probability of finding an electron can be expressed as:

$$P(\mathbf{x}_1, \mathbf{x}_2) = |\Psi(\mathbf{x}_1, \mathbf{x}_2)|^2 \quad (2.32)$$

The probability function can be expanded to allow  $P(\mathbf{r}_1, \mathbf{r}_2)$  to represent the probability of finding electron 1 at  $r_1$  and electron 2 at  $r_2$ :

$$P(\mathbf{r}_1, \mathbf{r}_2) = \int P(\mathbf{x}_1, \mathbf{x}_2) d\sigma_1 d\sigma_2 \quad (2.33)$$

Using Equations 2.31 and 2.32 the normalised probability function can be expressed as:

$$P(\mathbf{r}_1, \mathbf{r}_2) = \frac{1}{2} |\chi_i(\mathbf{x}_1)\chi_j(\mathbf{x}_2) - \chi_j(\mathbf{x}_1)\chi_i(\mathbf{x}_2)|^2 \quad (2.34)$$

Substituting in the values of  $\chi_i(\mathbf{x}_1)$  and  $\chi_j(\mathbf{x}_1)$  defined in Equation 2.30:

$$P(\mathbf{r}_1, \mathbf{r}_2) = \frac{1}{2} |\psi_i(\mathbf{r}_1)\alpha(\omega_1)\psi_j(\mathbf{r}_2)\beta(\omega_2) - \psi_i(\mathbf{r}_2)\alpha(\omega_2)\psi_j(\mathbf{r}_1)\beta(\omega_1)|^2 \quad (2.35)$$

Which simplifies to:

$$P(\mathbf{r}_1, \mathbf{r}_2)d\mathbf{r}_1d\mathbf{r}_2 = \frac{1}{2} [|\psi_i(\mathbf{r}_1)|^2|\psi_j(\mathbf{r}_2)|^2 + |\psi_i(\mathbf{r}_2)|^2|\psi_j(\mathbf{r}_1)|^2]d\mathbf{r}_1d\mathbf{r}_2 \quad (2.36)$$

The first term is the product of the probability of finding electron-1 at  $\mathbf{r}_1$  multiplied by the probability of finding electron-2 at  $\mathbf{r}_2$ , if electron-1 occupied  $\psi_i$  and electron-2 occupied  $\psi_j$ . In the second term,  $\psi_j$  is occupied by electron-1 and  $\psi_i$  with electron-2. As electrons are indistinguishable, the probability is the average of the two terms and hence the motion of the two electrons is uncorrelated. This is easiest to see if  $\psi_i = \psi_j$ , as in that case;

$$P(\mathbf{r}_1, \mathbf{r}_2) = |\psi_i(\mathbf{r}_1)|^2|\psi_i(\mathbf{r}_2)|^2 \quad (2.37)$$

There is a finite probability of finding two electrons which have opposite spin at the same point in space,  $P(\mathbf{r}_1, \mathbf{r}_2) \neq 0$ . However, if these electrons has the same spin ( $\beta$ ) then:

$$\begin{aligned} \chi_1(\mathbf{x}_1) &= \psi_i(\mathbf{r}_1)\beta(\omega_1) \\ \chi_2(\mathbf{x}_2) &= \psi_j(\mathbf{r}_2)\beta(\omega_2) \end{aligned} \quad (2.38)$$

The previous process can be repeated to obtain:

$$\begin{aligned} P(\mathbf{r}_1, \mathbf{r}_2) &= \frac{1}{2} \{ |\psi_i(\mathbf{r}_1)|^2|\psi_j(\mathbf{r}_2)|^2 + |\psi_i(\mathbf{r}_2)|^2|\psi_j(\mathbf{r}_1)|^2 \\ &\quad - [\psi_i^*(\mathbf{r}_1)\psi_j(\mathbf{r}_1)\psi_j^*(\mathbf{r}_2)\psi_i(\mathbf{r}_2) + \psi_i(\mathbf{r}_1)\psi_j^*(\mathbf{r}_1)\psi_j(\mathbf{r}_2)\psi_i^*(\mathbf{r}_2)] \} \end{aligned} \quad (2.39)$$

The probabilities are now correlated due to the extra cross term, this is Fermi-correlation. The probability of finding two electrons with parallel spins at the same point in space is zero.

As mentioned previously, HF theory only accounts for Fermi-correlation and neglects Coulomb correlation, which results in the underestimation of electron correlation and hence the HF energy is always higher than the exact energy. When using a sufficiently large basis set, the HF wavefunction accounts for roughly 99% of the total energy, for most systems. The difference between the exact energy and the HF energy is known as the electron correlation energy. [47]

$$E_{\text{corr}} = E_{\text{exact}} - E_{\text{HF}} \quad (2.40)$$

For convenience, the electron correlation energy can be split into two parts; ‘dynamic’ ( $E_D$ ) and ‘static’/‘non-dynamic’ ( $E_S$ ) correlation. Dynamic correlation

is associated with the instantaneous response of an electron to the positions of all other electrons, such as electrons within the same spatial orbital. As a direct contrast static correlation can be associated with electrons occupying different spatial orbitals however, it is also referred to as a near-degeneracy effect as it can be important in systems where multiple states are close to the ground state energy resulting in low-lying excitations. [3]

$$E_{\text{corr}} = E_{\text{D}} + E_{\text{S}} \quad (2.41)$$

The majority of chemical systems possess both dynamic and static correlation, however, in the helium atom the majority of the electron correlation is dynamic and at the dissociation limit in a  $\text{H}_2$  molecule the correlation is mostly static. These two examples can be used to highlight the differences between dynamic and static correlation.

Figure 2.6 gives a visual representation of dynamic correlation in the ground state of helium, with the electrons occupying the  $1s$  orbital. Dynamic correlation is inversely proportional to the distance between electrons ( $\frac{1}{r_{ij}}$ ) and hence the left-hand scenario in Figure 2.6 is more favourable.

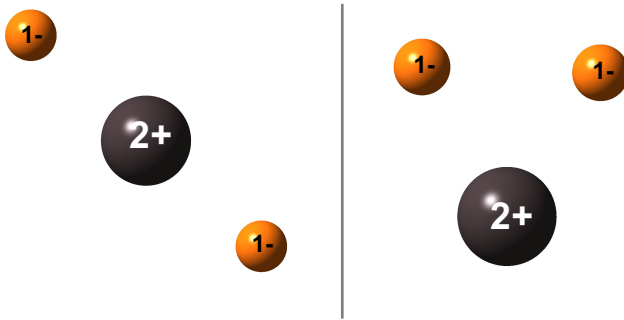


Figure 2.6: A visual representation of dynamic correlation in a helium atom, left arrangement is more favourable and lower in energy than the right

As an example of static correlation, consider a  $\text{H}_2$  molecule. At the equilibrium geometry, the bonding and antibonding orbitals have a distinctive energy difference. This results in mostly dynamic correlation between the two electrons, which are situated in the singularly occupied hydrogen  $1s$  orbitals. As the bond distance increases the energy difference between the bonding and antibonding orbitals decreases until the dissociation limit, where they become degenerate. As the bond length increases, so does the static correlation contribution. [3] During the bond stretching, there are two possible configurations for the electrons: one on each hydrogen atom or both electrons could become situated on the same hydrogen, as shown in Figure 2.7.

Hollet and Gill [48] suggest that static correlation has two ‘flavours’, with one that is similar to dissociating  $\text{H}_2$ , which can be captured by breaking the spin symmetry of the HF wavefunction and the other which cannot. This type of correlation

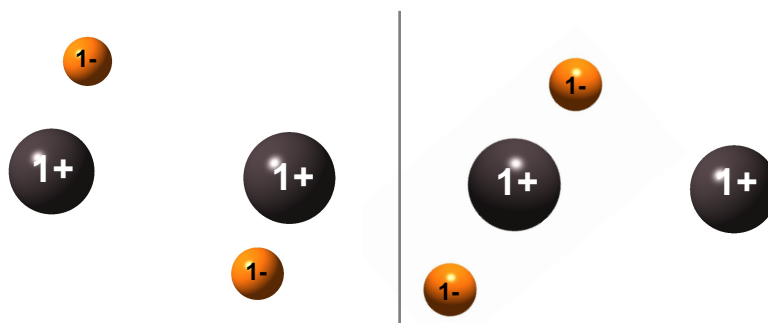


Figure 2.7: A visual representation of static correlation in the  $\text{H}_2$  molecule, left arrangement is more favourable and lower in energy than the right which shows ionic nature

is the most difficult of the two to accurately model as it requires large contributions of multiple Slater determinants.

Incorrect descriptions of static correlation are responsible for some of the biggest failures of HF in the literature. [49] Systems with significant static correlation are said to have multireference character and typical examples of these include: systems with partially occupied degenerate orbitals such as a low spin  $d_5$  complexes, systems with elongated or multiple bonds and systems which are electronically excited. [50]

## 2.11 Post Hartree–Fock Methods

HF methods result in energetically good one-determinant trial wavefunctions. However, HF methods do not take into account electron correlation (Section 2.10) and thus have limitations when describing certain chemical systems, such as those with large amount of static correlation. The HF method can be improved upon via a series of corrections which recover the electron correlation, such methods are referred to as post Hartree–Fock methods. There are several post Hartree–Fock methods which have been used to model actinide systems: Configuration Interaction (CI), [51] Complete/Restricted Active Space Self-Consistent Field (CASSCF/RASSCF), [52, 53] Coupled Cluster (CC) [54] and Møller-Plessett perturbation theory. [55] In this section CI, CASSCF/RASSCF and perturbation theory Post-HF methods are discussed.

### 2.11.1 Configuration Interaction

One way to improve on the HF method is to add additional Slater determinants which represent the excited states; known as configuration interaction (CI). This is achieved by replacing occupied orbitals in the HF Slater determinant with unoccupied orbitals and are denoted singly, doubly, triply ... *etc.* excited determinants based on how many occupied orbitals have been replaced. [3, 46, 56] Examples of such excitations are show in Figure 2.8, however, it is worth noting that there are

many variations of each excitation for a given system.

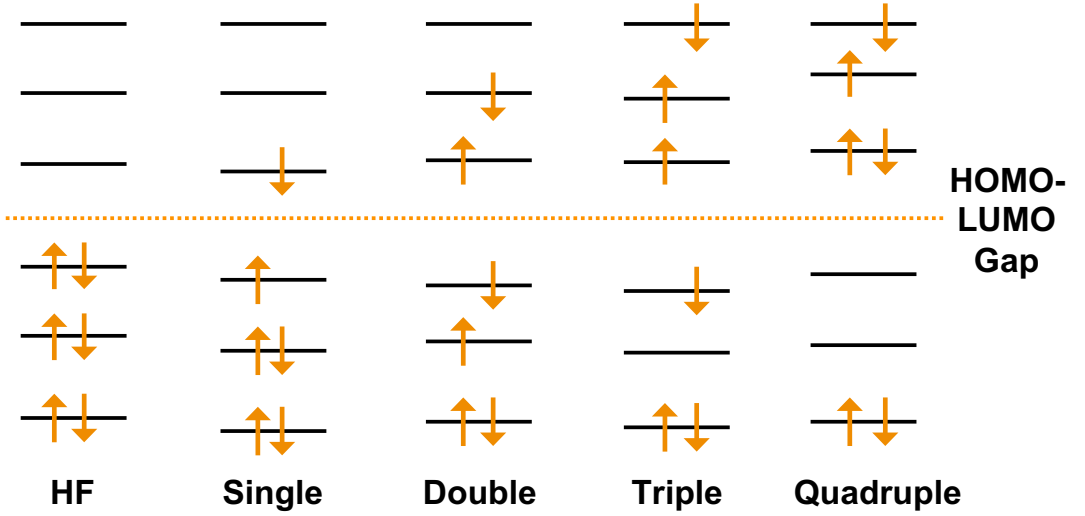


Figure 2.8: Excitations from the HF Slater determinant showing an example of single, double, triple and quadruple excitations; replacing 1, 2, 3 and 4 occupied spin orbitals with virtual orbitals.

Inclusion of all excited configurations, shown in Equation 2.42 is denoted *full configuration interaction* (FCI). FCI recovers all the electron correlation within the limitations of the basis set and hence if a complete basis set (*i.e.* a theoretical, infinite basis set) was used then this would result in the exact wavefunction. [3, 56]

$$|\Phi_0\rangle = c_0 |\Psi_0\rangle + \sum_{ar} c_a^r |\Psi_a^r\rangle + \sum_{\substack{a<b \\ r<s}} c_{ab}^{rs} |\Psi_{ab}^{rs}\rangle + \sum_{\substack{a<b<c \\ r<s<t}} c_{abc}^{rst} |\Psi_{abc}^{rst}\rangle + \sum_{\substack{a<b<c<d \\ r<s<t<u}} c_{abcd}^{rstu} |\Psi_{abcd}^{rstu}\rangle + \dots \quad (2.42)$$

Where the first term represents the HF determinant, the second represents the sum of all single excitations, the third all the double excitations and so on. It is worth noting that  $a < b$  *etc.* ensure that each excitation is only counted once. Equation 2.43 represents the shorthand notation of Equation 2.42.

$$|\Phi_0\rangle = c_0 |\Psi_0\rangle + c_S |\Psi_S\rangle + c_D |\Psi_D\rangle + c_T |\Psi_T\rangle + c_Q |\Psi_Q\rangle + \dots \quad (2.43)$$

$c_n$  represent the expansion coefficients, which are variables that minimise the energy of the system and can be found by diagonalisation of the CI Hamiltonian matrix:

$$\hat{H}^{\text{CI}} = \begin{vmatrix} \langle \Psi_0 | \hat{H} | \Psi_0 \rangle & \langle \Psi_0 | \hat{H} | \Psi_S \rangle & \langle \Psi_0 | \hat{H} | \Psi_D \rangle & \langle \Psi_0 | \hat{H} | \Psi_T \rangle & \langle \Psi_0 | \hat{H} | \Psi_Q \rangle & \cdots \\ \langle \Psi_S | \hat{H} | \Psi_0 \rangle & \langle \Psi_S | \hat{H} | \Psi_S \rangle & \langle \Psi_S | \hat{H} | \Psi_D \rangle & \langle \Psi_S | \hat{H} | \Psi_T \rangle & \langle \Psi_S | \hat{H} | \Psi_Q \rangle & \cdots \\ \langle \Psi_D | \hat{H} | \Psi_0 \rangle & \langle \Psi_D | \hat{H} | \Psi_S \rangle & \langle \Psi_D | \hat{H} | \Psi_D \rangle & \langle \Psi_D | \hat{H} | \Psi_T \rangle & \langle \Psi_D | \hat{H} | \Psi_Q \rangle & \cdots \\ \langle \Psi_T | \hat{H} | \Psi_0 \rangle & \langle \Psi_T | \hat{H} | \Psi_S \rangle & \langle \Psi_T | \hat{H} | \Psi_D \rangle & \langle \Psi_T | \hat{H} | \Psi_T \rangle & \langle \Psi_T | \hat{H} | \Psi_Q \rangle & \cdots \\ \langle \Psi_Q | \hat{H} | \Psi_0 \rangle & \langle \Psi_Q | \hat{H} | \Psi_S \rangle & \langle \Psi_Q | \hat{H} | \Psi_D \rangle & \langle \Psi_Q | \hat{H} | \Psi_T \rangle & \langle \Psi_Q | \hat{H} | \Psi_Q \rangle & \cdots \\ \vdots & \vdots & \vdots & \vdots & \vdots & \ddots \end{vmatrix} \quad (2.44)$$

The CI Hamiltonian matrix can be simplified (Equation 2.45) with the application of three rules:

1. Application of Brillouin's theorem [57]: "*Singly excited determinants ( $|\Psi_a^r\rangle$ ) will not interact directly with a HF reference determinant ( $|\Psi_0\rangle$ )*" *i.e.*  $\langle \Psi_0 | \hat{H} | \Psi_S \rangle = 0$
2. Application of the Slater-Condon rules [3, 58, 59]: "A CI matrix element can only be non-zero if two determinants differ by 0, 1 or 2 MOs." *i.e.*  $\langle \Psi_S | \hat{H} | \Psi_Q \rangle = 0$
3. When two determinants are identical (*i.e.* diagonal matrix elements), this results in the energy of a single-determinant wavefunction (labelled  $E_n$  in Equation 2.45)

The CI Hamiltonian matrix simplified to:

$$\hat{H}^{\text{CI}} = \begin{vmatrix} E_{\text{HF}} & 0 & \langle \Psi_0 | \hat{H} | \Psi_D \rangle & 0 & 0 & \cdots \\ 0 & E_S & \langle \Psi_S | \hat{H} | \Psi_D \rangle & \langle \Psi_S | \hat{H} | \Psi_T \rangle & 0 & \cdots \\ \langle \Psi_D | \hat{H} | \Psi_0 \rangle & \langle \Psi_D | \hat{H} | \Psi_S \rangle & E_D & \langle \Psi_D | \hat{H} | \Psi_T \rangle & \langle \Psi_D | \hat{H} | \Psi_Q \rangle & \cdots \\ 0 & \langle \Psi_T | \hat{H} | \Psi_S \rangle & \langle \Psi_T | \hat{H} | \Psi_D \rangle & E_T & \langle \Psi_T | \hat{H} | \Psi_Q \rangle & \cdots \\ 0 & 0 & \langle \Psi_Q | \hat{H} | \Psi_D \rangle & \langle \Psi_Q | \hat{H} | \Psi_T \rangle & E_Q & \cdots \\ \vdots & \vdots & \vdots & \vdots & \vdots & \ddots \end{vmatrix} \quad (2.45)$$

While FCI is a powerful method, unfortunately even with the use of a moderate basis set, the computational expense rapidly becomes intractable. The calculation size scales factorially with the number of electrons and hence FCI is limited to only the smallest of systems. Therefore, in order to make CI calculations computationally reasonable a truncated approach is taken. This is achieved by capping the excitation level the basis functions represent; the most common example of this is the CI singles and doubles (CISD), which limits the basis functions to those which represent single or double excitations relative to the ground state. [3, 56] For medium-sized molecules and basis sets, CISD still recovers  $\sim 80-90\%$  of electron correlation, [3] and CI with

singles, doubles and triples (CISDT) is considered the ‘gold standard’ of calculation and is typically used as a benchmark value for other systems.

### 2.11.2 The Complete/Restricted Active Space, Self-Consistent Field Methods (CASSCF/RASSCF)

Instead of performing FCI on the whole system the Complete/Restricted Active Space, Self-Consistent Field method only performs FCI on selected orbitals, which are chemically important in said system. In CASSCF orbitals are partitioned into active and inactive spaces. The chemically important orbitals are placed in the active space, which are typically a number of the highest occupied and lowest unoccupied orbitals from a HF calculation.

In a CASSCF calculation, the inactive orbitals are either fully occupied (core) or unoccupied (virtual), whereas the active orbitals are partially occupied. FCI (Section 2.11.1) is then performed on the active orbitals, *i.e.* all possible excitations are allowed and determinants are generated for each possible excitation. In CASSCF calculations it is usual for the notation to be in the form  $(n, m)$ -CASSCF where  $n$  is the number of electrons and  $m$  is the number of orbitals in the active space. [3]

As was discussed in the previous section (Section 2.11.1), FCI is very computationally expensive and hence this limits the amount of orbitals which can be placed in the active space, typically CASSCF calculations do not exceed 18 electrons. [60, 61] Table 2.1 gives the number of configuration state functions (CSFs) generated for an  $[n,n]$ -CASSCF wavefunction. [3]

Table 2.1: Number of configurations generated in an  $[n,n]$ -CASSCF wavefunction

$n$	Number of CSFs
2	3
4	20
6	175
8	1764
10	19404
12	226512
14	2760615

Due to the limited space in the active space, selection of the ‘important’ orbitals is imperative. Björn’s Rules [62] can be used in order to aid the selection of active orbitals:

- A number of the highest occupied orbitals

- A number of the lowest unoccupied orbitals
- Include conjugated orbitals
- Any bonding and antibonding orbitals relating to a bond which is of interest
- For each  $\pi$  bond: include two  $\pi$  orbitals
  - Otherwise most appropriate  $\pi$  orbitals selected by energy
- Transition metals: all orbitals with d-character
- Metals in high oxidation states require more active orbitals
- Lanthanides: 4f, 5d and 6s orbitals
- Actinides: 5f, 6d and 7s active
  - If highly charged then reduced to only 5f
  - Highly covalent interactions such as U-O in uranyl require more active orbitals ([12,12]) [63]

For more complex systems, allowing for all orbitals under Björn Rules quickly causes the active space to increase in size. For these larger systems the Restricted Active Space SCF (RASSCF) approach can be utilised which further partitions the orbitals. [51–53, 64–66] In the RASSCF approach the active space is split into three parts: RAS1, RAS2 & RAS3. RAS2 becomes the most important active space and hence FCI is utilised on these orbitals and the occupation number is not limited, much like in the active space area in CASSCF. The RAS1/ RAS3 spaces comprise of MOs which were doubly occupied/empty in the HF reference determinant. Additional configurations (to the RAS2) are generated by allowing excitations from the RAS1 into the RAS3 using truncated CI methods, usually CISD or CISDT. Figure 2.9 gives a visual representation of the partitioning in RASSCF in comparison to CASSCF.

Choosing an active space is challenging, however, there are two strategies for obtaining the best active space for a given system. The first method utilises a single point energy calculation with a method such as density functional theory (DFT, see Section 2.12) and then the important orbitals are selected based on Björn Rules. This method is likely to take a few attempts to get a good active space as the occupation numbers and visual appearance needs to be monitored after the CASSCF, if adjustment of the active space is required then it can be adjusted and the calculation re-run.

The second method is known as RAS probing, which is the expansion of the active space systematically with the addition of orbitals into RAS1 and RAS3. The occupation numbers can be utilised in order to assess if an orbital should be in the

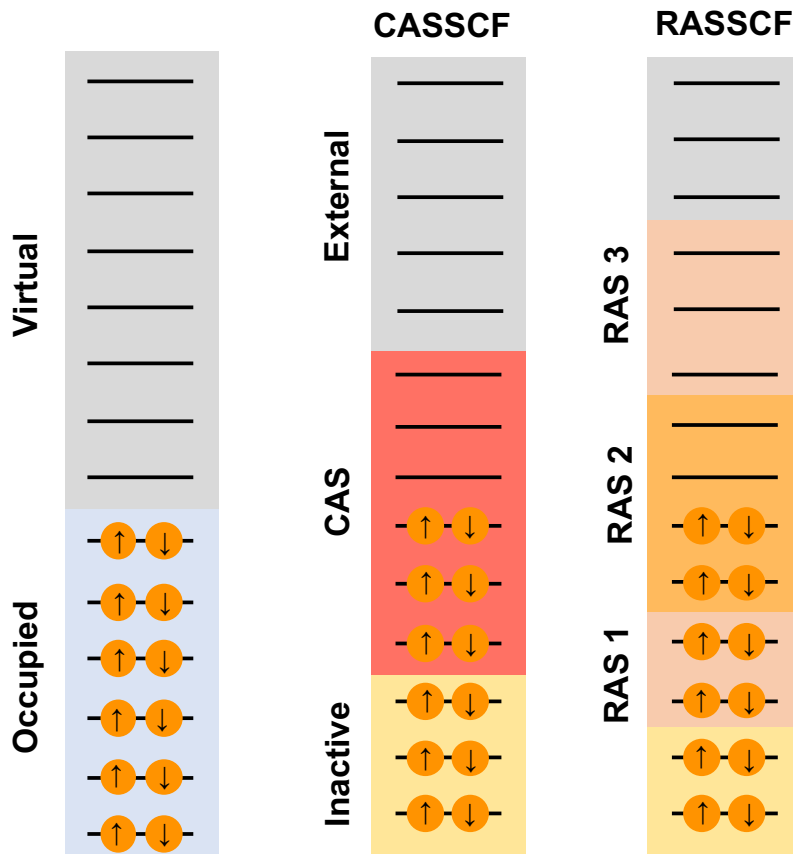


Figure 2.9: Representation of the partitioning in both CASSCF and RASSCF methods

active space. Typically values of less than 1.98 for an occupied orbital and greater than 0.02 for virtual orbitals indicate inclusion in the active space. For inclusion into the RAS2 partition, typically values of 1.95 or less and 0.05 or higher for occupied and virtual orbitals, respectively, indicate inclusion. Finally, one strongly occupied orbital should be paired with a weakly occupied orbital.

As CASSCF and RASSCF methods limit the number of active orbitals the focus of these methods is not on recovering the total correlation energy. Instead such calculations recover the part of the correlation energy which relates to the effects of near degeneracy, *i.e.* the static correlation. Second-order perturbation methods to both the CASSCF and RASSCF methods, referred to as CASPT2 [67, 68] and RASPT2 [62, 67], respectively, can be utilised to recover dynamic correlation (Section 2.11.3). Other methods for recovering dynamic correlation include the  $n$ -electron valence state perturbation theory (NEVPT2); this method will not be discussed in this thesis but, if desired, the reader is directed to several resources. [69–72]

### 2.11.3 Many-Body Perturbation Theory and CASPT2

Perturbation methods are utilised in quantum chemistry for adding corrections to solutions which employ an independent-particle approximation which is then termed a "Many-Body Perturbation Theory (MBPT). Perturbation theory approximates the value of a complex function by using an exact solution of a simpler related problem and then adding small corrections (perturbations) for additional factors. [73, 74] The Hamiltonian for a perturbed system can be described as:

$$\hat{H} = \hat{H}_0 + \varepsilon\hat{H}_p \quad (2.46)$$

$\hat{H}_0$  is the Hamiltonian for the unperturbed system,  $\varepsilon$  determines the strength of the perturbation and  $\hat{H}_p$  is a small perturbation. The Schrödinger equation with unperturbed Hamiltonian can be written as:

$$\hat{H}_0\Phi_i = E_i\Phi_i \quad \text{where } i = 0, 1, 2 \dots \infty \quad (2.47)$$

For simplicity only the ground state will be considered in this example ( $i = 0$ ). The perturbed Schrödinger equation is expressed as:

$$\hat{H}\Psi = W\Psi \quad (2.48)$$

This means that when  $\varepsilon = 0$ :  $\hat{H} = \hat{H}_0$ ,  $\Psi = \Phi_0$  and  $W = E_0$ , this is *unperturbed* or *zeroth-order* wavefunction and energy. As  $\varepsilon$  increases, the new energy and wavefunction change continuously and can therefore be expressed as a Taylor expansion in powers of the perturbation parameter  $\varepsilon$ .

$$\begin{aligned} W &= \varepsilon^0 W_0 + \varepsilon^1 W_1 + \varepsilon^2 W_2 + \varepsilon^3 W_3 + \dots \\ \Psi &= \varepsilon^0 \Psi_0 + \varepsilon^1 \Psi_1 + \varepsilon^2 \Psi_2 + \varepsilon^3 \Psi_3 + \dots \end{aligned} \quad (2.49)$$

The *first-order*, *second-order*, *etc.* *corrections* are represented by  $W_1/\Psi_1$  and  $W_2/\Psi_2$  respectively.

In order to obtain the perturbation equations for the zeroth, first, second and  $n^{\text{th}}$  order, the two expressions given in Equation 2.49 need to be substituted into Equation 2.48, shown in Equation 2.50.

$$\begin{aligned} &(\hat{H}_0 + \varepsilon\hat{H}_p)(\varepsilon^0\Psi_0 + \varepsilon^1\Psi_1 + \varepsilon^2\Psi_2 + \dots) \\ &= (\varepsilon^0 W_0 + \varepsilon^1 W_1 + \varepsilon^2 W_2 + \dots)(\varepsilon^0\Psi_0 + \varepsilon^1\Psi_1 + \varepsilon^2\Psi_2 + \dots) \end{aligned} \quad (2.50)$$

From this point, terms with the same power can be gathered and separated from the others forming the perturbation equations given in Equation 2.51.

$$\begin{aligned}
\varepsilon^0 : \hat{H}_0 \Psi_0 &= W_0 \Psi_0 \\
\varepsilon^1 : \hat{H}_0 \Psi_1 + \hat{H}_p \Psi_0 &= W_0 \Psi_1 + W_1 \Psi_0 \\
\varepsilon^2 : \hat{H}_0 \Psi_2 + \hat{H}_p \Psi_1 &= W_0 \Psi_2 + W_1 \Psi_1 + W_2 \Psi_0 \\
\varepsilon^n : \hat{H}_0 \Psi_n + \hat{H}_p \Psi_{n-1} &= \sum_{i=0}^n W_i \Psi_{n-i}
\end{aligned} \tag{2.51}$$

Møller-Plessett perturbation theory is a post-HF method which uses the sum over all the Fock operators for a system as the unperturbed Hamiltonian ( $\hat{H}_0$ ). This method has perturbations similar to those in Equation 2.51 to obtain different orders and hence accuracy of the method. The most common of which is the second order Møller-Plessett perturbation theory (MP2) as the costs of higher perturbations become excessively expensive for relatively small improvements in the molecular descriptions.

CASPT2 is a special case of MP2 described above. Using the multiconfigurational wavefunction obtained from a CASSCF calculation (which takes into account static correlation), the Hamiltonian of this calculation can be considered a reference Hamiltonian. In the CASPT2 method an improved wavefunction, which includes dynamic correlation, is generated from the reference Hamiltonian (obtained via the CASSCF calculation) via second order perturbations using the method described above. This method is truncated to second order and the reference  $\hat{H}_0$ ,  $W_0$  and  $\varepsilon^0 \Psi_0$  given in Equation 2.51 correspond to the CASSCF Hamiltonian, energy and wavefunction, respectively.

Post-HF methods offer significant improvement to HF energies due to their inclusion of electron correlation. Electron correlation is of particular importance in many chemical systems, with a specific example being systems with partially filled f-shells. While post-HF methods offer an improvement on HF methods, they are considerably more computationally expensive. HF calculations scale by a factor of 4 ( $N^4$ ) *i.e.* doubling the number of electrons in the system results in each iteration of the calculation taking  $2^4$  times longer. In contrast to this, FCI scales factorially and as such even using this on the chemically important orbitals in a system in a CASSCF/RASSCF calculation is very expensive when considering systems with f-elements. This makes post-HF methods impractical for general use in computational actinide chemistry. Instead a different method is utilised for the vast majority of actinide chemistry, Density Functional Theory (DFT).

## 2.12 Density Functional Theory

Up to this point different methods which involve obtaining accurate descriptions of the wavefunction have been discussed. While wavefunction methods are useful in solving quantum chemical calculations they do have some major disadvantages. The most notable of which is upon progression from the restricted single Slater determinant (Section 2.9) to multi-determinant description (Section 2.11), in order to account for electron correlation, the computational expense rapidly increases. Therefore, when using wavefunction methods there is this perpetual balancing act between obtaining an accurate representation of the system and keeping the computational cost to a minimum.

Interpretation of the wavefunction is not very accessible to the wider scientific community due to the need to manipulate and understand quantum mechanical calculations. A more intuitive approach to obtaining the energy of a system would be to use a physical *observable*, such as the electron density ( $\rho(\mathbf{r})$ ). The electron density for a many-electron system is:

$$\begin{aligned}\Psi(\mathbf{x}_1, \mathbf{x}_2 \cdots \mathbf{x}_n) &= |\chi_i(\mathbf{x}_1)\chi_j(\mathbf{x}_2) \cdots \chi_k(\mathbf{x}_n)\rangle \\ \rho(\mathbf{r}) &= \int |\Psi|^2 d\sigma_1, d\mathbf{x}_2 \cdots d\mathbf{x}_n\end{aligned}\tag{2.52}$$

Consider the Hamiltonian, which depends on the positions and atomic numbers of the nuclei and the total number of electrons in a system. The dependence on the total number of electrons highlights that the electron density is a useful physical property; integrating over all space gives the relationship:

$$N = \int \rho(\mathbf{r}) d\mathbf{r}\tag{2.53}$$

The total energy of a system in terms of electron density can be expressed as:

$$E[\rho(\mathbf{r})] = T[\rho(\mathbf{r})] + V[\rho(\mathbf{r})]\tag{2.54}$$

$E[\rho(\mathbf{r})]$  indicates that the energy is a function of the density and the density is a function of position  $\mathbf{r}$ , making the energy a function of a function, also known as a functional. Equation 2.54 defines the total energy of a system as the sum of the kinetic ( $T[\rho(\mathbf{r})]$ ) and potential ( $V[\rho(\mathbf{r})]$ ) energies.

Density functional theory (DFT) is based on this relationship and derives the energy and positions of the atomic nuclei from the electron density rather than the wavefunction. The energy as a functional of the electron density ( $E[\rho(\mathbf{r})]$ ) can be derived as:

$$E[\rho(\mathbf{r})] = T[\rho(\mathbf{r})] + V_{Ne}[\rho(\mathbf{r})] + V_{NN}[\rho(\mathbf{r})] + V_{ee}[\rho(\mathbf{r})]\tag{2.55}$$

Where  $T[\rho(\mathbf{r})]$  is the kinetic energy and  $V[\rho(\mathbf{r})]$  the potential energy which is

split into: nuclear-electron attraction ( $Ne$ ), nuclear-nuclear repulsion ( $NN$ ) and electron-electron repulsion ( $ee$ ). As was seen in Section 2.5 application of the Born–Oppenheimer approximation fixes the positions of the nuclei and hence  $V_{NN}[\rho(\mathbf{r})]$  is held constant. The electron-electron repulsion can be further divided (as in HF theory) into a Coulomb and exchange term,  $J[\rho(\mathbf{r})]$  and  $K_D[\rho(\mathbf{r})]$ , respectively. This defines the Thomas-Fermi-Dirac model [75–77]:

$$E[\rho(\mathbf{r})] = T[\rho(\mathbf{r})] + V_{Ne}[\rho(\mathbf{r})] + J[\rho(\mathbf{r})] + K_D[\rho(\mathbf{r})] \quad (2.56)$$

This model uses a uniform gas denoted ‘*Jellium*’ in order to generate approximations for the exchange and kinetic energy functionals. [76, 77] This medium comprises of an infinite number of electrons in an infinite space with a uniformly distributed positive charge. This is the simplest model for interacting electrons but it is worth noting that this model does not describe chemical bonding and hence does not describe molecular systems well.

### 2.12.1 Hohenberg-Kohn Theorems

From 1927→1964 not much improvement was made on the Thomas-Fermi-Dirac model and while this was useful for the solid-state physics community it was not appropriate for chemists as it produced large errors in molecular systems and no variational principle had been established. In 1964, Hohenberg and Kohn introduced two theorems which form the basis of DFT. [78]

From their paper [78], the first theorem states: ‘*the external potential ( $V_{ext}(\mathbf{r})$ ) is (to within a constant) a unique functional of  $\rho(\mathbf{r})$  ; since, in turn  $V_{ext}(\mathbf{r})$  fixes  $\hat{H}$  we see that the full many particle ground state is a unique functional of  $\rho(\mathbf{r})$ ’.*

This can be expressed mathematically as:

$$E[\rho(\mathbf{r})] = F[\rho(\mathbf{r})] + \int \rho(\mathbf{r})V_{ext}(\mathbf{r})d\mathbf{r} \quad (2.57)$$

$F[\rho(\mathbf{r})]$  is the Hohenberg-Kohn universal functional of the electron density. This is independent of the external potential and the exact form is unknown and therefore approximations need to be made.

The second theorem is known as the variational theorem; the energy of a trial density is greater than or equal to the true ground-state energy. [78, 79] This is simply the variational principle discussed in Section 2.3

$$F[\rho(\mathbf{r})] + \int \rho(\mathbf{r})V_{ext}(\mathbf{r})d\mathbf{r} \geq E_0 \quad (2.58)$$

### 2.12.2 Kohn-Sham Equations

The methods above utilise the electron density to generate a potential, which determines the Hamiltonian, which generates a wavefunction and then the energy of the system can be calculated. While the set-up of these methods is perhaps more approachable, the final step still requires solving the Schrödinger equation and hence such methods offer no advantage over wavefunction methods.

The solution to this came in 1965 with the Kohn–Sham approach. [80–82] They suggested that the Hamiltonian would be simpler to deal with if it represented a non-interacting system of electrons; therefore the Hamiltonian could be expressed as a sum of one-electron operators. Such a Hamiltonian would have eigenfunctions that are Slater determinants of the individual one-electron eigenfunctions, and eigenvalues which are simply the sum of the one-electron eigenvalues. The use of such a limited Hamiltonian seems counter-intuitive, however when used alongside the density it can be used to set a starting point. Such a starting point is a fictitious system of non-interacting electrons which have the same density in its ground state to that of the system of interest.

Using this fictitious system,  $F[\rho(\mathbf{r})]$  does not need to be obtained, instead a fictional system which has the same density as the system of interest (with interacting particles) is required. This model introduces orbitals which allows an improved representation of the kinetic energy term. The kinetic energy functional is split into an exact component (HF kinetic energy) and a small correction term, which gets incorporated into the exchange–correlation term ( $E_{xc}[\rho(\mathbf{r})]$ ). The Kohn–Sham DFT energy ( $E_{KS}$ ) can be expressed as:

$$E_{KS}[\rho(\mathbf{r})] = T_{NI}[\rho(\mathbf{r})] + V_{Ne}[\rho(\mathbf{r})] + J[\rho(\mathbf{r})] + E_{xc}[\rho(\mathbf{r})] \quad (2.59)$$

Where  $T_{NI}[\rho(\mathbf{r})]$  represents the kinetic energy of the non-interacting system,  $V_{Ne}[\rho(\mathbf{r})]$  is the nuclear-electron attractive energy and Coulombic interactions are denoted  $J[\rho(\mathbf{r})]$ .  $E_{xc}[\rho(\mathbf{r})]$  is the exchange–correlation term which comprises of the correction to the kinetic energy (mentioned above) and the exchange–correlation interactions between electrons. [3]

$$E_{xc}[\rho(\mathbf{r})] = (T[\rho(\mathbf{r})] - T_{NI}[\rho(\mathbf{r})] + (V_{ee}[\rho(\mathbf{r})] - J[\rho(\mathbf{r})])) \quad (2.60)$$

$E_{xc}[\rho(\mathbf{r})]$  can be found using Schrödinger-like equations known as the Kohn–Sham equations:

$$\left(-\frac{1}{2}\nabla^2 + V_{KS}(\mathbf{r})\right)\phi_i(\mathbf{r}) = \varepsilon_i\phi_i(\mathbf{r}) \quad (2.61)$$

$\varepsilon_i$  is the energy corresponding to the orbital  $\phi_i$  and  $V_{KS}$  represents the Kohn–Sham potential, which is the effective potential needed to generate the same electron density as found in a given system of interacting particles.

$$V_{\text{KS}}(\mathbf{r}) = V_{\text{Ne}}(\mathbf{r}) + \int \frac{\rho(\mathbf{r}')}{|\mathbf{r} - \mathbf{r}'|} d\mathbf{r}' + V_{\text{xc}}(\mathbf{r}) \quad (2.62)$$

$V_{\text{xc}}(\mathbf{r})$  is the exchange–correlation potential:

$$V_{\text{xc}}(\mathbf{r}) = \frac{\delta E_{\text{xc}}[\rho]}{\delta \rho(\mathbf{r})} \quad (2.63)$$

The exchange correlation function can be rewritten as:

$$E_{\text{xc}}[\rho] = E_{\text{x}}[\rho] + E_{\text{c}}[\rho] \quad (2.64)$$

$$E_{\text{xc}}[\rho] = \int \rho(\mathbf{r}) \varepsilon_{\text{x}}[\rho(\mathbf{r})] d\mathbf{r} + \int \rho(\mathbf{r}) \varepsilon_{\text{c}}[\rho(\mathbf{r})] d\mathbf{r}$$

$\varepsilon_{\text{x}}$  and  $\varepsilon_{\text{c}}$  denote the exchange and correlation energies densities.

The solutions to these equations are denoted Kohn–Sham orbitals ( $\phi_i^{\text{KS}}(\mathbf{r})$ ) and the total electron density of the system can be expressed as:

$$\rho(\mathbf{r}) = \sum_i |\phi_i^{\text{KS}}(\mathbf{r})|^2 \quad (2.65)$$

As was the case in HF theory, the Kohn–Sham equations are solved with the SCF process utilising an initial set of approximate orbitals. HF theory and Kohn–Sham DFT have many similarities, however, a key distinction is the HF theory is an approximation whereas Kohn–Sham DFT is an exact method on the condition that the exact form of  $E_{\text{xc}}$  is known and the electron density can be expressed using a single electronic configuration. However, in reality  $E_{\text{xc}}$  must be approximated.

### 2.12.3 Exchange–Correlation Functionals

Within DFT, there are a plethora of approximations for  $E_{\text{xc}}$ , termed ‘*exchange–correlation functionals*’ (xc-functionals) and the difference between DFT methods is the choice of which xc-functional is utilised. While in wavefunctional methods the quality of the approximations could be characterised via an ordering parameter *e.g.* the level of excitations included, in contrast when considering exchange–correlation functionals there is no obvious ordering parameter as these are largely empirical. In DFT, the hierarchy of xc-functionals was suggested by Perdew, which he termed ‘*Jacob’s Ladder of Chemical Accuracy*’, shown in Figure 2.10. [83] In this formalism, progressing up each ‘rung’ of the ladder would include more information about the behaviour of the density and as such the functionals have the potential to be more accurate. It is worth noting that each step up the ladder results in a greater computational expense.

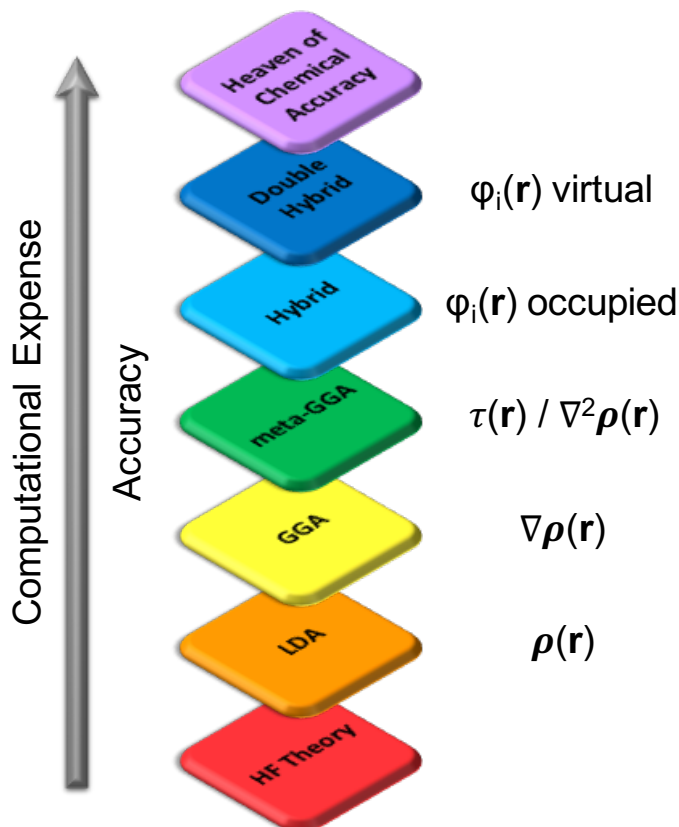


Figure 2.10: Schematic of ‘Jacob’s Ladder of Chemical Accuracy’ representing different types of exchange–correlation functional. Drawn with inspiration from [83]

### 2.12.3.1 The Local Density Approximations

The lowest ‘rung’ of Jacob’s Ladder is known as the Local Density Approximation (LDA), which is solely dependent on the electron density ( $\rho$ ) at a given point ( $\mathbf{r}$ ). [84, 85] In this model, the exchange–correlation energy is equal to that of a uniform gas at a given point in space and can be expressed as:

$$E_{\text{xc}}^{\text{LDA}}[\rho(\mathbf{r})] = \int \rho(\mathbf{r})\varepsilon_{\text{xc}}[\rho(\mathbf{r})] d\mathbf{r} \quad (2.66)$$

Where  $\varepsilon_{\text{xc}}$  is the exchange–correlation energy density.

As LDA functionals are only dependent on the electron density, they predict the electron density to be more homogenous than reality. These functionals also result in overbinding in molecules, typically by  $30 \text{ kcal mol}^{-1}$ , [86] as a result of their overestimation of the correlation and underestimation of the exchange energy by  $\sim 10\%$ . [84, 85]

### 2.12.3.2 Generalised-Gradient Approximation and meta-GGA xc-Functionals

The main shortcoming of LDA is the homogenous nature of the electron density, in chemical systems the electron density is inhomogeneous. Therefore, a systematic improvement to the description of the electron density is to make it dependent on the extent to which the density is locally changing. The second ‘rung’ of Jacob’s Ladder corresponds to ‘*Generalised-Gradient Approximation*’ in which  $E_{xc}$  is dependent on the electron density ( $\rho(\mathbf{r})$ ) and the gradient of the electron density ( $\nabla\rho(\mathbf{r})$ ) and have the general form:

$$E_{xc}^{\text{GGA}}[\rho(\mathbf{r})] = \int \rho(\mathbf{r})\varepsilon_{xc}[\rho(\mathbf{r}), \nabla\rho(\mathbf{r})] d\mathbf{r} \quad (2.67)$$

There are a multitude of GGA xc-functionals, each with different parameters to calculate  $E_{xc}$ , however, these parameters are found by two different methods: semi-empirically - using experimental data or non-empirically. Examples of semi-empirical and non-empirical GGA’s are BLYP [87, 88] and PBE [89, 90], respectively.

GGA xc-functionals perform reasonably well for geometries of chemical structures but are poor for other properties such as excitation energies. [86]

The next progression are known as ‘*meta-Generalised-Gradient Approximation*’, which offer two different forms of improvement to GGAs. The first of which is to utilise the Laplacian (or second-derivative) of the electron density and have the form:

$$E_{xc}^{\text{meta-GGA}}[\rho(\mathbf{r})] = \int \rho(\mathbf{r})\varepsilon_{xc}[\rho(\mathbf{r}), \nabla\rho(\mathbf{r}), \nabla^2\rho(\mathbf{r})] d\mathbf{r} \quad (2.68)$$

The second form is to include dependence on the kinetic-energy density ( $\tau(\mathbf{r})$ ) to the exchange–correlation potential in a GGA:

$$\tau(\mathbf{r}) = \sum_i^{\text{occupied}} \frac{1}{2} |\nabla\phi_i(\mathbf{r})|^2 \quad (2.69)$$

Where  $\phi_i$  represent the Kohn-Sham orbitals in the system.

A popular example of a meta-GGA xc-functional is TPSS, developed by Tao, Perdew, Staroverov and Scuseria. [91]

### 2.12.3.3 Hybrid xc-functionals

The above xc-functionals primarily depend on the electron density and its derivatives, these are denoted ‘*semi-local*’ or ‘*pure*’ functionals, the next progression would include of proportion of HF exchange, these are known as *Hybrid xc-functionals*. The amount of HF exchange included varies between xc-functionals and is constant within. Hybrid xc-functionals are expressed as the sum of the HF exchange functional ( $E_x^{\text{HF}}$ ), which is the HF exchange calculated using Kohn-Sham orbitals, and

any number of DFT xc-functionals described above:

$$E_{\text{xc}} = \alpha E_{\text{x}}^{\text{HF}} + (1 - \alpha) E_{\text{xc}}^{\text{DFT}} \quad (2.70)$$

Where  $\alpha$  is the coefficient which represents the amount of  $E_{\text{x}}^{\text{HF}}$  present and takes values between 0 and 1.

The first hybrid xc-functional was suggested by Becke [92], who included 50%  $E_{\text{x}}^{\text{HF}}$  in his xc-functional on the basis of developing a functional which was based on the adiabatic correction formalism. [6]

Popular hybrid xc-functionals in the literature are the semi-empirical B3LYP [88, 92–95] and the non-empirical PBE0 [89, 90, 96] functionals which are defined in Equations 2.71 and 2.72, respectively.

$$E_{\text{xc}}^{\text{B3LYP}} = 0.8 E_{\text{x}}^{\text{LDA}} + 0.72 E_{\text{x}}^{\text{B88X}} + 0.2 E_{\text{x}}^{\text{HF}} + 0.19 E_{\text{c}}^{\text{VWN}} + E_{\text{c}}^{\text{LYP}} \quad (2.71)$$

$$E_{\text{xc}}^{\text{PBE0}} = 0.25 E_{\text{x}}^{\text{HF}} + 0.75 E_{\text{x}}^{\text{PBE}} + E_{\text{c}}^{\text{PBE}} \quad (2.72)$$

B3LYP comprises of exchange functionals ( $E_{\text{x}}$ ) from: LDA ( $E_{\text{x}}^{\text{LDA}}$ ), Becke88 GGA ( $E_{\text{x}}^{\text{B88X}}$ ) [87, 97], with 20%  $E_{\text{x}}^{\text{HF}}$  and correlation functionals ( $E_{\text{c}}$ ) from: Vosko-Wilk-Nusair LDA ( $E_{\text{c}}^{\text{VWN}}$ ) [98] and the Lee, Yang, Parr GGA ( $E_{\text{c}}^{\text{LYP}}$ ). [88] The PBE0 functional mixes  $E_{\text{x}}^{\text{HF}}$  with the exchange functional of the Perdew-Burke-Ernzerhof GGA ( $E_{\text{x}}^{\text{PBE}}$ ) in a 1:3 ratio along with the full Perdew-Burke-Ernzerhof GGA correlation ( $E_{\text{c}}^{\text{PBE}}$ ).

Hybrid functionals improve several molecular properties over ‘pure’ xc-functionals, such as atomisation energies and excitation energies. [99]

#### 2.12.3.4 Double Hybrids

The final ‘rung’ on Jacob’s Ladder shown in Figure 2.10 includes virtual Kohn-Sham orbitals to better approximate  $E_{\text{xc}}$  and are known as ‘double hybrids’. As with hybrid xc-functionals, double hybrid xc-functionals include a proportion of  $E_{\text{x}}^{\text{HF}}$  and perturbative second-order correlation part (PT2) that is obtained from the Kohn-Sham (GGA) orbitals and eigenvalues.  $E_{\text{xc}}$  for a general double hybrid xc-functional can be expressed as:

$$E_{\text{xc}} = (1 - \alpha_x) E_{\text{x}}^{\text{DFT}} + \alpha_x E_{\text{x}}^{\text{HF}} + (1 - \alpha_c) E_{\text{c}}^{\text{DFT}} + \alpha_c E_{\text{c}}^{\text{PT2}} \quad (2.73)$$

These xc-functionals are the most computationally expensive xc-functionals. An example of such xc-functional is Grimme’s B2-PLYP [100] xc-functional.

### 2.12.3.5 Range-Separated Hybrids

In contrast to hybrid xc-functionals, which has a constant amount of  $E_x^{\text{HF}}$  included, ‘*range-separated hybrid*’ xc-functionals use the interelectron distance ( $r_{12}$ ) to define the HF contribution to exchange. In range-separated hybrid xc-functionals, the amount of  $E_x^{\text{HF}}$  can be partitioned into short and long-range components. This is achieved by splitting the Coulomb operator using the standard error function, erf as in Equation 2.74, with short-range interactions on the left and long-range the right, with the range of the separation indicated by  $\omega$ .

$$\frac{1}{r} = \frac{1 - \text{erf}(\omega r)}{r} + \frac{\text{erf}(\omega r)}{r} \quad (2.74)$$

For a particular  $\omega$  value, both the HF and DFT exchange energies can be separated into short-(SR), long-(LR) and full-range (FR) components and mixing these components gives rise to a generalised expression for a range-separated hybrid xc-functional:

$$E_{\text{xc}} = \alpha E_x^{\text{SR-HF}}(\omega) + (1 - \alpha) E_x^{\text{SR-DFT}} + \beta E_x^{\text{LR-HF}}(\omega) + (1 - \beta) E_x^{\text{LR-DFT}} + \gamma E_x^{\text{FR-HF}}(\omega) + (1 - \gamma) E_x^{\text{FR-DFT}} + E_c^{\text{DFT}} \quad (2.75)$$

The value of coefficients:  $\alpha$ ,  $\beta$  and  $\gamma$  can change the application of the range-separated hybrid xc-functional. The Heyd, Scuseria and Ernzerhof functional (HSE), [101] removes  $E_x^{\text{LR-HF}}$  by setting  $\beta = 0$ , this reduces computational expense and has been shown to be effective in solid-state studies. [102]

In contrast to the HSE functional, the LC- $\omega$ PBE [103] and  $\omega$ B97XF [104] functionals set  $\beta = 0$ . Functionals of this property result in the long-range HF exchange serving an an asymptotic correction to the exchange potential.

In the two scenario’s above  $\alpha + \beta = 1$ , removing this constraint could result in better thermochemical accuracy as thermochemical performance of a functional can be influenced by the long-range correction. [105] CAM-B3LYP [106] is an example of xc-functional which removes the asymptotic behaviour of having  $\alpha + \beta = 1$ .

### 2.12.4 Excited States

Thus far only methods which provide a good description of the ground state ( $\Psi_0$ ) have been discussed. Excited states of molecular systems are of particular importance for applications such as luminescent metal complexes, bioimaging, and dye-sensitised solar cells. [107] In this section, methods which allow excited state structure and characterisation to be generated are discussed.

A direct but complex approach to generating excited state structures is to solve the time-dependent Schrödinger equation for the many-electron wavefunction ( $\Psi(t)$ ):

$$\hat{H}(t)\Psi(t) = i\frac{\partial\Psi(t)}{\partial t}, \quad \hat{H}(t) = \hat{T} + \hat{V}_{ee} + \hat{V}_{\text{ext}}(t) \quad (2.76)$$

The time-dependent Hamiltonian consists of the kinetic energy ( $\hat{T}$ ), electron-electron repulsion energy ( $\hat{V}_{ee}$ ) and an ‘*external potential*’ ( $\hat{V}_{\text{ext}}$ ), which is the potential the electrons experience due to the nuclear attraction and from any external applied field *i.e.* a shining laser, these have the general form:

$$\hat{T} = -\frac{1}{2} \sum_{i=1}^N \nabla_i^2 \quad \hat{V}_{ee} = \frac{1}{2} \sum_{i \neq j}^N \frac{1}{|\mathbf{r}_i - \mathbf{r}_j|} \quad \hat{V}_{\text{ext}}(t) = \sum_{i=1}^N \nu_{\text{ext}}(\mathbf{r}_i, t) \quad (2.77)$$

It is worth noting that  $\hat{V}_{\text{ext}}$  can be expressed in any form, depending on the external applied force.

As has been discussed throughout this chapter, solving the many-body Schrödinger equation is no simple task. Therefore, DFT can be utilised again, for excited state calculations, of which the most commonly used method is the linear response formulation of time-dependent density functional theory (TD-DFT). [108]

#### 2.12.4.1 TD-DFT

Time-dependent density functional theory (TD-DFT) is comprised from two foundations: the Runge–Gross theorem [109, 110] and the time-dependent Kohn–Sham equation. [110] The Runge–Gross Theorem is an extension of the first Hohenberg–Kohn theorem (Section 2.12.1) to time-dependent system and states that given a fixed initial state ( $\Psi_0$ ), the density of a system ( $\rho(\mathbf{r}, t)$ ) is directly related to the external potential ( $\nu_{\text{ext}}(\mathbf{r}, t)$ ). Equation 2.78 defines the time-dependent density ( $\rho(\mathbf{r}, t)$ ) as a probability function:

$$\rho(\mathbf{r}, t) = N \int |\Psi(\mathbf{x}_1, \mathbf{x}_2 \cdots \mathbf{x}_n)|^2 d\sigma, d\mathbf{x}_2 \cdots d\mathbf{x}_n \quad (2.78)$$

From the Runge–Gross theorem, if  $\rho(\mathbf{r}, t)$  is known for a particular state, then the  $\nu_{\text{ext}}(\mathbf{r}, t)$  for this state can be identified, *i.e.* we can derive the external potential which resulted in the density. The Hamiltonian for the time-dependent Schrödinger equation is defined in Equation 2.76 and this is solely dependent on  $\nu_{\text{ext}}(\mathbf{r}, t)$  as the other two components are determined by electrons, where  $N$  is the number of electrons (Equation 2.78). This means that the time-dependent Schrödinger equation can then be solved for this initial state.

The theorem states, [109] that two different densities,  $\rho(\mathbf{r}, t)$  and  $\rho'(\mathbf{r}, t)$ , generated by the potentials  $\nu_{\text{ext}}(\mathbf{r}, t)$  and  $\nu'_{\text{ext}}(\mathbf{r}, t)$  from the same initial state  $\Psi_0$  always differ given that the potentials differ by more than a purely time-dependent function:

$$\nu_{\text{ext}}(\mathbf{r}, t) \neq \nu'_{\text{ext}}(\mathbf{r}, t) + c(t) \quad (2.79)$$

The proof of this theorem comes in two parts, firstly, showing one-to-one mapping between the external potential and the current density and secondly, one-to-one mapping between the current and electron densities. The proofs are explained extensively in references [109–111]

As was seen in the ground state, a Kohn-Sham system can be utilised in the time-dependent form. A time-dependent potential obtained using the above theorem can be compared with a Kohn-Sham fictitious system of non-interacting fermions with the same time-dependent density; the one-to-one mapping of the potentials and the densities described above means that the potential for the Kohn-Sham system ( $\nu_{\text{KS}}[\rho](\mathbf{r}, t)$ ) results in the same density as the interacting system. [110]

The Kohn-Sham equations can be written in a time-dependent form, with the time-dependent density expressed as:

$$\rho(\mathbf{r}, t) = \sum_{j=1}^N |\phi_j(\mathbf{r}, t)|^2 \quad (2.80)$$

The orbitals  $\phi_j(\mathbf{r}, t)$  satisfy the time-dependent Kohn-Sham equation:

$$i \frac{\partial \phi_j(\mathbf{r}, t)}{\partial t} = \left[ -\frac{\nabla^2}{2} + \nu_{\text{KS}}[\rho](\mathbf{r}, t) \right] \phi_j(\mathbf{r}, t) \quad (2.81)$$

$\nu_{\text{KS}}[\rho](\mathbf{r}, t)$  can be expressed in terms of the time-dependent Hartree potential ( $\nu_{\text{H}}(\mathbf{r}, t)$ ) and an exchange–correlation kernel ( $f_{\text{xc}}(\mathbf{r}, t)$ ), which is a second derivative of  $E_{\text{xc}}$  with respect to  $\rho$ .

$$\nu_{\text{KS}} = \nu_{\text{ext}}(\mathbf{r}, t) + \nu_{\text{H}}(\mathbf{r}, t) + f_{\text{xc}}(\mathbf{r}, t) \quad (2.82)$$

Where:

$$\nu_{\text{H}}[\rho](\mathbf{r}, t) = \int \frac{\rho(\mathbf{r}', t')}{|\mathbf{r} - \mathbf{r}'|} d\mathbf{r}' \quad (2.83)$$

As  $f_{\text{xc}}(\mathbf{r}, t)$  is analogous to  $V_{\text{xc}}(\mathbf{r})$  (Equation 2.63), the standard ground-state xc-functionals described in Section 2.12.3 can be utilised in TDDFT.

Unfortunately, the cost of calculating the full time-dependent Kohn-Sham equations can be very expensive for anything other than small systems. Instead, Linear response can be used which is reached via perturbation theory. [112] For a full derivation of linear response DFT, the reader is directed to [111]. The final result is the frequency-dependent Kohn-Sham response function, expressed as a sum over all states:

$$\chi_s(\mathbf{r}, \mathbf{r}', \omega) = \sum_{j,k} (f_k - f_j) \frac{\phi_j(\mathbf{r}) \phi_k^*(\mathbf{r}) \phi_j^*(\mathbf{r}') \phi_k(\mathbf{r}')}{\omega - (\epsilon_j - \epsilon_k) + i\eta} \quad (2.84)$$

$f_k$  is the occupation number of the ground state Kohn-Sham orbital  $\phi_k(\mathbf{r})$  with orbital energy  $\epsilon_k$ . [112]

This equation can be transformed into a matrix representation, as was showed by Casida. [111, 113] The excitation energies ( $\omega$ ) are obtained as solutions of the generalised eigenvalue problem: [105, 113]

$$\begin{vmatrix} A & B \\ B^* & A^* \end{vmatrix} \begin{pmatrix} X \\ Y \end{pmatrix} = \omega \begin{vmatrix} 1 & 0 \\ 0 & -1 \end{vmatrix} \begin{pmatrix} X \\ Y \end{pmatrix} \quad (2.85)$$

The X,Y vector represents the orbital transformation, ( $\mathbf{A}$ ) and  $\mathbf{B}$  are Hessian matrices; matrix  $\mathbf{B}$  couples the positive and negative eigenvalue solutions, which represent the excitation and de-excitation energies.

TD-DFT is a formally exact method however, errors are introduced by using approximate xc-functionals and hence this leads to problems in the description of: Rydberg excited states, large  $\pi$ -systems or charge transfer excited states. [114, 115] The self-interaction error which is present in the orbital energies can be held responsible for the error in the charge transfer excited states, [116] this error leads to an underestimation of the gap between the HOMO and the LUMO. Charge transfer excitations also show incorrect asymptotic behaviour in conventional TD-DFT calculations; this problem stems from the fact that the orbital energy of particle orbitals contains the coulomb repulsion between the accepting and donating orbitals, this interaction is not present in the charge transfer states and can only be correctly ‘cancelled’ if exact exchange is present. [116]

TD-DFT provides accurate results to valence excitations, within a few tenths of an eV. When calculating Rydberg excitations however these are significantly underestimated, the reasons for this when using conventional functionals were discussed previously. When calculating excitations with charge transfer, double excitations, Rydberg, ionic or multiplet characteristics in the excited states TD-DFT has a tendency to give larger errors and hence is problematic when considering electronic spectroscopy. [117]

TD-DFT has some problems, which can be problematic when modelling photochemical reactions. The main examples of these are; the underestimation of ionization thresholds and the underestimation of charge transfer excitations. [118] A further major problem with TD-DFT is that of imaginary excitations which occur in situations where the singlet ground state is higher in energy than *e.g.* a triplet state, this is referred to as the triplet instability. [119–121]

#### 2.12.4.2 Tamm–Dancoff Approximation

If the coupling between the positive and negative eigenvalue solutions is small, then matrix  $\mathbf{B}$  in Equation 2.85 can be set to zero. Setting matrix  $\mathbf{B}$  to zero simplifies the matrix equation shown in Equation 2.85 to Equation 2.86; which was first implemented by Hirata and Head-Gordon in 1999 [122] to give Tamm-Dancoff approximation (TDA) to TD-DFT excited states. They found that the excitation

energies were generally close to those of TD-DFT and in some cases specifically when there was a triplet instability problem with TD-DFT TDA performed better. Hence they concluded that TDA was a useful alternative to TD-DFT.

$$AX = \omega X \quad (2.86)$$

Equation 2.86 ensures all excitation energies are real and hence this overcomes the negative excitation problem sometimes seen in TD-DFT calculations.

Peach *et al.* [123] found that the application of TDA improves the triplet instability problem and recovers the correct state ordering in molecules where it is known to be a problem. They also found that it effects the corresponding singlet states, especially with naphthalene, which is challenging with TD-DFT, again restoring the correct state ordering.

## 2.13 Relativistic Effects

### 2.13.1 Effects in Atoms

Relativistic effect occur in atoms where the velocity of the innermost electrons reaches a significant proportion of the speed of light ( $c$ ). In atomic units, the radial velocity scales linearly with the nuclear charge [3] and as such when modelling atoms with  $Z > 40$  relativistic effects need to be taken into account.

The yellow colouring in gold arises from the relativistic motion of the innermost electrons. [124, 125] Gold is a classic example of the shortcomings of non-relativistic calculations and the need to use relativistic effects when modelling heavy elements. [126] Non-relativistic calculations predict the excitation energies of transitions between 5d→6s orbitals to be in the UV region, which would not account for the yellow colour. In contrast, accounting for the relativistic effects decreases the excitation energy to the middle of the visible region.

Relativistic effects can be split into two different components. The first component is known as scalar effects, which are caused by the high velocities of the innermost electrons as discussed above. A consequence of these higher velocities result in the mass of the fast-moving electrons to increase.

$$m_e = \frac{m_o}{\sqrt{1 - \frac{v^2}{c^2}}} \quad (2.87)$$

$m_o$  represents the rest mass of the electron,  $v$  is its radial velocity and  $c$  is the speed of light. The increase in  $v$  results in a contraction of the inner orbitals causing an increased stabilisation of the s and p orbitals. As a consequence of this contraction the d and f orbitals become extended and destabilised due to the increased screening effect between the nucleus and these orbitals.

The second component is known as spin-orbit coupling (SOC) effects; which is

the relativistic interaction of a particle's spin with its orbital motion inside a potential. A classic example within the chemical world occurs when the electromagnetic interaction between an electron's magnetic dipole, its motion within an orbital and the electrostatic field of the nucleus results in shifts of an electron's atomic energy levels. [127] SOC splits the orbital energy levels into pairs according to the following rule:

$$j = l + s \quad (2.88)$$

$j$  is the total angular momentum,  $l$  is the orbital angular momentum quantum number and  $s$  is the spin quantum number. Consider a 3p orbital ( $l = 1$ ),  $j$  can take values of  $\frac{3}{2}$  ( $s = +\frac{1}{2}$ ) or  $\frac{1}{2}$  ( $s = -\frac{1}{2}$ ). When spin-orbit coupling is weak, Russell-Saunders or L-S coupling [128] can be applied. In L-S coupling,  $j$  is calculated as the sum of the resultant orbital angular momentum ( $L = l_1 + l_2 + \dots$ ) *i.e.* the sum of the orbital angular momenta of the individual electrons ( $l$ ) and the sum of the total spin angular momentum ( $S = s_1 + s_2 + \dots$ ). In contrast, when spin-orbit coupling is strong,  $j$  is calculated on an individual electron basis and the total angular momentum is the sum of the individual  $j$  values ( $J = j_1 + j_2 + \dots$ ).

### 2.13.2 Relativistic Hamiltonian

The previous section highlighted when relativistic effects need to be considered. In quantum chemical calculations, the Hamiltonian can be modified to include either/both scalar relativistic and spin-orbit coupling terms. Dirac proposed a time-independent Schrödinger equation (Equation 2.89), for a free electron. [129]

$$[c\boldsymbol{\alpha} \cdot \hat{\mathbf{P}} + c^2\boldsymbol{\beta} + V]\Psi = E\Psi \quad (2.89)$$

The expression within the [ ] represents the Dirac Hamiltonian ( $\hat{H}_D$ ),  $\hat{\mathbf{P}}$  is the momentum operator,  $V$  is a potential and  $c$  is the speed of light.  $\boldsymbol{\alpha}$  and  $\boldsymbol{\beta}$  are 4×4 matrices, in which  $\boldsymbol{\alpha}$  is expressed in terms of three Pauli 2×2 matrices ( $\boldsymbol{\sigma}_{x,y,z}$ ) and  $\boldsymbol{\beta}$  in terms of a 2×2 matrix  $\mathbf{I}$ , which are shown in Equation 2.90

$$\boldsymbol{\alpha}_{x,y,z} = \begin{vmatrix} 0 & \boldsymbol{\sigma}_{x,y,z} \\ \boldsymbol{\sigma}_{x,y,z} & 0 \end{vmatrix} \quad \boldsymbol{\beta} = \begin{vmatrix} \mathbf{I} & 0 \\ 0 & \mathbf{I} \end{vmatrix} \quad (2.90)$$

$$\boldsymbol{\sigma}_x = \begin{vmatrix} 0 & 1 \\ 1 & 0 \end{vmatrix} \quad \boldsymbol{\sigma}_y = \begin{vmatrix} 0 & -i \\ i & 0 \end{vmatrix} \quad \boldsymbol{\sigma}_z = \begin{vmatrix} 1 & 0 \\ 0 & -1 \end{vmatrix} \quad \mathbf{I} = \begin{vmatrix} 1 & 0 \\ 0 & 1 \end{vmatrix}$$

The wavefunction described in Equation 2.89 is known as a spinor function and has four components; it describes an electron-positron pair and the spin pairs of each. This four-component wavefunction results in the Dirac equation being significantly more computationally expensive than the non-relativistic Schrödinger equation. It

is also not useful for molecular calculations and as it only describes one electron-positron pair.

In order to simulate a multi-electron system, a generalisation of the Dirac equation to a many-particle system can be made, such as the Dirac-Coulomb-Breit (DCB) Hamiltonian. [130, 131] DCB accounts for both scalar and spin-orbit relativistic effects.

$$\hat{H}_{DCB} = \sum_i \hat{h}_i + \sum_{i < j} \hat{h}_{ij} \quad (2.91)$$

The Dirac Hamiltonian is represented by  $\hat{h}_i$  and  $\hat{h}_{ij}$  is the two-particle term:

$$\hat{h}_{ij} = \frac{1}{r_{ij}} + \frac{1}{2r_{ij}} \left[ \boldsymbol{\alpha}_i \cdot \boldsymbol{\alpha}_j + \frac{(\boldsymbol{\alpha}_i \cdot \mathbf{r}_{ij})(\boldsymbol{\alpha}_j \cdot \mathbf{r}_{ij})}{r_{ij}^2} \right] \quad (2.92)$$

While applying the DCB Hamiltonian to a four-component wavefunction is still more computationally expensive than the non-relativistic Schrödinger equation, it is still the most accurate way of including relativistic effects in quantum chemical calculations.

Another method of including relativistic effects in a system is the zeroth-order regular approximation (ZORA). [132–136] This method decouples the two relativistic components which allows the spin-orbit coupling effects to be neglected, this is achieved with a perturbation expansion of the Dirac equation. [137]

$$\hat{H}_{scalar}^{ZORA} + \hat{H}_{spin-orbit}^{ZORA} = V + \boldsymbol{\sigma} \cdot \hat{P} \frac{c^2}{2c^2 - V} \boldsymbol{\sigma} \cdot \hat{P} \quad (2.93)$$

$\hat{P}$  is the momentum operator,  $V$  is a potential and  $\boldsymbol{\sigma}$  is the Pauli spin matrices defined in Equation 2.90.

The final computation method for inclusion of relativistic effects is the elimination of the positronic states present in the Dirac Hamiltonian. As mentioned previously, the Dirac Hamiltonian has four components; two large components from the electrons and two small components from the positrons. These small components are more computationally expensive compared to the large components and also contribute the least to the electron-electron interactions. These interactions can be eliminated via unitary transformation of the Dirac Hamiltonian which results in the Douglas-Kroll-Hess (DKH) Hamiltonian, [138–140] which decouples the description of the electrons and positronic negative states from each other. This decoupling results in an infinite series of operators (Equation 2.94), with  $\hat{\epsilon}_k$  representing the expansion terms.

$$\hat{H}_{DKH\infty} = \sum_{k=0}^{\infty} \hat{\epsilon}_k \quad (2.94)$$

This method can utilise many different orders, with each progressive order ob-

taining more accuracy but increasing in computational expense. Typically calculations are run at the second order,  $k = 2$  (DKH2) which provides a balance between accuracy and computational expense. [139, 141, 142]

### 2.13.3 Relativistic Pseudopotentials

Effective core potentials (ECP) or Pseudopotentials were discussed in Section 2.8.4.3. These are used to decrease computational expense in heavy elements by replacing the core electrons with a potential field whilst still allowing valence electrons to be treated explicitly. As noted previously, it is the core electrons which are more likely to experience relativistic effects and hence using a pseudopotential to model such effects on the core electrons presents a useful way to reduce computational expense while treating relativistic effects implicitly with a non-relativistic Hamiltonian. [32, 143–145]

A relativistic pseudopotential is generated by using a relativistic Hamiltonian on an all-electron wavefunction. F-block pseudopotentials have two main designs: one where the f-electrons are treated explicitly or one where they are treated as part of the core. The latter simplifies the calculation and reduces computational expensive but it also reduces the accuracy. [30, 32, 145–149] It is thought that relativistic pseudopotentials are more accurate than most common scalar relativistic methods described above and hence makes them a useful tool when modelling actinide systems. [150]

## 2.14 The Quantum Theory of Atoms in Molecules

Previous sections have discussed methods in which to solve the Schrödinger equation. Thus far only the energy given by the wavefunction has been considered, however there are other properties which can be of interest, these can also be derived from the wavefunction. For a given wavefunction of a system, is there a way of determining how to define an atom, the electron population associated with said atom, or if two atoms are bonded? This can be achieved by dividing the total molecular volume into sections, each with a single nucleus. Such sections are termed atomic basins ( $\Omega$ ) and the number of electrons present in these basins can be calculated by integrating the electron density. There are several different ways of partitioning the molecular volume but in this thesis Bader’s Quantum Theory of Atoms in Molecules (QTAIM) has been utilised. [151]

In the QTAIM method, the atomic basins are determined based on a topological analysis of the electron density. Each basin is defined by a surface which satisfies the zero-flux condition:

$$\nabla\rho(\mathbf{r}) \cdot \mathbf{n}(\mathbf{r}) = 0 \quad (2.95)$$

$\rho(\mathbf{r})$  is the electron density and  $\mathbf{n}(\mathbf{r})$  is a unit vector normal to the surface at the point  $\mathbf{r}$ . [152]

Critical points (CPs) can be found by taking the first derivative of the electron density and where this is zero, a critical point is defined.

$$\nabla\rho = \mathbf{i}\frac{d\rho}{dx} + \mathbf{j}\frac{d\rho}{dy} + \mathbf{k}\frac{d\rho}{dz} = \mathbf{0} \quad (2.96)$$

The zero vector ( $\mathbf{0}$ ) indicates that each individual derivative in the gradient operator ( $\nabla$ ) is zero. There are four types of critical point: nuclear, bond, ring and cage; each of these can be defined by determining the nature of the stationary point, *i.e.* taking the second derivative.

Determining the nature of the stationary points results in nine second derivatives of  $\rho(\mathbf{r})$ . When evaluating these at the CP at  $\mathbf{r}_c$  they can be arranged in a Hessian matrix  $\mathbf{A}(\mathbf{r}_c)$ : [151, 153]

$$\mathbf{A}(\mathbf{r}_c) = \begin{pmatrix} \frac{\partial^2\rho}{\partial x^2} & \frac{\partial^2\rho}{\partial x\partial y} & \frac{\partial^2\rho}{\partial x\partial z} \\ \frac{\partial^2\rho}{\partial y\partial x} & \frac{\partial^2\rho}{\partial y^2} & \frac{\partial^2\rho}{\partial y\partial z} \\ \frac{\partial^2\rho}{\partial z\partial x} & \frac{\partial^2\rho}{\partial z\partial y} & \frac{\partial^2\rho}{\partial z^2} \end{pmatrix}_{\mathbf{r}=\mathbf{r}_c} \quad (2.97)$$

The Hessian matrix is real and symmetric and thus can be diagonalised. This is done by rotating the coordinate system  $\mathbf{r}(x, y, z) \rightarrow \mathbf{r}(x', y', z')$  where the latter are the principle curvature axes of the CP. The diagonalised Hessian ( $\Lambda$ ) has the form: [151, 153]

$$\Lambda = \begin{pmatrix} \frac{\partial^2\rho}{\partial x'^2} & 0 & 0 \\ 0 & \frac{\partial^2\rho}{\partial y'^2} & 0 \\ 0 & 0 & \frac{\partial^2\rho}{\partial z'^2} \end{pmatrix}_{\mathbf{r}'=\mathbf{r}_c} = \begin{pmatrix} \lambda_1 & 0 & 0 \\ 0 & \lambda_2 & 0 \\ 0 & 0 & \lambda_3 \end{pmatrix} \quad (2.98)$$

$\lambda_1, \lambda_2$  and  $\lambda_3$  are the curvatures of the density with respect to the three principle axes and can be positive or negative. The sum of the signs of these three values, gives the signature ( $\sigma$ ) of the critical point (given in Table 2.2) and hence distinguishes between them. For example, if  $\lambda_1 = +$ ,  $\lambda_2 = -$  and  $\lambda_3 = -$  then  $\sigma = (+) + (-) + (-) = -1$  which corresponds to a bond critical point (BCP).

CPs are expressed in the form  $(\omega, \sigma)$ , the  $\omega$  is known as the rank and is defined as the number of non-zero curvatures of  $\rho$  at the critical point. The rank of a CP is nearly always 3, as CP's with  $\omega < 3$  are mathematically unstable and are generally not found in equilibrium charge distributions. [153] The characterisation of these critical points, in terms of rank and signature are show in Table 2.2.

As each basin contains a single nucleus, there is only one NCP, at the position

Table 2.2: Bond angles in minima complexes

Critical Point Nature	$(\omega, \sigma)$	Character
Nuclear (NCP)	(3, -3)	Local Maximum
Bond (BCP)	(3, -1)	1 <sup>st</sup> order saddle point
Ring (RCP)	(3, +1)	2 <sup>nd</sup> order saddle point
Cage (CCP)	(3, +3)	Local Minimum

of the nucleus, per basin. The BCP's are utilised in quantifying bond character, which occur when there are two negative curvatures and  $\rho$  is a maximum in the plane (which defines the interatomic surface) but a minimum along the final axis, which is perpendicular to the plane. Bond paths are defined as the lines of minimum density which join the BCPs to the NCPs. A molecular graph can be constructed from these bond paths, BCPs and NCPs. [154, 155] RCPs are found in the interior of a chemically bonded ring molecule, such as benzene, while a CCP occur in the enclosed space of several connected rings *e.g.* in the centre of a cubane molecule. Figure 2.11 shows the different types of CPs found in the cubane molecule. [153]

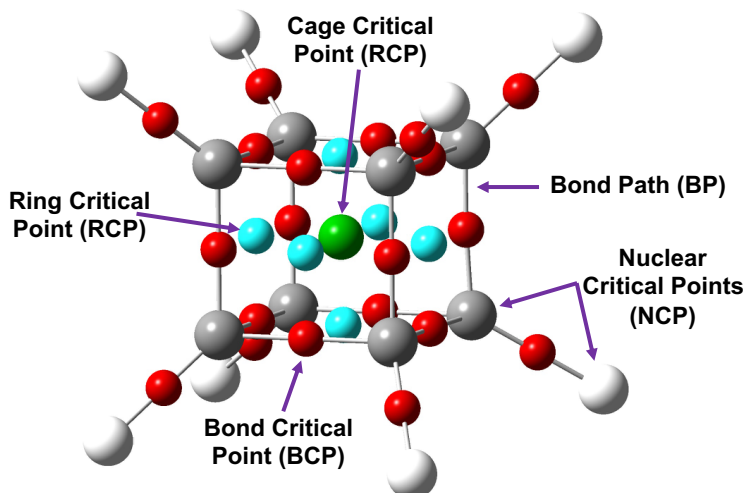


Figure 2.11: Cubane molecule with all the CPs labelled. The bond critical points are shown in red, nuclear critical points are grey (carbon) and white (hydrogen), the bond paths are the lines which link the NCPs and BCP. The ring critical points are located in the centre of each square face (blue) and the cage critical point is the green dot in the centre of the cube.

The total number (and type) of CPs in a molecule is given by the Poincaré-Hopf relationship:[151]

$$n_{NCP} - n_{BCP} + n_{RCP} - n_{CCP} = 1 \quad (2.99)$$

$n$  is the number of the specific CPs present. This equation provides a good check

to ensure all CPs have been accounted for.

### 2.14.1 Topological Properties of the Electron Density

In order to characterise the bonding within a molecule, three topological properties, at the BCPs, are generally used. The magnitude of the electron density at the BCP ( $\rho_{BCP}$ ) has been used to categorise the covalent character of a chemical bond *i.e.* its bond order ( $BO$ ). [153]

$$BO = \exp[A(\rho_{BCP} - B)] \quad (2.100)$$

$A$  and  $B$  are constants which depend on the nature of the bond. Typically covalent bonding interactions have a  $\rho_{BCP} > 0.2$  a.u. while a closed-shell interaction (hydrogen-bonding, Van der Waals and ionic) have  $\rho_{BCP} < 0.1$  a.u.

The Laplacian/second derivative of the BCP ( $\nabla^2\rho_{BCP}$ ) indicates regions where the electron density is depleted or increased. [3]  $\nabla^2\rho_{BCP}$  is the sum of the three curvatures of the density at the critical point (Equations 2.97 and 2.98), two of the curvatures ( $\lambda_1$  and  $\lambda_2$ ) are perpendicular to the bond and the third ( $\lambda_3$ ) lies along the bond path. The two curvatures perpendicular to the bond are negative and indicate the extent the density is concentrated along the bond path.  $\lambda_3$  measures the extent of the depletion of electron density in the region of the interatomic surface and has a positive value. The  $\nabla^2\rho_{BCP}$  is negative in covalent bonds due to the negative curvatures being more dominant than the positive curvature. The reverse is true for closed-shell interactions. However, not all systems fit into these two ideals, in strongly polar bonds (C-F/O/N) the Laplacian can be either positive or negative.

The final property is the energy density at the BCP ( $H_{BCP}$ ) which gives the total electronic energy when integrated over all space.  $H_{BCP}$  is negative for covalent interactions with the magnitude reflecting the degree of electron sharing. [156] Typically, for ionic interactions the  $H_{BCP}$  is positive.

### 2.14.2 Integrated Properties of the Electron Density

Molecular properties such as; atomic electron population, atomic charge, localisation and delocalisation can be calculated by integrating the electron density over all atomic basins. Each specific property is dependent on an operator ( $\hat{O}$ ) and as such the expectation value of an operator averaged over the molecular volume ( $\langle\hat{O}\rangle_{mol}$ ) can be expressed as the sum of the expectation values of this operator ( $\hat{O}$ ) averaged over all atomic basins. [151, 153, 157]

$$\langle\hat{O}\rangle_{mol} = \sum_i^N \left( N \int_{\Omega_i} \left\{ \int \frac{1}{2} [\Psi^* \hat{O} \Psi + (\hat{O} \Psi)^* \Psi] d\tau' \right\} d\mathbf{r} \right) \quad (2.101)$$

$$\langle \hat{O} \rangle_{mol} = \sum_i^N \int_{\Omega_i} \rho_O d\mathbf{r} = \sum_i^N O(\Omega_i) \quad (2.102)$$

$N$  is the number of atomic basins in the system,  $O(\Omega_i)$  is the average operator ( $\hat{O}$ ) over a basin ( $\Omega_i$ ).

The atomic population,  $N(\Omega)$  has the simplest form out of the integrated properties. This is calculated by integrating the electron density over a single basin and the operator is set to  $\hat{1}$ . [151, 153, 157]

$$N(A) = \int_{\Omega_A} \rho(\mathbf{r}) d\mathbf{r} \quad (2.103)$$

$N(A)$  is the atomic population in basin A. From the atomic population, the atomic charge can be obtained by subtracting  $N(A)$  from the nuclear charge ( $Z_A$ ).

$$q(A) = Z_A - N(A) \quad (2.104)$$

The delocalisation index,  $\delta$ , is a measure of the amount of electron sharing between two basins and is calculated by the magnitude of the exchange of electrons between the two basins. [151, 153] The delocalisation index between basins A and B is defined as:

$$\delta(A, B) = 2|F^\alpha(A, B)| + 2|F^\beta(A, B)| \quad (2.105)$$

$F^\sigma$  is the Fermi correlation (where  $\sigma$  depicts the spin). Assuming the orbital approximation:

$$F^\sigma(A, B) = - \sum_i \sum_j \int_A d\mathbf{r}_1 \int_B d\mathbf{r}_2 \{ \phi_i^*(\mathbf{r}_1) \phi_j(\mathbf{r}_1) \phi_j^*(\mathbf{r}_2) \phi_i(\mathbf{r}_2) \} \quad (2.106)$$

Which can be simplified to

$$F^\sigma(A, B) = - \sum_i \sum_j S_{ij}(A) S_{ji}(B) \quad (2.107)$$

$S_{ij}(A)$  is the overlap integral of spin orbitals  $\phi_i$  and  $\phi_j$  over atomic basin A, the delocalisation index can therefore be expressed in terms of overlap integrals. [158]

$$\delta(A, B) = \sum_{ij} S_{ij}(A) S_{ij}(B) \quad (2.108)$$

The localisation index,  $\lambda$ , can be defined as the number of electrons localised within an atomic basin; this can be calculated using Equation 2.105 but for a single atomic basin. Hence, the localisation of basin A can be expressed in terms of overlap. [158]

$$\lambda(A) = \sum_{ij} S_{ij}^2(A) \quad (2.109)$$

The atomic electron population can also be defined in terms of the localisation and delocalisation indices.

$$N(A) = \lambda(A) + \frac{1}{2} \sum_{B \neq A} \delta(A, B) \quad (2.110)$$

# References

- [1] G. R. Fowles, *Am. J. Phys.* **1962**, *30*, 308–309.
- [2] M. Born, R. Oppenheimer, *Ann. Phys.* **1927**, *84*, 457–484.
- [3] F. Jensen, *Introduction to Computational Chemistry*, Second Edi, John Wiley & Sons Ltd, **2011**, p. 620.
- [4] D. R. Hartree, *Proc. Camb. Phil. Soc.* **1928**, *24*, 426–437.
- [5] J. C. Slater, *Phys. Rev.* **1930**, *36*, 57–64.
- [6] C. J. Cramer, Second Edi, John Wiley & Sons, Ltd, **2004**.
- [7] I. Ema, J. M. García de la Vega, G. Ramírez, R. Lopez, J. Fernández Rico, H. Meissner, J. Paldus, *J. Comput. Chem* **2003**, *24*, 859–868.
- [8] G. te Velde, F. M. Bickelhaupt, E. J. Baerends, C. Fonseca Guerra, S. J. A. van Gisbergen, J. G. Snijders, T. Ziegler, *J. Comput. Chem.* **2001**, *22*, 931–967.
- [9] S. F. Boys, *Proc. R. Soc. London Ser. A: Mathematical and Physical Sciences* **1950**, *200*, 542–554.
- [10] B. P. Pritchard, D. Altarawy, B. Didier, T. D. Gibson, T. L. Windus, *J. Chem. Inf. Model.* **2019**, *59*, 4814–4820.
- [11] D. Feller, *J. Comput. Chem.* **1996**, *17*, 1571–1586.
- [12] K. L. Schuchardt, B. T. Didier, T. Elsethagen, L. Sun, V. Gurumoorthi, J. Chase, J. Li, T. L. Windus, *J. Chem. Inf. Model.* **2007**, *47*, 1045–1052.
- [13] B. O. Roos, R. Lindh, P. Å. Malmqvist, V. Veryazov, P. O. Widmark, *Chem. Phys. Lett.* **2005**, *409*, 295–299.
- [14] T. Clark, J. Chandrasekhar, G. W. Spitznagel, P. V. R. Schleyer, *J. Comput. Chem.* **1983**, *4*, 294–301.
- [15] M. J. Frisch, J. A. Pople, J. S. Binkley, *J. Chem. Phys.* **1984**, *80*, 3265–3269.
- [16] R. A. Kendall, T. H. J. Dunning, R. J. Harrison, *J. Chem. Phys.* **1992**, *96*, 6796–6806.
- [17] E. Papajak, D. G. Truhlar, *J. Chem. Theory Comput.* **2010**, *6*, 597–601.
- [18] E. Papajak, H. R. Leverentz, J. Zheng, D. G. Truhlar, *J. Chem. Theory Comput.* **2009**, *5*, 1197–1202.

- [19] F. Jensen, *J. Chem. Phys.* **2005**, *122*, 074111.
- [20] J. Almlöf, P. R. Taylor, *J. Chem. Phys.* **1987**, *86*, 4070–4077.
- [21] J. Almlöf, P. R. Taylor, *J. Chem. Phys.* **1990**, *92*, 551–560.
- [22] J. Almlöf, P. R. Taylor, *Adv. Quant. Chem.* **1991**, *22*, 301.
- [23] T. H. Dunning, *J. Chem. Phys.* **1989**, *90*, 1007–1023.
- [24] A. K. Wilson, T. Van Mourik, T. H. J. Dunning, *J. Mol. Struct.: THEOCHEM* **1996**, *388*, 339–349.
- [25] D. E. Woon, T. H. J. Dunning, *J. Chem. Phys.* **1995**, *103*, 4572–4585.
- [26] M. C. Payne, M. P. Teter, D. C. Allan, T. A. Arias, J. D. Joannopoulos, *Rev. Mod. Phys.* **1992**, *64*, 1045–1097.
- [27] T. R. Cundari, M. T. Benson, M. L. Lutz, S. O. Sommerer, *Rev. Comp. Chem* **1996**, *8*, 145.
- [28] G. Frenking, I. Antes, M. Böhme, S. Dapprich, A. W. Ehlers, V. Jonas, A. Nauhaus, M. Otto, R. Stegmann, A. Veldkamp, S. F. Vyboishchikov, *Rev. Comp. Chem* **1996**, 63.
- [29] M. Garcí-Hernández, C. Lauterbach, A. Krüger, S. Matveev, N. Rösch, *J. Comput. Chem* **2002**, *23*, 834–846.
- [30] A. Weigand, X. Cao, V. Vallet, J. P. Flament, M. Dolg, *J. Phys. Chem. A.* **2009**, *113*, 11509–11516.
- [31] W. Küchle, M. Dolg, H. Stoll, H. Preuss, *J. Chem. Phys.* **1994**, *100*, 7535–7542.
- [32] X. Cao, A. Weigand, *In Lanthanide and Actinide Chemistry*, (Ed.: M. Dolg), Wiley, **2015**, pp. 147–179.
- [33] A. W. Ehlers, M. Böhme, S. Dapprich, A. Gobbi, A. Hijllwarth, V. Jonas, K. F. Kiihler, R. Stegmann, A. Veldkamp, G. Frenking, *Chem. Phys. Lett.* **1993**, *208*, 111–114.
- [34] A. Hgllwarth, M. Biihme, S. Dapprich, A. W. Ehlers, A. Gobbi, V. Jonas, K. F. Kijhler, R. Stegmann, A. Veldkamp, G. Frenking, *Chem. Phys. Lett.* **1993**, *208*, 237–240.
- [35] A. Moritz, X. Cao, M. Dolg, *Theor. Chem. Acc.* **2007**, *117*, 473–481.
- [36] M. Hülsen, A. Weigand, M. Dolg, *Theor. Chem. Acc.* **2009**, *122*, 23–29.
- [37] P. J. Hay, W. R. Wadt, *J. Chem. Phys.* **1985**, *82*, 299–310.
- [38] M. Dolg, *Theor. Comput. Chem.* **2002**, *11*, 793–862.
- [39] W. Küchle, M. Dolg, H. Stoll, H. Preuss, *J. Chem. Phys.* **1994**, *100*, 7535–7542.

- [40] X. Cao, M. Dolg, H. Stoll, *J. Chem. Phys.* **2003**, *118*, 487–496.
- [41] X. Cao, M. Dolg, *J. Mol. Struct-THEOCHEM* **2004**, *673*, 203–209.
- [42] K. G. Dyall, *Theor. Chem. Acc.* **1998**, *99*, 366–371.
- [43] K. G. Dyall, *Theor. Chem. Acc.* **2002**, *108*, 335–340.
- [44] J. C. Slater, *Phys. Rev.* **1930**, *35*, 509–529.
- [45] W. Pauli, *Zeitschrift für Physik* **1925**, *31*, 765–783.
- [46] A. Szabo, N. S. Ostlund, *Modern Quantum Chemistry Introduction to Advanced Electronic Structure Theory*, illustrate, Courier Corporation, **1982**.
- [47] P. O. Löwdin, H. Shull, *Phys. Rev.* **1956**, *101*, 1730–1739.
- [48] J. W. Hollett, P. M. Gill, *J. Chem. Phys.* **2011**, *134*.
- [49] A. J. Cohen, P. Mori-Sánchez, W. Yang, *Science* **2008**, *321*, 792–794.
- [50] D. G. Truhlar, *J. Comput. Chem.* **2007**, *28*, 73.
- [51] B. O. Roos, P. E. Siegbahn, *Int. J. Quantum Chem.* **1980**, *17*, 485–500.
- [52] B. O. Roos, P. R. Taylor, *Chem. Phys.* **1980**, *48*, 157–173.
- [53] P. Å. Malmqvist, A. Rendell, B. O. Roos, *J. Phys. Chem.* **1990**, *94*, 5477–5482.
- [54] A. J. Garza, A. G. Sousa Alencar, G. E. Scuseria, *J. Chem. Phys.* **2015**, *143*.
- [55] J. K. Laerdahl, K. J. Faegri, L. Visscher, T. Saue, *J. Chem. Phys.* **1998**, *109*, 10806–10817.
- [56] C. D. Sherrill, H. F. Schaefer, *Adv. Quant. Chem.* **1999**, *34*, 143.
- [57] L. Brillouin, *J. Phys. Radium* **1932**, *3*, 373–389.
- [58] J. C. Slater, *Phys. Rev.* **1929**, *34*, 1293–1322.
- [59] E. U. Condon, *Phys. Rev.* **1930**, *36*, 1121–1133.
- [60] K. D. Vogiatzis, D. Ma, J. Olsen, L. Gagliardi, W. A. de Jong, *The Journal of Chemical Physics* **2017**, *147*, 184111.
- [61] J. E. T. Smith, B. Mussard, A. A. Holmes, S. Sharma, *Journal of Chemical Theory and Computation* **2017**, *13*, 5468–5478.
- [62] V. Veryazov, P. A. Malmqvist, B. O. Roos, *Int. J. Quantum Chem.* **2000**, *111*, 3329–3338.
- [63] K. Pierloot, E. Van Besien, *J. Chem. Phys.* **2005**, *123*.
- [64] L. Gagliardi, *Rev. Comput. Chem.* **2007**, *25*, 249–284.
- [65] A. Kerridge, (Ed.: M. Dolg), Wiley, **2015**, pp. 121–146.
- [66] P. O. Widmark, P. Å. Malmqvist, B. O. Roos, *Theor. Chim. Acta* **1990**, *77*, 291–306.

- [67] K. Andersson, B. Roos, *Int. J. Hydrogen Energy* **1993**, *45*, 591.
- [68] P. Pulay, *Int. J. Quantum Chem.* **2011**, *111*, 3273–3279.
- [69] C. Angeli, R. Cimiraglia, S. Evangelisti, T. Leininger, J. Malrieu, *J. Chem. Phys.* **2001**, *114*, 10252–10264.
- [70] C. Angeli, R. Cimiraglia, J. Malrieu, *J. Chem. Phys.* **2002**, *117*, 9138–9153.
- [71] C. Angeli, R. Cimiraglia, *Chem. Phys. Lett.* **2001**, *350*, 297–305.
- [72] R. W. A. Havenith, P. R. Taylor, C. Angeli, R. Cimiraglia, K. Ruud, *J. Chem. Phys.* **2014**, *120*, 4619–4625.
- [73] C. M. Bender, S. A. Orszag, New York, NY: Springer, **1999**.
- [74] M. H. Holmes, New York, NY: Springer, **2013**.
- [75] P. A. M. Dirac, *Proc. R. Soc. London Ser. A: Mathematical Physical and Engineering Sciences* **1930**, *126*, 360–365.
- [76] L. H. Thomas, *Proc. Camb. Phil. Soc.* **1927**, *23*, 542.
- [77] E. Fermi, *Rend. Accad. Lincei.* **1927**, *6*, 602.
- [78] P. Hohenberg, W. Kohn, *Phys. Rev.* **1964**, *136*, 864–871.
- [79] W. Koch, M. C. Holthausen, *A Chemist's Guide to Density Functional Theory*, Wiley - VCH, Weinheim - New York, **2nd edition**, **2001**.
- [80] W. Kohn, L. Sham, *J. Phys. Rev.* **1965**, *140*, 1133–1138.
- [81] W. Kohn, L. J. Sham, *Phys. Rev.* **1965**, *137*, 1697–1705.
- [82] L. J. Sham, W. Kohn, *Phys. Rev.* **1966**, *145*, 561–567.
- [83] J. P. Perdew, K. Schmidt, *In AIP Conference Proceedings* **2001**, *577*.
- [84] R. V. Leeuwen, E. J. Baerends, *Int. J. Quantum Chem.* **1994**, *54*, 711–730.
- [85] M. N. Gugelchuk, Y. J. Cui, *Mol. Struct. THEOCHEM* **1996**, *365*, 111–117.
- [86] D. Rappoport, N. R. M. Crawford, F. Furche, K. Burke in *Computational Inorganic and Bioinorganic Chemistry*, (Eds.: E. I. Solomon, R. A. Scott, R. B. King), Wiley, Chichester., **2009**, Chapter Part 1.
- [87] A. D. Becke, *Phys. Rev. A.* **1988**, *38*, 3098–3100.
- [88] C. Lee, W. Yang, R. G. Parr, *Phys. Rev. B.* **1988**, *37*, 785–789.
- [89] J. P. Perdew, Y. Wang, *Phys. Rev. B.* **1992**, *45*, 13244–13249.
- [90] J. P. Perdew, K. Burke, M. Ernzerhof, *Phys. Rev. Lett.* **1996**, *77*, 3865–3868.
- [91] J. Tao, J. P. Perdew, V. N. Staroverov, G. E. Scuseria, *Phys. Rev. Lett.* **2003**, *91*, 146401.
- [92] A. D. Becke, *J. Chem. Phys.* **1993**, *98*, 1372–1377.

- [93] B. Miehlich, A. Savin, H. Stoll, H. Preuss, *Chem. Phys. Lett.* **1989**, *157*, 200–206.
- [94] A. D. Becke, *Phys. Rev. A.* **1988**, *38*, 3098–3100.
- [95] R. Krishnan, J. S. Binkley, R. Seeger, J. A. Pople, *J. Chem. Phys.* **1980**, *72*, 650–654.
- [96] J. P. Perdew, M. Ernzerhof, K. Burke, *J. Chem. Phys.* **1996**, *105*, 9982.
- [97] J. P. Perdew, *Phys. Rev. B.* **1986**, *33*, 8822–8824.
- [98] S. H. Vosko, L. Wilk, M. Nusair, *Can. J. Phys.* **1980**, *58*, 1200–1211.
- [99] J. P. Perdew, M. Ernzerhof, K. Burke, *J. Chem. Phys.* **1996**, *105*, 9982–9985.
- [100] S. Grimme, *J. Chem. Phys.* **2006**, *124*, 034108.
- [101] J. Heyd, G. E. Scuseria, *J. Chem. Phys.* **2004**, *121*, 1187–1192.
- [102] J. Heyd, G. E. Scuseria, M. Ernzerhof, *J. Chem. Phys.* **2003**, *118*, 8207–8215.
- [103] O. A. Vydrov, G. E. Scuseria, *J. Chem. Phys.* **2006**, *125*, 234109.
- [104] J. D. Chai, M. Head-Gordon, *Phys. Chem. Chem. Phys.* **2008**, *10*, 6615–6620.
- [105] M. J. G. Peach, P. Penfield, T. Helgaker, D. J. Tozer, *J. Chem. Phys.* **2008**, *128*, 044118.
- [106] T. Yanai, D. P. Tew, N. C. Handy, *Chem. Phys. Lett.* **2004**, *393*, 51–57.
- [107] A. D. Laurent, C. Adamo, D. Jacquemin, *Phys. Chem. Chem. Phys.* **2014**, *16*, 14334–14356.
- [108] C. Adamo, D. Jacquemin, *Chem. Soc. Rev.* **2013**, *42*, 845–856.
- [109] E. Runge, E. K. U. Gross, *Phys. Rev. Lett.* **1984**, *53*, 997–1000.
- [110] R. V. Leeuwen, *Phys. Rev. Lett.* **1999**, *82*, 3863–3866.
- [111] E. K. U. Gross, N. T. Maitra in *Fundamentals of Time-Dependent Density Functional Theory*, (Eds.: M. A. L. Marques, N. T. Neepe T. Maitra, F. M. S. Nogueira, E. K. U. E.K.U. Gross, A. Rubio), Springer, **2012**, Chapter 4.
- [112] J. Gross, E. Dobson, M. Petersilka in *Topics in Current Chemistry*, (Ed.: R. F. Nalewajski), Springer, **1996**.
- [113] M. Casida in *Recent Advances in Density-Functional Methods Part 1*, (Ed.: D. P. Chong), World Scientific Publishing Co. Pte. Ltd., **1995**, Chapter 5.
- [114] A. Dreuw, J. L. Weisman, M. Head-Gordon, *J. Chem. Phys.* **2003**, *119*, 2943–2946.
- [115] D. J. Tozer, R. D. Amos, N. C. Handy, B. J. Roos, L. Serrano-Andres, *Mol. Phys.* **1999**, *97*, 859–868.

- [116] A. Dreuw, M. Head-Gordon, *J. Am. Chem. Soc.* **2004**, *126*, 4007–4016.
- [117] S. Grimme, *J. Chem. Phys.* **2013**, *138*, 244104.
- [118] F. Cordova, L. J. Doriol, A. Ipatov, M. E. Casida, C. Filippi, A. Vela, *J. Chem. Phys.* **2007**, *127*, 164111.
- [119] Č. J., J. Paldus, *J. Chem. Phys.* **1967**, *47*, 3967–3985.
- [120] A. Dreuw, M. Head-Gordon, *J. Chem. Phys.* **2005**, *105*, 4009–4037.
- [121] T. Yamada, S. Hirata, *J. Chem. Phys.* **2015**, *143*, 114112.
- [122] S. Hirata, M. Head-Gordon, *Chem. Phys. Lett.* **1999**, *314*, 291–299.
- [123] M. J. G. Peach, M. J. Williamson, D. J. Tozer, *J. Chem. Theory. Comput.* **2011**, *7*, 3578–3585.
- [124] P. Pyykko, *Chem. Rev.* **1988**, *88*, 563–594.
- [125] P. Pyykko, *Annu. Rev. Phys. Chem.* **2012**, *63*, 45–64.
- [126] N. Kaltsoyannis, *Dalton Trans.* **1996**, 1–11.
- [127] L. H. THOMAS, *Nature* **1926**, *117*, 514.
- [128] H. N. Russell, F. A. Saunders, *Astrophys. J.* **1925**, *61*, 38.
- [129] P. A. M. Dirac, *Proc. R. Soc. London Ser. A: Mathematical Physical and Engineering Sciences* **1929**, *123*, 714–733.
- [130] G. Breit, *Proc. Natl. Acad. Sci. U. S. A.* **1928**, *14*, 553–559.
- [131] K. G. Dyall, *J. Chem. Phys.* **1994**, *100*, 2118.
- [132] E. V. Lenthe, E. J. Baerends, J. G. Snijders, *J. Chem. Phys.* **1993**, *99*, 4597–4610.
- [133] J. L. Heully, I. Lindgren, E. Lindroth, A. M. Martensson-Pendrill, *Phys. Rev. A.* **1986**, *33*, 4426–4429.
- [134] J. L. Heully, I. Lindgren, E. Lindroth, E. Lundqvist, A. M. Martensson-Pendrill, *J. Phys. B: Atom. Mol. Phys.* **1986**, *19*, 2799–2815.
- [135] C. Chang, M. Pelissier, P. Durand, *Phys. Scr.* **1986**, *34*, 394.
- [136] E. V. Lenthe, J. G. Snijders, E. J. Baerends, *J. Chem. Phys.* **1996**, *105*, 2373.
- [137] E. v. Lenthe, J. G. Snijders, E. J. Baerends, *J. Chem. Phys.* **1996**, *105*, 6505.
- [138] N. M. Kroll, M. Douglas, *Ann. Phys. (N. Y).* **1974**, *83*, 89–155.
- [139] B. A. Hess, *Phys. Rev. A.* **1986**, *33*, 3742–3748.
- [140] M. Reiher, A. Wolf, *J. Chem. Phys.* **2004**, *121*, 2307.
- [141] G. Hong, M. Dolg, L. Li, *J. Chem. Phys.* **2001**, *334*, 396–402.
- [142] L. Lodi, J. Tennyson, *J. Phys. B: At. Mol. Opt. Phys.* **2010**, *43*, 133001.

- [143] M. Dolg, *Encyclopedia of Computational Chemistry*, (Ed.: E. H. F. Schaefer), Wiley, Chichester, **2002**.
- [144] W. Küchle, M. Dolg, H. Stoll, H. Preuss, *J. Chem. Phys.* **1994**, *100*, 7535–7542.
- [145] X. Cao, M. Dolg, *J. Chem. Phys.* **2001**, *115*, 7348.
- [146] N. Heinz, J. Zhang, M. Dolg, *J. Chem. Theory Comput.* **2014**, *10*, 5593–5598.
- [147] A. Weigand, X. Cao, T. Hangele, M. Dolg, *J. Phys. Chem. A.* **2014**, *118*, 2519–2530.
- [148] M. Hulsen, M. Dolg, P. Link, U. Ruschewitz, *Theor. Chem. Acc.* **2011**, *129*, 367–379.
- [149] T. Fujiwara, H. Mori, Y. Mochizuki, Y. Osanai, E. Miyoshi, *Chem. Phys. Lett.* **2011**, *510*, 261–266.
- [150] H. Stoll, B. Metz, M. Dolg, *J. Comput. Chem.* **2002**, *23*, 767–778.
- [151] R. F. Bader, *Atoms in Molecules: A Quantum Theory*, Oxford University Press: Oxford, **1990**.
- [152] A. Kerridge, *Chem. Commun.* **2017**, *53*, 6685–6695.
- [153] C. F. Matta, R. J. Boyd, *The Quantum Theory of Atoms in Molecules: From Solid State to DNA and Drug Design*, WILEY-VCH, **2007**.
- [154] R. F. Bader, *J. Phys. Chem. A.* **1998**, *102*, 7314–7323.
- [155] R. F. Bader, *J. Phys. Chem. A.* **2009**, *113*, 10391–10396.
- [156] D. Cremer, E. Kraka, *Angew. Chem. Int. Ed. Engl.* **1984**, *23*, 627–628.
- [157] P. S. V. Kumar, V. Raghavendra, V. Subramanian, *J. Chem. Sci.* **2016**, *128*, 1527–1536.
- [158] F. Cortés-Guzmán, R. F. Bader, *Coord. Chem. Rev.* **2005**, *249*, 633–662.

## Chapter 3

# Investigation of uranyl covalency via symmetry-preserving excited state structures

*In this chapter, the covalency of free uranyl is investigated via the exploration of excitations which maintain symmetry of the electronic wavefunction at both the ground and electronically excited state geometries. The excitations investigated involved excitation from bonding to antibonding MOs of the same irreducible representation, resulting in relatively simple excited state electronic structures. In order to probe the covalency at both the ground and excited state electronic structures and equilibrium geometries; QTAIM analysis was utilised, for the first time to probe the excited state electronic structure of an f-element complex. The three lowest energy excitations ( $\pi_u \rightarrow \pi_u^*$ ,  $\sigma_u \rightarrow \sigma_u^*$  and  $\pi_g \rightarrow \pi_g^*$ ) exhibit qualitatively similar behaviours, the highest energy  $\sigma_g \rightarrow \sigma_g^*$  excitation was often an outlier. Comparing the ground and excited state equilibrium geometries resulted in similar trends in the QTAIM metrics and on compiling the data the relative size and dependence of  $\Lambda$  can be predicted. For MOs with U 5f character ( $\pi_u$  and  $\sigma_u$ ) it was found that  $\Lambda$  is depended on the metal-ligand Hamiltonian matrix element  $H_{ML}$ , while for MOs with U 6d character ( $\pi_g$  and  $\sigma_g$ )  $\Lambda$  becomes increasingly dependent on the difference in fragment orbital energy levels ( $\Delta E_{ML}$ ). At the excited state equilibrium geometries a relationship between excitation energy and bond elongation was established which further enhanced the large magnitude of  $\Lambda$  and its dependence on  $H_{ML}$  for the MOs with U 5f character and the large bond elongation in the  $\pi_g \rightarrow \pi_g^*$  state could be understood by the enhanced charge transfer character in the excitation. The latter highlighting the importance of considering the excited state equilibrium geometries for such an investigation.*

### 3.1 Introduction

While covalency is well-established for the majority of the periodic table, understanding bonding interactions for actinide complexes is a continuously evolving area of research. Rationalising covalency in actinide complexes remains a challenging experimental and computational problem and deeper understanding is of great importance. [1–3] From a fundamental perspective, understanding the bonding interactions within actinide complexes aids in the assessment of the viability of novel synthetic complexes, [4, 5] while in a practical application, variation in the bonding character is of particular importance for spent fuel reprocessing in the nuclear power industry. Indeed, selective complexation exploits the variation in the bonding character of complexes and is used in the chemical separation of the chemically similar trivalent actinides and lanthanides. [6, 7]

Covalency, as defined by Heitler and London, [8] is fundamental to our understanding of chemical bonding. In transition metals, metal-ligand orbital mixing and overlap as mechanisms for covalent character is well established; however, the prevalence of covalent bonding in actinides is heavily debated. [9–11] Therefore, understanding the role of the 5f and 6d orbitals in covalent bonding of actinides remains an important goal in fundamental actinide chemistry. [12, 13] However, while the concept of covalency is well-established, there is no formal physical definition. At the theoretical ionic limit there is no mixing among the valence orbitals, deviations from this idealised picture can be considered through perturbation theory. The mixing between a metal ( $\phi_M$ ) and ligand ( $\phi_L$ ) orbital, with energies  $E_M$  and  $E_L$ , in a molecular orbital  $\varphi$  can be expressed as:

$$\varphi(\mathbf{r}) = \phi_M(\mathbf{r}) + \Lambda\phi_L(\mathbf{r}) \tag{3.1}$$

where the mixing coefficient  $\Lambda$  is given to first order by: [14]

$$\Lambda = \frac{H_{ML}}{\Delta E_{ML}} \tag{3.2}$$

Here  $H_{ML}$  is the Hamiltonian matrix element between the two orbitals and is approximately proportional to the overlap ( $S_{ML}$ ). [14] Since  $S_{ML}$  is correlated to the bond length, it follows that the same is true for  $H_{ML}$ .

In uranyl,  $H_{ML}$  is taken to be a measure of the strength of interactions between the uranium 5f/6d and oxygen 2p orbitals, whereas,  $\Delta E_{ML}$  is the energy difference between the metal and ligand orbitals. The mixing coefficient ( $\Lambda$ ) is a measure of the covalent character of the bond. Values of  $\Lambda$  are, in general, non-zero and maximum covalency is achieved when  $\Lambda = 1$ , *e.g.* in a homonuclear diatomic at its equilibrium geometry.

Equation 3.2 indicates that covalency can be driven by two factors: [15]

- Large values of  $H_{ML}$ , corresponding to overlap-driven covalency

- Small values of  $\Delta E_{\text{ML}}$ , corresponding to (energy) degeneracy-driven covalency

The inherent properties of actinides makes characterising the bonding interactions and therefore the origins of covalency, challenging for both experimentalists and theorists. Actinide complexes exhibit strong relativistic effects, weak crystal fields and strongly correlated valence electronic structures. [16, 17] These strongly-correlated systems result in ambiguous orbital-based descriptions of the electronic structure and as such, analysis using orbital-based methods should be contextualised with other approaches. [18–23] Analytical methods based on the experimentally observable electron density provide a robust and unambiguous alternative. Throughout this chapter and thesis, the Quantum Theory of Atoms in Molecules (QTAIM), developed by Bader, [24] will be utilised. QTAIM divides a molecule up into a contiguous set of space-filling atomic basins. This method provides insight into the bonding interactions via both topological and integrated properties of the electron density, which can be used to build up a picture of the covalency in a molecule. A detailed overview of this analysis can be found in this recent article. [15]

QTAIM has been successfully used to characterise the bonding interactions in many f-element complexes. [21, 23, 25–34] One of the earliest applications of QTAIM analysis in f-element chemistry was conducted by Kaltsoyannis and co-workers. [25, 26] In these contributions, the covalency in  $\text{AnCp}_4$  and  $\text{AnCp}_3$  complexes ( $\text{An}=\text{Th-Cm}$ ) were studied. The densities were generated using density functional theory (DFT) and the covalency was assigned using the magnitude of the topological QTAIM metric,  $\rho_{\text{BCP}}$ . This metric indicated that in these organometallic complexes, the interaction between the actinide and coordinating carbon was mainly ionic in character and this ionic character increased with atomic number. This trend was also established by Kerridge [32] in studies of  $\text{AnCOT}_2$  complexes ( $\text{COT}=\eta^5\text{-C}_8\text{H}_8$ ) where, in contrast to the previous contributions, the complete-active-space self-consistent-field (CASSCF) method was utilised to generate the simulated density. Kerridge also investigated the degree of electron sharing between the actinide and coordinating carbon species via the delocalisation index ( $\delta$ ), an integrated QTAIM metric, and found that both integrated and topological metrics gave the same broad trend.

Of more direct relevance to this chapter, QTAIM has also been utilised to study the covalency of uranyl and its complexes. Vallet *et al.* [23] found that free uranyl ( $\text{UO}_2^{2+}$ ) has strongly covalent interactions between the uranium and oxygen given by the large  $\rho_{\text{BCP}}$  and  $\delta$  metrics. They also concluded that there is a significant decrease in the magnitude of these metrics ( $\rho_{\text{BCP}}$  and  $\delta$ ) after ligation to the equatorial plane, indicating a decrease in covalency. Comparable bonding characteristics were also established by DiPietro and Kerridge [4] using similar techniques.

In this chapter, the covalency in uranyl is investigated via the exploration of excitations which maintain symmetry of the electronic wavefunction, considering

both ground and electronically excited state geometries. These excitations were chosen specifically to ensure that linearity of the uranyl unit is maintained since excitations are largely characterised as being from bonding to anti-bonding MOs of the same irreducible representation, giving relatively simple excited state electronic structures. Throughout this chapter, singlet excitations comprised of transitions from bonding to antibonding orbitals of the same character (e.g.  $\sigma_u \rightarrow \sigma_u^*$ ) will be investigated ( $S_4$ ,  $S_8$ ,  $S_{10}$  and  $S_{14}$  in Table 3.1), along with the optically allowed excitation of principally  $\sigma_u \rightarrow \delta_u$  character, which is allowed via spin-orbit coupling. [35–39]

The excitation energy, as well as the energy difference between a bonding ( $\phi$ ) and antibonding ( $\phi^*$ ) MO of the same irrep can be linked with the terms in Equation 3.2. These energy differences would be expected to be large when either charge transfer character is large (implying a small value of  $\Lambda$ ) and/or  $H_{ML}$  is large (which implies a large value  $S_{ML}$  but doesn't fully characterise  $\Lambda$ ).

## 3.2 Computational Details

Initially, simulations employed version 7.3 of the TURBOMOLE code [40] to explore the excitations of  $a_g$  symmetry within the  $d_{2h}$  point group. Once excitations of interest were identified, Gaussian09 (Revision E.01) [41] was employed and, unless explicitly stated, all presented results are derived using Gaussian. All simulations were performed at the hybrid Density Functional Theory (DFT) level, employing the B3LYP exchange-correlation functional. [42–46] The aug-cc-pVDZ basis set [47–49] was employed for oxygen along with Stuttgart RSC 1997 basis set and associated small core effective core potential for uranium, [50–52]. Geometry optimisations were performed for both ground and electronic excited state geometries and structures characterised as minima by vibrational frequency analysis. Electronic excitations were calculated at both the ground and excited state geometries employing the Tamm–Dancoff Approximation (TDA) [53] to Time Dependent-DFT. [54, 55] Version 19.02.13 of AIMAll [56] and version 3.6 of Multiwfn [57] were used in the density-based analysis of the simulated electronic structures. The latter was also employed in the generations of density difference data.

In the analysis of the QTAIM metrics, the variation in comparison to the ground state is discussed. These variations (shown in Figure 3.1) always compare the differences between the excited state electronic structures at the current geometry with the ground state minimum (ground state electronic structure at the ground state geometry,  $S_0$  in Figure 3.1)).

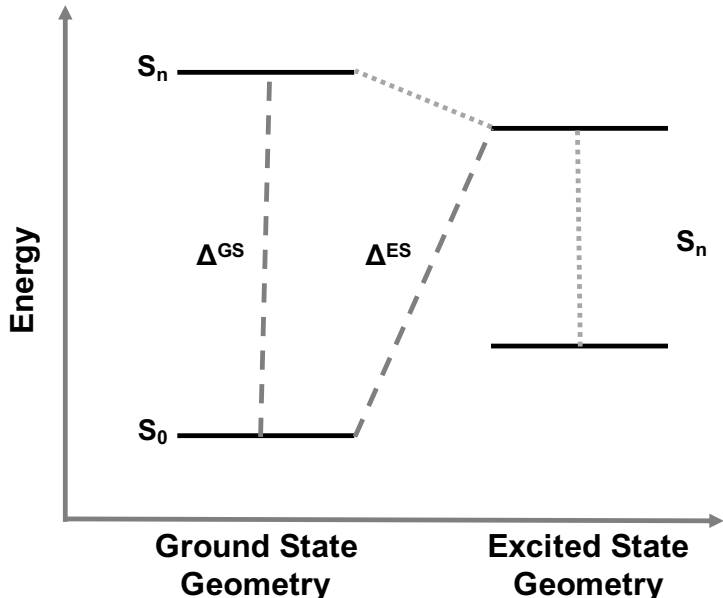


Figure 3.1: Simple Jablonski diagram depicting the variations discussed in the analysis of the QTAIM results

### 3.3 Results and Discussion

#### 3.3.1 Electronic Properties at the Ground State Geometry

Geometry optimisation of  $\text{UO}_2^{2+}$  produced a U-O bond length of 1.70 Å, in excellent agreement with previously reported values (1.68-1.72 Å). [58–60] The 15 lowest lying excitations of  $A_g$  symmetry, calculated using the TURBOMOLE programme are displayed in Table 3.1. It is worth noting that in uranyl there are several degenerate MOs pairs which are present in excitations:  $S_2$ ,  $S_3$ ,  $S_4$ ,  $S_7$ ,  $S_{10}$ ,  $S_{11}$  and  $S_{12}$ . These excitations have equal contributions from both pairs of MOs and in the case of excitation  $S_2/S_3$  and  $S_{11}/S_{12}$  the higher energy excitation has the same nature as the lower but the ordering of the MOs are reversed.

While the majority of these excitations have a single dominant transition, this is not the case for states  $S_7$  and  $S_8$ .  $S_7$  has equal weightings of two different transitions ( $5B_{1u} \rightarrow 7B_{1u}$  and  $3B_{2u}/3B_{3u} \rightarrow 5B_{2u}/5B_{3u}$ ), while  $S_8$  has 44% contribution from the MOs given in Table 3.1 ( $5B_{1u} \rightarrow 7B_{1u}$ ) and then a lower contribution (33 %) from the MOs which are involved in the  $S_{10}$  excitation ( $2B_{3g}/2B_{2g} \rightarrow 3B_{3g}/3B_{2g}$ ).

The rest of this chapter will mainly focus on electronic excitations in which the dominant orbital transition is between MOs with the same bonding and antibonding character, which are summarised in Table 3.2. As mentioned previously, the  $\pi \rightarrow \pi^*$  excitations are comprised of two symmetry-equivalent transitions and the  $\sigma_u \rightarrow \sigma_u^*$  excitation contains significant contributions (33%) from the  $\pi_g \rightarrow \pi_g^*$  transition.

Excitations involving transitions between MOs of u (*ungerade*) symmetry, possessing U 5f character, are shown to occur at lower energies than those of g (*gerade*) symmetry, possessing U 6d character. It then follows that transitions involving MOs

Table 3.1: Excitation energies ( $\Delta E$ ) and natures of the 15 lowest energy singlet excitations of  $A_g$  symmetry

State	Transition	$\Delta E$ (eV)	Hole MO	Particle MO
S <sub>1</sub>	5B <sub>1u</sub> →6B <sub>1u</sub>	3.53		
S <sub>2</sub> /S <sub>3</sub>	3B <sub>2u</sub> /3B <sub>3u</sub> →4B <sub>2u</sub> /4B <sub>3u</sub>	4.17/4.67		
S <sub>4</sub>	3B <sub>3u</sub> /3B <sub>2u</sub> →5B <sub>3u</sub> /5B <sub>2u</sub>	7.37		
S <sub>5</sub>	7A <sub>g</sub> →8A <sub>g</sub>	8.02		
S <sub>6</sub>	7A <sub>g</sub> →9A <sub>g</sub>	8.35		
S <sub>7</sub>	5B <sub>1u</sub> →7B <sub>1u</sub>	9.36		
	3B <sub>2u</sub> /3B <sub>3u</sub> →5B <sub>2u</sub> /5B <sub>3u</sub>			
S <sub>8</sub>	5B <sub>1u</sub> →7B <sub>1u</sub>	12.67		
S <sub>9</sub>	4B <sub>1u</sub> →6B <sub>1u</sub>	12.78		
S <sub>10</sub>	2B <sub>3g</sub> /2B <sub>2g</sub> →3B <sub>3g</sub> /3B <sub>2g</sub>	13.37		
S <sub>11</sub> /S <sub>12</sub>	3B <sub>2u</sub> /3B <sub>3u</sub> →6B <sub>2u</sub> /6B <sub>3u</sub>	14.33/14.35		
S <sub>13</sub>	5B <sub>1u</sub> →8B <sub>1u</sub>	15.13		
S <sub>14</sub>	7A <sub>g</sub> →10A <sub>g</sub>	16.62		
S <sub>15</sub>	5B <sub>1u</sub> →9B <sub>1u</sub>	17.84		

with U 5f character present greater covalent character, as measured by  $\Lambda$ , and/or smaller values  $H_{ML}$  when compared to those involving MOs with 6d character. Clark and co-workers [12] investigated the covalency of actinide chlorides and concluded that the 6d-orbitals were available for orbital mixing to a larger extent than the 5f-orbitals. They also stated that this observation is consistent with other accounts,

Table 3.2: Summary of electronic excitations between bonding and anti-bonding MOs of the same character at the ground state geometry

Excitation	$\pi_u \rightarrow \pi_u^*$	$\sigma_u \rightarrow \sigma_u^*$	$\pi_g \rightarrow \pi_g^*$	$\sigma_g \rightarrow \sigma_g^*$
State	S <sub>4</sub>	S <sub>8</sub>	S <sub>10</sub>	S <sub>14</sub>
$\Delta E$ (eV)	7.37	12.67	13.37	16.62
Contribution (%)	88	44	78	98

[61–63] which all suggest that 5f-orbitals have a small  $H_{ML}$  and hence limited participation in covalent bonding.

In order to further rationalise the difference in U 5f/6d bond character, integrated properties of the electron density were evaluated within the Quantum Theory of Atoms in Molecules (QTAIM) framework. Specifically, the atomic charge ( $q$ ), localisation index ( $\lambda$ ) and delocalisation index ( $\delta$ ) were considered. [4, 18, 32] While the atomic charge is a one-electron property obtained via integration of the total electron density in an atomic basin, the localisation and delocalisation indices are formally two-electron properties.  $\lambda$  provides a measure of the number of electrons localised on a given atom while  $\delta$  measures the number of electrons shared between two atoms and, in the absence of bond polarisation, acts as a bond order metric. [15] Combined, these metrics can provide detailed information regarding the nature and magnitude of bonding interactions, highlighting variation in both charge transfer and covalency.

Table 3.3: Integrated QTAIM metrics: charge ( $q$ ), localisation ( $\lambda$ ) and delocalisation ( $\delta$ ) indices at the ground (GS) and excited state electronic structures.

Metric	GS	$\pi_u \rightarrow \pi_u^*$	$\sigma_u \rightarrow \sigma_u^*$	$\pi_g \rightarrow \pi_g^*$	$\sigma_g \rightarrow \sigma_g^*$
$\Delta E$ (eV)	/	7.38	12.75	13.41	16.65
$q_U$ (a.u.)	3.153	3.102	3.046	2.972	3.367
$q_O$ (a.u.)	-0.576	-0.551	-0.523	-0.486	-0.683
$\lambda_U$	86.814	87.210	87.138	87.093	86.470
$\lambda_O$	7.476	7.661	7.569	7.459	7.373
$\delta_{U-O}$	2.045	1.692	1.816	1.943	2.174

Atomic charge data shows that, as excitation energy increases, increasing electronic charge is transferred to the uranium. From an orbital perspective, this implies

that the bonding MO has more oxygen character and the antibonding MO more uranium character. A partial exception to this trend is the high energy  $\sigma_g \rightarrow \sigma_g^*$  excitation, where, while the direction of charge transfer is reversed, it should be noted that this excitation does have the largest magnitude charge transfer character, and so a correlation between charge transfer character and excitation energy is established. This is commensurate with the excitation energy data which suggest reduced orbital mixing,  $\Lambda$ , with increasing excitation energy. This observation further verifies the analysis given that charge transfer would be expected to be minimal when  $\Lambda = 1$ .

It has been highlighted in the literature that reliance on charge data alone can lead to incorrect interpretations with regard to variation in uranyl bonding. [4] Here, while  $\lambda_U$  qualitatively mirrors the atomic charge data, with  $\Delta^{\text{GS}}\lambda > 0$  when charge is transferred to the uranium and  $\Delta^{\text{GS}}\lambda < 0$  when charge is transferred from the uranium, the overall trend is not replicated, *e.g.* the increase in electron localisation is largest for the lowest energy  $\pi_u \rightarrow \pi_u^*$  excitation. This is perhaps unsurprising, since  $\lambda$  alone is insufficient to characterise the electron population,  $N$ , of an atom, which can be formally defined in QTAIM as:

$$N_A = \lambda_A + \frac{1}{2} \sum_{A \neq B} \delta_{A,B} \quad (3.3)$$

A change in the  $\lambda$  of an atom can therefore be due to charge transfer from another atom, a change in the  $\delta$  between it and other atoms, or a combination of the two. Given that the variation in  $\delta_{U-O}$  opposes that of  $\lambda_U$  for all excitations and shows greater sensitivity to the excitation energy for the three lowest energy excitations, the atomic charge data can be rationalised. Charge transfer from O to U, as defined by the variation in  $\lambda$ , actually reduces with increased excitation energy, with the increase in  $\Delta^{\text{GS}}q_U$  strongly affected by a smaller reduction in  $\delta_{U-O}$  (note that the  $\sigma_g \rightarrow \sigma_g^*$  excitation shows qualitatively different behaviour, although the same general reasoning applies).

In a monodeterminantal wavefunction, the  $\delta$  can be interpreted in terms of the overlap between MOs [64] and, as such,  $\Delta^{\text{GS}}\delta$  would be expected to be largest when  $\Lambda$  is closest to 1. Since  $\delta_{U-O}$  reduces with increasing excitation energy, with the exception of the  $\sigma_g \rightarrow \sigma_g^*$  state, this further supports the assertion of the anticorrelation of  $\Lambda$  with  $\Delta E$ .

Returning our attention to the  $\sigma_g \rightarrow \sigma_g^*$  excitation, it can be noted from Figure 3.2 that the  $\sigma_g^*$  MO has rather diffuse character with significant O contribution. This observation allows a better understanding of the electronic structure data. As previously mentioned, the large excitation energy correlates with the substantial charge transfer character of the excitation, albeit with the charge being transferred to the oxygen centres. Here, both  $\lambda_U$  and  $\lambda_O$  reduce upon excitation and so the apparent charge transfer is explained by an increase in  $\delta_{U-O}$ . As discussed above, this is unexpected behaviour for an excitation into a formally antibonding MO and so it can be

rationalised that the increase in electronic charge on the (already anionic) oxygen centres has a substantial secondary effect on the electronic structure, causing the doubly occupied  $\sigma_u$  and  $\pi_{g/u}$  MOs to adopt more covalent character leading to the net increase in  $\delta_{U-O}$ . This dramatic behaviour suggests that  $\Lambda$  is smallest in  $\sigma_g$ , again strengthening the relationship between  $\Lambda$  and  $\Delta E$  that was identified previously.

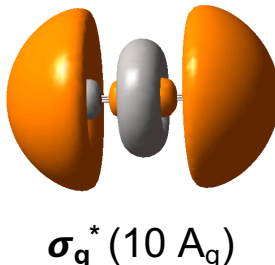


Figure 3.2:  $\sigma_g^*$  MO showing diffuse character with significant O contribution

In a simple two-level model, it would be expected that the energy difference between the bonding and antibonding MOs, and therefore the  $\phi \rightarrow \phi^*$  excitation energy, to increase monotonically with the magnitude of the Hamiltonian matrix element between the relevant metal and ligand levels. From the analysis above, this would imply an inverse relationship between  $\Lambda$  and  $H_{ML}$ . However, Equation 3.2 states the opposite, leading us to deduce that  $\Delta E_{ML}$  increasingly outweighs  $H_{ML}$  as the excitation energy increases, implying that  $\Delta E_{ML}$  dominates in covalent interactions involving U 6d contributions, whereas  $H_{ML}$  dominates for covalent interactions involving U 5f orbitals. Since the delocalisation indices themselves are unable to differentiate between overlap- and degeneracy-driven covalency, [15] we turn our attention to topological properties of the electron density.  $\rho_{BCP}$  measures the electron density at the bond critical point (BCP) between two chemically bonded species and gives an indication of the charge accumulated at the BCP. This metric would be expected to reflect the degree of overlap-driven covalency, with a common rule of thumb being that  $\rho_{BCP} > 0.2$  a.u. is indicative of a covalent interaction. However, this will only identify contributions due to  $\sigma$ -type interactions since  $\pi$ -interactions are characterised by a nodal plane in which the BCP typically lies. The Laplacian of  $\rho_{BCP}$  ( $\nabla^2 \rho_{BCP}$ ) is a complementary metric which can further aid in the characterisation of a bonding interaction. Finally, the magnitude of the energy density,  $H$ , which is negative for interactions which have significant electron sharing, can reflect the covalency of an interaction.

The results presented in Table 3.4 are surprising in that  $\rho_{BCP}$  increases in the electronically excited state. Since the excitations are into formally antibonding MOs, one would expect  $\rho_{BCP}$ , which reflects the degree of covalent character, to decrease in the excited state. However,  $\rho_{BCP}$  also correlates strongly with bond length and so the small increases found here may simply be reflective of the constrained geometry

Table 3.4: Topological QTAIM metrics (a.u.) at the ground and excited state electronic structures at the ground state geometry

Metric	GS	$\pi_u \rightarrow \pi_u^*$	$\sigma_u \rightarrow \sigma_u^*$	$\pi_g \rightarrow \pi_g^*$	$\sigma_g \rightarrow \sigma_g^*$
$\rho_{\text{BCP}}$ (a.u.)	0.332	0.358	0.359	0.364	0.338
$\nabla^2 \rho_{\text{BCP}}$ (a.u.)	0.529	0.312	0.565	0.236	0.381
$H$ (a.u.)	-0.347	-0.394	-0.394	-0.404	-0.356

associated with the vertical excitation (an analogous argument can also be made for  $H$ ). The analysis of topological properties is therefore delayed until excited state molecular structures have been considered.

### 3.3.2 Symmetric Stretching of the U-O bond

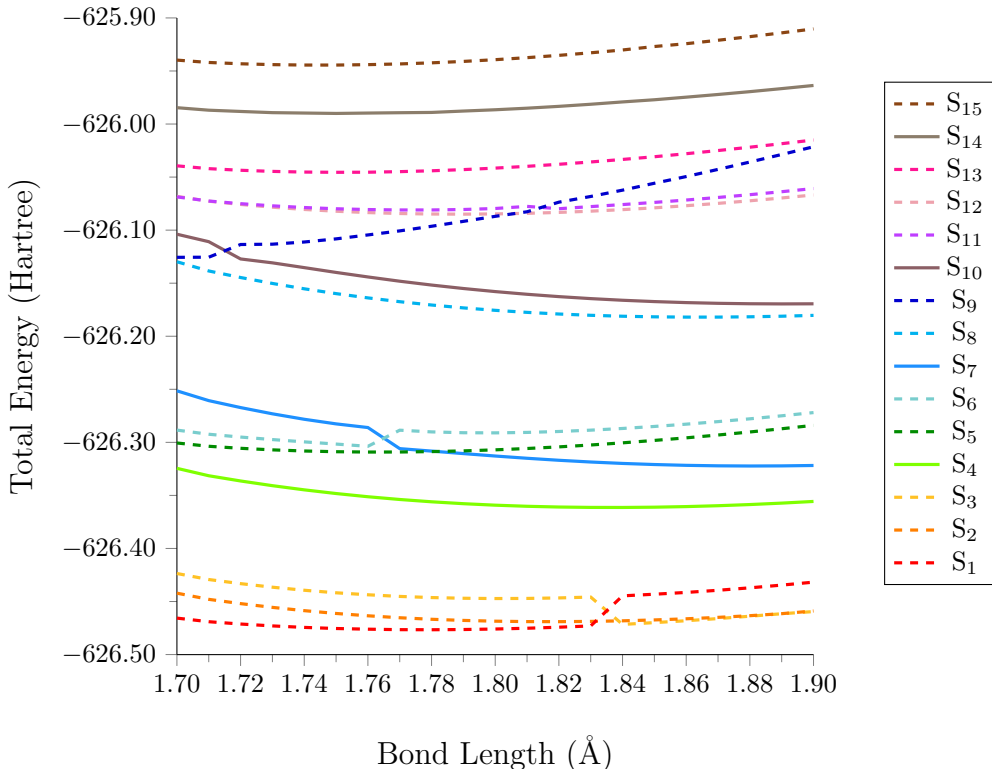


Figure 3.3: Potential energy surfaces of the 15 lowest lying excitations of  $A_g$  symmetry. State labels are indicated by the ordering of the excitations at the ground state as given in Table 3.1 and the excitations of interest are given as solid lines.

Before optimising the excited state geometries of interest, the uranyl bond was stretched and the potential energy surface (PES) of the 15 lowest-lying excitations

given in Table 3.1 were generated (Figure 3.3). Excited states  $S_4$ ,  $S_7$ ,  $S_{10}$  and  $S_{14}$  correspond to the  $\pi_u \rightarrow \pi_u^*$ ,  $\sigma_u \rightarrow \sigma_u^*$ ,  $\pi_g \rightarrow \pi_g^*$ ,  $\sigma_g \rightarrow \sigma_g^*$  excitations respectively and represented in figure 3.3 as solid lines.

The PES given in Figure 3.3 tracks the nature of the excitation rather than the ordering of the excitations at a particular geometry. For example, the lowest energy excitation at 1.82 Å has  $S_1$  nature and third lowest is  $S_3$  in nature, however at 1.84 Å,  $S_3$  becomes the lowest energy excitation and  $S_1$  the third lowest. In this particular example, as the U-O bond is elongated in the  $S_1$  excitation the contribution from the  $\sigma_u \rightarrow \delta_u$  decreases and the  $\pi_u \rightarrow \phi_u$  increases. The reverse trend is seen in  $S_3$  and this is an explanation for the crossing seen at 1.84 Å. Similar behaviour is also seen in state  $S_8$ , where as the U-O bond length increases there is an increasing contribution from the  $\pi_g \rightarrow \pi_g^*$  transition to the dominant  $\sigma_u \rightarrow \sigma_u^*$  and this is highlighted by the two PES curves converging.

Using the PES curves, the minimum point for each state can be isolated. For the states of interest these were at: 1.75 Å, 1.84 Å, 1.87 Å and 1.89 Å for states  $S_{14}$ ,  $S_4$ ,  $S_8$  and  $S_{10}$  respectively. These geometries were then used as the starting points for the excited state optimisations, the results of which are given in Section 3.3.3.

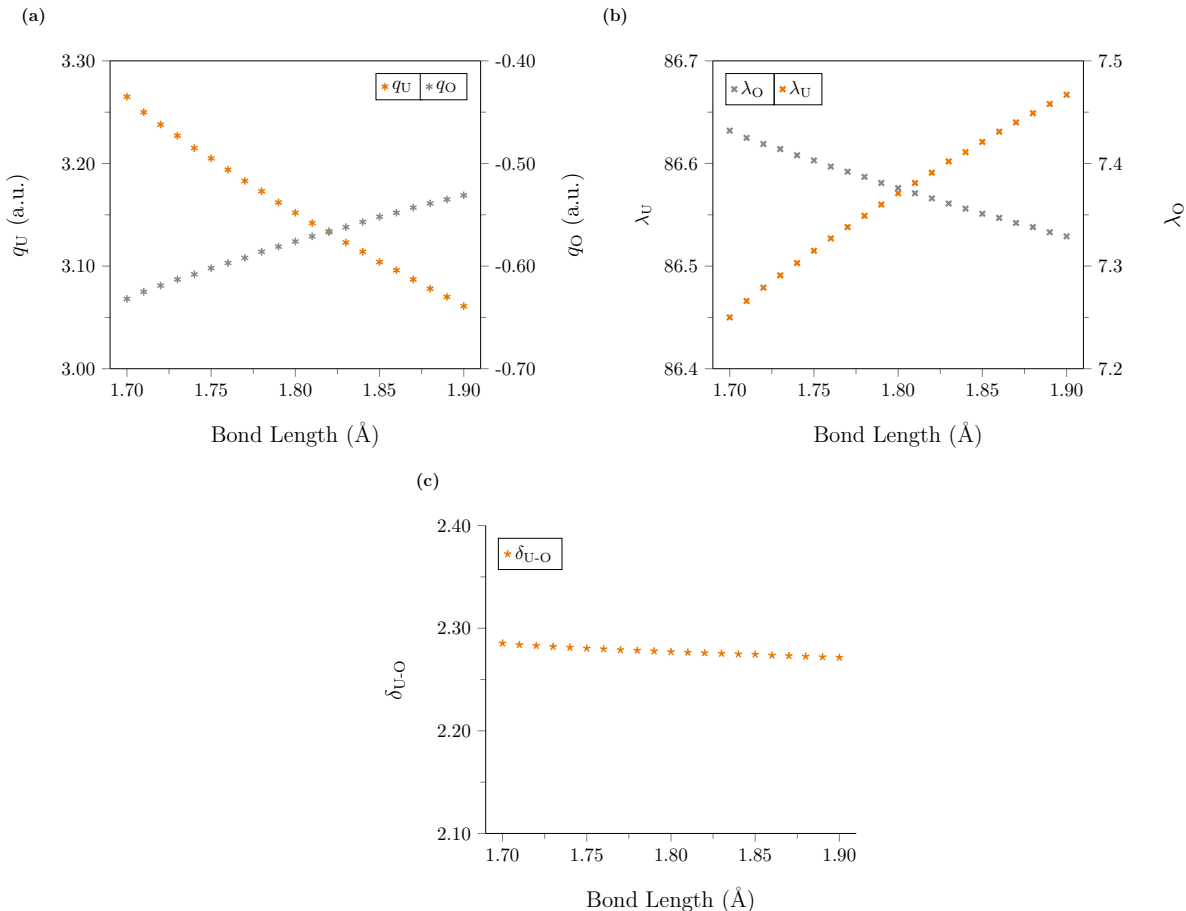


Figure 3.4: Trends in the QTAIM metrics: (a) charge ( $q$ ), (b) localisation index ( $\lambda$ ) and (c) delocalisation index ( $\delta$ ) as the U-O bond is elongated

The variation in QTAIM metrics (at the ground state electronic structures) are shown in Figure 3.4. As the U-O bond elongates;  $q_U$  becomes less positive,  $q_O$  becomes less negative,  $\lambda_U$  increases,  $\lambda_O$  decreases and  $\delta_{U-O}$  decreases. These trends indicate that as the U-O bond length increases, charge is transferred from the oxygen to the uranium and the covalency of the uranyl bond decreases.

### 3.3.2.1 Symmetry decomposition of QTAIM metrics

The high symmetry of uranyl allows  $\delta$  to be decomposed into their symmetry elements. Previous studies have employed such analysis to differentiate between 5f and 6d contributions to bonding interactions. [15, 18, 32, 65, 66] These symmetry-decomposed  $\delta$  are used here to understand how electrons are shared in the ground state as the U-O bond is elongated. Figure 3.5 shows how the symmetry-decomposed  $\delta$  vary with U-O bond length.

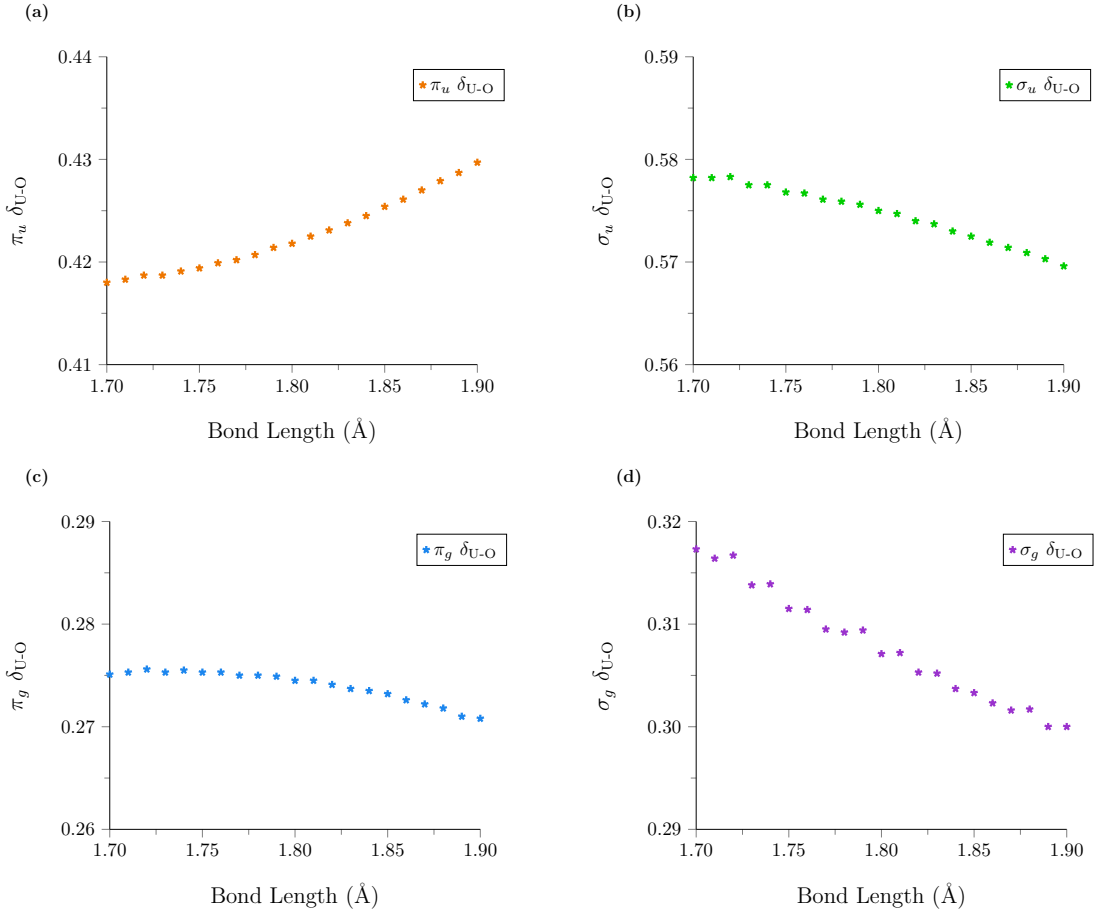


Figure 3.5: Variation in the symmetry-decomposed  $\delta$  metrics when the U-O bond is elongated

$\sigma_u$ ,  $\sigma_g$  and  $\pi_g$  symmetry-decomposed components decrease, while  $\pi_u$  increases. The magnitude of the increase/decrease in  $\delta$  varies between the symmetries with  $\sigma_g$  having the largest and  $\pi_g$  the smallest.

The total  $\delta$  reduces with increasing bond length, as would be expected. This behaviour is mirrored in the  $\sigma_u$  and  $\sigma_g$  components, however the  $\pi_u$  component increases with increasing bond length. Since orbital overlap (and therefore  $H_{\text{ML}}$ ) necessarily decreases with increasing bond length, these data can be interpreted in terms of the relative positions of the energy levels of the fragment orbitals comprising the MO. It can therefore be deduced that  $\Delta E_{\text{ML}}$  decreases more rapidly for the  $\pi_u$  MO in comparison to the others, suggesting that the fragment are brought more closely into resonance as the bond is elongated.

Table 3.5: Symmetry-decomposed  $\delta$  evaluated at the ground state minimum and the minimum value for each state on the PES given in Figure 3.3

State/ Geometry	r (Å)	$\delta_{\text{U-O}}$				
		Total	$\sigma_u$	$\pi_u$	$\sigma_g$	$\pi_g$
GS	1.70	2.282	0.578	0.418	0.317	0.275
$\sigma_g \rightarrow \sigma_g^*$	1.75	2.278	0.577	0.419	0.312	0.275
$\pi_u \rightarrow \pi_u^*$	1.84	2.273	0.573	0.425	0.304	0.273
$\sigma_u \rightarrow \sigma_u^*$	1.87	2.272	0.572	0.426	0.302	0.273
$\pi_g \rightarrow \pi_g^*$	1.89	2.270	0.570	0.429	0.300	0.271

As mentioned previously the PES in Figure 3.3 can be used to obtain the minimum geometries for the excitations of interest. These minimum values and the corresponding symmetry-decomposed  $\delta$  are summarised in Table 3.5.

### 3.3.3 Electronic Properties at Excited State Geometries

Table 3.6: Characterisation of electronic excitations ( $\Delta E$ ) at the excited state geometries of uranyl, the Stokes shift when compared to the excitation energy at the ground state geometries and the elongation of the U-O bond compared to the ground state geometry ( $\Delta r$ ).

Excitation	$\pi_u \rightarrow \pi_u^*$	$\sigma_u \rightarrow \sigma_u^*$	$\pi_g \rightarrow \pi_g^*$	$\sigma_g \rightarrow \sigma_g^*$
$\Delta E$ (eV)	5.55	10.16	9.91	16.37
Contribution (%)	47	23	66	98
Stokes Shift (eV)	1.83	2.59	3.50	0.28
$\Delta r$ (Å)	0.135	0.166	0.194	0.051

Excited state minima geometries were obtained for the;  $\pi_u \rightarrow \pi_u^*$ ,  $\sigma_u \rightarrow \sigma_u^*$ ,  $\pi_g \rightarrow \pi_g^*$  and  $\sigma_g \rightarrow \sigma_g^*$  states. Upon excitation, the U-O bond length increases and the excitation energy is red shifted; Table 3.6 summarises the excitation energy ( $\Delta E$ ) and U-O bond increase ( $\Delta r$ ) for the four excited state geometries. Again, the  $\sigma_g \rightarrow \sigma_g^*$  state exhibits a quantitatively different behaviour, with only a modest bond elongation.

Figure 3.6 compares the density difference generated at both the ground and excited state geometries for each excitation. Inspection of these density differences reveals that the  $\sigma_g \rightarrow \sigma_g^*$  state exhibits a qualitatively different redistribution of charge to the rest of the states and consequently a variation in the interplay between ionic and covalent bond character, providing a potential origin for the calculated bond length.

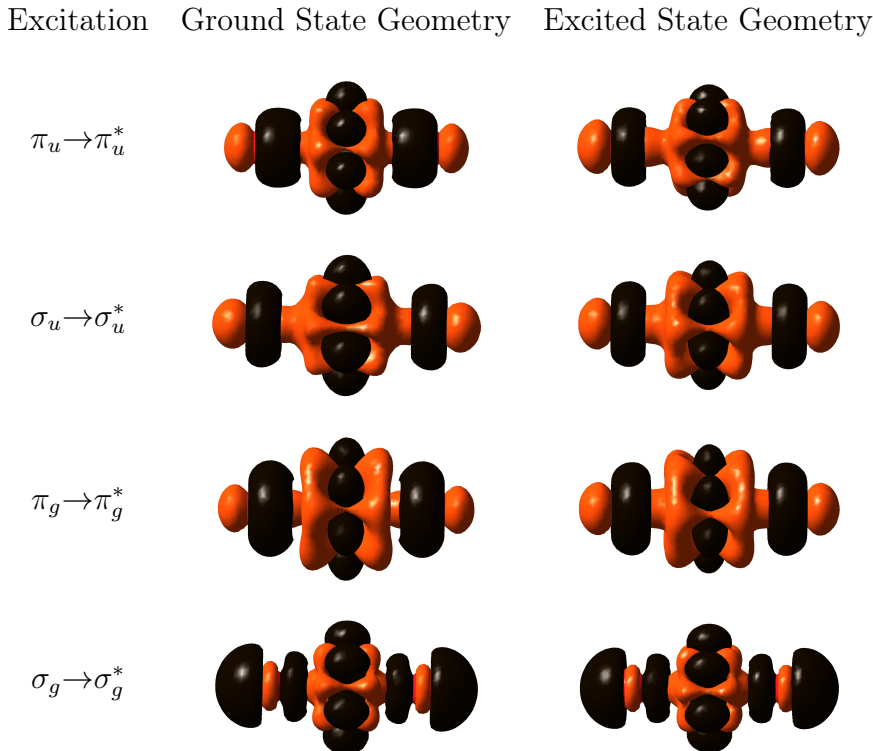


Figure 3.6: Comparison of density differences at ground (left) and excited (right) state geometries. Orange/black represents positive/negative electron density

For the three excited states with qualitatively similar excitation character ( $\pi_u \rightarrow \pi_u^*$ ,  $\sigma_u \rightarrow \sigma_u^*$  and  $\pi_g \rightarrow \pi_g^*$ ), the variation in bond length follows the same trend as found for the vertical excitation energies in Section 3.3.1. This provides further evidence that the reduction in  $\Lambda$  is due to an increasingly dominant  $\Delta E_{\text{ML}}$  contribution, rather than a decreasing  $H_{\text{ML}}$ , since only the latter would be expected to directly impact on bond stability. Diabatic excitations in which  $\Delta r$  is large imply that  $H_{\text{ML}}$  is also substantial as  $H_{\text{ML}}$  is approximately proportional to the overlap ( $S_{\text{ML}}$ ) which is in turn correlated to bond length.

The excitation energies and corresponding orbital contributions, at the relative

excited state minima are summarised in Table 3.6. This contribution remains unchanged for the  $\sigma_g \rightarrow \sigma_g^*$  state but is significantly reduced for the other states, presumably reflecting the deviation from monodeterminantal character as the bond is stretched. In contrast to the ground state geometries, both the  $\pi_u \rightarrow \pi_u^*$  and  $\pi_g \rightarrow \pi_g^*$  states include both sets of excitations from the transition of interest, *i.e.* 22 $\rightarrow$ 29, 21 $\rightarrow$ 28 transitions giving a higher contribution (47 %) and transitions 21 $\rightarrow$ 29, 22 $\rightarrow$ 28 giving a slightly lower contribution (41 %) for the  $\pi_u \rightarrow \pi_u^*$  state. Interestingly, summing the two sets of  $\pi \rightarrow \pi^*$  transitions (4 transitions in total), the total contribution for  $\pi_u \rightarrow \pi_u^*$  is the same as that at the ground state geometry (88 %), while for the  $\pi_g \rightarrow \pi_g^*$  state the total contribution is larger (98 %) than at the ground state geometry (78 %). At the ground state geometry, the  $\sigma_u \rightarrow \sigma_u^*$  state had contributions from one set of  $\pi_g \rightarrow \pi_g^*$  transitions (33 %). However, at the excited state geometry, the same double contribution of the  $\pi_g \rightarrow \pi_g^*$  transitions (as seen at the  $\pi_u \rightarrow \pi_u^*$  and  $\pi_g \rightarrow \pi_g^*$  excited state geometries) also occurs in the  $\sigma_u \rightarrow \sigma_u^*$  excitation, which comprises a sum of 58 % contribution from both sets of  $\pi_g \rightarrow \pi_g^*$  transitions .

Excitation energies are all reduced in magnitude when compared to those at the ground state minima, indicating relative destabilisation of the ground state electronic structure at the excited state geometries, and so the Stokes shift, calculated here as the difference between the vertical excitation energy at the excited and ground state geometry, describes a red shift for each excited state. The Stokes shift may be utilised to provide further bonding insight, *e.g.* a small Stokes shift may be indicative of the dependence of  $\Lambda$  on  $\Delta E_{\text{ML}}$  rather than  $H_{\text{ML}}$ , however, it also correlates strongly with variation in bond length (see Table 3.6), and for the states under consideration here this latter correlation restricts further interpretation in terms of electronic structure.

Table 3.7: Charge ( $q$ ), localisation index ( $\lambda$ ) and delocalisation index ( $\delta$ ) at the excited state electronic structures at the excited state geometries of the states of interest

Metric	$\pi_u \rightarrow \pi_u^*$	$\pi_g \rightarrow \pi_g^*$	$\sigma_u \rightarrow \sigma_u^*$	$\sigma_g \rightarrow \sigma_g^*$
$\Delta E$ (eV)	5.55	9.91	10.16	16.37
$q_U$ (a.u.)	3.031	2.738	2.846	3.318
$q_O$ (a.u.)	-0.515	-0.369	-0.423	-0.658
$\lambda_U$	87.342	87.376	87.621	86.538
$\lambda_O$	7.653	7.365	7.628	7.363
$\delta_{U-O}$	1.634	1.892	1.535	2.155

Integrated QTAIM metrics for the excited state electronic structures at the excited state geometries are given in Table 3.7. At the ground state geometries excitation resulted in: a decrease in  $q_U$  and  $\delta_{U-O}$ , an increase in  $\lambda_O$  and  $\lambda_U$  and  $q_O$  becoming less negative for the  $\pi_u \rightarrow \pi_u^*$ ,  $\sigma_u \rightarrow \sigma_u^*$  and  $\pi_g \rightarrow \pi_g^*$  states and the reverse trends were seen in the  $\sigma_g \rightarrow \sigma_g^*$  excitation. At the excited state geometries, the same trends are seen in comparison to the ground state electronic structure at the ground state geometry, with the exception of  $\lambda_O$  decreasing in the  $\pi_g \rightarrow \pi_g^*$  state, which was reversed at the ground state geometries.

While the overall trends in the metrics remain constant to those at the ground state geometries (Table 3.3), the magnitude of the difference to the ground state electronic structure at the ground state geometry varies. For example, the redistribution of charge is accentuated, with enhanced electron localisation as might be expected at longer bond lengths.  $\lambda_U$  is substantial for the three lowest energy excited states and while this is accompanied by an increase in  $\lambda_O$  for the state involving MOs with U 5f character, commensurate with enhanced ionic character,  $\Delta^{\text{ES}}\lambda_O$  is negative (and substantially larger than that seen at the ground state geometry) in the  $\pi_g \rightarrow \pi_g^*$  state, indicative of enhanced charge transfer character to the excitation.

Figures 3.7, 3.8 and 3.9 summarise the  $q$ ,  $\lambda$  and  $\delta$  metrics at excited state electronic structures at both the ground and excited state and how they compare to the ground state electronic structure at the ground state geometry.

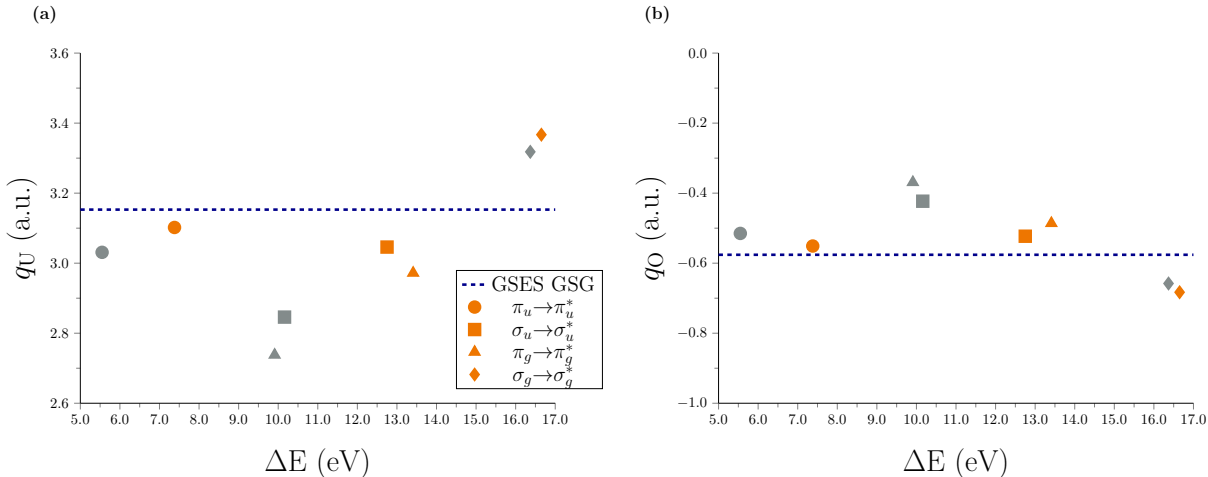


Figure 3.7: Graphs showing how (a)  $q_U$  and (b)  $q_O$  QTAIM metrics at the excited state electronic structures at both the ground (orange) and excited state (grey) geometries vary from  $q_U$  and  $q_O$  at ground state electronic structure at the ground state geometry (line).

Table 3.8 summarises the topological QTAIM parameters at the excited state electronic structure at the excited state geometries. In contrast to Table 3.4,  $\rho_{\text{BCP}}$  decreases and  $H$  increases at the excited state geometries, as would be expected for excitations into formally antibonding MOs. The trends in these variations correlate strongly with the increase in bond length, with the strength of this correlation

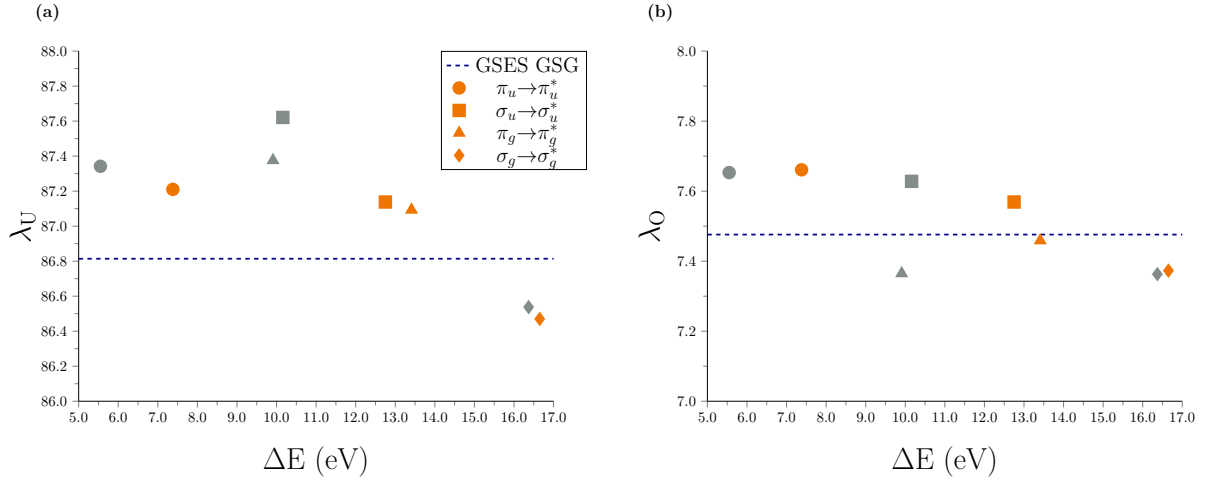


Figure 3.8: Graphs showing how (a)  $\lambda_U$  and (b)  $\lambda_O$  QTAIM metrics at the excited state electronic structures at both the ground (orange) and excited state (grey) geometries vary from  $\lambda_U$  and  $\lambda_O$  at ground state electronic structure at the ground state geometry (line).

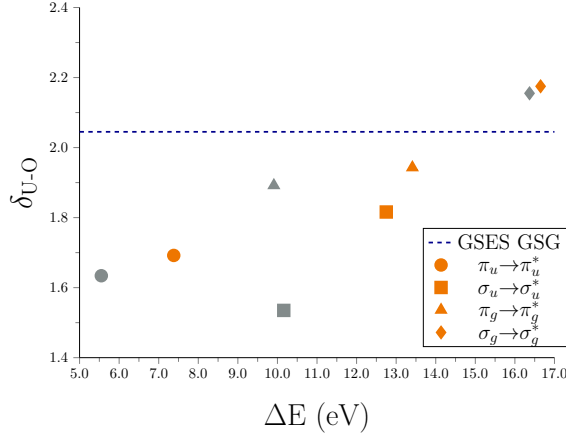


Figure 3.9: Graphs showing how  $\delta_{U-O}$  QTAIM metrics at the excited state electronic structures at both the ground (orange) and excited state (grey) geometries vary from  $\delta_{U-O}$  at ground state electronic structure at the ground state geometry (line).

meaning that further bond characterisation is not possible.

These data allow us to make further observations regarding  $\Lambda$  for the orbital excitations associated with each state. At the ground state geometry, it was deduced that for the  $\pi_g$  MO,  $\Lambda$  was strongly dependent on  $H_{ML}$  and relatively small. The  $\pi_g \rightarrow \pi_g^*$  state provides the largest values of both  $\Delta r$  and the Stokes shift. This state also has the largest redistribution of charge, opposing  $\lambda$  and a low variation in electron  $\delta$ . This provides further evidence that  $\Lambda$  is indeed significantly dependent on  $H_{ML}$  in the  $\pi_g$  MO and that there is a degree of charge transfer character in the excitation, particularly apparent when considering the electronic structure at the excited state minima. This latter point again supports the view of a small value of  $\Lambda$  in the  $\pi_g$  MO.

Table 3.8: Topological QTAIM (a.u.) parameters at the excited state electronic structures at the excited state geometries of the states of interest

Metric	$\pi_u \rightarrow \pi_u^*$	$\sigma_u \rightarrow \sigma_u^*$	$\pi_g \rightarrow \pi_g^*$	$\sigma_g \rightarrow \sigma_g^*$
$\rho_{\text{BCP}}$ (a.u.)	0.265	0.250	0.235	0.300
$\nabla^2 \rho_{\text{BCP}}$ (a.u.)	0.333	0.447	0.350	0.410
$H$ (a.u.)	-0.216	-0.188	-0.164	-0.283

The  $\pi_u \rightarrow \pi_u^*$  and  $\sigma_u \rightarrow \sigma_u^*$  excited state minima give similar, albeit enhanced, changes in QTAIM metrics to those found at the ground state geometry. The variation in  $\delta$  is largest in these two states and this, along with the small redistribution of charge, again supports the view that  $\Lambda$  is largest for the  $\pi_u$  and  $\sigma_u$  MOs. Since the excitation energies are lowest for these states, it can be tentatively suggested that  $H_{\text{ML}}$  is relatively small (although still substantial, as evidenced by the pronounced increase in bond lengths) and the large value of  $\Lambda$  is due to the interplay between  $H_{\text{ML}}$  and  $\Delta E_{\text{ML}}$ .

Finally the  $\sigma_g \rightarrow \sigma_g^*$  excited state minima gives very similar metrics to those at the ground state geometry, which is expected given the small change in geometry and excitation energy. Therefore, the analysis given at the ground state geometry is still holds at the excited state geometry.

### 3.3.4 The Optically Active Excited State

Previous computational studies [35, 37–39, 60] have determined that the lowest lying optically active excited state in uranyl can be primarily described as a triplet excitation from the  $\sigma_u$  into the non-bonding  $5f_\delta$  orbital, allowed via spin-orbit coupling. [35–39] This excitation was simulated using the same model chemistry as that employed for our studies of symmetry-preserving excitations, and a vertical excitation energy of 2.43 eV was calculated, in reasonable agreement with the CASPT2 literature value of 2.79 eV calculated in the absence of spin-orbit coupling [60] and our own CASSCF calculated value of 2.95 eV. Relaxation of the excited state geometry produced an increase in bond length to 1.747 Å, again in reasonable agreement with the CASPT2 literature value of 1.765 Å, and an excited state energy of 2.18 eV at the excited state minimum. QTAIM metrics at both the ground and excited state geometries are summarised in Table 3.9.

All QTAIM metrics report little to no change in electronic structure upon excitation into the U based  $5f_\delta$  orbital, which would only be expected if the  $\sigma_u$  MO were

Table 3.9: Comparison of the QTAIM metrics: charge ( $q$ ), localisation index ( $\lambda$ ), delocalisation index ( $\delta$ ),  $\rho_{\text{BCP}}$ ,  $\nabla^2\rho_{\text{BCP}}$  and  $H$  at the ground (GS) and excited (ES) state equilibrium geometries at the excited state electronic structure for the optically active  $\sigma_u \rightarrow \delta_u$  excitation

Metric	Geometry		Metric	Geometry	
	GS	ES		GS	ES
$q_{\text{U}}$ (a.u.)	3.150	3.031	$q_{\text{O}}$ (a.u.)	-0.575	-0.515
$\lambda_{\text{U}}$	26.747	27.342	$\lambda_{\text{O}}$	7.403	7.653
$\delta_{\text{U-O}}$	2.108	2.099	$H$ (a.u.)	-0.350	-0.278
$\rho_{\text{BCP}}$ (a.u.)	0.334	0.296	$\nabla^2\rho_{\text{BCP}}$ (a.u.)	0.511	0.488

also entirely localised on the U centre. Since the previous analysis in Sections 3.3.1 and 3.3.3 revealed this not to be the case, with the  $\sigma_u$  MO having substantial contributions from both U and O centres, these data can therefore be interpreted as showing a reorganisation amongst the other MOs to accommodate the charge localised in the  $5f_{\delta}$  orbital. Since this reorganisation must therefore involve charge transfer from the U centre, and noting that  $\delta_{\text{U-O}}$  increases upon excitation, it can be deduced that  $\lambda$  must increase amongst the other MOs, although it cannot be determined which specific MOs experience this increase.

### 3.4 Conclusions and Outlook

Electron-density based analyses of f-element complexes have grown in utility in recent years. [4, 5, 12, 15, 18, 61, 65] In this chapter, QTAIM analysis has been applied, for the first time, to probe the excited state electronic structure of an f-element complex. This analysis has been shown to characterise bond covalency in this compound, as well as its origins. Investigations of vertical excitations at the ground state geometry demonstrated an inverse relationship between the orbital mixing coefficient,  $\Lambda$ , and the excitation energy. Furthermore, it was found that, for MOs with U 5f character (*e.g.*  $\sigma_u$  and  $\pi_u$ ),  $\Lambda$  was more dependent on the metal-ligand Hamiltonian matrix element  $H_{\text{ML}}$ , whereas for those with U 6d character (*e.g.*  $\sigma_g$  and  $\pi_g$ ),  $\Lambda$  became increasingly dependent on the difference in fragment orbital energy levels,  $\Delta E_{\text{ML}}$ . Further analysis of the electronic structure showed that charge transfer from O to U reduced as the excitation energy increased, as did the degree of electron sharing between the two centres. The  $\sigma_g \rightarrow \sigma_g^*$  excited state often exhibited quantitatively different behaviour, and this was characterised as being due to a very low value of  $\Lambda$  in the  $\sigma_g$  MO and a difference in the dominant atomic contribution to

this MO, leading to significant redistribution of charge amongst the other orbitals in this state.

When considering the relaxed excited state geometries, a relationship between excitation energy and bond elongation was established. This was commensurate with the large magnitude of  $\Lambda$  and its dependence on  $H_{\text{ML}}$  for the  $\sigma_u$  and  $\pi_u$  MOs, however further analysis revealed that the large bond elongation associated with the  $\pi_g \rightarrow \pi_g^*$  state could be understood by also recognising enhanced charge transfer character in the excitation. The  $\sigma_g \rightarrow \sigma_g^*$  excitation was again an outlier, where the charge transfer character of the excitation was balanced by the redistribution of charge discussed above.

The dependence of  $\Lambda$  on  $H_{\text{ML}}$  for excitations involving 5f MOs has also been concluded in the literature, in particular for actinide halides. [12, 65] Tanti *et al.* [65] concluded that the 5f contributions to overlap-driven covalency were larger than 6d for a uranyl and uranium halide complexes. Similar findings were also observed across the actinide series by Clark and co-workers; [12] they further evaluate and suggest that as you traverse the actinides, “the positive effects from  $\Delta E_{\text{ML}}$  outweigh negative impacts from  $H_{\text{ML}}$  and covalency increases.” This contribution presents an expansion of these conclusions and suggests that these trends also extend into the excited state.

In contrast to the literature however, herein it is concluded that excitations involving the U5f MOs have a larger  $\Lambda$  than excitations involving U6d MOs. [61–63] This is largely due to the anticorrelation between  $\Lambda$  and excitation energy and the large  $\Lambda$  value is due to the interplay between  $H_{\text{ML}}$  and  $\Delta E_{\text{ML}}$ , which has also been indicated in the literature. [12]

The calculated ground state delocalisation indices were decomposed into their symmetry-distinct components. It would be expected that delocalisation indices would decrease with increasing bond length, but the  $\pi_u$  component exhibited the opposite behaviour, suggesting enhanced degeneracy-driven covalency with increasing bond length for this component.

Finally, the leading orbital contribution to the lowest energy optically accessible state in uranyl was investigated. QTAIM metrics revealed little difference between ground and excited state electronic structures, which could be interpreted in terms of the previously analysed states an increase in covalent character amongst the bonding MOs which offset the charge localisation due to excitation into the non-bonding U 5f<sub>j</sub> orbital.

This chapter has demonstrated that analysis of excited state electronic structures can be used to characterise properties of the ground state that would be otherwise challenging to access. Future studies will apply these techniques to more complicated f-element systems to better understand the relative contribution of overlap- and degeneracy-driven covalency to bonding in these compounds. The following chapters

will utilise the same methodology to simple linear complexes of uranyl and uranyl complexes in which the uranyl unit is significantly bent.

# References

- [1] A. Formanuk, A. M. Ariciu, F. Ortu, R. Beekmeyer, A. Kerridge, F. Tuna, E. J. McInnes, D. P. Mills, *Nat. Chem.* **2017**, *9*, 578–583.
- [2] L. R. Morss, N. Edelstein, J. Fuger, J. J. Katz, *The Chemistry of the Actinide and Transactinide Elements*, 4th, Springer, **2010**.
- [3] L. S. Natrajan, M. H. Paden, *f-block elements recovery*, Vol. 58, **2013**, pp. 140–184.
- [4] P. Di Pietro, A. Kerridge, *Inorg. Chem.* **2016**, *55*, 573–583.
- [5] P. Di Pietro, A. Kerridge, *Phys. Chem. Chem. Phys.* **2016**, *18*, 16830–16839.
- [6] H. H. Dam, D. N. Reinhoudt, W. Verboom, *Chem. Soc. Rev.* **2007**, *36*, 367–377.
- [7] F. W. Lewis, M. J. Hudson, L. M. Harwood, *Synlett* **2011**, *18*, 2609–2632.
- [8] W. Heitler, F. London, *Eur. Phys. J. A.* **1927**, *6-7*, 455–472.
- [9] J. L. Krinsky, S. G. Minasian, J. Arnold, *Inorg. Chem.* **2011**, *50*, 345–357.
- [10] F. Cotton, *Chemical Applications of Group Theory*, 3rd, John Wiley & Sons: New York, **2004**.
- [11] K. N. Raymond, C. W. Eigenbrot, *Acc. Chem. Res.* **1980**, *13*, 276–283.
- [12] J. Su, E. R. Batista, K. S. Boland, S. E. Bone, J. A. Bradley, S. K. Cary, D. L. Clark, S. D. Conradson, A. S. Ditter, N. Kaltsoyannis, J. M. Keith, A. Kerridge, S. A. Kozimor, M. W. Löble, R. L. Martin, S. G. Minasian, V. Mocko, H. S. La Pierre, G. T. Seidler, D. K. Shuh, M. P. Wilkerson, L. E. Wolfsberg, P. Yang, *J. Am. Chem. Soc.* **2018**, *140*, 17977–17984.
- [13] R. M. Diamond, K. Street, G. T. Seaborg, *J. Am. Chem. Soc.* **1954**, *76*, 1461–1469.
- [14] S. G. Minasian, J. M. Keith, E. R. Batista, K. S. Boland, D. L. Clark, S. D. Conradson, S. A. Kozimor, R. L. Martin, D. E. Schwarz, D. K. Shuh, G. L. Wagner, M. P. Wilkerson, L. E. Wolfsberg, P. Yang, *J. Am. Chem. Soc.* **2012**, *134*, 5586–5597.
- [15] A. Kerridge, *Chem. Commun.* **2017**, *53*, 6685–6695.

- [16] M. Dolg, *Encyclopedia of Computational Chemistry*, (Ed.: E. H. F. Schaefer), Wiley, Chichester, **2002**.
- [17] M. Seth, P. Schwerdtfeger, M. Dolg, P. Fulde, *J. Am. Chem. Soc.* **1995**, *117*, 6597–6598.
- [18] R. Beekmeyer, A. Kerridge, *Inorganics* **2015**, *3*, 482–499.
- [19] M. Dolg, P. Fulde, W. Kuchle, C. S. Neumann, H. Stoll, *J. Chem. Phys.* **1991**, *94*, 3011–3017.
- [20] A. Kerridge, R. Coates, N. Kaltsoyannis, *J. Phys. Chem. A.* **2009**, *113*, 2896–2905.
- [21] A. Kerridge, *Dalton Trans.* **2013**, *42*, 16428–16436.
- [22] O. Mooßen, M. Dolg, *Chem. Phys. Lett.* **2014**, *594*, 47–50.
- [23] V. Vallet, U. Wahlgren, I. Grenthe, *J. Phys. Chem. A.* **2012**, *116*, 12373–12380.
- [24] R. F. Bader, *Atoms in Molecules: A Quantum Theory*, Oxford University Press: Oxford, **1990**.
- [25] I. Kirker, N. Kaltsoyannis, *Dalton Trans.* **2011**, *40*, 124–131.
- [26] M. J. Tassell, N. Kaltsoyannis, *Dalton Trans.* **2010**, *39*, 6576–6588.
- [27] P. L. Arnold, Z. R. Turner, N. Kaltsoyannis, P. Pelekanaki, R. M. Bellabarba, R. P. Tooze, *Chem. Eur. J.* **2010**, *16*, 9623–9629.
- [28] V. V. Zhurov, E. A. Zhurova, A. I. Stash, A. A. Pinkerton, *J. Phys. Chem. A.* **2011**, *115*, 13016–13023.
- [29] M. B. Jones, A. J. Gaunt, *Chem. Rev.* **2013**, *113*, 1137–1198.
- [30] A. C. Behrle, C. L. Barnes, N. Kaltsoyannis, J. R. Walensky, *Inorg. Chem.* **2013**, *52*, 10623–10631.
- [31] S. Wu, P. M. Kowalski, N. Yu, T. Malcherek, W. Depmeier, D. Bosbach, S. Wang, E. V. Suleimanov, T. E. Albrecht-Schmitt, E. V. Alekseev, *Inorg. Chem.* **2014**, *53*, 7650–7660.
- [32] A. Kerridge, *RSC Adv.* **2014**, *4*, 12078–12086.
- [33] Q. R. Huang, J. R. Kingham, N. Kaltsoyannis, *Dalton Trans.* **2015**, *44*, 2554–2566.
- [34] S. M. Mansell, N. Kaltsoyannis, P. L. Arnold, *J. Am. Chem. Soc.* **2011**, *133*, 9036–9051.
- [35] K. Pierloot, E. Van Besien, E. Van Lenthe, E. J. Baerends, *J. Chem. Phys.* **2007**, *126*.
- [36] L. Gagliardi, B. O. Roos, P.-Å. Malmqvist, J. M. Dyke, *J. Phys. Chem. A.* **2001**, *105*, 10602–10606.

- [37] P. Tecmer, A. S. P. Gomes, U. Ekström, L. Visscher, *Phys. Chem. Chem. Phys.* **2011**, *13*, 6249–6259.
- [38] P. Tecmer, R. Bast, K. Ruud, L. Visscher, *J. Phys. Chem. A* **2012**, *116*, 7397–7404.
- [39] P. Tecmer, N. Govind, K. Kowalski, W. A. De Jong, L. Visscher, *J. Chem. Phys.* **2013**, *139*.
- [40] R. Ahlrichs, M. Bär, M. Häser, H. Horn, C. Kölmel, *Chem. Phys. Lett.* **1989**, *162*, 165–169.
- [41] M. J. Frisch, G. W. Trucks, H. B. Schlegel, G. E. S. an M. A. Robb, J. R. Cheeseman, J. A. J. Montgomery, T. Vreven, K. N. Kudin, J. C. Burant, J. M. Millam, S. S. Iyengar, J. Tomasi, V. Barone, B. Mennucci, M. Cossi, G. Scalmani, N. Rega, G. A. Petersson, H. Nakatsuji, M. Hada, M. Ehara, K. Toyota, R. Fukuda, J. Hasegawa, M. Ishida, T. Nakajima, Y. Honda, O. Kitao, H. Nakai, M. Klene, X. Li, J. E. Knox, H. P. Hratchian, J. B. Cross, V. Bakken, C. Adamo, J. Jaramillo, R. Gomperts, R. E. Stratmann, O. Yazyez, A. J. Austin, R. Cammi, C. Pomelli, J. W. Ochterski, P. Y. Ayala, K. Morokuma, G. A. Voth, P. Salvador, J. J. Dannenberg, V. G. Zakrzewski, S. Dapprich, A. D. Daniels, M. C. Strain, O. Farkas, D. K. Malick, A. D. Rabuck, K. Raghavachari, J. B. Foresmann, J. V. Ortiz, Q. Cui, A. G. Baboul, S. Clifford, J. Cioslowski, B. B. Stefanov, G. Liu, A. Liashenko, P. Piskorz, I. Komaromi, R. L. Martin, D. J. Fox, T. Keith, M. A. Al.Laham, C. Y. Peng, A. Nanayakkara, M. Challacombe, P. M. W. Gill, B. Johnson, W. Chen, M. W. Wong, C. Gonzalez, J. A. Pople, *Gaussian 09. 2015 Gaussian Inc. Wallingford CT*.
- [42] B. Miehlich, A. Savin, H. Stoll, H. Preuss, *Chem. Phys. Lett.* **1989**, *157*, 200–206.
- [43] C. Lee, W. Yang, R. G. Parr, *Phys. Rev. B* **1988**, *37*, 785–789.
- [44] A. D. Becke, *J. Chem. Phys.* **1993**, *98*, 1372–1377.
- [45] A. D. Becke, *Phys. Rev. A* **1988**, *38*, 3098–3100.
- [46] R. Krishnan, J. S. Binkley, R. Seeger, J. A. Pople, *J. Chem. Phys.* **1980**, *72*, 650–654.
- [47] T. H. J. Dunning, *J. Chem. Phys.* **1989**, *90*, 1007–1023.
- [48] R. A. Kendall, T. H. J. Dunning, R. J. Harrison, *J. Chem. Phys.* **1992**, *96*, 6796–6806.
- [49] D. E. Woon, T. H. J. Dunning, *J. Chem. Phys.* **1993**, *98*, 1358–1371.
- [50] W. Küchle, M. Dolg, H. Stoll, H. Preuss, *J. Chem. Phys.* **1994**, *100*, 7535–7542.

- [51] X. Cao, M. Dolg, H. Stoll, *J. Chem. Phys.* **2003**, *118*, 487–496.
- [52] X. Cao, M. Dolg, *J. Mol. Struct-THEOCHEM* **2004**, *673*, 203–209.
- [53] S. Hirata, M. Head-Gordon, *Chem. Phys. Lett.* **1999**, *314*, 291–299.
- [54] E. Runge, E. K. U. Gross, *Phys. Rev. Lett.* **1984**, *53*, 997–1000.
- [55] E. K. U. Gross, W. Kohn in *Density Functional Theory of many-fermion systems*, (Ed.: P.-O. Löwdin), **1990**, pp. 255–291.
- [56] T. A. Keith, AIMAll, **2014**.
- [57] T. Lu, F. Chen, *J. Comput. Chem.* **2012**, *33*, 580–592.
- [58] F. Real, A. S. P. Gomes, L. Visscher, V. Vallete, E. Eliav, *J. Phys. Chem. A.* **2009**, *113*, 12504–12511.
- [59] F. Wei, G. Wu, W. H. Schwarz, J. Li, *Theor. Chem. Acc.* **2011**, *129*, 467–481.
- [60] K. Pierloot, E. Van Besien, *J. Chem. Phys.* **2005**, *123*.
- [61] N. Kaltsoyannis, *Inorg. Chem.* **2013**, *52*, 3407–3413.
- [62] M. Pepper, B. E. Bursten, *Chem. Rev.* **1991**, *91*, 719–741.
- [63] H. M. Crosswhite, H. Crosswhite, W. T. Carnall, A. P. Paszek, *J. Chem. Phys.* **1980**, *72*.
- [64] X. Fradera, M. A. Austen, R. F. Bader, *J. Phys.Chem. A.* **1999**, *103*, 304–314.
- [65] J. Tanti, M. Lincoln, A. Kerridge, *Inorganics* **2018**, *6*, 88.
- [66] I. Fryer-Kanssen, A. Kerridge, *Chem. Commun.* **2018**, *54*, 9761–9764.

## Chapter 4

# Exploring covalency in uranyl complexes with a variety of equatorial ligands

*In this chapter, the effect of equatorial ligation on the electronic structure and bonding of simple uranyl complexes is studied. Building on the investigation of  $[UO_2]^{2+}$  in Chapter 3, the  $\sigma_u \rightarrow \delta_u$  excitation is investigated at both the ground and electronically excited states of these complexes. At the ground state geometries, variation in the excitation energies were attributed to the relative stabilisation/destabilisation of the hole/particle MOs. It was found that in the ground state the QTAIM metrics for complexes with soft donor atoms, such as sulfur, had the biggest deviations from those of  $[UO_2]^{2+}$ , obtained in the previous chapter (Chapter 3). In contrast, complexes which comprised of bidentate oxygen coordination resulted in the smallest deviations from  $[UO_2]^{2+}$ . In agreement with previous studies it was concluded that upon coordination to the equatorial plane, the delocalisation in the uranyl bond ( $\delta_{U-O_{yl}}$ ) decreases, resulting in an increase in localisation of charge on the uranyl oxygens ( $O_{yl}$ ). At the excited state geometries the U- $O_{yl}$  and U-L bond lengths increase slightly and the excitation energy is red-shifted. Interestingly, at the excited state geometries  $\delta_{U-O_{yl}}$  increased for some complexes, as was seen in  $[UO_2]^{2+}$ , but decreased in others. This decrease in  $\delta_{U-O_{yl}}$  was attributed to the increase in the delocalisation index between the uranium and equatorial ligand. This work highlights the need to explore the excited state geometries with QTAIM analysis as excitations in complexes which appear to be similar at the ground state geometries have comparatively different properties at the excited state geometries.*

## 4.1 Introduction

The insight gained from the study of free uranyl ( $[\text{UO}_2]^{2+}$ ) in Chapter 3 provides a foundation to interpret the electronic structure of uranyl coordination complexes. Hence, this provides enlightenment into how the covalency in uranyl changes upon equatorial ligation. Variation in the bonding character of actinide complexes has important applications both fundamentally and practically. [1–3] From a fundamental perspective, understanding the bonding interactions within actinide complexes aids in the assessment of the viability of novel synthetic complexes, [4, 5] and from a practical perspective, variation in the bonding character is of particular importance for spent fuel reprocessing in the nuclear power industry. [6, 7] In comparison to the later actinides, (more prevalent in terms of spent fuel reprocessing), the covalent interactions in uranyl complexes is expected to be more pronounced as covalency decreases across the actinide series [8, 9] and hence uranyl is a good starting point to investigate the covalency.

Chapter 3 focused on the covalency of free uranyl via exploration of excitations which maintain symmetry of the electronic wavefunction at both the ground and electronically excited state geometries. This chapter applies the same methodology to simple uranyl complexes (Figure 4.1); unlike the previous chapter however, where multiple excitations were investigated, this chapter solely focuses on the optically allowed excitation of principally  $\sigma_u \rightarrow \delta_u$  triplet character. Herein the effect of equatorial ligation on the electronic structure of the uranyl unit at both the ground and electronically excited state geometries is investigated.

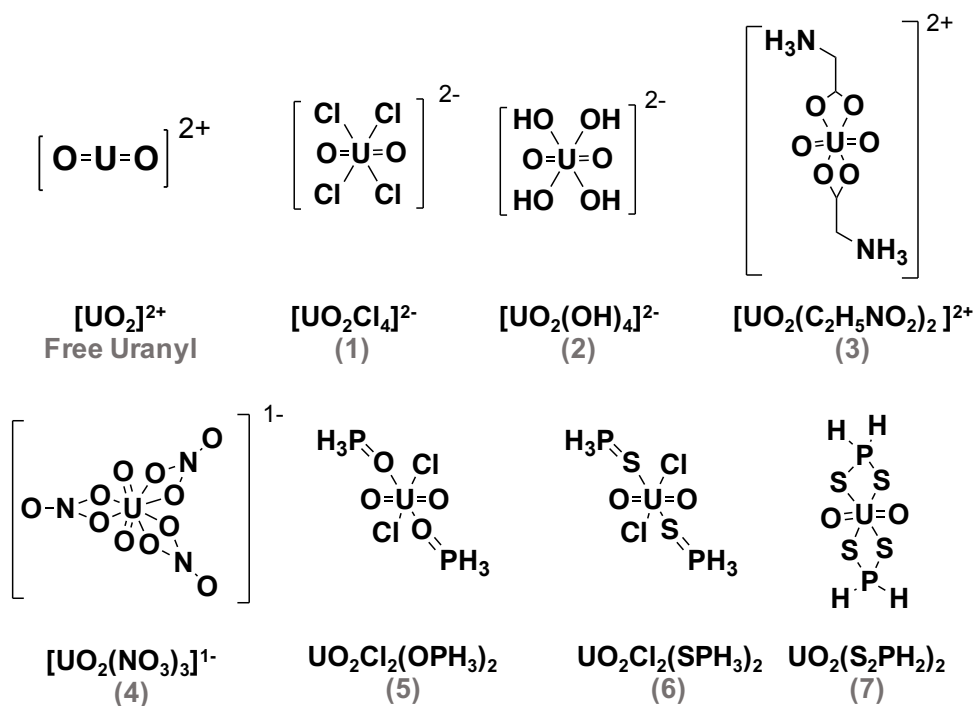


Figure 4.1: Uranyl complexes studied in this chapter

All complexes, with the exception of (6), have been synthesised and their absorption and/or emission spectra studied in the literature. [10–15] Complex (1) is perhaps the most commonly studied uranyl complex in the literature, [10, 16–20] whilst (2) has been previously studied with density-based analyses at the ground state. [4] These complexes were selected to ensure a range of different ligand coordination type with monodentate and bidentate coordination. These complexes are mainly focused on oxygen coordination with different ligands, giving a range of overall charges to the complex. Sulfur coordination is also studied to give a soft donor contrast to the hard withdrawing oxygen ligand nature.

Previous work reports weakening in the U-O<sub>yl</sub> bond upon equatorial ligation for a number of different complexes. [4, 5, 21, 22] Ingram *et. al* [22] systematically substituted water for hydroxide ligands in a uranyl pentahydrate complex ([UO<sub>2</sub>(H<sub>2</sub>O)<sub>5</sub>]<sup>2+</sup>) and investigated the effect of this on the electronic structure and bonding of the complex. They found that the U-O<sub>yl</sub> bond strength decreased as the neutral  $\sigma$ -donor water ligand was replaced by the negatively charged  $\pi$ -donor hydroxide ligands. This was attributed to a reduction in the ionic character caused by the electron charge build up on the uranium centre. Tsushima [21] later contradicted this via use of molecular orbital analysis on a number of different uranyl complexes. This study indicated that the U-O<sub>yl</sub> bond is weakened by  $\sigma$  and/or  $\pi$  contributions from the coordinating ligands as they compete with the uranyl oxygen over the U 5f, 6p or 6d orbitals. These contrasting conclusions highlight the necessity for density-based analysis as DFT is known to produce ambiguous orbital-based descriptions of strongly correlated systems. [23–28] Most relevant to this investigation is the work by DiPietro and Kerridge [4] in which they investigate the covalency in uranyl complexes with first row monodentate equatorial ligands with analysis from the (experimentally observable) electron density. They found that as the equatorial bond strength increased, density was transferred from the U-O<sub>yl</sub> bonding region to the uranyl oxygens and to the equatorial bonding region.

Switching the focus to excited state investigations, there have been numerous studies; both theoretically and experimentally on the low-lying excitations of uranyl complexes. [14–16, 18, 19, 29–36] Denning [17, 31] conducted spectroscopic studies on crystalline CsUO<sub>2</sub>Cl<sub>4</sub> and CsUO<sub>2</sub>(NO<sub>3</sub>)<sub>3</sub> and found that the low-lying excitation energies were similar between the two complexes. This trend was also found theoretically by Matsika and Pitzer [19] and Zhang and Pitzer [33], who compared the spectra of free uranyl, uranyl chloride and uranyl nitrate using relativistic core and spin-orbit potentials and multireference graphical unitary group approach configuration interaction as implemented in the COLUMBUS suite of programs. They found that the addition of equatorial ligands had minimal effect on the low-lying excitation energies; 2.66 eV, 2.65 eV and 2.69 eV, for free uranyl, uranyl chloride and uranyl nitrate respectively. These observations suggest that the presence/nature of

weakly bound equatorial ligands has little effect on the low-lying excitations. [18]

As in the previous chapter, QTAIM analysis is utilised to rationalise trends in covalency in both the ground and electronically excited states. This chapter will be split into two results sections; one for each geometry (ground and electronic excited state). At the ground state geometry the focus will be primarily on the effect of equatorial ligation on the electronic structure and bonding of the uranyl unit and how this compares to that in free uranyl. In the previous chapter, it was found that there was little change in the QTAIM metrics in the excited state electronic structures at the ground state geometries and hence in the following chapters excited state analysis is only performed and discussed at the corresponding excited state geometries. At the electronically excited state geometries, the trends in covalency will be analysed for the different complexes for the optically allowed excitation with dominant  $\sigma_u \rightarrow \delta_u$  character. Comparisons will then be made between the ground state electronic structure at the ground state geometry and the excited state electronic structure at the electronically excited state geometry ( $\Delta^{\text{ES}}$  in Figure 4.2).

## 4.2 Computational Details

All simulations were performed at the hybrid DFT level, using the B3LYP [37–41] exchange–correlation functional in the Gaussian09 (Revision E.01) programme. [42] The Stuttgart RSC 1997 [43–45] basis set and associated small effective core potential (60 electrons), acquired from the basis-set exchange [46–48] was used for uranium while the correlation consistent aug-cc-pVDZ [49–51] Dunning basis set was implemented for the light elements (H, C, N, O, P, S, Cl). Geometry optimisations at both ground and excited state geometries are characterised as minima by vibrational frequency analysis. The Tamm–Dancoff Approximation (TDA) [52] to Time Dependent-DFT [53, 54] was used to calculate electronic excitations at both the ground and excited state geometries. QTAIM analysis was conducted using version 19.02.12 of AIMAll [55] and density difference plots were generated using version 3.6 of Multiwfn. [56]

## 4.3 Results and Discussion

The complexes studied in this investigation (Figure 4.1), have all been studied experimentally, with the exception of (6), which is included in order to have a link between (5) and (7). It is also worth noting that the experimental equivalents of (5) and (7) have phenyl groups in place of the hydrogens; these were truncated to save computational expense and justified by initial studies where one phenyl group was substituted resulted in an insignificant differences to the geometry and excitation energies.

Throughout this chapter, comparisons will be made between the complexes and

the ligands. As some complexes have two different ligand types, the ligands are split into neutral -  $L^0$ : ( $\text{OPH}_3$ ,  $\text{SPH}_2$  and  $\text{C}_2\text{H}_5\text{NO}_2$ ) and negatively charged -  $L^-$ : ( $\text{Cl}$ ,  $\text{OH}$ ,  $\text{NO}_3$  and  $\text{S}_2\text{PH}_2$ ) for the geometric and integrated QTAIM properties.

### 4.3.1 Ground State Geometries

Table 4.1 compares the uranium-ligand ( $\text{U-O}_{\text{yl}}$ ,  $\text{U-L}^0$  and  $\text{U-L}^-$ ) bond lengths of the uranyl complexes calculated in this study to the experimental literature.

Table 4.1: Uranyl Complex average bond lengths calculated in this study (DFT) vs the experimental literature (Exp)

Complex	$\text{U-O}_{\text{yl}}$ (Å)		$\text{U-L}^0$ (Å)		$\text{U-L}^-$ (Å)	
	DFT	Exp	DFT	Exp	DFT	Exp
(1) $[\text{UO}_2\text{Cl}_4]^{2-}$ [10]	1.78	1.77	/	/	2.76	2.68
(2) $[\text{UO}_2(\text{OH})_4]^{2-}$ [11]	1.81	1.82	/	/	2.31	2.26
(3) $[\text{UO}_2(\text{C}_2\text{H}_5\text{NO}_2)_2]^{2+}$ [12]	1.75	1.77	2.46	2.53	/	/
(4) $[\text{UO}_2(\text{NO}_3)_2]^{1-}$ [13]	1.77	1.78	/	/	2.51	2.47
(5) $\text{UO}_2\text{Cl}_2(\text{OPH}_3)_2^\dagger$ [14]	1.77	1.75	2.41	2.31	2.69	2.65
(6) $\text{UO}_2\text{Cl}_2(\text{SPH}_3)_2^*$	1.78	/	2.93	/	2.65	/
(7) $\text{UO}_2(\text{S}_2\text{PH}_2)_2$ [15]	1.76	1.75	/	/	2.89	2.86

<sup>†</sup> Structure truncated from experiment    \* Non-existent in experimental literature

Upon complexation the  $\text{U-O}_{\text{yl}}$  bond elongates (1.70 Å in free uranyl); the largest of which occurs in the complexes with an overall negative charge ((1) and (2)). Despite most of the complexes comprising of oxygen coordination, there is quite a variation in the U-O bond lengths. This is due to the different ligand environment the oxygen is in, *i.e.* the bidentate ligands have larger U-O bond length than the monodentate ligands. There is good agreement between the DFT and experimental results, with the bigger discrepancies being between the uranium-ligand bond lengths. The difference between the DFT and experimental bond lengths are more prominent in the neutral U-O/S compared with the negatively charged U-O/S; while for the U-Cl bonds the discrepancy is larger for the negatively charged complex ((1)) than the neutral complex ((5)).

Figure 4.2 represents the four lowest-lying excitations in free uranyl and uranyl complexes. In free uranyl, these excitations involve transitions from the  $\sigma_u$  bonding MO to either of the non-bonding  $\delta_u$  and  $\phi_u$  MOs. These non-bonding MOs are degenerate pairs in free uranyl and hence the excitation to each non-bonding MO is degenerate. As the symmetry decreases, *i.e.* upon complexation, the non-bonding MOs are no longer degenerate, however, for each complex the four lowest energy virtual orbitals have similar characteristics to the non-bonding MOs of free uranyl. As the MOs of the uranyl complexes are qualitatively similar to those in free uranyl

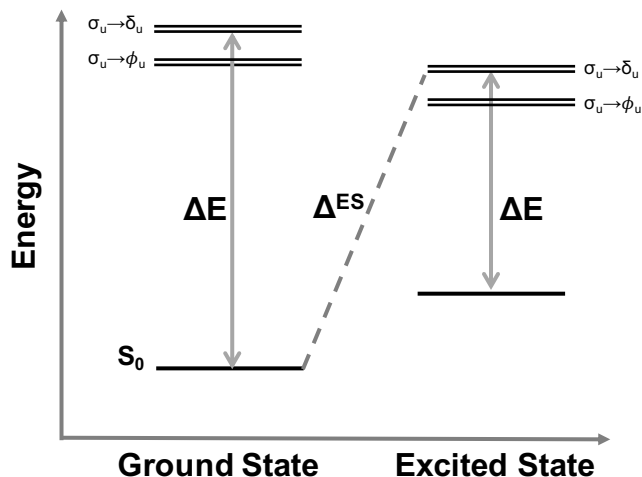


Figure 4.2: A schematic of the 4 lowest-lying excitations in uranyl complexes.  $\Delta E$  is the excitation energy, in this case for the  $\sigma_u \rightarrow \delta_u$  excitation.  $\Delta^{\text{ES}}$  compares the excited state electronic structure at the excited state geometry to the ground state electronic structure at the ground state geometry, this will be the comparison made in Section 4.3.2

(Figure 4.3), for convenience the same nomenclature will be used for the MOs of the complexes *i.e.*  $\delta_u$ . This study only focuses on the optically accessible  $\sigma_u \rightarrow \delta_u$  excitation, which was also investigated in free uranyl in Chapter 3. It is worth noting that the positions of these excitations vary across the complexes depending on the stabilisation/destabilisation of the particle MO.

It was also found that equatorial ligation resulted in two bonding MOs which have  $\sigma_u$  nature; arising from the bonding and anti-bonding interactions between the uranium centre and the coordinating ligands;  $\sigma_u^+$  for bonding and  $\sigma_u^-$  for anti-bonding as shown in Figure 4.3. The  $\sigma_u^-$  MO is less stable than the  $\sigma_u^+$  and in general has the larger contribution to the excitation. Complexes (2) and (3) only contain a single MO of  $\sigma_u$  nature; the MO in (2) is  $\sigma_u^+$  in nature, whereas for the particle MO in (3) the electron density of the MO is concentrated solely on the uranyl unit, as in free uranyl.

As with the geometric properties, the excitation energies ( $\Delta E$ ) at the ground state geometries can be compared to the absorption energies from experimental literature. In general, there is good agreement between the DFT and experimental excitation energies with most DFT values being an underestimation of the experimental values. However, it is worth noting that these calculations are done in the absence of spin-orbit coupling (SOC) and so it would not be expected that these results would match the experiment. In Chapter 5, SOC calculations were conducted on free uranyl and this resulted in the excitation energies being red-shifted by 0.3 eV. Assuming the effect of SOC is consistent across the uranyl complexes, then the calculated values, in the presence of SOC would have less agreement with experiment and therefore it is perhaps serendipitous that the DFT values are in close

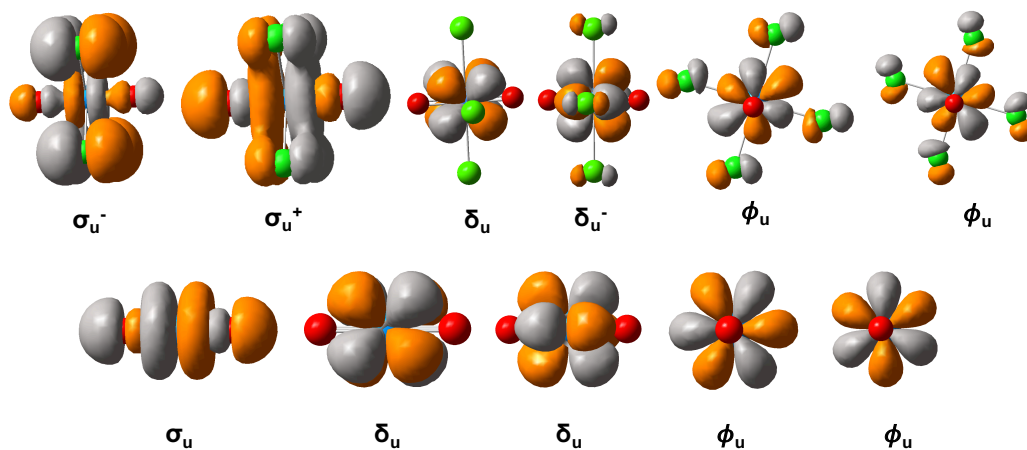


Figure 4.3: Comparison of the MOs of free uranyl and complex (1) which are involved in excitations depicted in Figure 3.1.  $\sigma_u^+$  and  $\sigma_u^-$  represent the  $\sigma_u$  MOs which are a result of either bonding or anti-bonding interactions between the uranium centre and the coordinating chloride ligands respectively.

agreement with the experimental results.

Table 4.2: Uranyl Complex excitation energies ( $\Delta E$ ) for the excitation of interest; comparison of calculated DFT values to experimental absorption energies (Exp)

Complex	DFT $\Delta E$ (eV)	Exp $\Delta E$ (eV)
(Free Uranyl) $[\text{UO}_2]^{2+}$	2.43	/
(1) $[\text{UO}_2\text{Cl}_4]^{2-}$ [16, 19, 20]	2.51/2.59	2.49
(2) $[\text{UO}_2(\text{OH})_4]^{2-}$	2.72/2.86	/
(3) $[\text{UO}_2(\text{C}_2\text{H}_5\text{NO}_2)_2]^{2+}$ [32]	2.63/2.72	2.69*
(4) $\text{UO}_2(\text{NO}_3)_3]^{1-}$ [13, 57]	2.72 <sup>†</sup>	2.69
(5) $\text{UO}_2\text{Cl}_2(\text{OPH}_3)_2$ [14]	2.45/2.55	2.82
(6) $\text{UO}_2\text{Cl}_2(\text{SPH}_3)_2$	2.48/3.76	/
(7) $\text{UO}_2(\text{S}_2\text{PH}_2)_2$ [15]	3.34/3.43	3.10/4.05

\* DFT literature value

<sup>†</sup> Same excitation energy to 2 d.p.

Upon complexation, the nature of the excited states changes in comparison to free uranyl; most of the excitations consist of two  $\sigma_u \rightarrow \delta_u$  contributions, from both  $\sigma_u^-$  and  $\sigma_u^+$  MOs. These two contributions sum to give  $> 90\%$  overall  $\sigma_u \rightarrow \delta_u$  contribution to the excitation, with the exception of (6), which has significantly lower total  $\sigma_u \rightarrow \delta_u$  contribution. As mentioned previously, complexes (2) and (3) have only a single MO of  $\sigma_u$  nature and hence in these complexes the excitation consists of a single contribution of  $\sim 90\%$ . Complexes (1) and (5) have roughly equal contributions from both transitions ( $\sim 55\%$  and  $\sim 45\%$ ), whereas in complexes (4) and (7) these contributions are weighted  $\sim 70\%$  and  $\sim 25\%$ .

Complex (6) has many differences to the other complexes. Firstly, the four lowest-lying virtual MOs, shown in Figure 4.4 have considerably more  $\phi_u/\delta_u$  mixing than in the other complexes, this results in three similar MOs of mostly  $\phi_u$  nature (MOs 76, 78 and 79) and one MO which has some  $\delta_u$  (MO 77) nature. Second, the excitations which involve transitions of interest occur at largely different energies, with both of these excitations having considerably lower  $\sigma_u \rightarrow \delta_u$  contributions (43 % and 57 %) in comparison to the other complexes. Unlike complex (7), the lower energy excitation comprises of roughly equal contributions from transitions involving both  $\sigma_u$  MOs but unlike the other complexes, this excitation also has contributions from  $\sigma_u \rightarrow \phi_u$  transition (MO 76), (again equal contributions from both  $\sigma_u$  MOs). The higher energy excitation is more similar to (7) as the contribution from  $\sigma_u^+$  is larger than the contribution from  $\sigma_u^-$  (38 % vs 19 %), however this excitation also consists of a transition from a MO which has electron density focused in the equatorial ligands rather than on the uranyl unit to the  $\delta_u$  MO.

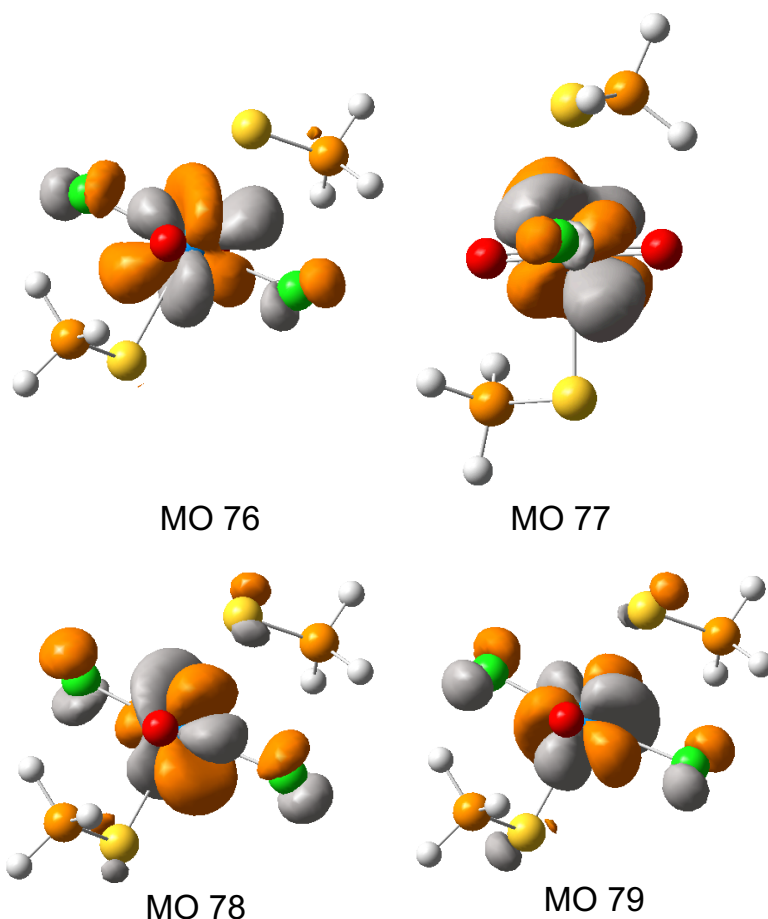


Figure 4.4: The four lowest-lying virtual MOs of complex (6); MOs 76, 78 and 79 have mostly  $\phi_u$  nature and MO 77 showing some  $\delta_u$  nature.

The excitation energy in the complexes is blue shifted in comparison to the free uranyl, with the largest shifts seen in the sulfur complexes. The excitation energies for all complexes, except those containing sulfur, have small increases in excitation energy as predicted by the literature. [17–19, 31, 33] In a one electron example, an

increase in excitation energy would be expected to be mirrored by a stabilisation of the hole MO ( $\sigma_u$ ) and/or destabilisation of the particle MO ( $\delta_u$ ). In every complex, with the exception of (6), there are two distinctive  $\delta_u$  MOs, with the lower energy  $\delta_u$  MO ( $\delta_u$  in Figure 4.3) being non-bonding in nature with nodes along the U-ligand bond, whereas the higher energy  $\delta_u$  MO ( $\delta_u^-$  in Figure 4.3) is destabilised by antibonding interactions between the uranium 6d and equatorial p orbitals.

The excitation energies can be rationalised by investigation of the nature of the particle/hole MOs. Complex (7) has the largest excitation energies; in which the stabilised  $\sigma_u^+$  MO has a significantly larger contribution (70 %) to the excitation than the destabilised  $\sigma_u^-$  MO. This behaviour is also seen in the higher energy excitation in (6). The lowest excitation energies are found in complexes (1) and (5), where the contribution from the destabilised  $\sigma_u^-$  MO is slightly larger than the  $\sigma_u^+$  MO. Complexes (2) and (3) have slightly higher excitation energies than complexes (1) and (5); in these complexes only a single  $\sigma_u$  MO is present which could be more stabilised than the  $\sigma_u^-$  MO due to the absence of antibonding. Complex (4) is interesting as it has two excitations which are nearly degenerate in energy; the main reason for this that the two  $\delta_u$  MOs are related by a 45° rotation (Figure 4.5). The excitation energy is higher than some of the complexes despite the  $\sigma_u^-$  MOs having a significantly larger contribution (70 %) to the excitation than the  $\sigma_u^+$  MO. A contributing factor to this increase in excitation energy could be due to both the  $\delta_u$  MOs having antibonding character between the uranium 6d and nitrate 2p orbitals.

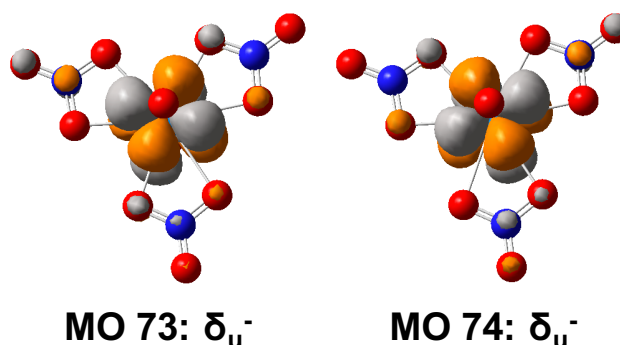


Figure 4.5: MO 73 and 74 in complex (4) which are related by a 45° rotation and both have some antibonding character between the uranium 6d and nitrate 2p orbitals

Density difference plots were generated and can be used to compare the two different  $\sigma_u \rightarrow \delta_u$  excitations in the complexes to each other. As mentioned previously, in free uranyl the two excitations of  $\sigma_u \rightarrow \delta_u$  character are degenerate and correspond to excitations  $T_3$  and  $T_4$ . Despite the excitation energies and character being degenerate, the density difference plots for  $T_3$  and  $T_4$  have different natures (Figure 4.6). It was found that most complexes had at least one excitation which displayed similar characteristics in the density difference plots to  $T_3$  of free uranyl, with (2) being the exception having density differences similar to  $T_4$  of free uranyl.

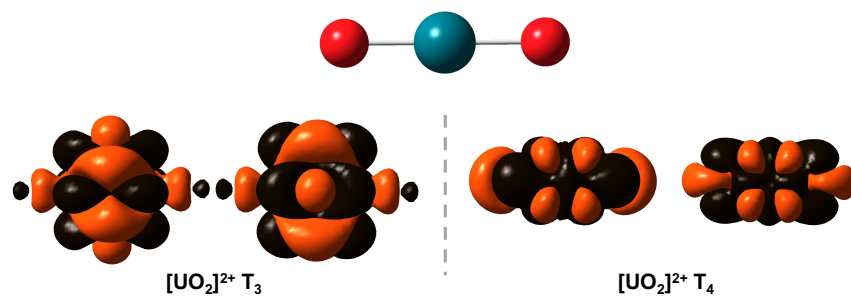
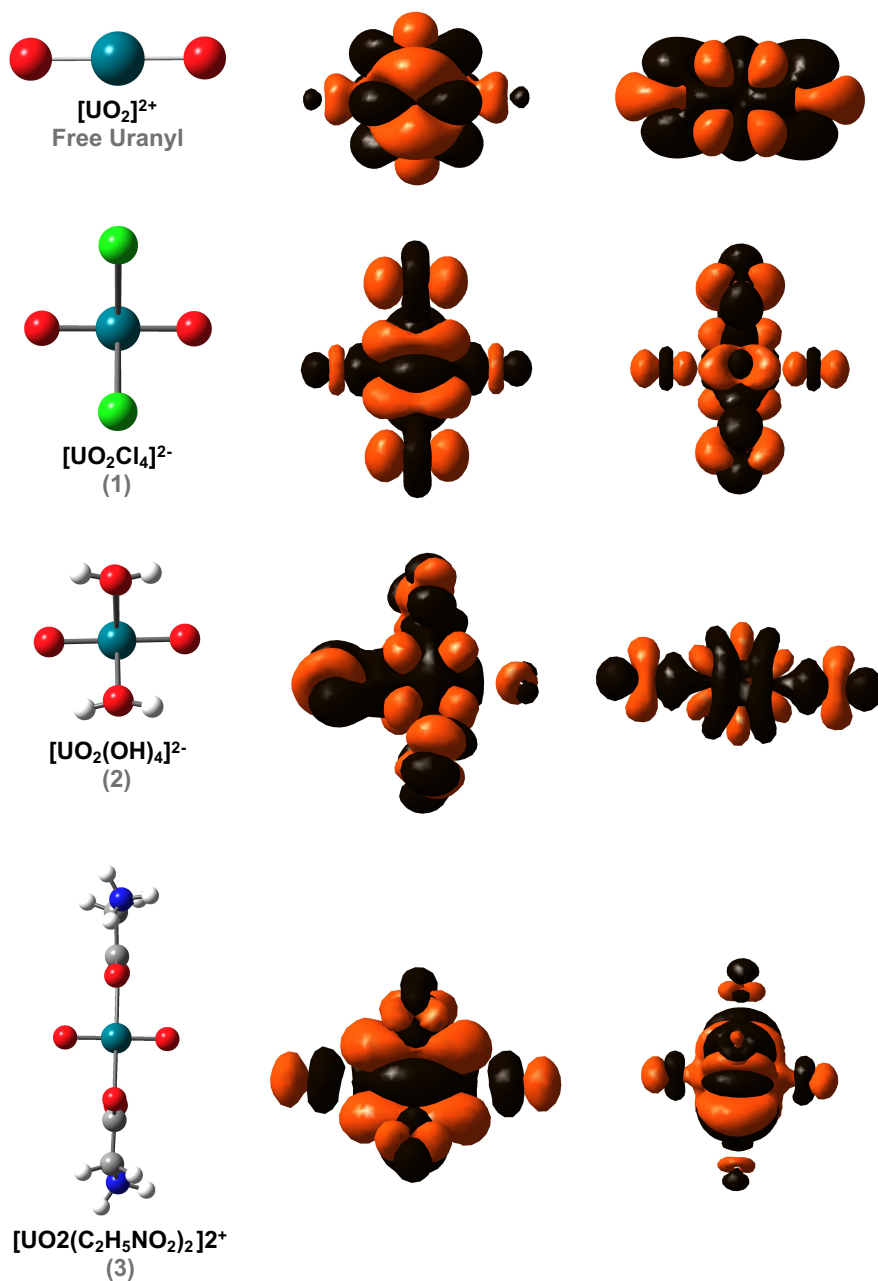


Figure 4.6: Density difference plots (from two different perspectives) for both  $\sigma_u \rightarrow \delta_u$  excitations in free uranyl. Orange indicated areas of positive electron density and black negative.



The density difference plots for all the complexes are given in Figure 4.7; in some cases where the density on the equatorial ligands is minimal these have been cropped

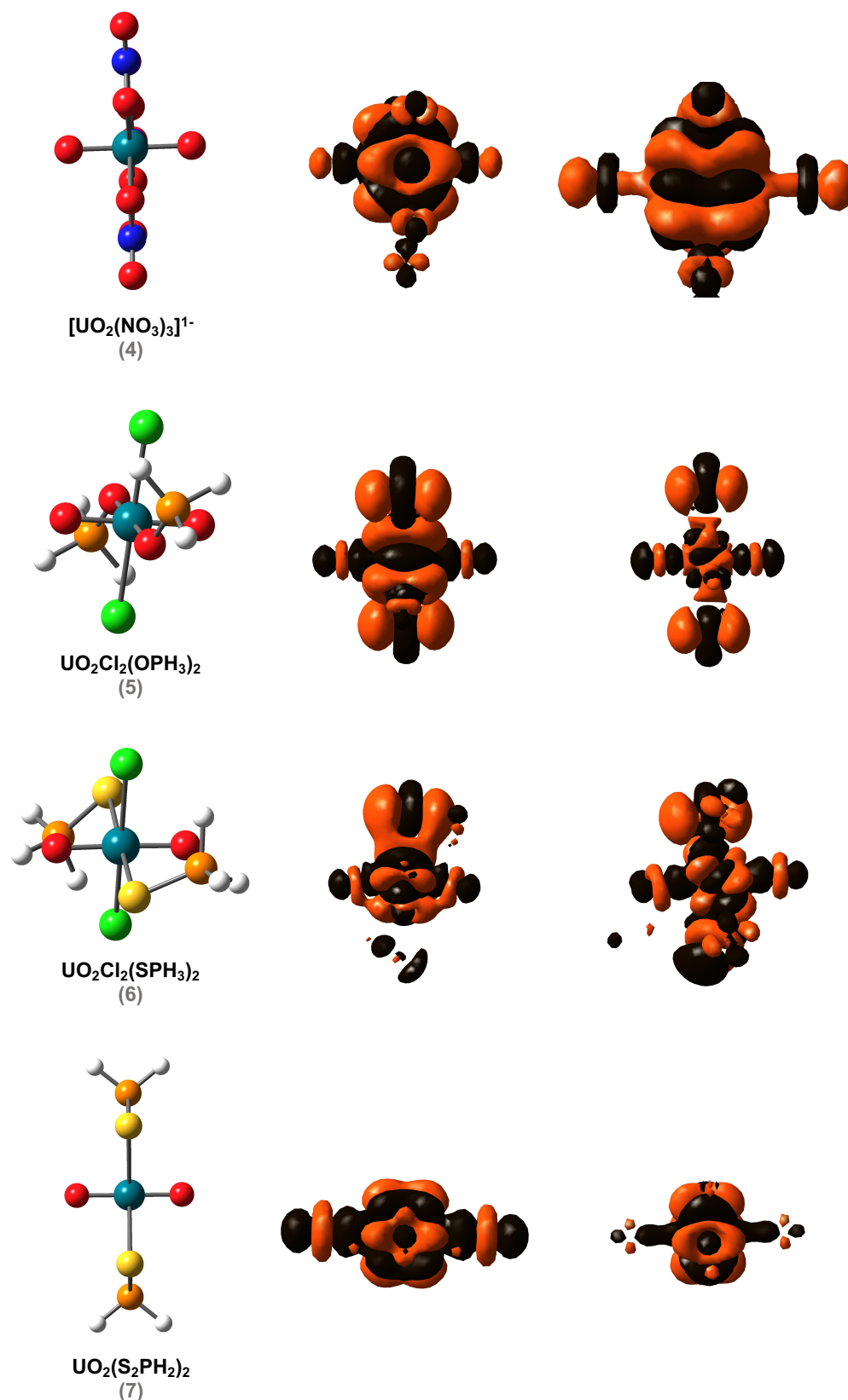


Figure 4.7: Density difference plots for free uranyl and uranyl complexes, with the lowest energy excitation on the left and the highest on the right.

out in order to keep the focus on the uranyl unit in order to make comparisons to free uranyl easier. From the density differences it is clear that both the excitations in

(1), (4) and (7) have very similar nature to  $T_3$  of free uranyl as well as the lowest energy excitation in the (3) and (5) complexes. (2) is the only complex which has density differences similar to that of  $T_4$  in free uranyl with the lower energy excitation being the most similar. The remaining excitations/complexes all have small similarities to  $T_3$  of free uranyl particularly focused on the uranium centre but the rest of the density is dissimilar.

Table 4.3: Topological QTAIM properties of the coordinating atoms to uranium in the ground state electronic structure at the ground state geometries; U- $O_{yl}$  and U-L. L: O, Cl or S; for the complexes which have both O/S and Cl coordination the U-Cl metrics are given second.

Complex	$\rho_{BCP}$ (a.u.)		$\nabla^2\rho_{BCP}$ (a.u.)		$H_{BCP}$ (a.u.)	
	U- $O_{yl}$	U-L	U- $O_{yl}$	U-L	U- $O_{yl}$	U-L
(Free Uranyl) $[UO_2]^{2+}$	0.331	/	0.529	/	-0.347	/
(1) $[UO_2Cl_4]^{2-}$	0.285	0.049	0.392	0.140	-0.251	-0.005
(2) $[UO_2(OH)_4]^{2-}$	0.257	0.081	0.351	0.288	-0.200	-0.009
(3) $[UO_2(C_2H_5NO_2)_2]^{2+}$	0.294	0.057	0.488	0.205	-0.272	-0.004
(4) $[UO_2(NO_3)_3]^{1-}$	0.278	0.052	0.465	0.186	-0.242	-0.003
(5) $UO_2Cl_2(OPH_3)_2$	0.290	0.059/ 0.056	0.391	0.251/ 0.165	-0.261	-0.001/ -0.007
(6) $UO_2Cl_2(SPH_3)_2$	0.291	0.038/ 0.063	0.361	0.094/ 0.175	-0.262	-0.003/ -0.010
(7) $UO_2(S_2PH_2)_2$	0.305	0.042	0.327	0.103	-0.287	-0.004

Table 4.3 gives the topological QTAIM values for each complex in the ground state electronic structure at the ground state geometry. Upon complexation, the topological metrics on the uranyl unit all decrease, indicating a decrease in covalency in the uranyl unit upon complexation. By performing linear regression, it was found that there is a correlation between  $\rho_{BCP}$  and bond length, for both the U- $O_{yl}$  and U-L bonds. This correlation is somewhat expected as an increase in bond length would decrease the MO overlap and hence decrease the covalency of the bond. The linear correlation between bond length and  $\rho_{BCP}$  is stronger with the uranyl bond than with the equatorial ligand as shown by Figure 4.8. The weaker correlation for the equatorial ligands is also expected as there would be other factors such as charge and electronegativity which would factor into the topological properties of the U-L

bond.

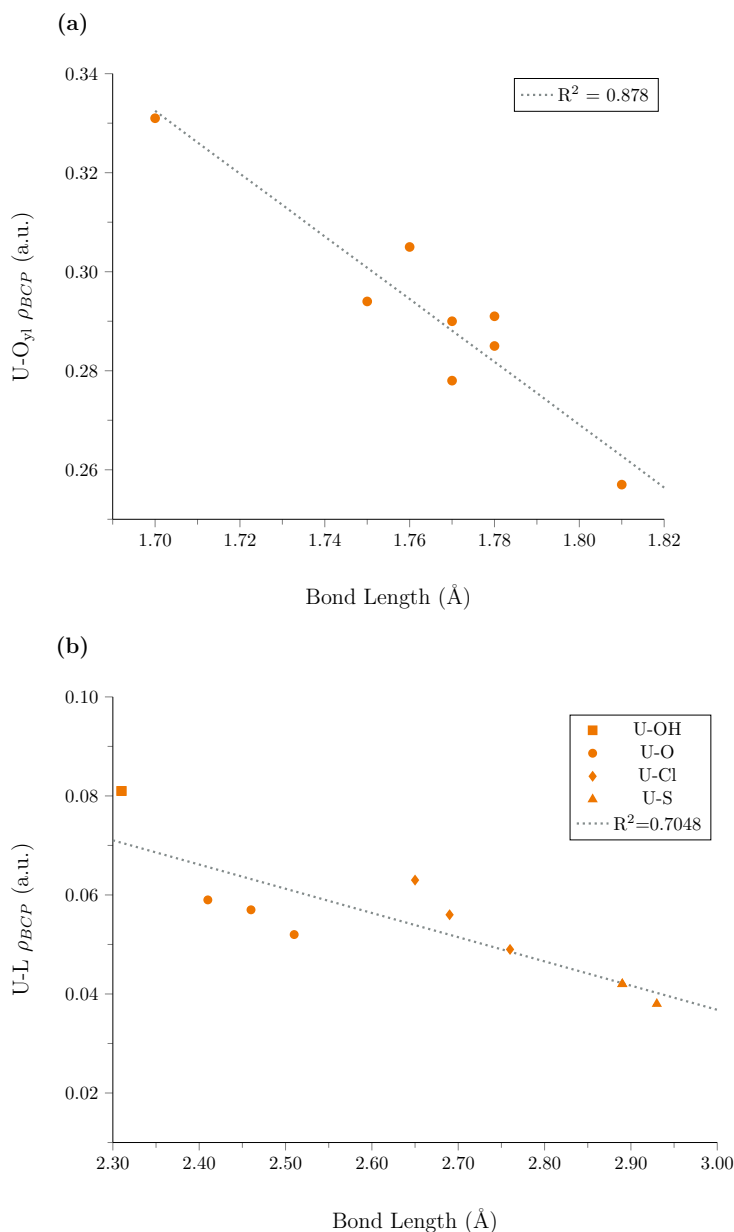


Figure 4.8: Linear regression performed on data given in Table 4.3 for both  $U-O_{yl}$  and  $U-L$  bonds. These plots show negative correlation between bond length and  $\rho_{BCP}$  for  $U-O_{yl}$  (a) and  $U-L$  (b) bonds, with (a) having better linear correlation.

From the data in Table 4.3, it is clear that there is no direct correlation between the overall charge of the ligand and  $\rho_{BCP}$ . The data points in Figure 4.8 are grouped into equatorial ligand type: oxygen, chloride and sulfur, which is in descending order of bond length and electronegativity. When considering a single  $U-L$  type, *i.e.* the oxygen ligands, then the ordering of  $\rho_{BCP}$  can be explained by the polarisability of the ligand as a whole.  $OH^-$  is by far the most polar (difference in electronegativity between the O and H is the largest), then  $C_2H_5NO_2$  (O-C bond),  $OPH_3$  and finally

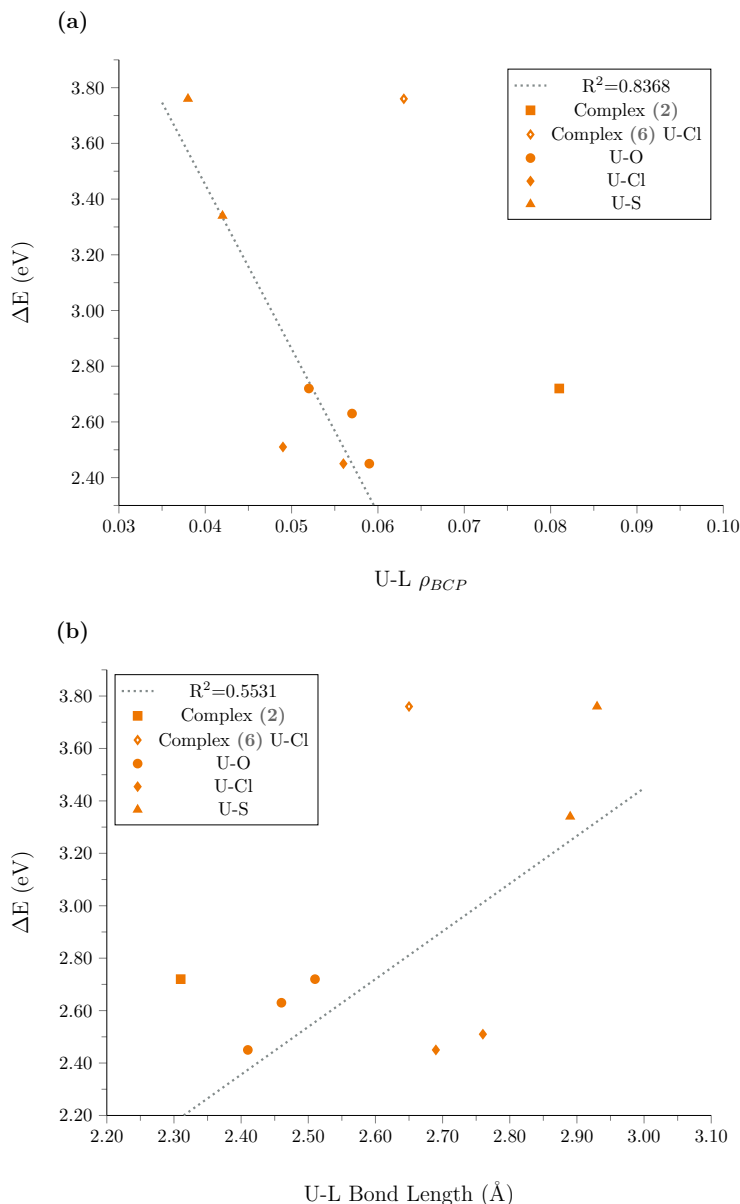


Figure 4.9: Linear regression performed on data from Tables 4.3, 4.1 and 4.2 for U-L bonds. These plots show (a) negative correlation between U-L  $\rho_{BCP}$  and  $\Delta E$  and (b) positive correlation between U-L bond length and  $\Delta E$ . Data points from (2) and the U-Cl bond in (6) are omitted from the linear regression but are given in the plots.

$\text{NO}_3^-$  is the least polar as oxygen and nitrogen have similar electronegativities.

As discussed previously, upon complexation, the  $\sigma_u$  MO interacts with the ligand p-orbitals resulting in the  $\sigma_u^+$  and  $\sigma_u^-$  MOs. The stronger the interaction between the uranium and coordinating ligand (U-L  $\rho_{BCP}$ ), the larger the splitting between the  $\sigma_u^+$  and  $\sigma_u^-$  MOs, resulting in the  $\sigma_u^-$  MO being more destabilised relative to the  $\sigma_u^+$ . This relative destabilisation of the  $\sigma_u^-$  MO results in the excitation energy decreasing. Figure 4.9 shows (a) strong negative correlation between excitation

energy ( $\Delta E$ ) and U-L  $\rho_{BCP}$  with **(b)** showing general positive correlation between excitation energy and U-L bond length, when complex **(2)** and the U-Cl bond in **(6)** are omitted. It is worth noting that there is no correlation between the respective U-O<sub>y1</sub> values and  $\Delta E$ .

It was hypothesised that as  $\rho_{BCP}$  U-O<sub>y1</sub> decreases, then  $\rho_{BCP}$  U-L would increase as the covalency between axial uranyl oxygen is decreasing upon complexation it would be intuitive to assume that this loss in covalency would be distributed to the equatorial ligands. Figure 4.10 shows that this is generally the case, however, this correlation is not as strong as that between bond length and  $\rho_{BCP}$ . As in **(b)** in Figure 4.8, the data is grouped but in this case there is no obvious explanation as to why these U-L types are clumped together. Complexes: **(1)**, **(4)** and the SPH<sub>3</sub> ligand in **(6)** fall below the trend line, complexes: **(3)**, both ligand types in complex **(5)** and the Cl ligand in **(2)** are grouped about the trend line, with complexes **(7)** and **(2)** situated the further right and left, respectively.

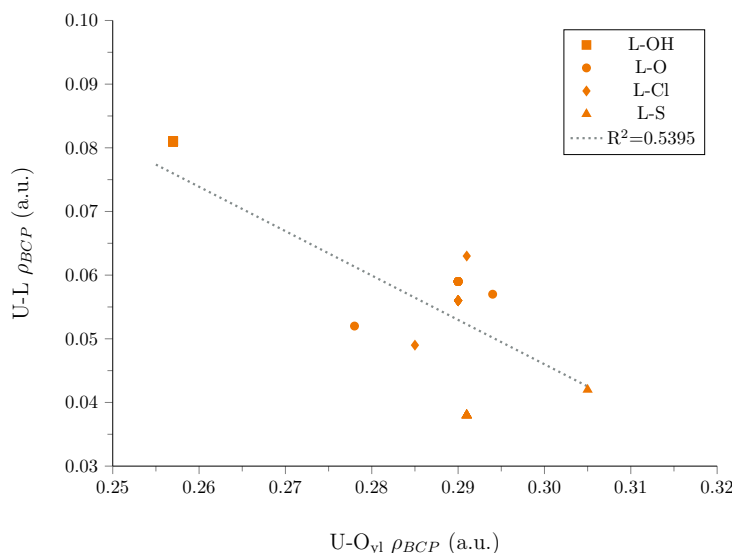


Figure 4.10:  $\rho_{BCP}$  values of the U-O<sub>y1</sub> bond vs U-L bond, showing a reasonable dependency between the  $\rho_{BCP}$  values of the uranyl bond and the equatorial ligands.

In order to fully rationalise the changes in the electronic structure upon complexation, the integrated properties need to be considered. Tables 4.4 and 4.5 give the one and two electron integrated properties of the uranyl unit in the complexes. It is worth noting that the effective core potential used replaces 60 electrons in uranium, as these are core electrons it can be assumed they are localised in the core region of the uranium. The integrated QTAIM metrics are focused solely on uranyl as the focus is on understanding how the covalency of the uranyl unit changes upon complexation. In addition to this, looking at the QTAIM metrics of the coordinating atom of the equatorial ligand won't give the full picture as they are a part of a bigger ligand. Herein, charge transfer and covalency within the ligand cannot be accounted

for by only considering the metrics for the coordinating atom. The delocalisation index ( $\delta$ ) between the uranium and coordinating ligand (U-L) is considered in Table 4.5 in order to rationalise the the U-L bond covalency and give a comparison to the  $\rho_{\text{BCP}}$  data discussed previously.

Table 4.4: Charge ( $q$ ) and localisation ( $\lambda$ ) indices associated with the uranyl unit in the ground state electronic structure at the ground state geometries.

Complex	$q$ (a.u.)			$\lambda$		
	U	O <sub>y1</sub>	UO <sub>2</sub>	U	O <sub>y1</sub>	UO <sub>2</sub>
(Free Uranyl) [UO <sub>2</sub> ] <sup>2+</sup>	3.153	-0.576	2.00	86.814	7.476	106.017
(1) [UO <sub>2</sub> Cl <sub>4</sub> ] <sup>2-</sup>	2.746	-0.914	0.917	86.673	7.863	106.009
(2) [UO <sub>2</sub> (OH) <sub>4</sub> ] <sup>2-</sup>	2.980	-0.985	1.010	86.005	7.908	105.506
(3) [UO <sub>2</sub> (C <sub>2</sub> H <sub>5</sub> NO <sub>2</sub> ) <sub>2</sub> ] <sup>2+</sup>	2.957	-0.738	1.481	86.555	7.697	105.677
(4) [UO <sub>2</sub> (NO <sub>3</sub> ) <sub>3</sub> ] <sup>1-</sup>	2.917	-0.806	1.304	86.484	7.794	105.596
(5) UO <sub>2</sub> Cl <sub>2</sub> (OPH <sub>3</sub> ) <sub>2</sub>	2.825	-0.884	1.057	86.617	7.834	105.921
(6) UO <sub>2</sub> Cl <sub>2</sub> (SPH <sub>3</sub> ) <sub>2</sub>	2.668	-0.924	0.820	86.700	7.836	106.030
(7) UO <sub>2</sub> (S <sub>2</sub> PH <sub>2</sub> ) <sub>2</sub>	2.643	-0.928	0.787	86.830	7.826	106.321

In general, upon complexation all metrics except  $\lambda_{\text{O}_{y1}}$  decrease. This indicates that upon complexation, there is an increase in electronic charge and electron population on the uranyl unit which implies a charge transfer from the equatorial ligands to the uranyl unit. The smallest change in charge on the uranyl unit occurs in the complexes with bidentate oxygen ligands ((3) and (4)), while the largest occurs in the complexes containing sulfur ((6) and (7)). The complexes can be ordered from largest to smallest positive charge ( $q$ ) on the uranyl unit:

$$\text{(Free Uranyl)} > \text{(3)} > \text{(4)} > \text{(5)} > \text{(2)} > \text{(1)} > \text{(6)} > \text{(7)}$$

From a chemical perspective, it would be expected that the ligands containing sulfur would be the most electron donating, with the oxygen ligands being the least and unsurprisingly this is what the QTAIM data in Table 4.4 rationalises. The above ordering remains the same when considering the  $q_{\text{U}}$  and  $q_{\text{O}_{y1}}$  ( $q_{\text{O}_{y1}}$  smallest negative to largest negative charge) with the exception of complex (2), which has the largest decrease in charge on the O<sub>y1</sub> centre and the smallest decrease in charge on

Table 4.5: Delocalisation ( $\delta$ ) indices associated with the U-O<sub>y1</sub> bond and the U-L bonds at ground state electronic structure at the ground state geometries

Complex	$\delta_{\text{U-O}_{y1}}$	$\delta_{\text{U-L}^0}$	$\delta_{\text{U-L}^-}$
(Free Uranyl) [UO <sub>2</sub> ] <sup>2+</sup>	2.045	/	/
(1) [UO <sub>2</sub> Cl <sub>4</sub> ] <sup>2-</sup>	1.750	/	0.493
(2) [UO <sub>2</sub> (OH) <sub>4</sub> ] <sup>2-</sup>	1.800	/	0.587
(3) [UO <sub>2</sub> (C <sub>2</sub> H <sub>5</sub> NO <sub>2</sub> ) <sub>2</sub> ] <sup>2+</sup>	1.788	0.344	/
(4) [UO <sub>2</sub> (NO <sub>3</sub> ) <sub>3</sub> ] <sup>1-</sup>	1.691	/	0.291
(5) UO <sub>2</sub> Cl <sub>2</sub> (OPH <sub>3</sub> ) <sub>2</sub>	1.761	0.347	0.472
(6) UO <sub>2</sub> Cl <sub>2</sub> (SPH <sub>3</sub> ) <sub>2</sub>	1.779	0.362	0.519
(7) UO <sub>2</sub> (S <sub>2</sub> PH <sub>2</sub> ) <sub>2</sub>	1.871	/	0.372

the uranium centre. An electronegativity argument, (similar to that made for the topological QTAIM data) can also be made for this ordering; the oxygen ligands are the most electronegative, followed by the chloride and finally the sulfur ligands. The only discrepancy to this argument is that (2) would be expected to be the most electronegative out of the oxygen ligands but is the last in the list above.

The proportion of charge transfer (CT) upon complexation was investigated and the results are shown in Table 4.6.  $\Delta q_U$  and  $\Delta q_{\text{O}_{y1}}$  were calculated by subtracting the charge on the atom in the complex from that in free uranyl and the CT Ratio was found by:  $\Delta q_{\text{O}_{y1}} / \Delta q_U$ . From the data it is clear that for the majority of complexes, charge is transferred from the equatorial ligands onto both the uranium and oxygen centres of the uranyl unit equally, with a slightly higher proportion going to the uranium over the oxygens. Complex (2) however, is an exception where the majority of the charge from the equatorial ligands goes to the oxygen over the uranium. A potential reason for this to occur could be due to the polar nature of the hydroxide ligand; if the uranyl oxygens become more negatively charge upon complexation then there could be the possibility of intramolecular hydrogen bonding between the equatorial OH ligand and the uranyl oxygens. Potential correlations between the CT ratio and other metrics, such as bond length and  $\rho_{\text{BCP}}$  were investigated but no discernable trends were observed.

As expected from the topological data,  $\delta_{\text{U-O}_{y1}}$  decreases across all complexes and also correlates with  $\rho_{\text{BCP}}$ , with (2) being an exception. Figure 4.11 shows the

Table 4.6: Changes in charge on the uranium and oxygen centres in the complexes in comparison to free uranyl and the ratio of these differences

Complex	$\Delta q_U$ (a.u.)	$\Delta q_{O_{yl}}$ (a.u.)	CT Ratio
(1) $[\text{UO}_2\text{Cl}_4]^{2-}$	0.406	0.338	0.832
(2) $[\text{UO}_2(\text{OH})_4]^{2-}$	0.172	0.409	2.371
(3) $[\text{UO}_2(\text{C}_2\text{H}_5\text{NO}_2)_2]^{2+}$	0.196	0.162	0.826
(4) $[\text{UO}_2(\text{NO}_3)_3]^{1-}$	0.235	0.230	0.977
(5) $\text{UO}_2\text{Cl}_2(\text{OPH}_3)_2$	0.328	0.307	0.937
(6) $\text{UO}_2\text{Cl}_2(\text{SPH}_3)_2$	0.485	0.348	0.717
(7) $\text{UO}_2(\text{S}_2\text{PH}_2)_2$	0.510	0.352	0.690

positive correlation between  $\delta$  and  $\rho_{\text{BCP}}$  for both U- $\text{O}_{yl}$  and U-L bonds. In the case of the U- $\text{O}_{yl}$  bond, only complex (2) is an outlier whereas for the U-L bond, the other oxygen coordinating complexes; (3), (4) and the U- $\text{OPH}_3$  bond in (5) fall outside the trend line. As discussed previously, these oxygen coordinating complexes have the three lowest  $q$ ,  $\lambda$  and  $\delta_{\text{U-L}}$  metrics, however there is not an explanation as to why these would be outliers in this trend. As was seen in Figure 4.8 the ligands are grouped in terms of the coordinating ligand atom, with U-OH, U-Cl and U-S in the same positioning.

The decrease in  $\delta_{\text{U-}\text{O}_{yl}}$  upon complexation can result in: an increase in  $\lambda_{\text{UO}_2}$ , an increase in  $\delta_{\text{U-L}}$  or a combination of the two. The resulting rearrangement of charge could be more complex, however, with the charge moving from the U- $\text{O}_{yl}$  bond to throughout the equatorial ligand and not just situated at the U-L bond. However, this complex movement of charge is beyond the scope of this study.

Figure 4.12 shows positive correlation between  $\delta_{\text{U-}\text{O}_{yl}}$  and  $\delta_{\text{U-L}}$ , with the exception of complex (7). This correlation is the opposite to what would be expected if the charge transfers to the equatorial ligands. However, this figure only considers a single U-L/U- $\text{O}_{yl}$  bond and therefore in order to obtain a full picture, the total  $\delta_{\text{U-L}}$  and  $\delta_{\text{U-}\text{O}_{yl}}$  needs to be calculated.

In order to evaluate where the transfer of charge from the U- $\text{O}_{yl}$  bond accumulates, comparisons of  $\delta_{\text{U-L}}$  and  $\lambda_{\text{UO}_2}$  can be made to the total delocalisation on the uranyl unit ( $\delta_{\text{UO}_2}$ ) ( $2 \times \delta_{\text{U-}\text{O}_{yl}} + \delta_{\text{O}_{yl}-\text{O}_{yl}}$ ). For this part of the investigation,  $\lambda_{\text{UO}_2}$  does not include  $\delta_{\text{UO}_2}$  ( $\sum \delta_{\text{U-}\text{O}_{yl}} + \delta_{\text{O}_{yl}-\text{O}_{yl}}$ ) as in given in Table 4.4 but is simply the sum of the localisation indices in the uranyl unit ( $\sum \lambda_{\text{O}_{yl}} + \lambda_{\text{U}}$ ). Table 4.7 gives the total values of all the metrics compared in Figures 4.13 and 4.14.

Figures 4.13 and 4.14 show that there is no obvious correlation between  $\delta_{\text{UO}_2}$  and either  $\lambda_{\text{UO}_2}$  or  $\delta_{\text{U-L}}$ , indicating that the overall movement of charge is more complex. However, these plots show that  $\lambda_{\text{UO}_2}$  and  $\delta_{\text{U-L}}$  are correlated to each other due to the data sets forming similar distributions, particularly for the complexes which contain

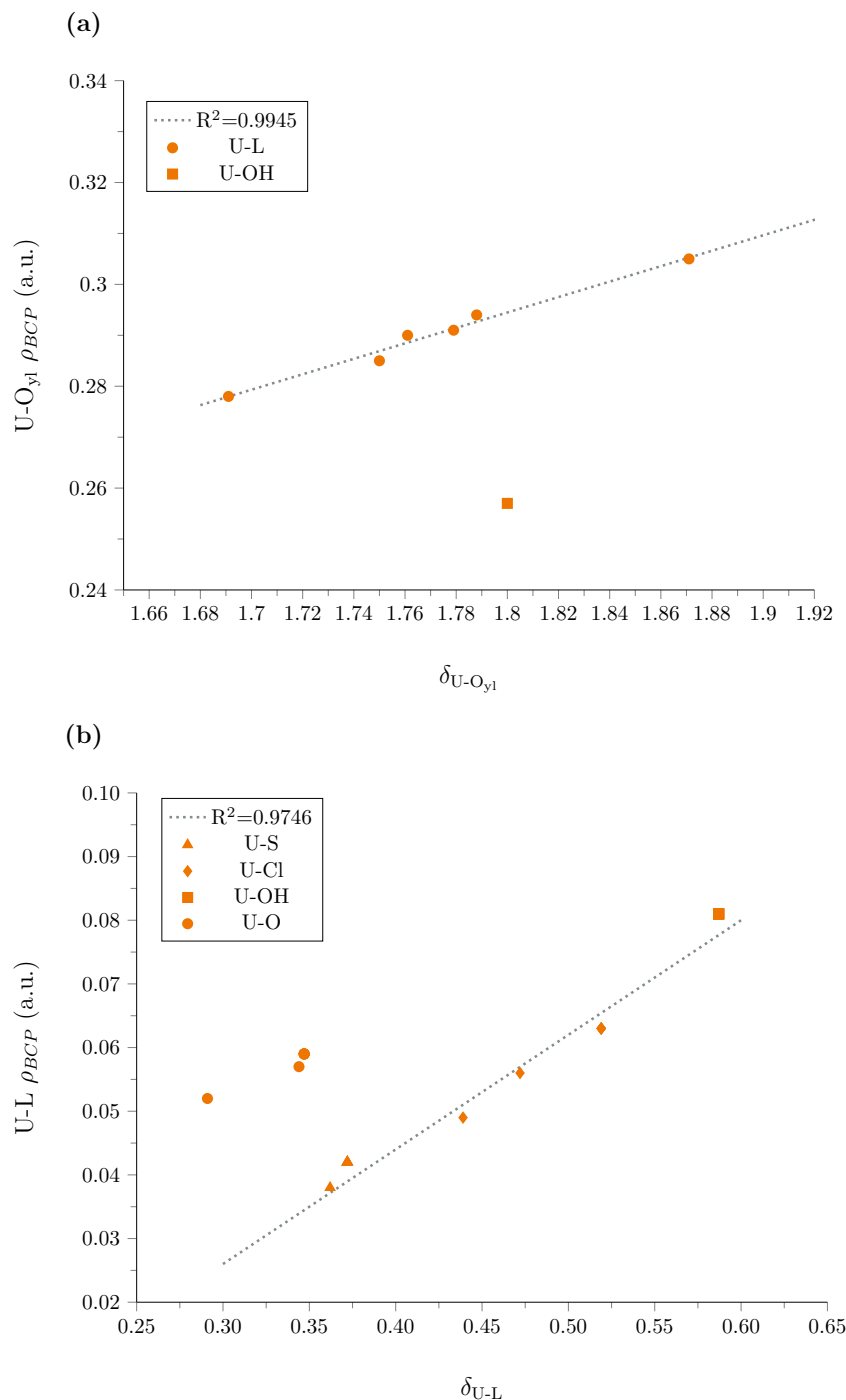


Figure 4.11: Graphs showing positive correlation between  $\delta$  and  $\rho_{BCP}$  for both (a) U-O<sub>y1</sub> and (b) U-L bonds.

chloride ligands ((1), (5) and (6)). An exception to this general pattern is complex (2) which has the lowest  $\lambda_{UO_2}$  value and the highest  $\delta_{U-L}$  value, which implies that there is a much stronger effect from the  $\delta_{U-L}$  than  $\lambda_{UO_2}$ . This seems to contradict the effect experienced by the other complexes, which have a larger increase in  $\lambda_{UO_2}$  and a much less pronounced increase in  $\delta_{U-L}$  in comparison. Combining both the total  $\lambda_{UO_2}$  and total  $\delta_{U-L}$  results in most of the complexes being in a similar region to

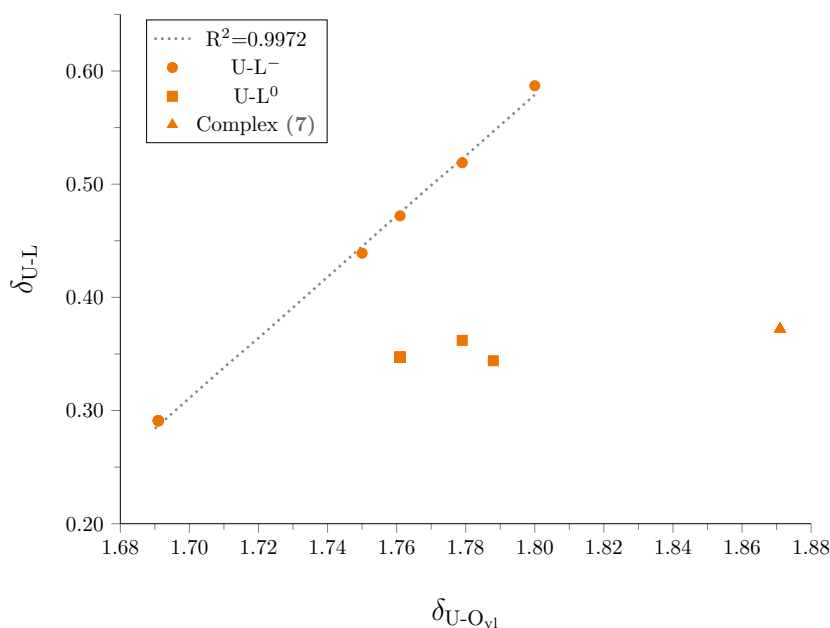


Figure 4.12:  $\delta$  values of  $U-O_{y1}$  vs  $U-L$  bonds, showing positive correlation between  $\delta_{U-O_{y1}}$  and  $\delta_{U-L^-}$ , with complex (7) being an outlier and no correlation between  $\delta_{U-O_{y1}}$  and  $\delta_{U-L^+}$

Table 4.7: Total values of all metrics used in Figures 4.13 and 4.14

Complex	Total $\delta_{UO_2}$	Total $\lambda_{UO_2}$	Total $\delta_{U-L}$	Total $\lambda_{UO_2}$ + Total $\delta_{U-L}$
(1) $[UO_2Cl_4]^{2-}$	3.610	102.399	1.756	104.155
(2) $[UO_2(OH)_4]^{2-}$	3.685	101.821	2.348	104.169
(3) $[UO_2(C_2H_5NO_2)_2]^{2+}$	3.728	101.949	1.376	103.325
(4) $[UO_2(NO_3)_3]^{1-}$	3.524	102.071	1.746	103.817
(5) $UO_2Cl_2(OPH_3)_2$	3.637	102.284	1.638	103.922
(6) $UO_2Cl_2(SPH_3)_2$	3.658	102.372	1.762	104.134
(7) $UO_2(S_2PH_2)_2$	3.839	102.482	1.488	103.970

Free uranyl values:  $\delta_{UO_2} = 4.251$ ,  $\lambda_{UO_2} = 101.766$

each other, with the exception of (3), which is much lower suggesting that the gain in electron density on both the uranyl unit and the U-L bonding region is much less in than in the other complexes. A potential explanation for this is the zwitterionic nature of the equatorial ligand in complex (3), this nature will likely cause any ‘excess’ charge gained at the negative end of the glycine ligand (coordinating end) to transfer through to the positive end of the ligand.

Despite there not being any correlation in Figures 4.13 and 4.14, the data in Tables 4.4 and 4.7 show that upon complexation  $\lambda_{UO_2}$  increases compared to free uranyl, which is solely due to  $\lambda_{O_{y1}}$ . This indicates that some of the electron density

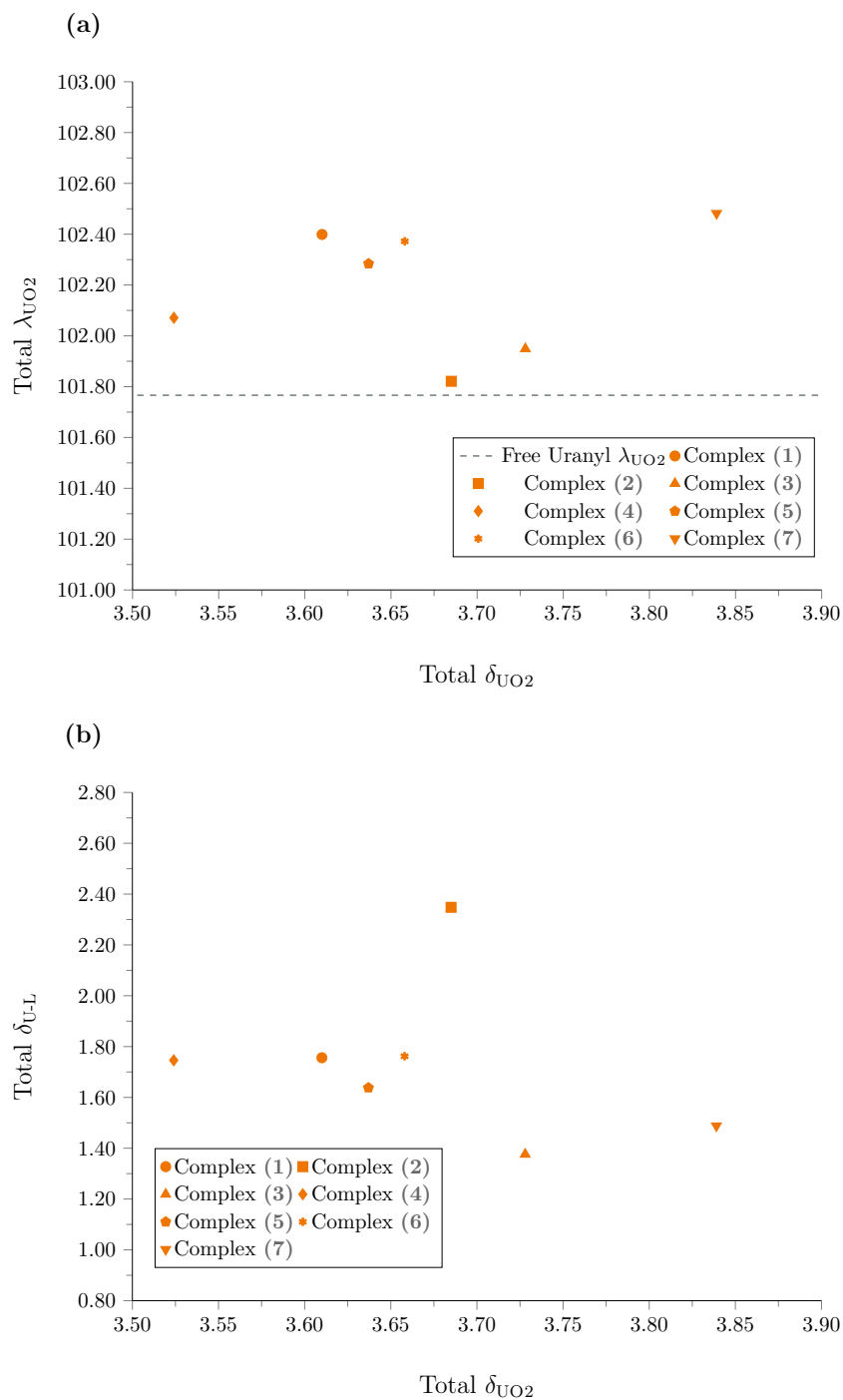


Figure 4.13: Comparison of the total delocalisation on the uranyl unit ( $\delta_{U-O_2}$ ) against **(a)** total localisation on the uranyl unit ( $\lambda_{UO_2}$ ) and **(b)** total delocalisation between the uranium-equatorial ligands ( $\delta_{U-L}$ )

transfers from the  $U-O_{y1}$  bonding region to  $O_{y1}$ , which was seen in previous studies. [4] The lack of correlation between  $\lambda_{UO_2}$  and  $\delta_{UO_2}$  indicates that not all the charge is transferred to  $O_{y1}$ . In contrast to the  $\lambda_{UO_2}$  values, which can be compared to

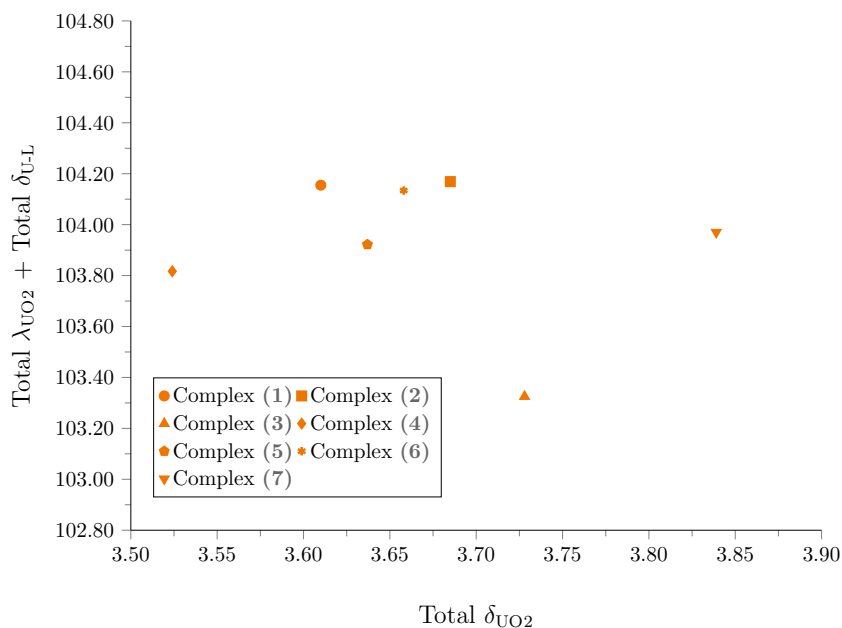


Figure 4.14: Comparison of the total delocalisation on the uranyl unit ( $\delta_{U-O_2}$ ) against the combined total of the uranyl localisation ( $\lambda_{UO_2}$ ) and the delocalisation indices between the uranium and equatorial ligands ( $\delta_{U-L}$ ).

free uranyl in order to compare the changes to the electronic structure, the same comparisons cannot be made for  $\delta_{U-L}$ . It is highly likely that the charge is also transferred to the bonding region between uranium and the equatorial ligands, with the largest contribution coming from complex (2). Finally, Figure 4.14 shows that not all the charge transferred from the the U-O<sub>yl</sub> bonding region is accounted for by the gain  $\lambda_{UO_2}$  and  $\delta_{U-L}$  and hence suggests that the transfer of charge is more complex and likely distributed throughout the equatorial ligands.

### 4.3.2 Excited State Geometries

The excited state geometries for both excitations were calculated for all complexes except for in complex (2) and the higher excited state in complex (6). Multiple attempts were conducted for these structures but the correct excitation nature at the excited state geometries could not be isolated.

Tables 4.8 and 4.9 compare the excitation energies and the U-O<sub>yl</sub> and U-L bond lengths at the ground and excited state geometries. At the excited state geometries, both U-O<sub>yl</sub> and U-L bond lengths elongate and the excitation energy is red shifted. The increase in U-O<sub>yl</sub> bond length and red shift in excitation energies are comparable to free uranyl studied in Chapter 3. Complex (7) is an exception as the excitation energies are considerably more red-shifted than in the other complexes and the elongation of the U-S bond is much larger. Due to the higher energy excitation in complex (6) being elusive, unfortunately there is no comparable exci-

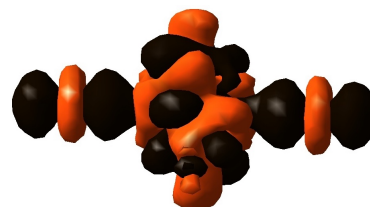
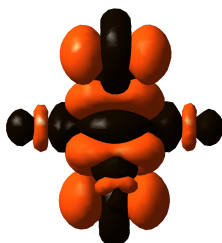
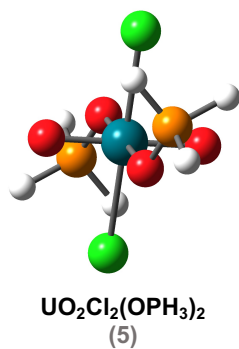
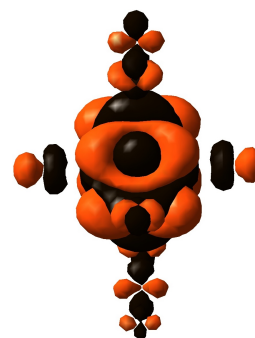
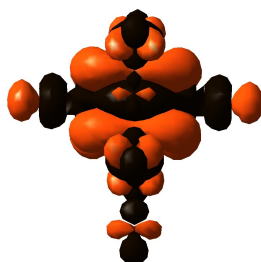
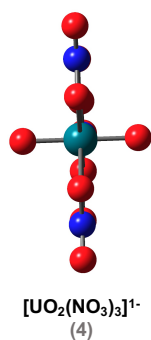
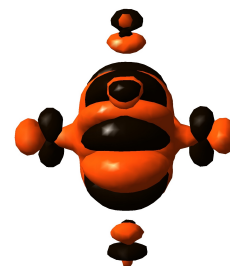
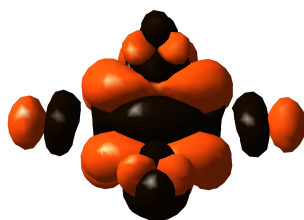
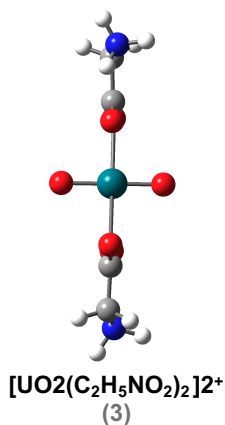
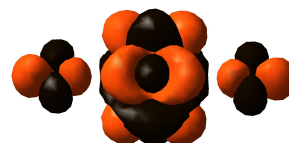
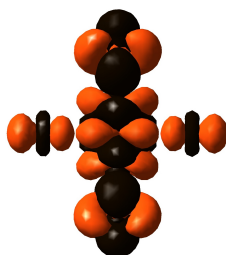
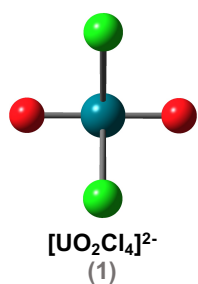
Table 4.8: Excitation energies of the  $\sigma_u \rightarrow \delta_u$  excitation at both the ground (GS) and excited state (ES) geometries

Complex	State	$\Delta E$ (eV)			State	$\Delta E$ (eV)	
		GS	ES			GS	ES
(Free Uranyl)[UO <sub>2</sub> ] <sup>2+</sup>	T <sub>3</sub>	2.43	2.18				
(1) [UO <sub>2</sub> Cl <sub>4</sub> ] <sup>2-</sup>	T <sub>1</sub>	2.51	2.40		T <sub>2</sub>	2.59	2.49
(3) [UO <sub>2</sub> (C <sub>2</sub> H <sub>5</sub> NO <sub>2</sub> ) <sub>2</sub> ] <sup>2+</sup>	T <sub>1</sub>	2.63	2.43		T <sub>3</sub>	2.72	2.52
(4) [UO <sub>2</sub> (NO <sub>3</sub> ) <sub>3</sub> ] <sup>1-</sup>	T <sub>1</sub>	2.72	2.54		T <sub>2</sub>	2.72	2.52
(5) UO <sub>2</sub> Cl <sub>2</sub> (OPH <sub>3</sub> ) <sub>2</sub>	T <sub>1</sub>	2.45	2.33		T <sub>2</sub>	2.55	2.42
(6) UO <sub>2</sub> Cl <sub>2</sub> (SPH <sub>3</sub> ) <sub>2</sub>	T <sub>1</sub>	2.48	2.35				
(7) UO <sub>2</sub> (S <sub>2</sub> PH <sub>2</sub> ) <sub>2</sub>	T <sub>29</sub>	3.34	2.91		T <sub>31</sub>	3.43	2.96

Table 4.9: Bond elongation ( $\Delta r$ ) in excited state geometries

Complex	State	$\Delta r$ (Å)		
		U-O <sub>y1</sub>	U-L <sup>0</sup>	U-L <sup>-</sup>
(Free Uranyl) [UO <sub>2</sub> ] <sup>2+</sup>	T <sub>3</sub>	0.05	/	/
(1) [UO <sub>2</sub> Cl <sub>4</sub> ] <sup>2-</sup>	T <sub>1</sub>	0.03	/	0.01
	T <sub>2</sub>	0.03	/	0.02
(3) [UO <sub>2</sub> (C <sub>2</sub> H <sub>5</sub> NO <sub>2</sub> ) <sub>2</sub> ] <sup>2+</sup>	T <sub>1</sub>	0.05	0.01	/
	T <sub>3</sub>	0.05	0.01	/
(4) [UO <sub>2</sub> (NO <sub>3</sub> ) <sub>3</sub> ] <sup>1-</sup>	T <sub>1</sub>	0.05	/	0.00
	T <sub>2</sub>	0.05	/	0.00
(5) UO <sub>2</sub> Cl <sub>2</sub> (OPH <sub>3</sub> ) <sub>2</sub>	T <sub>1</sub>	0.04	0.00	0.02
	T <sub>2</sub>	0.04	0.01	0.03
(6) UO <sub>2</sub> Cl <sub>2</sub> (SPH <sub>3</sub> ) <sub>2</sub>	T <sub>1</sub>	0.02	0.03	0.03
(7) UO <sub>2</sub> (S <sub>2</sub> PH <sub>2</sub> ) <sub>2</sub>	T <sub>29</sub>	0.00	/	0.23
	T <sub>31</sub>	0.01	/	0.23

tation in another complex to see if this behaviour is consistent across higher energy excitations.



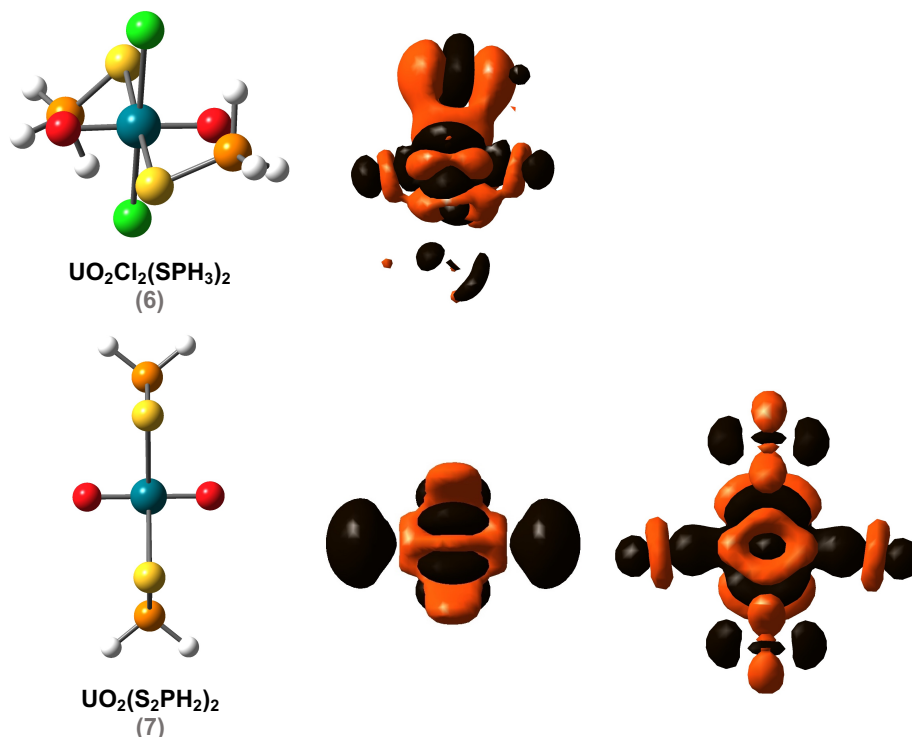


Figure 4.15: Density difference plots for the uranyl complexes at the excited state geometry, the lowest energy excitation on the left and the higher on the right.

Density difference plots were also generated at the excited state geometries (Figure 4.15), as was the case at the ground state geometries, electron density on the ligands is truncated in places in order to give a clearer picture of the uranyl unit. Largely the nature of the excitations are the same as at the ground state geometries and hence further evidence that the correct state was isolated. At the excited state geometries of the chloride complex, both density difference plots have the same nature as each other (Figure 4.15 shows them at different angles) which corresponds to  $T_2$  at the ground state geometry (Figure 4.7). The only state which is dissimilar to the ground state is  $T_{29}$  of complex (7). The nature of this excitation state was found to be the same as that of the ground state equivalent but with a larger contribution from the more stabilised  $\sigma_u^+$  MO: 90%  $\sigma_u^+ \rightarrow \delta_u$ , 10%  $\sigma_u^- \rightarrow \delta_u$  in comparison to 70%  $\sigma_u^+ \rightarrow \delta_u$ , 25%  $\sigma_u^- \rightarrow \delta_u$  at the ground state geometry. While there is no obvious evidence for the different character in this excitation in the MO characters and contributions, it is plausible that the QTAIM data will provide evidence for the difference in electronic structure causing a fluctuation in the density difference.

Table 4.10: Topological QTAIM properties of the coordinating atoms to uranium, in the excited state electronic structures at the excited state geometries; U-O<sub>yl</sub> and U-L. L:O, Cl or S; for the complexes which have both O/S and Cl coordination the U-Cl metrics are given on the second row.

Complex State	$\rho_{\text{BCP}}$ (a.u.)		$\nabla^2\rho_{\text{BCP}}$ (a.u.)		$H_{\text{BCP}}$ (a.u.)	
	U-O <sub>yl</sub>	U-L	U-O <sub>yl</sub>	U-L	U-O <sub>yl</sub>	U-L
(Free Uranyl) [UO <sub>2</sub> ] <sup>2+</sup> T <sub>3</sub>	0.296	/	0.488	/	-0.278	/
(1) [UO <sub>2</sub> Cl <sub>4</sub> ] <sup>2-</sup> T <sub>1</sub>	0.265	0.045	0.352	0.134	-0.217	-0.003
T <sub>2</sub>	0.261	0.046	0.385	0.127	-0.212	-0.003
(3) [UO <sub>2</sub> (C <sub>2</sub> H <sub>5</sub> NO <sub>2</sub> ) <sub>2</sub> ] <sup>2+</sup> T <sub>1</sub>	0.262	0.058	0.461	0.192	-0.215	-0.004
T <sub>3</sub>	0.265	0.059	0.480	0.198	-0.219	-0.004
(4) [UO <sub>2</sub> (NO <sub>3</sub> ) <sub>3</sub> ] <sup>1-</sup> T <sub>1</sub>	0.247	0.052	0.449	0.173	-0.190	-0.003
T <sub>2</sub>	0.247	0.052	0.449	0.172	-0.190	-0.003
(5) UO <sub>2</sub> Cl <sub>2</sub> (OPH <sub>3</sub> ) <sub>2</sub> T <sub>1</sub>	0.259	0.058 0.055	0.423	0.239 0.150	-0.209	-0.001 -0.007
T <sub>2</sub>	0.263	0.057 0.054	0.427	0.287 0.149	-0.215	-0.001 -0.007
(6) UO <sub>2</sub> Cl <sub>2</sub> (SPH <sub>3</sub> ) <sub>2</sub> T <sub>1</sub>	0.263	0.037 0.059	0.401	0.084 0.160	-0.215	-0.003 -0.009
(7) UO <sub>2</sub> (S <sub>2</sub> PH <sub>2</sub> ) <sub>2</sub> T <sub>29</sub>	0.314	0.029	0.279	0.052	-0.302	-0.002
T <sub>31</sub>	0.278	0.027	0.422	0.066	-0.243	-0.001

The QTAIM properties at the excited state geometries are given in Tables 4.10, 4.11, and 4.12. The following analysis will compare the ground state electronic structures at the ground state geometries to the excited state electronic structure at the excited state geometries,  $\Delta^{\text{ES}}$  in Figure 4.2.

Upon excitation the topological properties decrease at the U-O<sub>yl</sub> BCP for all complexes by roughly the same magnitude with the exception of the T<sub>29</sub> in complex (7), which increases but by roughly half the magnitude that the other complexes

Table 4.11: Charge ( $q$ ) and localisation index ( $\lambda$ ) integrated QTAIM metrics associated with the uranyl unit in the excited state electronic structures at the excited state geometries)

Complex State	$q$ (a.u.)			$\lambda$			
	U	O <sub>y1</sub>	UO <sub>2</sub>	U	O <sub>y1</sub>	UO <sub>2</sub>	
(Free Uranyl) [UO <sub>2</sub> ] <sup>2+</sup> T <sub>3</sub>	3.103	-0.552	2.000	86.802	7.372	106.005	
(1) [UO <sub>2</sub> Cl <sub>4</sub> ] <sup>2-</sup> T <sub>1</sub>	2.644	-1.024	0.596	86.818	7.990	106.411	
	T <sub>2</sub>	2.671	-0.945	0.782	86.749	7.890	105.995
(3) [UO <sub>2</sub> (C <sub>2</sub> H <sub>5</sub> NO <sub>2</sub> ) <sub>2</sub> ] <sup>2+</sup> T <sub>1</sub>	2.906	-0.731	1.444	86.533	7.618	105.658	
	T <sub>3</sub>	2.914	-0.722	1.470	86.616	7.634	105.695
(4) [UO <sub>2</sub> (NO <sub>3</sub> ) <sub>3</sub> ] <sup>1-</sup> T <sub>1</sub>	2.871	-0.802	1.268	86.478	7.720	105.569	
	T <sub>2</sub>	2.870	-0.802	1.267	86.469	7.720	105.561
(5) UO <sub>2</sub> Cl <sub>2</sub> (OPH <sub>3</sub> ) <sub>2</sub> T <sub>1</sub>	2.794	-0.835	1.123	86.512	7.831	105.636	
	T <sub>2</sub>	2.786	-0.843	1.100	86.583	7.763	105.706
(6) UO <sub>2</sub> Cl <sub>2</sub> (SPH <sub>3</sub> ) <sub>2</sub> T <sub>1</sub>	2.637	-0.871	0.895	86.616	7.740	105.693	
(7) UO <sub>2</sub> (S <sub>2</sub> PH <sub>2</sub> ) <sub>2</sub> T <sub>29</sub>	2.875	-0.801	1.273	86.387	7.624	105.922	
	T <sub>31</sub>	2.459	-0.900	0.659	87.172	7.849	106.517

decrease by. This decrease is to be expected as the bond length has increased corresponding to a decrease in overlap at the excited state geometry. It is worth noting that the overall decrease in U-O<sub>y1</sub>  $\rho_{\text{BCP}}$  is much larger than the decrease in U-L  $\rho_{\text{BCP}}$  upon excitation. This indicates that there is movement of charge from both U-O<sub>y1</sub> and U-L bonding regions but a much larger portion from the U-O<sub>y1</sub>. This is expected as the nature of the excitation investigated is mostly localised on the uranyl unit and so it is anticipated that the changes in metric on the equatorial ligands will be marginal at the excited state geometries.

Table 4.12: Delocalisation ( $\delta$ ) indices associated with the uranyl unit in the excited state electronic structures at the excited state geometries

Complex	$\delta_{\text{U-O}_{\text{yl}}}$	$\delta_{\text{U-L}^0}$	$\delta_{\text{U-L}^-}$
(Free Uranyl) $[\text{UO}_2]^{2+}$ T <sub>3</sub>	2.099	/	/
(1) $[\text{UO}_2\text{Cl}_4]^{2-}$ T <sub>1</sub>	1.772	/	0.397
T <sub>2</sub>	1.689	/	0.448
(3) $[\text{UO}_2(\text{C}_2\text{H}_5\text{NO}_2)_2]^{2+}$ T <sub>1</sub>	1.813	0.335	/
T <sub>3</sub>	1.786	0.335	/
(4) $[\text{UO}_2(\text{NO}_3)_3]^{1-}$ T <sub>1</sub>	1.697	/	0.300
T <sub>2</sub>	1.697	/	0.300
(5) $\text{UO}_2\text{Cl}_2(\text{OPH}_3)_2$ T <sub>1</sub>	1.726	0.362	0.587
T <sub>2</sub>	1.709	0.353	0.558
(6) $\text{UO}_2\text{Cl}_2(\text{SPH}_3)_2$ T <sub>1</sub>	1.724	0.381	0.644
(7) $\text{UO}_2(\text{S}_2\text{PH}_2)_2$ T <sub>29</sub>	2.091	/	0.344
T <sub>31</sub>	1.739	/	0.323

As was the case at the ground state geometries, (Figure 4.8) there is negative correlation between the bond length and  $\rho_{\text{BCP}}$  for both the U-O<sub>yl</sub> and U-L bonds as shown by Figure 4.16. It is worth noting that there are more data points at the excited state electronic structures at the excited state geometries as each complex has two excitations displayed in Figure 4.16. The two different excitations are represented with filled and un-filled markers corresponding to the lower and higher energy excitations for a given complex. Interestingly, in comparison to the ground state electronic structures at the ground state geometries, there is better linearity for the U-L bond than the for the U-O<sub>yl</sub> bond in the excited state electronic structures at the excited state geometries. This is likely due to  $\Delta^{\text{ES}} \rho_{\text{BCP}}$  being much larger for U-O<sub>yl</sub> than U-L in comparison to  $\Delta r$ , this larger change in  $\rho_{\text{BCP}}$  is not reciprocated in the bond length data and thus results in the negative correlation being less linear.

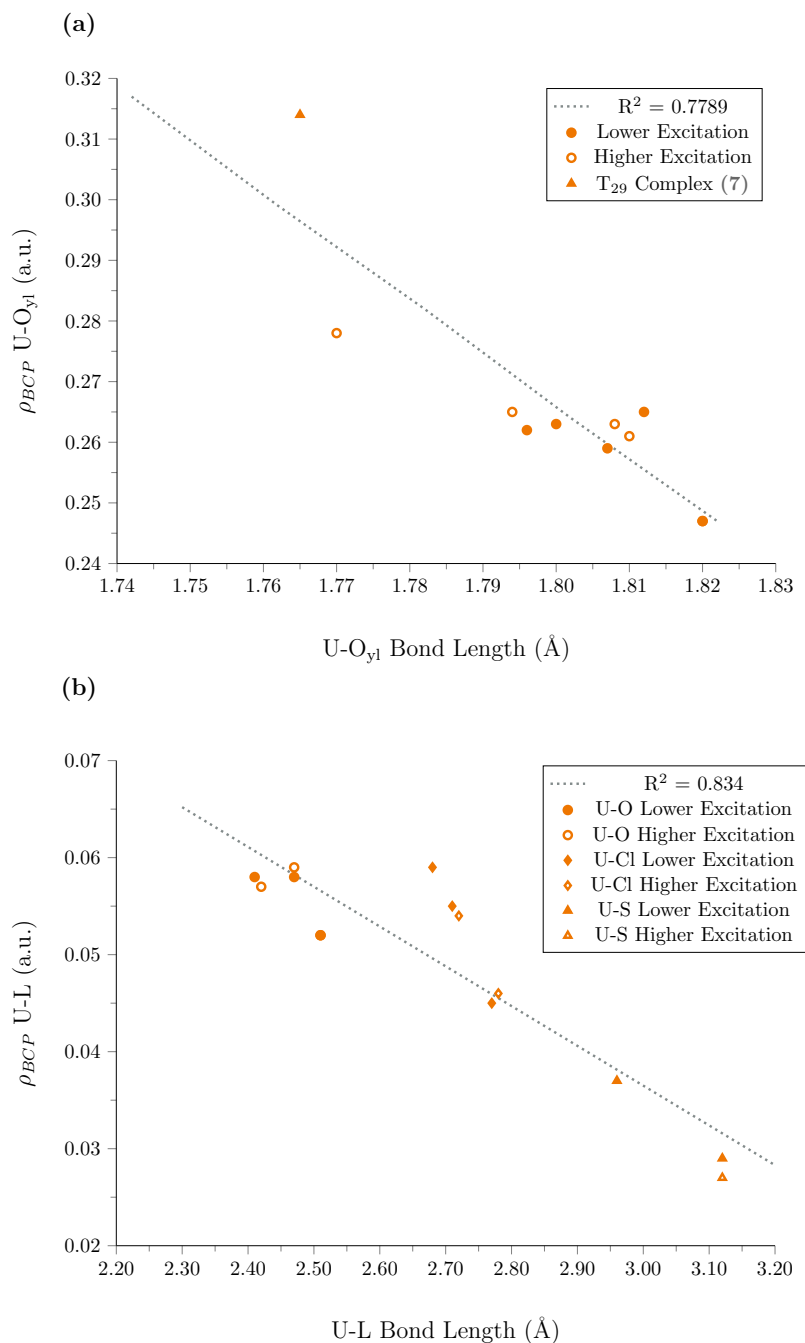


Figure 4.16: Graphs showing negative correlation between bond length and  $\rho_{BCP}$  at the excited state electronic structures at the excited state geometries for U-O<sub>yl</sub> (a) and U-L (b). The two different excitations for each complex are represented with filled and unfilled marker for the lower and higher energy excitations respectively.

At the ground state electronic structures at the ground state geometries, it was found that U-L  $\rho_{BCP}$  and  $\Delta E$  were negatively correlated and U-L bond length and  $\Delta E$  were positively correlated (Figure 4.9). Figure 4.17 shows that in general these correlations are also present in the excited state electronic structures at the excited state geometries but are weaker. In comparison to the data in Figure 4.9, data

sets between the coordinating ligand type are much closer together, particularly in **(b)** which has very strong positive correlation within the ligand groups. It is worth noting that out of the three sulfur data points, the two close together higher the rest of the data correspond to complex (7) with the sole lower data point representing  $T_1$  of complex (6).

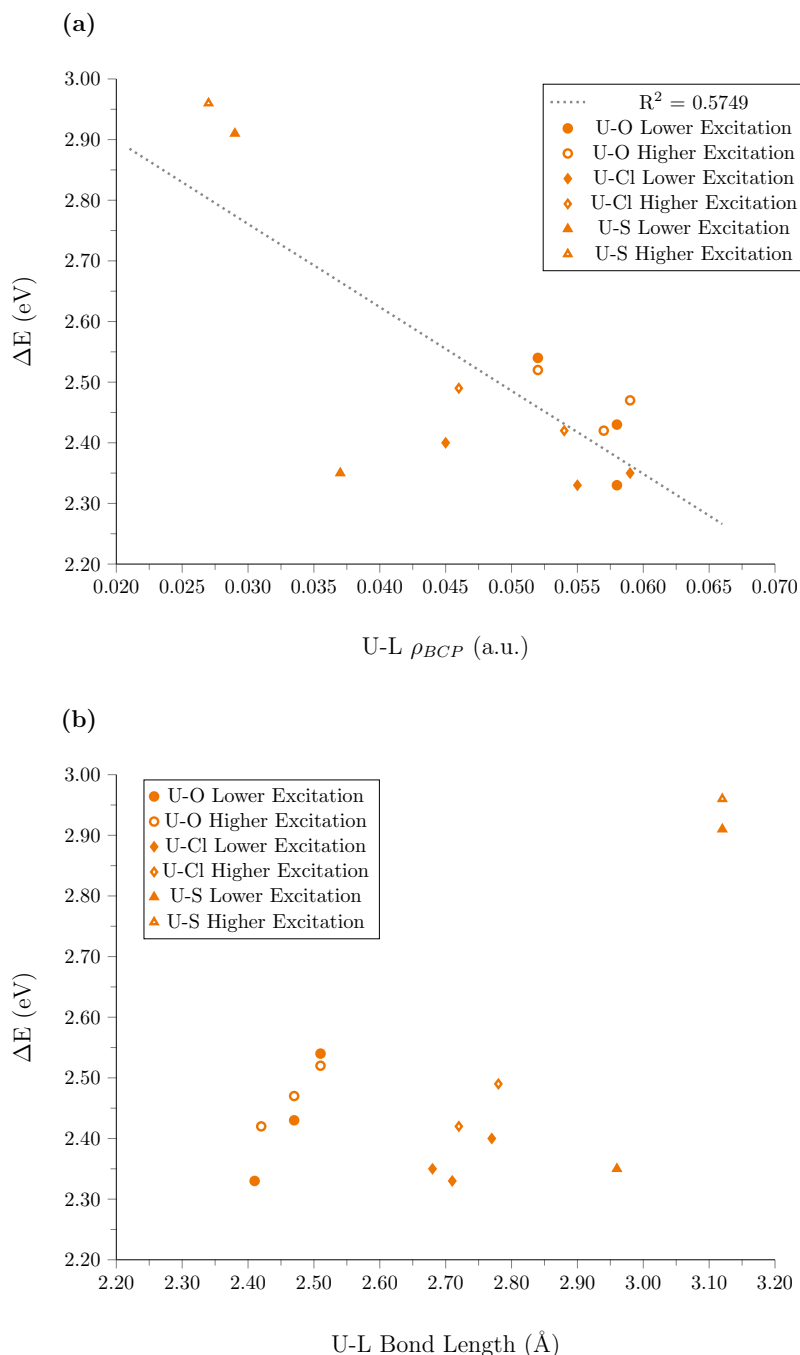


Figure 4.17: Graphs showing **(a)** general negative correlation between  $\rho_{BCP}$  U-L and excitation energy and **(b)** positive correlation between U-L bond length and excitation energy for each coordinating ligand type at the excited state electronic structures at the excited state geometries

In contrast to the ground state electronic structures at the ground state geometry, where there was no correlation between  $\text{U-O}_{\text{yl}} \rho_{\text{BCP}}$  and  $\Delta E$ , at the excited state electronic structures at the excited state geometries there is general positive correlation between the two metrics as shown in Figure 4.18.

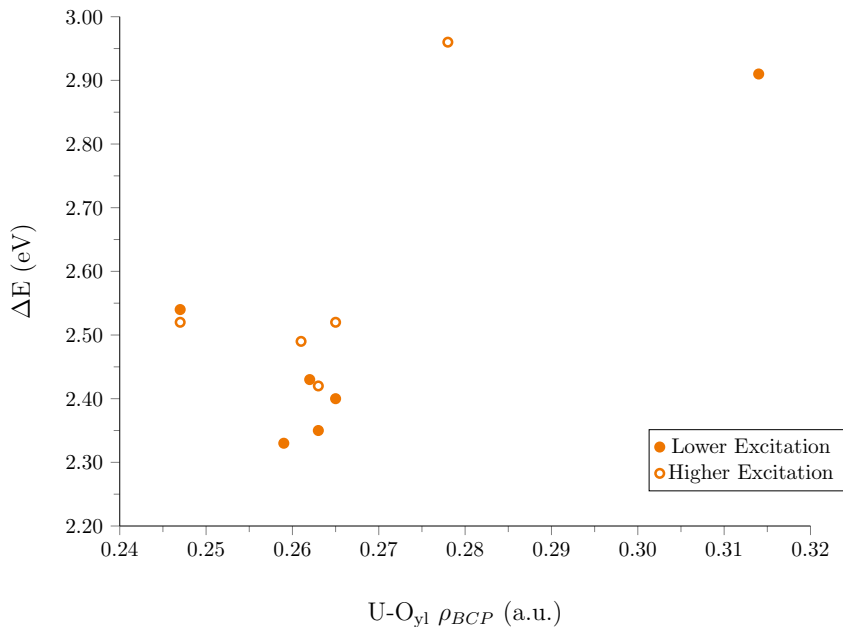


Figure 4.18: Graph showing general positive correlation between  $\text{U-O}_{\text{yl}} \rho_{\text{BCP}}$  and  $\Delta E$  at the excited state electronic structures at the excited state geometries

Interestingly, when  $\text{U-O}_{\text{yl}}$  bond length is plotted against  $\Delta E$  two curves form (Figure 4.19), one each for the higher and lower energy excitations; in which the excitation energy decreases with increasing  $\text{U-O}_{\text{yl}}$  bond length until  $\sim 1.805 \text{ \AA}$  and then increases past this point. The minimum point on these curves represents the minimum separation between the hole (bonding  $\sigma_u$ ) and particle (non-bonding  $\delta_u$ ) MOs. As the  $\text{U-O}_{\text{yl}}$  bond length decreases, the hole MO is stabilised as this causes an increase in  $\text{U-O}_{\text{yl}}$  orbital overlap and as a result of this relative stabilisation the excitation energy is blue shifted. At larger bond lengths there is a stronger interaction between uranium and the equatorial ligands which results in increased density in the equatorial plane and this results in a destabilisation in the particle MO.

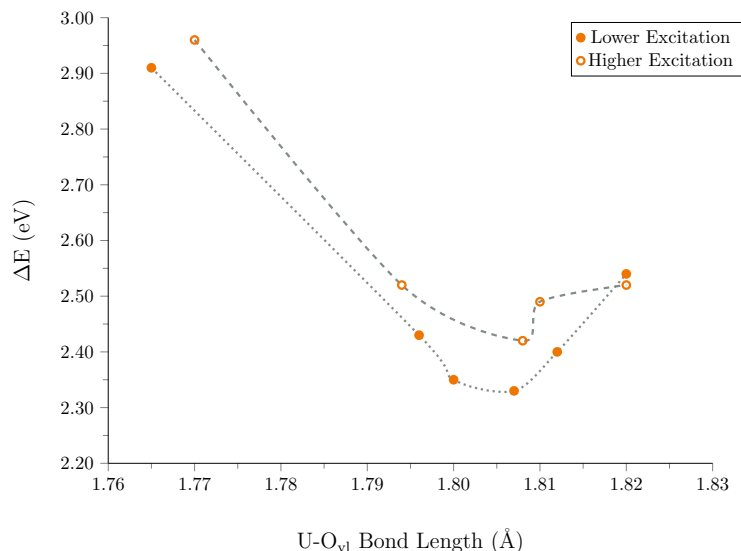


Figure 4.19: Correlation between U-O<sub>y1</sub> bond length and excitation energy, giving two curves for the higher and lower excited states at the excited state electronic structures at the excited state geometries

Figure 4.20 shows that there is no correlation between U-O<sub>y1</sub>  $\rho_{BCP}$  and U-L  $\rho_{BCP}$ , unlike at the ground state electronic structure at the ground state geometries (Figure 4.10). Interestingly, there is little variation between the metrics of the two excited states in each complex and no trends between the lower energy and higher energy excitations, with the exception of Figure 4.19. This suggests that there is little variation in the electronic structures between the excited state electronic structures at the excited state geometries in the complexes.

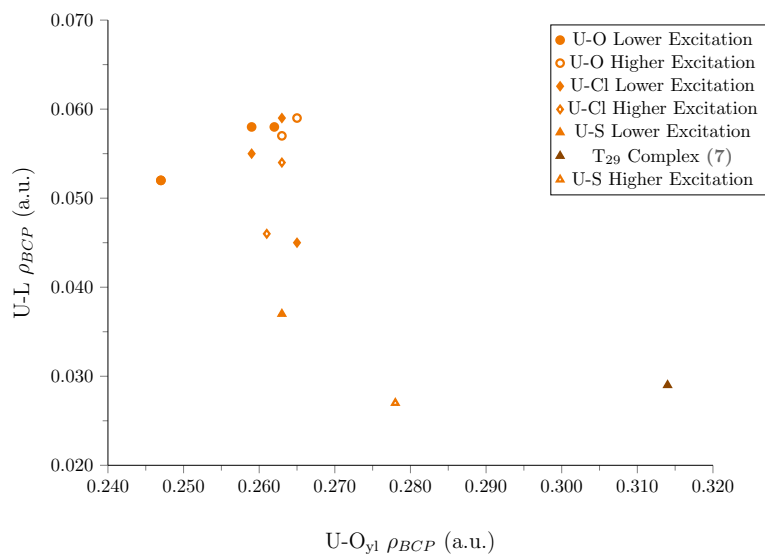


Figure 4.20: Graph showing no correlation between U-O<sub>y1</sub>  $\rho_{BCP}$  and U-L  $\rho_{BCP}$  at the excited state electronic structures at the excited state geometries

The topological data shows that upon excitation, charge is transferred from the bonding region of U-O<sub>yl</sub> but in order to rationalise the distribution of this charge the integrated properties, given in Tables 4.11 and 4.12, need to be considered.

In Chapter 3, it was found that comparing the excited state electronic structure at the excited state geometry to the ground state electronic structure at the ground state geometry ( $\Delta^{\text{ES}}$ ) of the  $\sigma_u \rightarrow \delta_u$  excitation resulted in;  $q_U$ ,  $\lambda_{\text{O}_{yl}}$  and  $\lambda_U$  decreasing,  $q_{\text{O}_{yl}}$  becoming less negative and  $\delta_{\text{U-O}_{yl}}$  increasing. This implies that in free uranyl, charge is transferred from the O<sub>yl</sub> and U centres to the U-O<sub>yl</sub> bonding region and hence the U-O<sub>yl</sub> bond increases in covalency at the excited state geometry.

At the excited state electronic structures at the excited state geometries, half the complexes exhibit the same increase in  $\delta_{\text{U-O}_{yl}}$  as in free uranyl, whilst in the other complexes  $\delta_{\text{U-O}_{yl}}$  decreases in the excited state geometries. An increase in  $\delta_{\text{U-O}_{yl}}$  is observed in: T<sub>1</sub> (1), T<sub>1</sub> (3), T<sub>1</sub> (4), T<sub>2</sub> (4) and T<sub>29</sub> (7). This trend was unexpected from the topological data and as such there is no correlation between  $\rho_{\text{BCP}}$  and  $\delta_{\text{U-O}_{yl}}$  at the excited state electronic structures at the excited state geometries (Figure 4.21) in contrast to linear correlation seen at the ground state geometries ((a) in Figure 4.11). It is also worth noting that there is no obvious chemical explanation for which complexes increase in  $\delta_{\text{U-O}_{yl}}$  and which decrease, especially as some complexes exhibit both trends in  $\delta_{\text{U-O}_{yl}}$  for their different excited state geometries, *i.e.* T<sub>1</sub> and T<sub>2</sub> in complex (1). Instead, the rest of the trends in the integrated QTAIM properties provide a clarification to the changes in electronic structure at the excited state geometries.

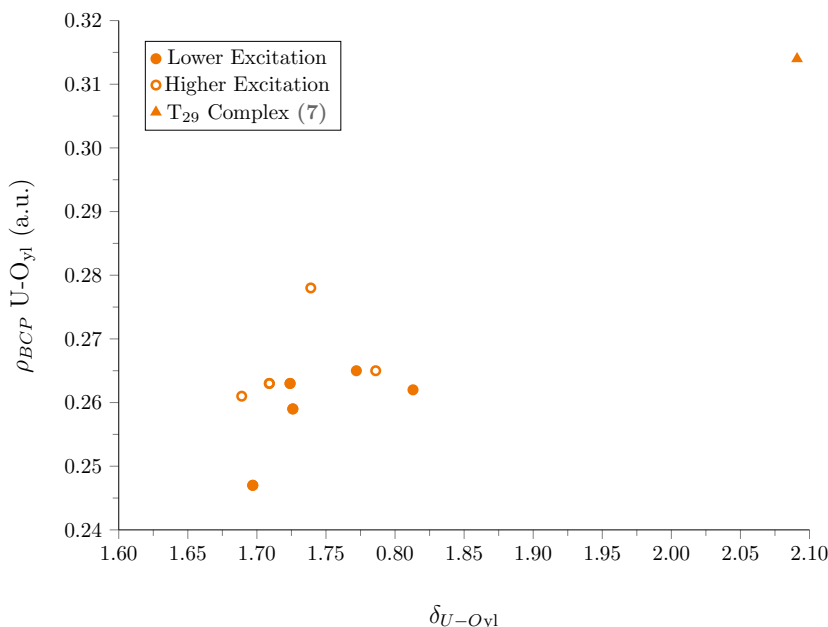


Figure 4.21: Graph showing no correlation between U-O<sub>yl</sub>  $\rho_{\text{BCP}}$  and  $\delta_{\text{U-O}_{yl}}$  at the excited state electronic structures at the excited state geometries

Interestingly, there is positive correlation between  $\rho_{BCP}$  and  $\delta_{U-L}$  for the U-L bonds of a individual ligand type as shown by Figure 4.22. These trends are very similar to those seen at the ground state ((b) in Figure 4.11) and when omitting the U-O data points the  $R^2$  value for the U-S and U-Cl data points becomes 0.903.

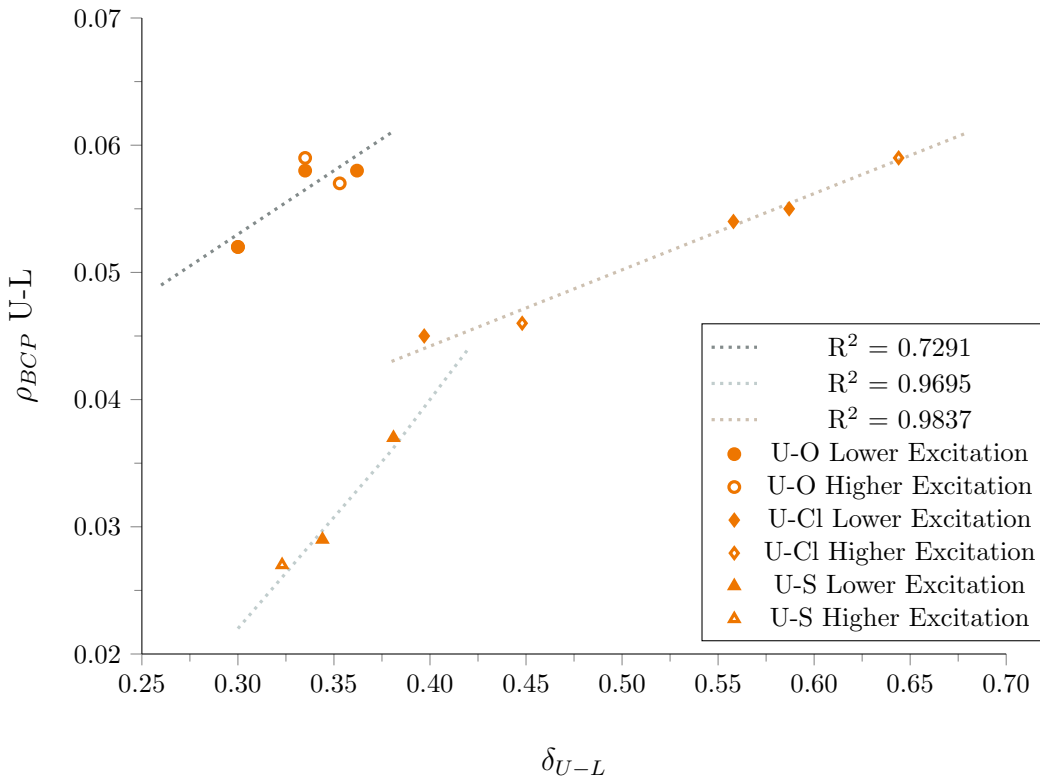


Figure 4.22: Graph showing positive correlation between U-L  $\rho_{BCP}$  and  $\delta_{U-L}$  of individual at the excited state electronic structures at the excited state geometries

Examination of the  $\delta_{U-L}$  metrics can provide some insight into the divide in the  $\delta_{U-O_{y1}}$  data. Again the increase/decrease in  $\delta_{U-L}$  is divided across the excited state geometries, a decrease is seen in complexes:  $T_1$  (1) and both excitations in complexes (3) and (7). These trends indicate that charge is transferred from the U-L bonding region to the U- $O_{y1}$  bonding region for:  $T_1$  (1),  $T_1$  (3) and  $T_{29}$  (7). However this data does not explain the increase in  $\delta_{U-O_{y1}}$  seen in both excited state geometries of (4) or the decrease in  $\delta_{U-O_{y1}}$  in  $T_{31}$  of complex (7).

$\lambda_U$  and  $\lambda_{O_{y1}}$  decrease in the excited state electronic structure of the excited state geometries for all complexes except:  $T_{31}$  (7) and both excited states of complex (1). It is worth noting that in  $T_3$  (3)  $\lambda_U$  increases and  $\lambda_{O_{y1}}$  decreases. The decrease in  $\lambda_U$  and  $\lambda_{O_{y1}}$  for both excited states of complex (4) indicates that charge is transferred from the U and  $O_{y1}$  centres to the U-L and U- $O_{y1}$  bonding regions. The increase in  $\lambda_U$  and  $\lambda_{O_{y1}}$  in  $T_{31}$  (7) indicates that charge is transferred from the U-L and U- $O_{y1}$  bonding regions onto the U and  $O_{y1}$  centres.

In contrast to the rest of the excited state geometries, both the excited state geometries of complex (1) show an increase in negative charge on  $O_{y1}$  and this is consistent with an increase in ionic interaction in the U- $O_{y1}$  bond. In all other excited state geometries  $q_{O_{y1}}$  becomes less negative which is balanced by  $q_U$  decreasing (*i.e.* becoming more negative) and as such there is little deviation between  $q_{UO_2}$  in the ground and excited state geometries for all the complexes except (1).

Table 4.13: Summary of the transfer of charge occurring at the excited state electronic structures at the excited state geometries

Complex	Excited State	Movement of Charge
(Free Uranyl) $[UO_2]^{2+}$	$T_3$	U, $O_{y1}$ → U- $O_{y1}$
(1) $[UO_2Cl_4]^{2-}$	$T_1$	U-L → U, $O_{y1}$ , U- $O_{y1}$
	$T_2$	U- $O_{y1}$ → U, $O_{y1}$ , U-L
(3) $[UO_2(C_2H_5NO_2)_2]^{2+}$	$T_1$	$O_{y1}$ , U, U-L → U- $O_{y1}$
	$T_3$	$O_{y1}$ , U- $O_{y1}$ , U-L → U
(4) $[UO_2(NO_3)_3]^{1-}$	$T_1$	$O_{y1}$ , U → U- $O_{y1}$ , U-L
	$T_2$	$O_{y1}$ , U → U- $O_{y1}$ , U-L
(5) $UO_2Cl_2(OPH_3)_2$	$T_1$	$O_{y1}$ , U, U- $O_{y1}$ → U-L
	$T_2$	$O_{y1}$ , U, U- $O_{y1}$ → U-L
(6) $UO_2Cl_2(SPH_3)_2$	$T_1$	$O_{y1}$ , U, U- $O_{y1}$ → U-L
	$T_{29}$	$O_{y1}$ , U, U-L → U- $O_{y1}$
(7) $UO_2(S_2PH_2)_2$	$T_{31}$	U- $O_{y1}$ , U-L → $O_{y1}$ , U

Table 4.13 summarises the movement of charges in the complexes for each excited state geometry. From this it is clear that the movement of charge is dependent on the complex and the excited state in some cases. However, most excited state geometries depict that charge is transferred from the U/ $O_{y1}$  atoms to the U-L and/or U- $O_{y1}$  bonding regions. The outliers to this trend are both excited states for complex (1),  $T_3$  of complex (3) and  $T_{31}$  of complex (7).

## 4.4 Conclusions

In this chapter QTAIM metrics were analysed at both the ground and electronically excited state geometries of different uranyl complexes. Equatorial ligation resulted in two bonding MOs which both had overall  $\sigma_u$  nature; these MOs had bonding ( $\sigma_u^+$ ) and antibonding ( $\sigma_u^-$ ) interactions between the uranium and the equatorial ligands, with the bonding  $\sigma_u$  MO being more stabilised in comparison to the antibonding  $\sigma_u$  MO. Upon analysing the  $\sigma_u \rightarrow \delta_u$  excitation, it was found that in all the complexes, both the  $\sigma_u^+$  and  $\sigma_u^-$  MOs contributed to the overall excitation and the excitation energies could be rationalised by which  $\sigma_u$  MO had the larger contribution to the excitation. Upon equatorial ligation the excitation energy of the  $\sigma_u \rightarrow \delta_u$  excitation was blue-shifted in comparison to free uranyl.

Upon analysis of the QTAIM metrics, it was concluded that equatorial complexation results in:  $\rho_{\text{BCP}}$ ,  $\lambda_{\text{U}}$  and  $\delta_{\text{U-O}_{y1}}$  all decrease,  $\lambda_{\text{O}_{y1}}$  increases and  $q_{\text{U}}$  and  $q_{\text{O}_{y1}}$  become more negative. This is consistent with charge moving from the U-O<sub>y1</sub> bonding region to the O<sub>y1</sub> centres, the covalency of the U-O<sub>y1</sub> bond decreasing and an increase in the ionic nature of the U-O<sub>y1</sub> bond.

Investigation into trends between the total  $\delta_{\text{U-O}_{y1}}$  and combinations of total  $\delta_{\text{U-L}}$  and localisation on  $\lambda_{\text{UO}_2}$  resulted in no overall correlation. However this investigation showed that total  $\lambda_{\text{UO}_2}$  in the complexes increased in comparison to free uranyl, which was solely due to the increase in  $\lambda_{\text{O}_{y1}}$ . This is consistent with some of the electron density being transferred from the U-O<sub>y1</sub> bonding region onto the O<sub>y1</sub>; although the lack of correlation highlights that not all the charge is transferred to O<sub>y1</sub>. As free uranyl does not have any equatorial ligands, the same comparison could not be made for  $\delta_{\text{U-L}}$  however, it was concluded that it is highly likely that charge is also transferred to U-L bonding region with largest contribution coming from complex (2). This investigation was summarised with the conclusion that the transfer of charge is more complex with the likelihood of the charge being distributed throughout the equatorial ligands being the most plausible explanation for the gain in  $\lambda_{\text{UO}_2}$  and  $\delta_{\text{U-L}}$  not equalling the loss in  $\delta_{\text{U-O}_{y1}}$ .

At the excited state geometries there was little change in both the excitation energy and the bond lengths; there was a red shift in the excitation energy and an increase in U-O<sub>y1</sub> and U-L bond lengths in agreement with that seen in free uranyl. In contrast to the ground state however, the excited state QTAIM metrics were somewhat complex to examine, with no matching ordering of trends or even the same trends between complexes at different excited state structures. Overall, there were some similarities in across the complexes in terms of the  $\rho_{\text{BCP}}$ ,  $q$  and  $\lambda$ . The largest variation was seen in  $\delta$ , with half the excited state complexes increasing and half decreasing for both  $\delta_{\text{U-L}}$  and  $\delta_{\text{U-O}_{y1}}$  but these did not commensurate with each other, *i.e.* the an excited state geometry which increased in  $\delta_{\text{U-O}_{y1}}$  did not always show a decrease in  $\delta_{\text{U-L}}$ . For most of the excited state geometries, it was concluded

that charge is transferred from the U and/or  $O_{yl}$  centres to the U- $O_{yl}$  and/or U-L bonding regions. Interestingly, an increase in ionic character of the U- $O_{yl}$  bond was only seen in both excited states for complex (1).

Despite the QTAIM metrics, excitation energy and nature of these complexes being relatively similar at the ground state geometry, at the excited state geometries these complexes all exhibit different behaviours to each other even though the geometries are only marginally different to those in the ground state. This highlights the significance of exploring the excited state geometries through QTAIM analysis as the change electronic structure impacts the changes in bonding within similar complexes and excited state natures. In the future, further work exploring excited state geometries of different excitations can be utilised to further explore trends in covalency of simple uranyl complexes. Combining the excitations studied in Chapter 3 could provide an interesting starting point and comparison. It may also be beneficial to only study complexes which have the same equatorial ligand as to best find trends between nature of the ligand binding and the covalency. The sulfur complexes exhibited the most substantial changes to that of free uranyl and hence investigations of other soft ligands could give an interesting comparison to the sulfur complexes studies here.

# References

- [1] A. Formanuk, A. M. Ariciu, F. Ortu, R. Beekmeyer, A. Kerridge, F. Tuna, E. J. McInnes, D. P. Mills, *Nat. Chem.* **2017**, *9*, 578–583.
- [2] L. R. Morss, N. Edelstein, J. Fuger, J. J. Katz, *The Chemistry of the Actinide and Transactinide Elements*, 4th, Springer, **2010**.
- [3] L. S. Natrajan, M. H. Paden, *f-block elements recovery*, Vol. 58, **2013**, pp. 140–184.
- [4] P. Di Pietro, A. Kerridge, *Inorg. Chem.* **2016**, *55*, 573–583.
- [5] P. Di Pietro, A. Kerridge, *Phys. Chem. Chem. Phys.* **2016**, *18*, 16830–16839.
- [6] H. H. Dam, D. N. Reinhoudt, W. Verboom, *Chem. Soc. Rev.* **2007**, *36*, 367–377.
- [7] F. W. Lewis, M. J. Hudson, L. M. Harwood, *Synlett* **2011**, *18*, 2609–2632.
- [8] I. Kirker, N. Kaltsoyannis, *Dalton Trans.* **2011**, *40*, 124–131.
- [9] N. Kaltsoyannis, *Inorg. Chem.* **2013**, *52*, 3407–3413.
- [10] K. Servaes, C. Hennig, R. Van Deun, C. Görrler-Walrand, *Inorg. Chem.* **2005**, *44*, 7705–7707.
- [11] D. L. Clark, S. D. Conradson, R. J. Donohoe, D. W. Keogh, D. E. Morris, P. D. Palmer, R. D. Rogers, C. D. Tait, *Inorg. Chem.* **1999**, *38*, 1456–1466.
- [12] N. W. Alcock, D. J. Flanders, T. J. Kemp, M. A. Shand, *J. Chem. Soc. Dalton Trans* **1985**, 517–521.
- [13] T. Bäcker, A. V. Mudring, *Z. Anorg. Allg. Chem.* **2010**, *636*, 1002–1005.
- [14] E. Hashem, T. McCabe, C. Schulzke, R. J. Baker, *Dalton Trans.* **2014**, *43*, 1125–1131.
- [15] D. Meng, N. Pu, L. Mei, T. Sun, L. Xu, W. Shi, J. Chen, C. Xu, *J. Radioanal. Nucl. Chem.* **2018**, *317*, 121–129.
- [16] K. Pierloot, E. Van Besien, E. Van Lenthe, E. J. Baerends, *J. Chem. Phys.* **2007**, *126*.
- [17] R. G. Denning, *J. Phys. Chem. A.* **2007**, *111*, 4125–4143.
- [18] K. Pierloot, E. Van Besien, *J. Chem. Phys.* **2005**, *123*.

- [19] S. Matsika, R. M. Pitzer, *J. Phys. Chem. A* **2001**, *105*, 637–645.
- [20] D. N. Sanwal, D. D. Pant, *Proc. Indian Acad. Sci. - Section A* **1969**, *69*, 324–337.
- [21] S. Tsushima, *Dalton Trans.* **2011**, *40*, 6732–6737.
- [22] K. I. Ingram, L. J. L. Häller, N. Kaltsoyannis, *Dalton Trans.* **2006**, *2*, 2403–2414.
- [23] R. Beekmeyer, A. Kerridge, *Inorganics* **2015**, *3*, 482–499.
- [24] M. Dolg, P. Fulde, W. Kuchle, C. S. Neumann, H. Stoll, *J. Chem. Phys.* **1991**, *94*, 3011–3017.
- [25] A. Kerridge, R. Coates, N. Kaltsoyannis, *J. Phys. Chem. A* **2009**, *113*, 2896–2905.
- [26] A. Kerridge, *Dalton Trans.* **2013**, *42*, 16428–16436.
- [27] O. Mooßen, M. Dolg, *Chem. Phys. Lett.* **2014**, *594*, 47–50.
- [28] V. Vallet, U. Wahlgren, I. Grenthe, *J. Phys. Chem. A* **2012**, *116*, 12373–12380.
- [29] P. Tecmer, A. S. P. Gomes, U. Ekström, L. Visscher, *Phys. Chem. Chem. Phys.* **2011**, *13*, 6249–6259.
- [30] P. Tecmer, N. Govind, K. Kowalski, W. A. De Jong, L. Visscher, *J. Chem. Phys.* **2013**, *139*.
- [31] R. G. Denning in *Electronic Structure and Bonding in Actinyl Ions*, **1992**, pp. 217–276.
- [32] J. Su, K. Zhang, W. H. Eugen Schwarz, J. Li, *Inorg. Chem.* **2011**, *50*, 2082–2093.
- [33] Z. Zhang, R. M. Pitzer, *J. Phys. Chem. A* **1999**, *103*, 6880–6886.
- [34] C. Görller-Walrand, L. G. Vanquickenborne, *J. Chem. Phys.* **1971**, *54*, 4178–4186.
- [35] C. Görller-Walrand, L. G. Vanquickenborne, *J. Chem. Phys.* **1972**, *57*, 1436–1440.
- [36] C. Görller-Walrand, S. De Houwer, L. Fluyt, K. Binnemans, *Phys. Chem. Chem. Phys.* **2004**, *6*, 3292–3298.
- [37] B. Miehlich, A. Savin, H. Stoll, H. Preuss, *Chem. Phys. Lett.* **1989**, *157*, 200–206.
- [38] C. Lee, W. Yang, R. G. Parr, *Phys. Rev. B* **1988**, *37*, 785–789.
- [39] A. D. Becke, *J. Chem. Phys.* **1993**, *98*, 1372–1377.
- [40] A. D. Becke, *Phys. Rev. A* **1988**, *38*, 3098–3100.

- [41] R. Krishnan, J. S. Binkley, R. Seeger, J. A. Pople, *J. Chem. Phys.* **1980**, *72*, 650–654.
- [42] M. J. Frisch, G. W. Trucks, H. B. Schlegel, G. E. S. an M. A. Robb, J. R. Cheeseman, J. A. J. Montgomery, T. Vreven, K. N. Kudin, J. C. Burant, J. M. Millam, S. S. Iyengar, J. Tomasi, V. Barone, B. Mennucci, M. Cossi, G. Scalmani, N. Rega, G. A. Petersson, H. Nakatsuji, M. Hada, M. Ehara, K. Toyota, R. Fukuda, J. Hasegawa, M. Ishida, T. Nakajima, Y. Honda, O. Kitao, H. Nakai, M. Klene, X. Li, J. E. Knox, H. P. Hratchian, J. B. Cross, V. Bakken, C. Adamo, J. Jaramillo, R. Gomperts, R. E. Stratmann, O. Yazyez, A. J. Austin, R. Cammi, C. Pomelli, J. W. Ochterski, P. Y. Ayala, K. Morokuma, G. A. Voth, P. Salvador, J. J. Dannenberg, V. G. Zakrzewski, S. Dapprich, A. D. Daniels, M. C. Strain, O. Farkas, D. K. Malick, A. D. Rabuck, K. Raghavachari, J. B. Foresmann, J. V. Ortiz, Q. Cui, A. G. Baboul, S. Clifford, J. Cioslowski, B. B. Stefanov, G. Liu, A. Liashenko, P. Piskorz, I. Komaromi, R. L. Martin, D. J. Fox, T. Keith, M. A. Al.Laham, C. Y. Peng, A. Nanayakkara, M. Challacombe, P. M. W. Gill, B. Johnson, W. Chen, M. W. Wong, C. Gonzalez, J. A. Pople, *Gaussian 09. 2015 Gaussian Inc. Wallingford CT*.
- [43] W. Küchle, M. Dolg, H. Stoll, H. Preuss, *J. Chem. Phys.* **1994**, *100*, 7535–7542.
- [44] X. Cao, M. Dolg, H. Stoll, *J. Chem. Phys.* **2003**, *118*, 487–496.
- [45] X. Cao, M. Dolg, *J. Mol. Struc-THEOCHEM* **2004**, *673*, 203–209.
- [46] D. Feller, *J. Comput. Chem.* **1996**, *17*, 1571–1586.
- [47] B. P. Pritchard, D. Altarawy, B. Didier, T. D. Gibson, T. L. Windus, *J. Chem. Inf. Model.* **2019**, *59*, 4814–4820.
- [48] K. L. Schuchardt, B. T. Didier, T. Elsethagen, L. Sun, V. Gurumoorthi, J. Chase, J. Li, T. L. Windus, *J. Chem. Inf. Model.* **2007**, *47*, 1045–1052.
- [49] T. H. J. Dunning, *J. Chem. Phys.* **1989**, *90*, 1007–1023.
- [50] R. A. Kendall, T. H. J. Dunning, R. J. Harrison, *J. Chem. Phys.* **1992**, *96*, 6796–6806.
- [51] D. E. Woon, T. H. J. Dunning, *J. Chem. Phys.* **1993**, *98*, 1358–1371.
- [52] S. Hirata, M. Head-Gordon, *Chem. Phys. Lett.* **1999**, *314*, 291–299.
- [53] E. Runge, E. K. U. Gross, *Phys. Rev. Lett.* **1984**, *53*, 997–1000.
- [54] E. K. U. Gross, W. Kohn in *Density Functional Theory of many-fermion systems*, (Ed.: P.-O. Löwdin), **1990**, pp. 255–291.
- [55] T. A. Keith, AIMAll, **2014**.
- [56] T. Lu, F. Chen, *J. Comput. Chem.* **2012**, *33*, 580–592.

- [57] K. Servaes, C. Hennig, I. Billard, C. Gaillard, K. Binnemans, C. Görrler-Walrand, R. Van Deun, *Eur. J. Inorg. Chem.* **2007**, 5120–5126.

## Chapter 5

# Investigating the effect of bending the uranyl unit on electronic structure and bonding

*Building on the previous chapter herein, the uranyl unit is distorted and the corresponding effect of this on the electronic structure, bonding and excitation energies are investigated. Firstly, the low-lying excitations in free uranyl were studied with active space methods and it was found that as the uranyl unit deviates from linearity, excitation energies from ungerade hole MOs are red shifted. Spin-orbit coupled calculations also revealed that as the uranyl unit is distorted the  $\sigma_u \rightarrow \delta_u$  excitation becomes more optically accessible. Synthetically realised complexes with a significantly small O-U-O angle were then studied ((i) - (iii)) using the same methodology as in Chapter 4. QTAIM analysis at the ground state geometry indicated that the origin of the bending in these complexes was steric in origin as the QTAIM results were quantitatively similar to those studied in Chapter 4. It was hypothesised that exciting out of a bonding orbital into a non-bonding orbital could weaken the  $U-O_{yl}$  bond and further enhance bending at the excited state geometries. At the excited state geometries further distortion of the uranyl unit was achieved and the QTAIM analysis showed a weakening of the  $U-O_{yl}$  bond as predicted. Building on these findings theoretical complexes were designed ((a) - (e)) and these complexes had significantly smaller angles than in the literature. From these promising theoretical complexes, it can be suggested that to initiate a significant bend in uranyl, small, rigid negatively charged macrocycles should be utilised in order to ensure side-on coordination with uranyl and significant bonding interactions between the uranyl unit and the coordinating macrocycle.*

## 5.1 Introduction

There is growing interest in increasing the reactivity of the uranyl unit, in order to further explore organometallic and coordination chemistry of uranyl; potentially leading to many chemical applications. [1–4] Most notable of which is the reduction of the uranyl unit, which has been utilised in the treatment of contaminated legacy sites. [5–9] There are currently two promising strategies to increase the reactivity of uranyl: by distorting the planarity of the equatorial coordination plane [10–13] and breaking the linearity of the uranyl unit. [1, 10, 14, 15] Within this work, the linearity of the uranyl unit was broken via bending. The distortion from linearity weakens the U-O bonds and, as such increases the reactivity of the uranyl unit. This chapter is solely interested in the effects of bending on the covalency and investigating ligands which will enhance the bending.

There are two factors which cause bending in the uranyl unit, the first is unfavourable steric interactions and the second electronic in origin. [16] The former are somewhat straightforward to predict, however, there are six reported complexes which possess a significant bending of the O-U-O unit (angles between  $176^\circ$  and  $167^\circ$ ) without significant steric interaction. [17–21] These six complexes either contain a methanediide or bridged oxo clusters ligand types. In all of these complexes, the uranyl oxygens bend away from the electron donating ligands, with the largest distortions occurring in the uranyl methanediide complexes, due to their stronger donating ability. These examples do not feature ligands with bulky substituents such as: a 12-membered pyridinophane macrocycle ( $^{\text{H}}\text{N}4$ ), phenanthroline or O-2,6- $^t\text{Bu}_2\text{C}_6\text{H}_3$ , (studied in Section 5.3.2) and therefore steric interactions are not the predominant cause of distortion in these cases.

Across the plethora of uranyl complexes, the uranyl unit is always in the *trans* conformation; there have been several attempts to synthesise complexes with the uranyl unit in the *cis* conformation, but so far these have been unsuccessful. [22–25] According to the Cambridge Structural Database, [26] the vast majority of the 4000+ uranyl complexes record the O-U-O angle in the uranyl unit to be  $175^\circ$  or larger. [16] Pedrick *et al.* [10] investigated the coordination of a 12-membered macrocyclic ligand (2,11-diaza[3,3](2,6) pyridinophane) to uranyl, in which they hypothesised that the coordination of a 16-member or less macrocycle to uranyl would induce a *trans* to *cis* isomerisation in the uranyl unit. Although they did not achieve the desired outcome, this complexation resulted in one of the smallest O-U-O angles in the literature,  $162.8^\circ$ .

Crown ethers are cyclic compounds made up of a number of repeating ether units which are known to selectively complex with metal cations in a way so as to match the size of the cation radii with the cavity size. [27, 28] This property is of particular interest to the final study in this chapter (Section 5.3.3) as the size of the crown ether dictates which binding mode is favoured. A crown ether can

bind a metal cation by either inclusion, where the cation is encapsulated within the crown ether or forming an outer-sphere complex where the cation is partially exposed and allowing solvation to occur. [29] Therefore, smaller crown ethers can be utilised to ensure side-on complexation and hence maximising steric interaction between the cyclic ring and the uranyl oxygens and with the aim of initiating a bend. Binnemans and co-workers [30] experimentally studied the spectroscopic properties of uranyl complexation with crown ethers and their analogues with a variation of pore sizes. They reported that crown ethers with six oxygen atoms (*i.e.* 18C6) have the ideal cavity size to coordinate uranyl via inclusion; which is consistent with other literature. [31–34] It has also been shown that 12C4 actinyl complexes readily hydrate and hence side on coordination of 12C4 with actinyls is preferred. In contrast when complexed with larger crown ethers, hydration was not achieved and thus indicating the actinyl was complexed via inclusion. [35] A set of computation studies on various complexes of uranyl and 12C4 was conducted by Jian *et al.* [36]; they reported a series of small O-U-O angles when the 12C4 was bound side on, the smallest of which was the  $[\text{UO}_2(12\text{C4-H})]^+$  complex ( $120.7^\circ$ ).

Another class of macrocycles which have been known to complex uranyl are porphyrinoid-based macrocycles; the Sessler group [37] have extensively studied large Schiff-based expanded porphyrins, such as the 18-membered alaskaphyrin ( $\text{C}_{36}\text{H}_{42}\text{N}_6\text{O}_4$ ). The complexes, all larger than 16 membered rings, were found to bind uranyl via inclusion. [13, 38–47]

This chapter is comprised of three separate studies all investigating the optically allowed excitation of principally  $\sigma_u \rightarrow \delta_u$  character and the effect of this excitation on the distortion of the uranyl unit at the excited state geometries of the complexes. It was hypothesised that by exciting out of a bonding orbital into a non-bonding orbital that the U-O<sub>y1</sub> bond would weaken and hence facilitate enhanced bending of the uranyl unit.

Firstly, free uranyl was studied at a range of different O-U-O angles, 180-150° using multiconfigurational methods (Section 5.3.1). In this study, the six lowest lying excitations of each irrep of the  $c_{2v}$  point group were investigated ( $a_1$ ,  $a_2$ ,  $b_1$  &  $b_2$ ). These excitations correspond exclusively to transitions between the bonding and non-bonding MOs (Figure 5.1). This investigation was a preliminary study of how bending affects the excitation energies and in particular the optically accessible excitation of principally  $\sigma_u \rightarrow \delta_u$  character. Initially it was imperative to investigate whether the  $\sigma_u \rightarrow \delta_u$  excitation becomes more optically accessible when the uranyl unit deviates from linear. The general changes in the excitation energies of states involving bonding to non-bonding MOs with both triplet and singlet spin are investigated with second order multiconfigurational perturbation theory (CASPT2; Section 2.11.2) and spin-orbit coupled calculations were also run with the restricted active space state interaction method (RASSI), specifically focusing on how the oscil-

lator strength varies in the  $\sigma_u \rightarrow \delta_u$  triplet excitation. Currently, the smallest O-U-O angle synthetically synthesised is no smaller than  $160^\circ$  and hence it was decided that the minimum angle studied would be  $150^\circ$ .

Second, experimentally relevant complexes which have some of the smallest O-U-O angles in the literature, as reviewed by Hayton were investigated at both the ground and excited state geometries. [1, 10, 16, 48] Three complexes from this review, (i) - (iii), shown in Figure 5.4, were selected based on a variety of ligand coordination and that were sufficiently small for efficient computation. QTAIM analysis was used to investigate the electronic structure and bonding of the uranyl unit in these complexes. The optically allowed excitation of principally  $\sigma_u \rightarrow \delta_u$  nature at both ground and excited state geometries was also investigated. By exploring this excitation, further investigation into the electronic structure can give insight into potential weakening of the U-O bonds and subsequent photochemical availability.

Finally, theoretical complexes, (a)-(e), with small macrocyclic ligands were studied in an attempt to further decrease the O-U-O angle. The literature suggests that in order to dictate side-on complexation, a macrocycle of similar size to 12C4 or 16-membered porphyrin-based ligand would be ideal. [10, 35] Two different types of macrocycle were chosen: crown ether and aromatic porphyrinoid, which bind via oxygen and nitrogen respectively. It was rationalised that as oxygen and nitrogen are strongly electron donating they would have strong interactions with uranium and this donating effect would also further initiate a bend through electronic origins as well as steric interactions from the macrocyclic rings. The 12C4 and 8C4 (known as tetroxocane [49]) crown ether ligands were chosen as the crown ethers to study. 8C4 has been known to bind lithium but in a so-called 'perching complex', where the lithium ion is above the plane of the crown ether. [50–52] Porphyrin and phthalocyanine macrocycles were also chosen as these porphyrinoid macrocycles have similar structures to that of the macrocycles studied by Pedrick *et. al* and although slightly larger (16-membered rings compared to 12-membered) it was hypothesised that the rigidity of these aromatic macrocycles would increase the steric interactions and initiate a larger bend. It was hypothesised that side-on coordination of these macrocycles would cause a bend in the uranyl unit due to unfavourable steric interactions and this may be emphasised at the excited state geometries.

## 5.2 Methodology

### 5.2.1 Bending bare uranyl - Multiconfigurational study

All calculations were performed using version 19.11 of openmolcas [53, 54] with the ANO-RCC all-electron basis set [55–59] utilising the contractions U(9s8p6d4f1g) and O(4s3p2d). This contraction was specifically selected to match the aug-cc-pVDZ [60, 61] basis set used in Chapters 3, 4 and 6.

Singlet and triplet excitations were run for each irrep of the  $c_{2v}$  point group ( $a_1$ ,  $a_2$ ,  $b_1$  &  $b_2$ ) at the CASPT2 level. These calculations were conducted with no IPEA (Ionisation Potential Electron Affinities) shift as it was found that the excitations energies best matched the literature [62–64] when the default IPEA was not used. The IPEA shift modifies the energies of active orbitals so that they are closer to the ionisation energies and electron affinities of hole orbitals. [53, 54, 65] A (12,16) active space, as defined in Section 2.11.2 of Chapter 2, was utilised, which contained the bonding, non-bonding and antibonding orbitals of uranyl, shown in Figure 5.1.

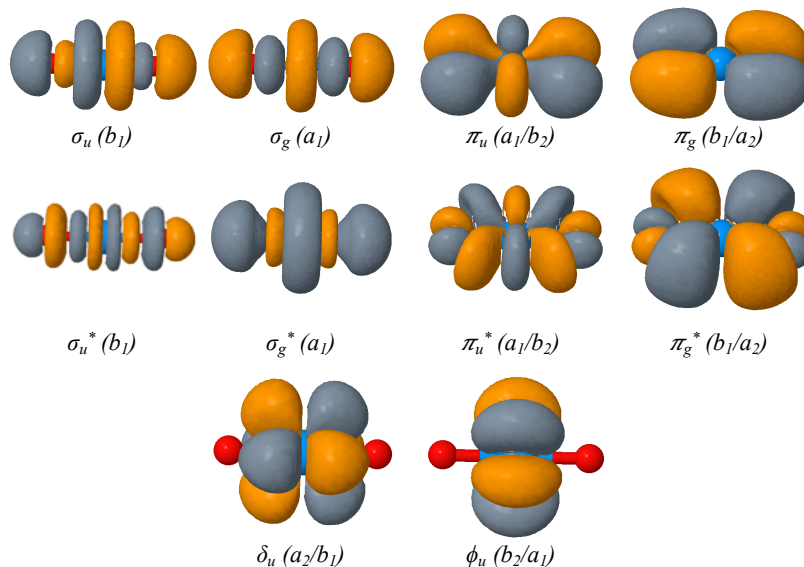


Figure 5.1: Bonding (top) antibonding (middle) and non-bonding (bottom) MOs of uranyl included in the active space. The irrep, in the  $c_{2v}$  point group is noted in brackets and only one of the two degenerate MOs are shown for the  $\pi_u$ ,  $\pi_g$ ,  $\delta_u$  and  $\phi_u$  MOs.

For each given irrep of the  $c_{2v}$  point group, the 6 lowest excitations were recorded, for both singlet and triplet spins, these excitations encompass all transitions between the bonding and non-bonding MOs; the break-down of these excitations in terms of irreps are shown in Table 5.1.

### 5.2.2 DFT Studies

For both DFT studies; the hybrid B3LYP [66–70] exchange–correlation functional was utilised in the Gaussian09 (Revision E.01) [71] programme. The Stuttgart RSC 1997 [72–74] basis set and associated small effective core potential (60 electrons), acquired from the basis-set exchange [55–57] was used for uranium while the correlation consistent cc-pVDZ [60, 75] Dunning basis set was implemented for the small elements (H, C, N, O). Geometry optimisations and excitations using the Tamm–Dancoff Approximation (TDA) [76] to TD-DFT were calculated for both the ground and excited state geometries. All structures were characterised as minima by vibrational frequency analysis. QTAIM analysis on the uranyl unit for the com-

Table 5.1: Symmetry properties of the irreps which contribute to the six lowest excitations for each irrep.

Irrep	Transition	MO Character		Irrep	Transition	MO Character
A <sub>1</sub>	b <sub>1</sub> →b <sub>1</sub>	$\sigma_u \rightarrow \delta_u$		B <sub>1</sub>	b <sub>1</sub> →a <sub>1</sub>	$\sigma_u \rightarrow \phi_u$
	a <sub>1</sub> →a <sub>1</sub>	$\pi_u \rightarrow \phi_u$			a <sub>1</sub> →b <sub>1</sub>	$\pi_u \rightarrow \delta_u$
	b <sub>2</sub> →b <sub>2</sub>	$\pi_u \rightarrow \phi_u$			b <sub>2</sub> →a <sub>2</sub>	$\pi_u \rightarrow \delta_u$
	a <sub>1</sub> →a <sub>1</sub>	$\sigma_g \rightarrow \phi_u$			a <sub>1</sub> →b <sub>1</sub>	$\sigma_g \rightarrow \delta_u$
	b <sub>1</sub> →b <sub>1</sub>	$\pi_g \rightarrow \delta_u$			b <sub>1</sub> →a <sub>1</sub>	$\pi_g \rightarrow \phi_u$
	a <sub>2</sub> →a <sub>2</sub>	$\pi_g \rightarrow \delta_u$			a <sub>2</sub> →b <sub>2</sub>	$\pi_g \rightarrow \phi_u$
A <sub>2</sub>	b <sub>1</sub> →b <sub>2</sub>	$\sigma_u \rightarrow \phi_u$		B <sub>2</sub>	b <sub>1</sub> →a <sub>2</sub>	$\sigma_u \rightarrow \delta_u$
	a <sub>1</sub> →a <sub>2</sub>	$\pi_u \rightarrow \delta_u$			a <sub>1</sub> →b <sub>2</sub>	$\pi_u \rightarrow \phi_u$
	b <sub>2</sub> →b <sub>1</sub>	$\pi_u \rightarrow \delta_u$			b <sub>2</sub> →a <sub>1</sub>	$\pi_u \rightarrow \phi_u$
	a <sub>1</sub> →a <sub>2</sub>	$\sigma_g \rightarrow \delta_u$			a <sub>1</sub> →b <sub>2</sub>	$\sigma_g \rightarrow \phi_u$
	b <sub>1</sub> →b <sub>2</sub>	$\pi_g \rightarrow \phi_u$			b <sub>1</sub> →a <sub>2</sub>	$\pi_g \rightarrow \delta_u$
	a <sub>2</sub> →a <sub>1</sub>	$\pi_g \rightarrow \phi_u$			a <sub>2</sub> →b <sub>1</sub>	$\pi_g \rightarrow \delta_u$

plexes was conducted using version 19.02.12 of AIMAll [77] and density difference plots were generated using version 3.6 of Multiwfn. [78]

It is worth noting the basis set change; in Chapters 3, 4 and 6, the aug-cc-pVDZ basis set was used; however for these larger complexes, obtaining minima geometries at both the ground and excited states was problematic. It was found that using a smaller basis set (cc-pVDZ) decreased convergence time and had limited impact on the excitation energies of the complexes when compared to the aug-cc-pVDZ [61, 79] basis set. A selection of the complexes from Chapter 4 were optimised using the cc-pVDZ basis set and the results are given in Table 5.2. It was found that the difference in the excitation energies at both the ground and excited state geometries between the aug-cc-pVDZ and cc-pVDZ basis sets was minimal, with the largest deviation in excitation energy being 0.06 eV. In free uranyl the  $\sigma_u \rightarrow \delta_u$  excitation energies are degenerate but for the other complexes excitations involving both  $\delta_u$  orbitals are given.

In the final study (Section 5.3.3), version 7.3 of the TURBOMOLE code [80] was used for the ground state investigation, while Gaussian was used for the excited state study; with the same model chemistry as Section 5.3.2. The distance from the uranyl to the plane of the macrocycle (Table 5.13) was calculated by placing an unbound atom in the centre of the macrocyclic ring and taking the distance from that the the uranyl unit. The crown ethers have two different values as the oxygens in the rings sit at different heights, in these cases, the unbound atom was place in the centre of each diagonal pair of oxygens and the distance to the uranyl unit was measured. Thermochemical corrections were calculated using the freeh

Table 5.2: Excitation energies ( $\Delta E$ ) of the optically allowed excitation of principally  $\sigma_u \rightarrow \delta_u$  character calculated on a selection of complexes from Chapter 4 with both aug-cc-pVDZ and cc-pVDZ basis sets at both the ground and excited state geometries.

Complex	Ground State $\Delta E$ (eV)		Excited State $\Delta E$ (eV)	
	aug-cc-pVDZ	cc-pVDZ	aug-cc-pVDZ	cc-pVDZ
Free Uranyl $[\text{UO}_2]^{2+}$	2.43	2.42	2.18	2.17
(1) $[\text{UO}_2\text{Cl}_4]^{2-}$	2.51/2.59	2.50/2.59	2.40/2.49	2.39/2.48
(3) $[\text{UO}_2(\text{C}_2\text{H}_5\text{NO}_2)_2]^{2+}$	2.63/2.72	2.61/2.71	2.43/2.52	2.41/2.46
(5) $\text{UO}_2\text{Cl}_2(\text{OPH}_3)_2$	2.47/2.57	2.45/2.56	2.34/2.44	*/2.43

\*The lower energy state for complex (5) could not be found with the cc-pVDZ basis set, but is not needed for the purpose of this study

internal module in TURBOMOLE. In order to obtain the energies of the theoretical novel complexes in solvent; the COSMO (conductor-like screening model) method [81] was utilised with an infinite dielectric constant to simulate water and a single-point energy calculation was run on the minima geometries from the gas phase calculations.

## 5.3 Results and discussion

### 5.3.1 Bending bare uranyl

The excitation energy as a function of the angle deviation from  $180^\circ$  for the singlet and triplet excitations of each state are shown in Figure 5.2.

Looking at the overall ordering of the excitations energies, transitions from the same hole MOs have similar energies to each other *i.e.*  $\sigma_u \rightarrow \delta_u$  and  $\sigma_u \rightarrow \phi_u$ . In general, the excitation energy of the transition to a  $\delta_u$  MO is lower in energy than the corresponding  $\phi_u$  MO, suggesting that the  $\delta$  MO is more stabilised than the  $\phi_u$  MO. The reasoning for the ordering of the excitation energies in terms of the hole MOs is somewhat trivial as it corresponds to the relative stabilisation and ordering of the bonding MOs established in the literature. [82–84] As expected, excitations from the  $\sigma_u$  MO are much lower in energy than excitation from the other MOs and this is due to the relative destabilisation of the  $\sigma_u$  MO via a "pushing from below" mechanism involving the pseudocore  $\text{U}6p_\sigma$  orbital. [62, 85–88]

In the singlet excitations, there is a clear trend between the parity of the hole MO and the excitation energy. Transitions which involve ungerade parity hole MOs ( $\sigma_u$  and  $\pi_u$ ) decrease in energy as the uranyl unit becomes more bent. In contrast, excitations involving gerade parity MOs ( $\sigma_g$  and  $\pi_g$ ) increase in energy as the uranyl unit deviates from linear. This trend causes the order of the excitations to rearrange

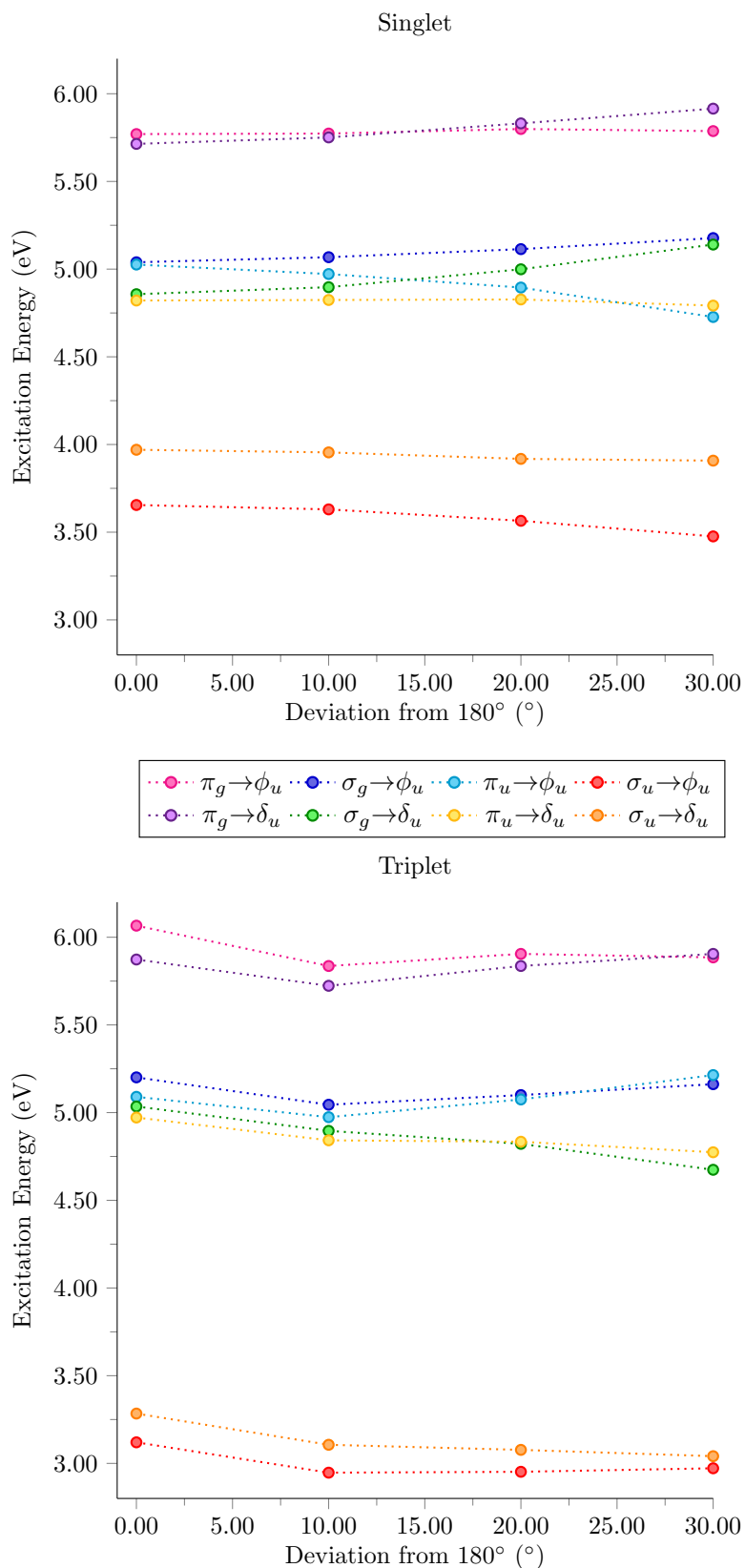


Figure 5.2: Trends in the excitation energy of the singlet (top) and triplet (bottom) states as the uranyl unit deviates from linearity.

and can be seen by the crossings of the potential energy surfaces.

For the triplet excitations, the trends are largely similar to the singlets, how-

ever there are variations at each angle. Firstly, bending the uranyl unit by  $10^\circ$  to  $170^\circ$  causes a decrease in all excitations by a similar magnitude. Second, bending from  $170^\circ \rightarrow 160^\circ$  results in the same trend as the singlet excitations, in which excitations involving ungerade holes decrease in energy and those involving gerade holes increase in energy. Finally, further bending from  $160^\circ \rightarrow 150^\circ$  causes the two excitations involving the  $\sigma_g$  hole to increase in energy as well as the  $\pi_g \rightarrow \delta_u$  and  $\sigma_u \rightarrow \delta_u$  excitations. Overall, these trends largely match those of the singlet, with the exception of the  $\pi_g \rightarrow \phi_u$  and  $\sigma_u \rightarrow \delta_u$  excitations. It is worth noting that in the  $\sigma_u \rightarrow \delta_u$  excitation, the increase in excitation energy from  $160^\circ \rightarrow 150^\circ$  is significantly smaller than that of the other excitations which increase in energy.

Largely the singlet and triplet data show similar trends; with excitations involving the gerade hole MOs increasing in energy and those with ungerade MOs decreasing in energy. There are two dominant factors which can contribute to the increase in excitation energy; stabilisation of the hole MOs and/or destabilisation of the particle MOs. As the excitations are paired up into their respective hole MOs with significant energy gaps between three of them (excitations involving  $\sigma_g$  and  $\pi_u$  MOs have similar energies) and the increase or decrease in excitation energy is dependent on the parity of the hole MO, it can be speculated that the changes in excitation energy as the uranyl unit is bent are dependent on the stabilisation/destabilisation of the hole MOs.

These results suggest that the gerade hole MOs are stabilised and the ungerade hole MOs destabilised as the uranyl unit bends. In Chapter 3 it was found that the covalency decreased with increasing excitation energy and thus excitations with ungerade parity MOs have higher covalency than excitations with gerade parity. These results follow the same trend with the excitation energies as Chapter 3 and therefore it can be suggested that the destabilised ungerade MOs have increased covalency than the gerade MOs. It is also worth noting that for the particle MOs, excitations involving  $\delta_u$  MOs give the largest increase and smallest decrease in excitation energy *i.e.* the changes are more positive than those involving the  $\phi_u$  particle MOs. This indicates that the  $\delta_u$  MOs are more destabilised in comparison to the  $\phi_u$  MOs.

Figure 5.3 shows how the bonding and non-bonding MOs change as the uranyl unit bends. The  $\sigma_u$  and  $\delta_u$  MOs vary the most upon bending with increased orbital overlap between the uranium 5f and oxygen 2p orbitals. The increased differences in the  $\delta_u$  MOs as the uranyl unit bends is evidence that the  $\delta_u$  MOs become more destabilised, particularly in comparison to the other particle MOs ( $\phi_u$ ) which remain unchanged upon bending. The  $\sigma_g$ ,  $\pi_g$  hole MOs are relatively unchanged upon bending and this is commensurate with the increased excitation energies. There is a small change in the  $\pi_u$  MOs as the uranyl unit is distorted, however these are very minor and do not give an obvious visual explanation for the destabilisation of the

$\pi_u$  MOs.

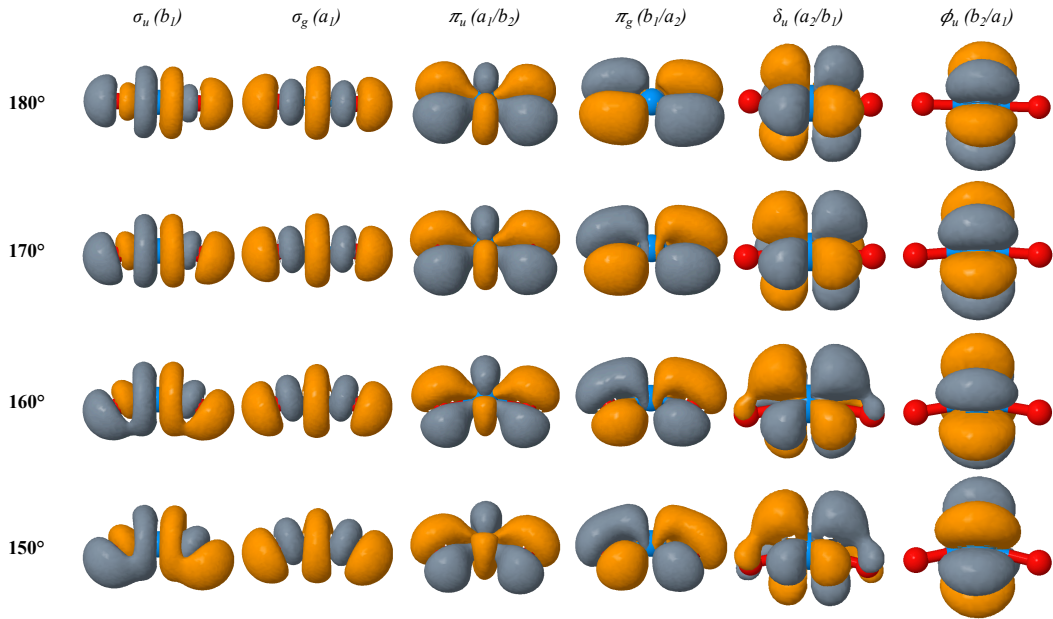


Figure 5.3: The effect of distorting the O-U-O angle on the hole and particle MOs investigated in this study.

RASSI calculations at each geometry, which includes spin-orbit coupling interactions, were performed in order to see if the  $\sigma_u \rightarrow \delta_u$  remain optically assessable as the O-U-O bond is distorted. The excitation energy ( $\Delta E$ ) of the spin orbit free (SOF) and spin orbit coupled (SOC)  $\sigma_u \rightarrow \delta_u$  excitations, the overall percentage contribution from the  $\sigma_u \rightarrow \delta_u$  transition and the oscillator strength, for each angle is given in Table 5.3. There are two SOF states which can contribute to the overall contribution of the  $\sigma_u \rightarrow \delta_u$  excitation, with  $a_1$  and  $b_2$  symmetry and hence excitations have a degenerate nature, where SOF states ‘swap’ but the excitation energy and overall contributions remain constant.

At each geometry, there are multiple  $\sigma_u \rightarrow \delta_u$  excitations, each one has a degenerate pair and these remain degenerate as the uranyl unit is bent. The RASSI results showed that there were 3 excitations which had significant (65 %)  $\sigma_u \rightarrow \delta_u$  contributions and these are given in Table 5.3. Each of these three excitations are distinctive and have individual characteristics which allow easy tracking between geometries. Firstly, the lowest energy excitation has equal contributions ( $\sim 50$  %) from both spin-orbit free (SOF) states for a minimum total of 97% contribution. Second, a single  $\sigma_u \rightarrow \delta_u$  SOF state ( $\sim 70$  %) and equal contributions from both SOF  $\sigma_u \rightarrow \phi_u$  triplet excitations ( $\sim 10$  %). The final excitation is the highest in energy and consists of equal contributions from both  $\sigma_u \rightarrow \delta_u$  SOF states ( $\sim 33$  % each) and then a single  $\sigma_u \rightarrow \phi_u$  triplet SOF state ( $\sim 31$  %).

It is worth highlighting that some of the excitations in Table 5.3 do not have an exact oscillator strength value; most notably in the linear geometry; this is due to the values being below the cutoff threshold of the calculation ( $1 \times 10^{-5}$ ) and are

Table 5.3: Spin orbit free (SOF) and Spin orbit coupled (SOC) excitation energy and oscillator strength for the  $\sigma_u \rightarrow \delta_u$  triplet excitation

Uranyl Angle ( $^\circ$ )	SOF $\Delta E$ (eV)	SOC $\Delta E$ (eV)	Contribution (%)	Oscillator Strength
180	2.95	2.68	99	$<10^{-5}$
		2.96	69	$<10^{-5}$
		3.34	66	$<10^{-5}$
170	2.95	2.68	99	$<10^{-5}$
		2.95 <sup>†</sup>	70	$2.17 \times 10^{-5}$
		2.95 <sup>†</sup>	70	$2.27 \times 10^{-5}$
160	2.95	3.33	67	$<10^{-5}$
		2.95 <sup>†</sup>	72	$6.78 \times 10^{-5}$
		2.95 <sup>†</sup>	72	$7.69 \times 10^{-5}$
150	2.97	3.33	69	$<10^{-5}$
		2.70	97	$1.25 \times 10^{-5}$
		2.96 <sup>†</sup>	75	$1.05 \times 10^{-4}$
150	2.97	2.96 <sup>†</sup>	75	$1.38 \times 10^{-4}$
		2.96 <sup>†</sup>	75	$1.38 \times 10^{-4}$
		3.33	72	$<10^{-5}$

<sup>†</sup> degenerate excitations

henceforth labelled as  $< 10^{-5}$ . The second lowest excitation for all distorted states is recorded twice in Table 5.3 as despite being degenerate in energy and nature, the corresponding oscillator strength values differ. The only example where this is not the case is in the lowest energy excitation at  $150^\circ$  where only one of the degenerate pair of excitations has an oscillator strength value associated with it.

From the RASSI results, it is clear that the oscillator strengths increase as the uranyl unit is distorted and hence the  $\sigma_u \rightarrow \delta_u$  excitation becomes more optically accessible. This is a positive result for the rest of the work given in this chapter and hence justifies the focus of investigating this excitation in more complex bent uranyl complexes.

### 5.3.2 Synthetically realised complexes

The complexes studied, from the experimental literature are shown in Figure 5.4. Table 5.4 compares the calculated and experimental uranium-ligand bond lengths and O-U-O angle. Throughout this section the coordinating ligands will be labelled as:  $O_{yl}$ ,  $L^0$  and  $L^-$ ; corresponding to the uranyl oxygen, neutral ligands (N, N and O(THF)) and negatively charge ligands (Cl, OTf and O(Phen)), respectively.

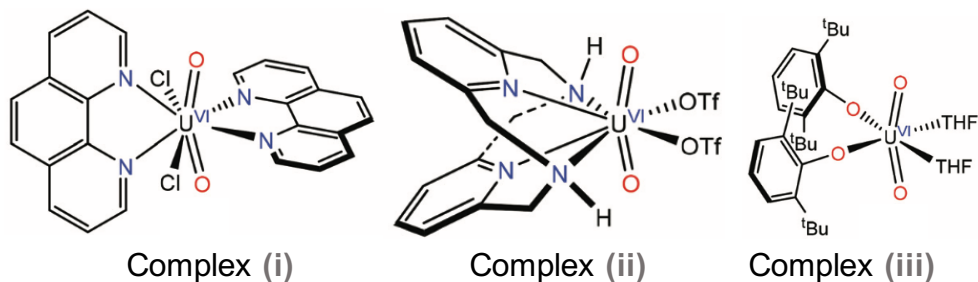


Figure 5.4: Experimental complexes studied in this investigation, reference [16] for a review

#### 5.3.2.1 Ground State Geometry

At the ground state geometries, there is good agreement between the experimental and DFT geometries, shown in Table 5.4. [1, 10, 48] The DFT values are mostly larger than the experimental, with the U- $O_{yl}$  bond lengths in considerably better agreement than the U-L bond lengths (average difference 0.009 for U- $O_{yl}$  and 0.069 for U-L).

Table 5.4: Comparison of the average bond lengths between the uranium centre and ligands between this study (DFT) and the experimental literature [1, 10, 48] (Exp).  $L_1$  are the neutral ligands and  $L_2$  the negatively charged ligands. ( $L_1$ : N, N and O(THF) and  $L_2$ : Cl, OTf and O(Phen) for complexes (i) - (iii) respectively.)

Complex	U- $O_{yl}$ (Å)		U- $L_1$ (Å)		U- $L_2$ (Å)		O-U-O (°)	
	Exp	DFT	Exp	DFT	Exp	DFT	Exp	DFT
Complex (i)	1.778	1.781	2.706	2.788	2.675	2.691	161.8	162.6
Complex (ii)	1.771	1.775	2.611	2.740	2.405	2.334	162.8	168.3
Complex (iii)	1.773	1.793	2.459	2.555	2.200	2.211	167.8	166.5

In free uranyl, the triplet  $\sigma_u \rightarrow \delta_u$  excitation energy with the cc-pVDZ basis set is 2.42 eV; the excitation consists of a single hole  $\rightarrow$  particle transition of 98% contribution. As was the case in Chapter 4, these complexes have several MOs in which there is  $\sigma_u$  character in the uranyl unit; shown in Figure 5.5. In contrast to Chapter 4,

where there was a clear bonding/antibonding interactions between the uranium and equatorial equatorial ligands orbitals arising in two MOs of  $\sigma_u$  character; the MOs here are more complex however, you can see some bonding/antibonding interactions. The total contribution of  $\sigma_u \rightarrow \delta_u$  character is given in Table 5.5 by summing all three contributions from the three different  $\sigma_u$  MOs. For these complexes, the T<sub>3</sub> excitation in complex (i) has the largest contribution of  $\sigma_u \rightarrow \delta_u$  nature (93.7%) and T<sub>2</sub> in complex (ii) has the lowest (40.8%).

Table 5.5: Excitation energies ( $\Delta E$ ), and overall contribution of the  $\sigma_u \rightarrow \delta_u$  excitation at the ground state geometry

Complex	State	$\Delta E$ (eV)	Contribution (%)	State	$\Delta E$ (eV)	Contribution (%)
(i)	T <sub>1</sub>	2.46	60.4	T <sub>3</sub>	2.56	93.7
(ii)	T <sub>1</sub>	2.37	73.9	T <sub>2</sub>	2.44	40.8
(iii)	T <sub>9</sub>	2.41	75.1	T <sub>29</sub>	3.59	62.9

The excitation energies in the complexes are similar to free uranyl, with each complex having one excitation very close, between +0.01 & +0.04 eV, to that of free uranyl (2.42 eV). As the O-U-O angle decreases, the excitation energy increases, commensurate with the CASPT2 study (Figure 5.2). As discussed previously, (Section 5.3.1) a contributing factor to an increase in excitation energy can be the stabilisation of the hole MO ( $\sigma_u$ ) and/or destabilisation of the particle MO ( $\delta_u$ ).

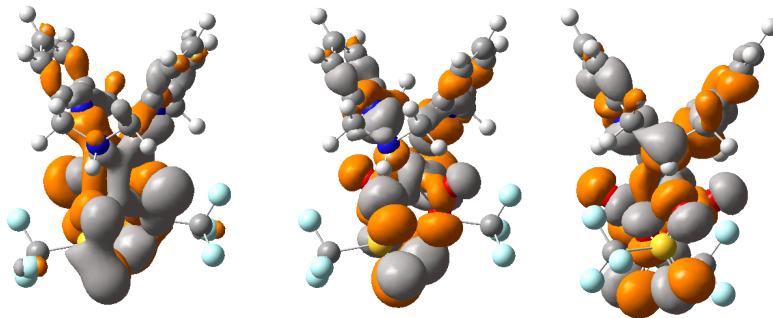


Figure 5.5: Complex (ii) MOs with  $\sigma_u$  character; arranged left to right in order of energy where left is the lowest energy MO (145, 159 & 161)

The ground state QTAIM metrics are given in Tables 5.6 and 5.7; as was the case in Chapter 4 comparisons to the excited state are only conducted at the relaxed excited state geometries (Section 5.3.2.2).

In comparison to free uranyl, studied in Chapter 3, the complexes all have lower values for the topological metrics, indicating that there is a decrease in the covalency of the U-O<sub>y1</sub> bond upon complexation, as was the case in Chapter 4. This is somewhat intuitive as there is now a full coordination sphere and hence the electron sharing in the uranyl unit will decrease in order for the uranium to coordinate with

Table 5.6: Topological QTAIM metrics:  $\rho_{\text{BCP}}$ ,  $\nabla^2\rho_{\text{BCP}}$  and  $H_{\text{BCP}}$  at the ground state geometries.

Bond	Metric	Complex (i)	Complex (ii)	Complex (iii)
U-O <sub>yl</sub>	$\rho_{\text{BCP}}$	0.284	0.285	0.282
	$\nabla^2\rho_{\text{BCP}}$	0.368	0.391	0.301
	$H_{\text{BCP}}$	-0.250	-0.253	-0.246
U-L <sup>0</sup>	$\rho_{\text{BCP}}$	0.032	0.036	0.041
	$\nabla^2\rho_{\text{BCP}}$	0.101	0.109	0.172
	$H_{\text{BCP}}$	0.0002	-0.002	0.001
U-L <sup>-</sup>	$\rho_{\text{BCP}}$	0.057	0.067	0.084
	$\nabla^2\rho_{\text{BCP}}$	0.161	0.301	0.408
	$H_{\text{BCP}}$	-0.008	-0.002	-0.006

the equatorial ligands. These values are also comparable to those seen in the previous chapter (Chapter 4), very similar to complex (1) ( $[\text{UO}_2\text{Cl}_4]^{2-}$ ), indicating that the bending of the O-U-O unit does not have much effect.

The covalency is much more enhanced in the uranyl unit in comparison to the coordinating ligands, which is shown by the larger metrics for U-O<sub>yl</sub> than U-L<sup>0</sup> and U-L<sup>-</sup>. The U-O<sub>yl</sub> metrics are very similar between complexes and hence the small variation in the O-U-O angle is not affecting the topological properties of the U-O<sub>yl</sub> bond.

When comparing the two different ligand interactions, metrics for the negatively charged ligands (L<sup>-</sup>) are larger in magnitude. As the  $\rho_{\text{BCP}}$  values are all significantly lower than 0.2, the increase in the metrics for L<sup>-</sup> are purely electrostatic as  $\rho_{\text{BCP}}$  indicates the charge accumulated at the BCP. This is also the case for the U-O ligand bonds (L<sup>0</sup> and L<sup>-</sup> in complex (iii) and L<sup>-</sup> in complex (ii)), which have a larger magnitude than nitrogen or chlorine ligands. Oxygen is more electronegative than both nitrogen and chlorine and hence there is a larger charge accumulated at the BCP for U-O bonds than U-Cl or U-N.

The integrated properties of the electron density; charge ( $q$ ), localisation index ( $\lambda$ ) and delocalisation index ( $\delta$ ), are given for the coordinating atoms in Table 5.7. It is worth noting that during the computation, an ECP replaced 60 core electrons in uranium and therefore when considering the localisation index, these 60 electrons are added as they are also localised on the uranium.

Upon complexation, the same trends as in chapter 4 were observed:  $q_{\text{O}}$ ,  $q_{\text{U}}$ ,  $\delta_{\text{U-O}_{yl}}$ ,  $q_{\text{UO}_2}$ ,  $\lambda_{\text{UO}_2}$  and  $\lambda_{\text{U}}$  decrease ( $q_{\text{O}}$  and  $q_{\text{U}}$  become more negative) and  $\lambda_{\text{O}_{yl}}$  increases. The decrease in  $\delta_{\text{U-O}_{yl}}$  further indicates a decrease in the covalency in the uranyl unit, while an increase in the  $\lambda_{\text{O}_{yl}}$  potentially suggests an increase in

Table 5.7: Integrated QTAIM metrics:  $q$ ,  $\lambda$  and  $\delta$  at the ground state geometries.

Atom	Metric	Complex (i)	Complex (ii)	Complex (iii)
U	$q$	2.704	2.797	2.786
	$\lambda$	86.680	86.606	86.765
O <sub>y1</sub>	$q$	-0.877	-0.824	-1.011
	$\lambda$	7.780	7.749	7.884
	$\delta$	1.755	1.732	1.785
UO <sub>2</sub>	$q$	0.950	1.149	0.764
	$\lambda$	105.847	105.682	106.169
L <sup>0</sup>	$\delta$	0.193	0.210	0.223
L <sup>-</sup>	$\delta$	0.478	0.394	0.492

the reactivity.  $\delta_{\text{U-L}^0}/\delta_{\text{U-L}^-}$  are much lower at the  $\delta_{\text{U-O}_{y1}}$ , again in agreement with the topological metrics in Table 5.6. When comparing the uranyl metrics between the complexes, the overall trend is that the magnitude of the metric is largest in complex (iii) and smallest in complex (ii). The exception is  $q_{\text{U}}$ , which decreases with decreasing O-U-O angle (complex (ii) > complex (iii) > complex (i)).

Overall, the metrics in Tables 5.6 and 5.7 are very similar to those of the linear uranyl complexes studied in Chapter 4. The QTAIM analysis here provides little evidence for electronic effects contributing to the bending in the uranyl unit and therefore the bending is likely to be steric in origin.

### 5.3.2.2 Excited State Geometries

Table 5.8 compares the O-U-O angle and the excitation energy of the  $\sigma_u \rightarrow \delta_u$  excitation at both the ground and excited state geometries. It was expected that exciting from a bonding to a non-bonding MO would weaken the U-O<sub>yl</sub> bond and result in a larger O-U-O bend and this was the case for all complexes except complex (iii) T<sub>29</sub>. As was the case in Chapter 4, the excitation energy is red-shifted at the excited state geometries, indicating relative destabilisation of the ground state. This red shift is loosely correlated with the increase in bending of the uranyl unit, complex (ii) exhibits the largest changes in both excitation energy and O-U-O bending.

Table 5.8: Comparison of the O-U-O bond angle (Angle) and excitation energy ( $\Delta E$ ) for the  $\sigma_u \rightarrow \delta_u$  triplet excitation at the ground and excited state geometries

Complex	State	Ground State Geometry		Excited State Geometry	
		Angle (°)	$\Delta E$ (eV)	Angle (°)	$\Delta E$ (eV)
Complex (i)	T <sub>1</sub>	162.6	2.46	162.1	2.37
	T <sub>3</sub>		2.56	158.9	2.45
Complex (ii)	T <sub>1</sub>	168.3	2.37	162.9	2.11
	T <sub>2</sub>		2.44	165.7	2.25
Complex (iii)	T <sub>9</sub>	166.5	2.41	164.1	2.24
	T <sub>29</sub>		3.59	171.2	3.01

Upon excitation, most of the uranium-ligand bond lengths increase with the biggest increase seen in the U-O<sub>yl</sub> bond. These results are commensurate with the excited state geometries calculated in Chapter 4. The larger increase in the U-O<sub>yl</sub> over the equatorial ligands is expected as the excitation is from a bonding to a non-bonding MO and hence the equatorial ligands are not involved in the excitations. Interestingly the distance between the uranium and the macrocyclic ligand (complex (ii) L<sup>0</sup>) decreases upon excitation and this could be a possible reason for the larger increase in the bending of the uranyl unit due to increased steric interactions.

QTAIM metrics of the excited state electronic structure at the excited state geometries are given in Tables 5.10 and 5.11. In comparison to the ground state electronic structure at ground state geometries (Tables 5.6 and 5.7), the metrics for the U-O<sub>yl</sub> bonds decrease, indicating a decrease in covalency and hence an explanation for the slightly enhanced bending. As was the case at the ground state geometries, the uranyl metrics are all similar across the complexes. When compared to the free uranyl study, (Chapter 3), the decrease in the uranyl metrics are very similar, indicating a consistent change in the electronic structure upon excitation. In

Table 5.9: Geomertic bond lengths ( $\text{\AA}$ ) at the excited state geometries.

Complex	State	U-O <sub>yl</sub>	U-L <sup>0</sup>	U-L <sup>-</sup>
Complex (i)	T <sub>1</sub>	1.811	2.793	2.713
	T <sub>3</sub>	1.823	2.785	2.735
Complex (ii)	T <sub>1</sub>	1.813	2.703	2.367
	T <sub>2</sub>	1.814	2.732	2.370
Complex (iii)	T <sub>9</sub>	1.815	2.565	2.236
	T <sub>29</sub>	1.821	2.533	2.330

contrast to the metrics associated with the uranyl unit, there is very little change in the metrics for the uranium-ligand BCPs, given that these are not directly involved in the excitation.

Table 5.10: QTAIM topological metrics at the excited state electronic structures at the excited state geometry

Bond	Metric	Complex (i)		Complex (ii)		Complex (iii)	
		T <sub>1</sub>	T <sub>3</sub>	T <sub>1</sub>	T <sub>2</sub>	T <sub>9</sub>	T <sub>29</sub>
U-O <sub>yl</sub>	$\rho_{\text{BCP}}$	0.258	0.258	0.259	0.260	0.262	0.279
	$\nabla^2\rho_{\text{BCP}}$	0.401	0.365	0.399	0.404	0.362	0.266
	$H_{\text{BCP}}$	-0.206	-0.205	-0.207	-0.209	-0.212	-0.236
U-L <sup>0</sup>	$\rho_{\text{BCP}}$	0.032	0.031	0.039	0.038	0.040	0.045
	$\nabla^2\rho_{\text{BCP}}$	0.095	0.101	0.113	0.106	0.167	0.178
	$H_{\text{BCP}}$	-0.0001	0.0004	-0.002	-0.001	0.001	0.0005
U-L <sup>-</sup>	$\rho_{\text{BCP}}$	0.055	0.049	0.062	0.064	0.078	0.065
	$\nabla^2\rho_{\text{BCP}}$	0.145	0.149	0.268	0.274	0.385	0.309
	$H_{\text{BCP}}$	-0.007	-0.004	-0.001	-0.002	-0.004	-0.0005

As was the case for the topological metrics, the integrated metrics involving the uranyl unit have the biggest changes. At the excited state geometries,  $\delta_{\text{U-O}_{yl}}$  decreases, with the exception of complex (iii) T<sub>29</sub>, indicating a decrease in electron sharing at the excited state geometries. This is also consistent with the decrease in O-U-O angle for all complexes except complex (iii) T<sub>29</sub>.  $q_{\text{O}_{yl}}$  becomes more negative for geometries of complex (i) and less negative for complexes (ii) and (iii) and this is largely reflected in the  $\lambda_{\text{O}_{yl}}$  metrics, which all decrease except for T<sub>3</sub> of complex (i) (you would also expect  $\lambda_{\text{O}_{yl}}$  to increase for T<sub>1</sub> of complex (i) too).  $q_{\text{U}}$  decreases

Table 5.11: QTAIM integrated metrics at the excited state electronic structures at the excited state geometry

Atom	Metric	Complex (i)		Complex (ii)		Complex (iii)	
		T <sub>1</sub>	T <sub>3</sub>	T <sub>1</sub>	T <sub>2</sub>	T <sub>9</sub>	T <sub>29</sub>
U	$q$	2.689	2.625	2.756	2.759	2.689	2.930
	$\lambda$	86.570	86.810	86.825	86.724	86.703	26.224
O <sub>y1</sub>	$q$	-0.834	-0.964	-0.806	-0.804	-1.024	-0.934
	$\lambda$	7.690	7.881	7.669	7.680	7.873	7.715
	$\delta$	1.708	1.753	1.703	1.678	1.676	1.976
UO <sub>2</sub>	$q$	1.022	0.697	1.145	1.152	0.641	1.062
	$\lambda$	105.548	106.142	105.765	105.630	105.882	105.681
L <sup>0</sup>	$\delta$	0.197	0.187	0.255	0.243	0.218	0.268
L <sup>-</sup>	$\delta$	0.585	0.407	0.385	0.378	0.539	0.476

for all structures except complex (iii) T<sub>29</sub> and  $\lambda_U$  increases in half the geometries (T<sub>3</sub> complex (i) and T<sub>1</sub> & T<sub>2</sub> complex (ii)). The changes in  $\delta_{U-L^-}$  varies between complexes; in complex (ii) for both structures  $\delta_{U-L^0}$  increases and  $\delta_{U-L^-}$  decreases. In complex (i), the lower energy structure (T<sub>1</sub>) both  $\delta_{U-L^0}$  and  $\delta_{U-L^-}$  increase, while in the higher energy structure (T<sub>3</sub>) they both decrease. Finally in complex (iii),  $\delta_{U-L^0}$  decreases and  $\delta_{U-L^-}$  increases in T<sub>9</sub>, while the reverse trend is seen in T<sub>29</sub>.

At the excited state geometries, the uranyl unit becomes more bent for all but one state (complex (iii) T<sub>29</sub>) and this is reflected in the decrease in  $\delta_{U-O_{y1}}$  and thus indicating a decrease in covalency. It is also worth noting that the smallest angles are seen in the complex (i) structures and the uranyl oxygens at the excited state geometries increase in negative charge, indicating increased reactivity.

### 5.3.3 Theoretical complexes

From the previous section, it was concluded that steric interaction was the main source of bending in the synthetically realised complexes. It was thought that complexation by a macrocyclic ligand would maximise steric interaction and enhance bending. This idea originated from work by Pedrick *et.al* [10], who synthesized one of the complexes studied in the previous section (Complex (ii)). It was thought that a more rigid variation of this macrocycle would initiate a more significant bend. It was also expected that oxygen and nitrogen donor ligands would be a good choice as they have a strong interaction with uranium and hence a potential pathway for bending via electronic origins.

There are two types of macrocycles used this investigation (Figure 5.6), crown ethers and porphyrinoids, and the rationale for choosing these ligands is discussed in Section 5.1. The 18C6 crown ether is included as it is experimentally known to bind uranyl via inclusion and is therefore used as a reference. [31–34] Figure 5.6 shows the macrocycles investigated, macrocycles: (A)-(C) denote the crown ethers while complexes (D) and (E) are the porphyrinoids (porphyrin [porph] and phthalocyanine [phthalo] respectively).

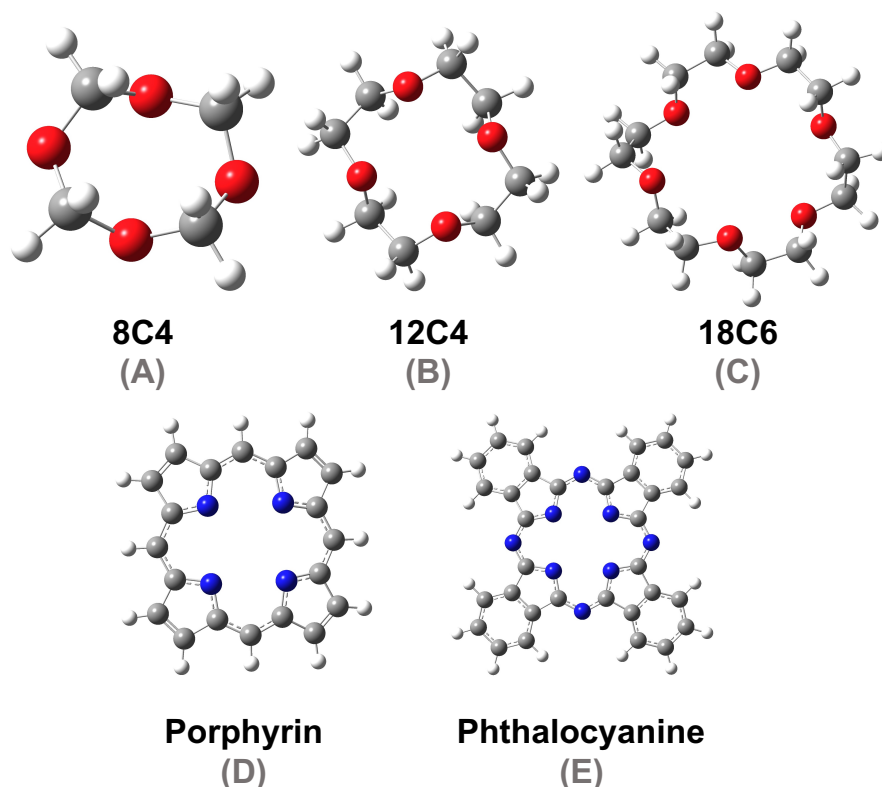


Figure 5.6: Macrocyles studied: (A)-(C) denote the crown ethers while complexes (D) and (E) are the porphyrinoids (porphyrin [porph] and phthalocyanine [phthalo] respectively).

### 5.3.3.1 Ground state geometries

Initially, both binding modes (side-on and inclusion) of the macrocycles were investigated; as shown by Figure 5.7. The pore size of the un-coordinated macrocycles, found by halving the bisecting distance, O-U-O angle and the difference in energy between the binding modes are compared in Table 5.12.

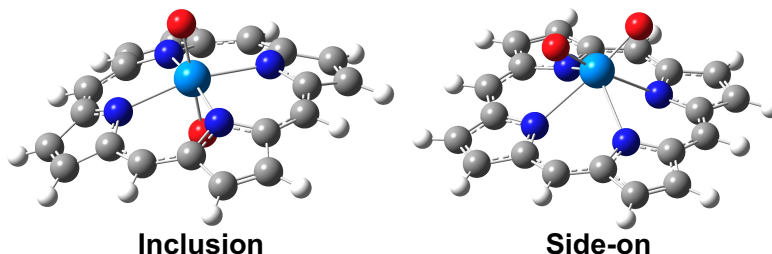


Figure 5.7: Inclusion vs side-on coordination of the uranyl unit to the porphyrin macrocycle

Table 5.12: Comparing uranyl bond angle (O-U-O) and energy difference ( $\delta E$ ) between the inclusion and side-on binding in minima geometries

Complex	Pore Size ( $\text{\AA}$ )	Binding	O-U-O ( $^\circ$ )	$\delta E$ (eV)
(A) 8C4	1.68	Side-on	159.3	/
(B) 12C4	2.04	Inclusion	176.8	2.684
		Side-on	98.3	
(C) 18C6	2.60	Inclusion	177.2	-1.730
		Side-on	109.7	
(D) Porph	2.03	Inclusion	179.8	0.550
		Side-on	95.9	
(E) Phthalo	1.95	Inclusion	179.7	1.404
		Side-on	98.3	

For all macrocycles, except the (C), the side-on coordination complexes are more stable. The pore size for the (A) crown ether was found to be too small to complex to uranyl via inclusion as when calculated the (A) ring dissociated into 4  $\text{CH}_2\text{O}$  molecules. Macrocycles (B), (D) and (E) have very similar pore sizes, when un-coordinated. Due to the rigid nature of macrocycles (D) and (E), the pore size does not change when coordinated. In contrast, the pore size in macrocycle (B) changes depending on the coordination; for inclusion coordination the pore size

increases to 2.25 Å and decreases to 1.97/1.29 Å when uranyl is bound by side-on coordination. This is the main reason for the large increase in the stability of the side-on coordination of macrocycle (B) over the inclusion complex, in comparison to complexes (D) and (E). Both macrocycles (D) and (E) have a variation in the diagonal N-N distance; the smaller of the two being recorded in Table 5.12. The larger pore size for (E) corresponds to the smallest pore size in (D) and hence provides further explanation to the increase in relative stability of the (E) over the (D) side-on complexes.

The single point energies of the macrocycles (D) and (E) at the uncomplexed, side-on and inclusion conformations, without the uranyl unit were also calculated. These showed that there was little difference between the energies of the uncomplexed and side-on coordination ( $\sim 0.01$  a.u.). In contrast, the difference between macrocycles (D) and (E) in the uncomplexed and inclusion conformations showed that (E) is much more destabilised than (D) and hence the reason for the overall increase in stability when comparing the inclusion and side-on conformations.

In addition to the side-on coordination being preferred; the uranyl unit is also distorted in these complexes. This is particularly prominent in complexes (D) and (E); where the uranyl is almost *cis* uranyl; which is emphasised by the equatorial O-U-N angle, which is 173° in (D) and 176° in (E).

Table 5.13 gives the average distance from the uranium to the macrocycle oxygens (U-M), the uranyl unit to the plane of the macrocycle (UO<sub>2</sub>-P) and the uranium to the uranyl oxygens (U-O<sub>y1</sub>). There are two UO<sub>2</sub>-P distances presented for (A) and (B) as the oxygens do not occupy the same plane. Specific details for the uranyl-plane of macrocycle measurement can be found in Section 5.2.2. In complex (C), the 18C6 crown ether curved upwards, see Figure 5.8 as if to encase the UO<sub>2</sub> and therefore a UO<sub>2</sub>-P measurement was not taken.

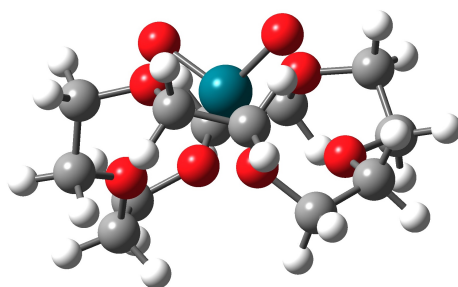


Figure 5.8: (C) (18C6) side-on complex, showing the crown ether unit curving as if to encase the uranyl unit

In complexes (A) - (C), the U-M bond lengths are slightly longer than in complexes (D) & (E); typically, U-N bonds are slightly longer than U-O bonds. [89] This correlates with the O-U-O angle, which is smaller in (D) & (E) than the rest, and hence suggesting that the uranyl unit is more distorted due to steric interactions. As the pore size decreases, the uranyl unit becomes closer to the plane

Table 5.13: Important bond lengths (Å): uranium to macrocycle O/N (U-M), distance of the uranyl unit above the macrocycle plane (UO<sub>2</sub>-P) and the U-O bond length in the uranyl unit (U-O<sub>yl</sub>); in the side-on coordinated complexes.

Complex/ Length (Å)	(A) 8C4	(B) 12C4	(C) 18C6	(D) Porph	(E) Phthalo
U-M	2.48 2.95	2.52	2.57	2.46	2.43
UO <sub>2</sub> -P	2.04 2.31 <sup>†</sup>	1.60 1.75 <sup>†</sup>	*	1.41	1.31
U-O <sub>yl</sub>	1.73	1.76	1.80	1.82	1.82
Pore	1.68	2.04	2.60	2.03	1.95

\* (C) curved upwards, no clear UO<sub>2</sub>-P measurement

<sup>†</sup> (A) & (B) have staggered oxygens; two U-P values

of the macrocycle, with the exception of (A). As the O-U-O angle is smaller in complexes (D) & (E), the U-O<sub>yl</sub> bond length is therefore larger than in complexes (A) - (C). The major difference between the complexes (D) & (E) is the height of the uranyl unit above the macrocycle plane (UO<sub>2</sub>-P).

The uranyl vibrational modes for both coordination types are given in Table 5.14; there are two modes of interest, the symmetric and asymmetric stretches. In free uranyl, the symmetric stretch is at a lower wavenumber than the asymmetric stretch. [89]

For all complexes, except (C), the vibrational frequencies are higher for the side-on coordination over inclusion. When considering vibrational analysis, generally the higher the frequency, the more force is required to vibrate the bond and hence it is more difficult to activate and this can therefore correlate to bond strength. [89–93] The vibrational data given in Table 5.14 indicates that for the side-on complexes, the U-O bond becomes weaker upon complexation. There is a positive correlation between the O-U-O bond angle and the vibrational frequency, the smaller the angle, the lower the frequency. In comparison to the side-on complexes, the inclusion complexes have a much smaller O-U-O angle range, close to 180° and this is reflected in the vibrational data. Interestingly, the side-on complexes of (D) & (E) result in the asymmetric stretch being lower than the symmetric and in general as the uranyl unit is distorted, the asymmetric stretch decreases more drastically than the symmetric. A possible explanation for this could be due to the repulsion caused in the symmetric stretch when the oxygens are moving towards the uranium, at a

Table 5.14: Comparing the symmetric and asymmetric stretches ( $\text{cm}^{-1}$ ) of the uranyl unit in the complexes

Complex	Binding	Symmetric	Asymmetric
$(\text{UO}_2)^{2+}$	/	1074.5	1169.30
(A) 8C4	Side-on	966.79	1052.50
(B) 12C4	Side-on Inclusion	912.85 885.84	949.85 985.93
(C) 18C6	Side-on Inclusion	858.92 918.54	869.87 999.72
(D) Porph	Side-on Inclusion	879.02 849.17	822.91 936.16
(E) Phthalo	Side-on Inclusion	881.93 861.11	827.92 929.33

smaller O-U-O angle the oxygen's are much closer together in the symmetric stretch than in a linear arrangement.

In order to further understand the origins of the bending in the side-on complexes, QTAIM analysis was conducted; topological and integrated properties of the electron density at important critical points are shown in Tables 5.15 and 5.16.

Table 5.15: Topological properties at the important critical points: electron density ( $\rho$ ), laplacian of electron density ( $\nabla^2\rho$ ) and energy density ( $H$ ) at the ground state electronic structure at the ground state geometries.

Complex/ Bond	Metric	(A) 8C4	(B) 12C4	(D) Porph	(E) Phthalo
U-O <sub>yl</sub>	$\rho_{\text{BCP}}$	0.341	0.312	0.271	0.272
	$\nabla^2\rho_{\text{BCP}}$	0.228	0.262	0.371	0.366
	$H_{\text{BCP}}$	-0.356	-0.298	-0.222	-0.223
U-M	$\rho_{\text{BCP}}$	0.056	0.051	0.068	0.071
	$\nabla^2\rho_{\text{BCP}}$	0.139	0.172	0.174	0.183
	$H_{\text{BCP}}$	-0.003	-0.002	-0.008	-0.010

It is worth noting that only two of the oxygens in (A) appear to be bonding,

this was confirmed by analysing the output file, which only had two oxygens in the crown ether ring present in the topological data. From the geometry analysis given in Table 5.13 it was noted that there are two different U-O (U-crown ether) (A) bond lengths: 2.48 & 2.95 Å, the longer is much larger than typical U-O bond lengths and hence these can be considered as 'non-bonding' with the uranium. Therefore, the QTAIM data in Tables 5.15 and 5.16 for complex (A) is the average from the two 'bound' oxygens (U-O bond length 2.48 Å). Due to the inflexibility of crown ether (A) it cannot rearrange itself to bind the uranium with all four oxygens the way crown ether (B) does.

Table 5.16: Integrated properties: charge ( $q$ ), localisation ( $\lambda$ ) and delocalisation ( $\delta$ ) indices for the ground state electronic structures at the ground state geometries.

Complex/ Atom	Metric	(A) 8C4	(B) 12C4	(D) Porph	(E) Phthalo
U	$q$	2.993	2.929	2.812	2.810
	$\lambda$	86.296	86.189	86.105	86.097
$O_{yl}$	$q$	-0.708	-0.748	-0.867	-0.865
	$\lambda$	7.507	7.557	7.737	7.738
	$\delta$	2.176	2.137	1.997	2.003
$UO_2$	$q$	1.578	1.433	1.077	1.081
	$\lambda$	105.752	105.629	105.646	105.644
M	$\delta$	0.378	0.325	0.461	0.465

The topological properties at the bond critical points are given in Table 5.15; these values indicate that the interaction between the uranium and the macrocycle O/N is stronger in complexes (D) & (E) than in (A) & (B). This is further enhanced by the larger magnitudes of  $U-O_{yl} \rho_{BCP}$  and  $H_{BCP}$  in (A) & (B), indicating that the U- $O_{yl}$  bond has increased covalency. The integrated properties also support these conclusions as  $\delta_{U-O_{yl}}$  is larger in (A) & (B) while  $\delta_{U-M}$  is smaller.

There is a significant difference in  $q_{UO_2}$  between the two types of macrocycle; with this being significantly smaller in complexes (D) & (E). It would be expected that this decrease in  $q_{UO_2}$  would be reflected in the  $\lambda_{UO_2}$ ; however this is not the case as  $\lambda_{UO_2}$  is very consistent between the complexes. The difference in  $q_{UO_2}$  between (D)/(E) and (A) & (B) can be attributed to the increase in the  $\delta_{U-M}$  in the porphyrinoid complexes;  $\delta_{U-M}$  increases by 0.13 between the two types of macrocycle, which when accounting for all four U-M bonds is roughly the value of the difference between the charges on the uranyl unit between the two types of macrocycle ( $\sim 0.45$ ).

The QTAIM analysis shows that the complexes (D) & (E) reduce the covalency in the  $\text{UO}_2$  unit and hence the uranyl unit can be more distorted.

Comparing these macrocyclic complexes to those studied in the previous section (Section 5.3.2), it was found that the topological metrics are all larger than complexes (i) - (iii) for the O/N coordination ( $L^0$  values in Table 5.6). For complexes (D) & (E), this is likely because the porphyrinoids are negatively charged compared to the  $L^0$  U-N ligands being neutral in the previous study. In comparison to complex (ii) the macrocyclic complexes have: increased  $q_U$  and  $\delta$ , decreased  $\lambda_U$  and  $\lambda_{\text{O}_{\text{yl}}}$  and less negative  $q_{\text{O}}$ . This is consistent with an increase in covalency between both  $\text{U-O}_{\text{yl}}$  and  $\text{U-L}$  in comparison to (ii) and a increase in  $q_{\text{UO}_2}$  (less negative) which arises from the decrease in  $\lambda_U$  and  $\lambda_{\text{O}_{\text{yl}}}$ . This increase in covalency in the uranyl unit is likely due to the partially filled coordination sphere of the macrocyclic complexes, further comparison to complexes (i) - (iii) will be replicated later when the coordination sphere of the macrocyclic complexes is complete.

Table 5.17: Excitation energies ( $\Delta E$ ) for the triplet  $\sigma_u \rightarrow \delta_u$  excitation for the complexes studied

Complex	State	$\Delta E$ (eV)		State	$\Delta E$ (eV)
(A) 8C4	T <sub>3</sub>	2.27		T <sub>4</sub>	2.34
(B) 12C4	T <sub>3</sub>	2.35		T <sub>4</sub>	2.54
(D) Porph	T <sub>13</sub>	2.64		T <sub>20</sub>	3.00
(E) Phthalo	T <sub>8</sub>	2.59		T <sub>17</sub>	2.92

As with the previous studies in this chapter, the  $\sigma_u \rightarrow \delta_u$  excitation is studied and the resultant excitation energies are given in Table 5.17. In agreement with the previous two studies (Sections 5.3.1 and 5.3.2), the smaller the O-U-O angle, the larger the excitation energy. The blue shift in excitation energy indicates that the  $\delta_u$  MO is more destabilised, possibly due to steric interactions from the uranyl oxygens, which would be closer to the  $\delta_u$  MO electron density as the uranyl unit bends. This was also seen in Section 5.3.2, however complexes (A) & (B) have a lower excitation energy than the complexes in Section 5.3.2 and a smaller O-U-O angle. The reason for this may be due to the unfilled coordination sphere in these complexes and therefore comparisons to other complexes will be held until the coordination sphere is filled.

In order to build a more chemically representative picture of the trends involved, the study of each complex was repeated with a completed solvation sphere. This was done by adding two of the same small solvent molecules to uranyl. For each type of

macrocycle (porphyrinoid and crown ether), two different ligands were investigated; water ( $\text{H}_2\text{O}$ ) and THF for (D) & (E) and hydroxide (OH) and phenoxide (Phen) ligands for (A) & (B); the minima geometries are shown in Figure 5.9.

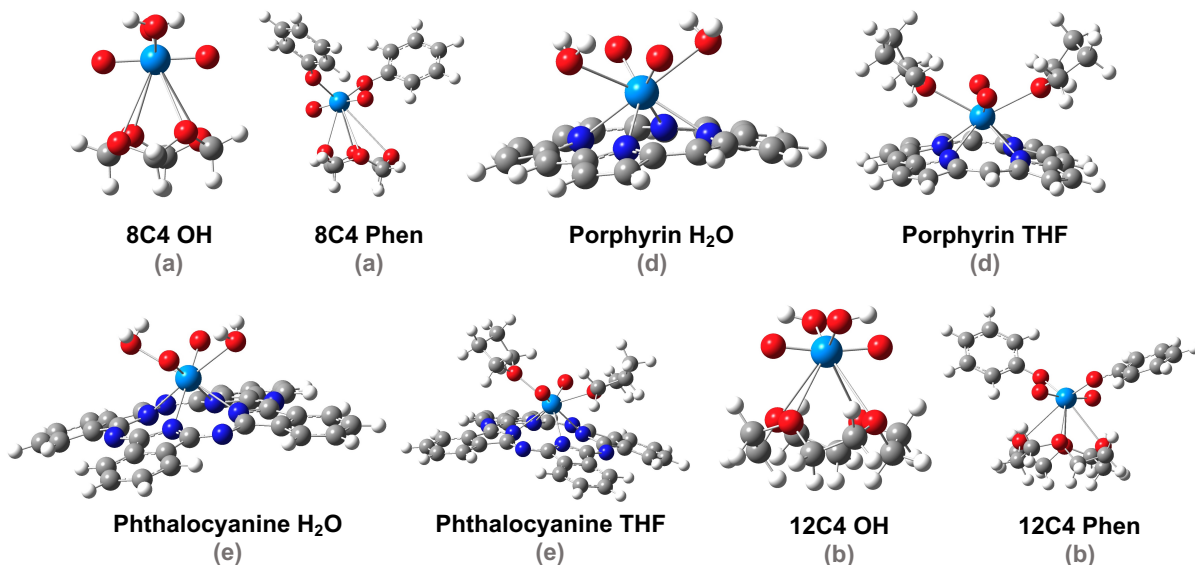


Figure 5.9: Fully coordinated complexes

Table 5.18 shows that upon complexation the O-U-O bond angle increases, with the largest increase seen with the complexation of the larger ligands (THF and phenoxide). The uranyl angle in complexes (D) & (E) are still significantly low in comparison to the literature, [10, 16] whereas in complexes (A) & (B) the uranyl unit is close to linear.

Table 5.18: Uranyl bond angles at the ground state geometries of the complexes

Complex	Ligand	Angle ( $^\circ$ )	Complex	Ligand	Angle ( $^\circ$ )
(a)	None	159.3	(d)	None	95.9
8C4	OH	179.8	Porph	$\text{H}_2\text{O}$	99.9
	Phen	173.7		THF	111.6
(b)	None	135.7	(e)	None	98.3
12C4	OH	169.7	Phthalo	$\text{H}_2\text{O}$	105.1
	Phen	170.0		THF	121.1

Table 5.19 gives the average distance from the uranium to the macrocycle O/N (U-M), the uranyl unit to the plane of the macrocycle ( $\text{UO}_2\text{-P}$ ), the uranium to the ligand ( $\text{U-O}_{\text{lig}}$ ) and the uranium to the uranyl oxygens ( $\text{U-O}_{\text{y1}}$ ). As seen previously, complex (a) has two different U-M bond lengths and is suspected that only two of the oxygens are interacting with the uranium (smallest of the bond lengths). The bond

lengths for the  $\text{UO}_2(\text{OH})_2(\text{H}_2\text{O})_2$  complex have also been included in Table 5.19 as this will be used as a reference complex.

Table 5.19: Important bond lengths ( $\text{\AA}$ ) in the fully coordinated complexes: uranium to macrocycle O/N (U-M), distance of the uranyl unit above the macrocycle plane ( $\text{UO}_2\text{-P}$ ), uranium to ligand ( $\text{U-O}_{\text{lig}}$ ) and the U-O bond length in uranyl ( $\text{U-O}_{\text{yl}}$ )

Complex	Ligand		U-M	$\text{UO}_2\text{-P}$	$\text{U-O}_{\text{lig}}$	$\text{U-O}_{\text{yl}}$
(a)	OH		2.94/3.33	2.79/2.54	2.14	1.79
8C4	Phenoxide		2.79/3.82	2.89	2.16	1.78
(b)	OH		3.02	2.27	2.15	1.79
12C4	Phenoxide		3.00	2.27	2.18	1.78
(d)	$\text{H}_2\text{O}$		2.49	1.39	2.7	1.85
Porph	THF		2.55	1.48	2.63	1.83
(e)	$\text{H}_2\text{O}$		2.48	1.48	2.72	1.84
Phthalo	THF		2.54	1.57	2.57	1.83

Bond Lengths for reference  $\text{UO}_2(\text{OH})_2(\text{H}_2\text{O})_2$  complex:  
 U-OH: 2.17  $\text{\AA}$ , U-OH<sub>2</sub>: 2.57  $\text{\AA}$  and U-O<sub>yl</sub>: 1.79  $\text{\AA}$

In comparison to the bare uranyl complexes (Table 5.13), the  $\text{U-O}_{\text{yl}}$  bond length has increased for all complexes. In complexes (a) & (b), the distance between the uranyl unit and the macrocycle plane ( $\text{UO}_2\text{-P}$ ) has increased by 0.5  $\text{\AA}$ . As the uranyl unit is further away from the macrocycle, there is less steric interaction from the crown ether macrocycle and hence the uranyl unit becomes more linear. This is also seen in complexes (d) & (e), but not to the same extent as the biggest increase is 0.09  $\text{\AA}$ .

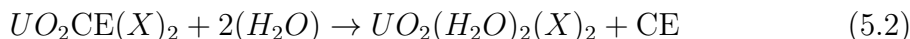
The vibrational data is given in Table 5.20; shows the symmetric and asymmetric stretches of the uranyl unit in the complexes. The theoretical complexes all have lower vibrations than the  $\text{UO}_2(\text{OH})_2(\text{H}_2\text{O})_2$  complex; which indicates that the U-O bond weakens when coordinated to a macrocycle. The values in complex (a) are very close to the  $\text{UO}_2(\text{OH})_2(\text{H}_2\text{O})_2$ , which was expected as the O-U-O angle is almost linear in this complex. The vibrations are all lower than in the corresponding ‘free’ complexes (Table 5.14); again, this was expected as now the coordination sphere is filled, the  $\text{U-O}_{\text{yl}}$  bond would become weaker as its coordinated to more ligands, the vibrations for free uranyl are much higher than the  $\text{UO}_2(\text{OH})_2(\text{H}_2\text{O})_2$  complex used as a reference. As with the ‘free’ complexes the symmetric stretches in complexes (d) & (e) are higher in wavenumber than the asymmetric stretch, in comparison to the rest, in which the symmetric stretch has a lower wavenumber than the asymmetric

stretch.

Table 5.20: Comparing the symmetric and asymmetric stretches ( $\text{cm}^{-1}$ ) in the uranyl unit

Complex	Ligand	Symmetric	Asymmetric
$\text{UO}_2(\text{OH})_2(\text{H}_2\text{O})_2$	/	858.66	937.50
(a)	OH	860.59	934.49
8C4	Phen	845.11	950.42
(b)	OH	847.94	922.51
12C4	Phen	842.32	936.71
(d)	$\text{H}_2\text{O}$	832.41	780.66
Porph	THF	824.31	791.51
(e)	$\text{H}_2\text{O}$	844.70	798.84
Phthalo	THF	816.16	809.34

Exchange reactions can be constructed in order to assess the relative stability of these complexes in comparison to a reference complex,  $\text{UO}_2(\text{OH})_2(\text{H}_2\text{O})_2$ . [94] These are shown in Equations 5.1 and 5.2 for complexes (d)/(e), and (a)/(b) respectively.



Equation 5.1 represents complexes (d) & (e), with ligand X ( $\text{H}_2\text{O}$  or THF) on the left hand side with the right-hand side giving the protonated (d)/(e) macrocycle ( $\text{H}_2\text{P}_{\text{or}}$ ) and the variation of the reference complex. In Equation 5.2 CE denotes the (a)/(b), crown ether macrocycle and X represents the hydroxide/phenoxide ligands.

In order to calculate these stabilities computationally, both solvent and thermochemical corrections are made to provide the free energy. The thermally corrected energy differences calculated in both the gas and solvent phases are shown in Table 5.21 (note the thermal correction is the same for both the gas and the solvent phase). The thermal correction was calculated from the difference between the thermally corrected gas phase and the gas phase values. The solvent and gas phase differences are very close in energy, with the largest difference being 0.15 eV for hydroxide ligation in complex (a).

The data in Table 5.21 shows that the reference complexes and the individual macrocycle *i.e.* the right-hand side of the equation are more stable than the the-

Table 5.21: Electronic reaction energies (eV) for both the gas and solvent phases

Complex	Ligand	Uncorrected		Thermally Corrected	
		Gas	Solvent	Gas	Solvent
(a) 8C4	OH	1.05	0.89	0.65	0.50
	Phen	1.01	0.98	0.76	0.73
(b) 12C4	OH	0.60	0.50	0.32	0.21
	Phen	0.61	0.64	0.49	0.52
(d) Porph	H <sub>2</sub> O	1.53	1.63	1.21	1.30
	THF	1.87	1.83	1.62	1.58
(e) Phthalo	H <sub>2</sub> O	1.68	1.75	1.38	1.45
	THF	1.67	1.60	1.42	1.35

oretical complexes. Out of these theoretical complexes, the hydroxide ligation in complex (b) is most likely to exist in solvent, which is unsurprising as the 12C4 uranyl complex has been experimentally studied. [35] Complexes with the crown ether macrocycles ((a) & (b)) are more stable when compared to the complexes which contain porphyrinoid rings ((d)/(e)) with the hydroxide complexes more stable in solvent. In comparison, water ligation in complexes (d) & (e) are less stable in solvent. In the gas phase, the complexes with smaller ligands (OH and H<sub>2</sub>O) are more stabilised than the larger ligand equivalent and therefore these were used in the excited state investigation (which is conducted in the gas phase).

From this point, Gaussian09 (Revision E.01) [71] was used in order to obtain excited state geometries. The excitation energy ( $\Delta E$ ) of the  $\sigma_u \rightarrow \delta_u$  excitation is given in Table 5.22;  $\delta$  compares the excitation energies of the fully coordinated complexes to the bare uranyl equivalents (Table 5.17). By comparing the overall nature of these excitations, it was found that the higher energy excitation in the bare uranyl complexes best matched the excitations given in Table 5.22.

When the coordination sphere is completed, the excitation of interest increases in energy, with the biggest deviations seen in complexes (d) & (e). This could be due to the destabilisation of the  $\delta_u$  MO's in these complexes. As with the other complexes, the excitation energy increases with decreasing O-U-O angle. However, upon comparison to complexes (i) - (iii) studied in Section 5.3.2 this trend does not hold as complexes (i) - (iii) have smaller O-U-O angles than complexes (a) & (b) and lower excitation energies.

The topological and integrated QTAIM metrics are given in Tables 5.23 and 5.24 at the ground state electronic structure for the ground state geometries of the fully

Table 5.22: Excitation energies ( $\Delta E$ ), for the OH/H<sub>2</sub>O ligand complexes and the smallest difference in energy ( $\delta$ ) to the bare complexes in Table 5.17, for the  $\sigma_u \rightarrow \delta_u$  triplet excitation

Complex	State	$\Delta E$ (eV)	$\delta$ (eV)
UO <sub>2</sub> (OH) <sub>2</sub> (H <sub>2</sub> O) <sub>2</sub>	T <sub>1</sub>	2.54	/
(a) 8C4	T <sub>1</sub>	2.52	0.18
(b) 12C4	T <sub>1</sub>	2.60	0.06
(d) Porph	T <sub>32</sub>	3.35	0.35
(e) Phthalo	T <sub>32</sub>	3.27	0.35

coordinated complexes.

Table 5.23:  $\rho_{\text{BCP}}$ ,  $\nabla^2 \rho_{\text{BCP}}$  and  $H_{\text{BCP}}$  QTAIM metrics at the uranium-oxygen (U-O<sub>yl</sub>), uranium-ligand (U-L) and uranium-macrocycle (U-M) BCPs at the ground state electronic structures of the fully coordinated complexes at the ground state geometries.

Complex/Bond	Metric	(a) 8C4	(b) 12C4	(d) Porph	(e) Phthalo
U-O <sub>yl</sub>	$\rho_{\text{BCP}}$	0.278	0.275	0.246	0.248
	$\nabla^2 \rho_{\text{BCP}}$	0.381	0.393	0.429	0.429
	$H_{\text{BCP}}$	-0.240	-0.235	-0.183	-0.186
U-L	$\rho_{\text{BCP}}$	0.117	0.114	0.033	0.036
	$\nabla^2 \rho_{\text{BCP}}$	0.442	0.424	0.118	0.136
	$H_{\text{BCP}}$	-0.028	-0.026	-0.0002	0.0002
U-M	$\rho_{\text{BCP}}$	0.020	0.016	0.059	0.060
	$\nabla^2 \rho_{\text{BCP}}$	0.073	0.060	0.186	0.194
	$H_{\text{BCP}}$	-0.0005	-0.001	-0.004	-0.005

In comparison to the topological properties given in Table 5.15, the  $\rho_{\text{BCP}}$  values at both the U-O<sub>yl</sub> and U-M critical points decrease. The  $\rho_{\text{BCP}}$  values at the U-L critical points are much larger in complexes (a) & (b), indicating that there is increased covalency between the uranyl and the hydroxide ligands than between the uranyl and the water ligands in the porphyrinoid complexes ((d) & (e)). In complexes (d) & (e) the  $\rho_{\text{BCP}}$  values between the uranyl and water ligands are lower than those at the U-M critical point, which suggests that there is increased

covalency between the uranyl and the macrocycle than the water ligands. The  $H_{BCP}$  values also give the same trends.

Table 5.24:  $q$ ,  $\lambda$  and  $\delta$  QTAIM metrics at the ground state electronic structures of the fully coordinated complexes at the ground state geometries.

Complex/Bond	Metric	(a) 8C4	(b) 12C4	(d) Porph	(e) Phthalo
U	$q$	2.749	2.769	2.724	2.720
	$\lambda$	86.629	86.625	86.649	86.680
$O_{y1}$	$q$	-0.876	-0.877	-1.036	-1.047
	$\lambda$	7.834	7.812	7.946	7.970
	$\delta$	1.726	1.697	1.755	1.763
$UO_2$	$q$	0.996	1.016	0.626	0.652
	$\lambda$	105.861	105.750	106.187	106.103
L	$\delta$	0.767	0.742	0.185	0.198
M	$\delta$	0.108	0.081	0.338	0.329

$\delta$  also indicates that there is a stronger interaction between the uranium and the porphyrinoid macrocycles (U-M) (complexes (d) & (e)) than the water (U-L). In complexes (d) & (e),  $\delta_{U-O_{y1}}$  and  $\delta_{U-M}$  both decrease upon full coordination; with  $\delta_{U-M}$  being much larger than  $\delta_{U-L}$ . In contrast, complexes (a) & (b) have a more significant decrease in  $\delta_{U-M}$  upon filling the coordination sphere, with  $\delta_{U-L}$  being much larger than  $\delta_{U-M}$ . Upon ligation of the water/hydroxide ligands;  $q_{O_{y1}}$  and  $q_U$  decrease, *i.e.* they become more negatively charged and hence the overall charge on the uranyl unit decreases.  $\lambda_{O_{y1}}$ ,  $\lambda_U$  and  $\lambda_{UO_2}$  increase, due to increased charge.

Overall, the QTAIM data indicates that the fully coordinated complexes have a decreased interaction with the macrocycles, which was hypothesised due to the increase in U-M distance. The data also shows that there is very little interaction between the macrocycle and the uranyl unit in complexes (a) & (b), hence there are less steric interactions and therefore the O-U-O angle becomes more linear. There is evidence of interaction between the uranyl and the porphyrinoid macrocycles (complexes (d) & (e)) and hence the O-U-O angle is still significantly distorted.

### 5.3.4 Excited state geometries

The excitation energy and O-U-O angle at both the ground and excited state geometries are summarised in Table 5.25. At the excited state geometries, the excitation energies are red shifted and the O-U-O angle increases (becomes less

bent). The increase in the O-U-O angle is surprising, given that in Section 5.3.2.2 a decrease in O-U-O angle was seen at the excited state geometries. In order to rationalise this increase in O-U-O angle, both the geometric and QTAIM metrics need to be analysed and compared to those in the previous section. Interestingly, in complex (a), the O-U-O angle becomes more bent, but the uranyl oxygens bend towards the crown ether and not away, as shown in Figure 5.10.

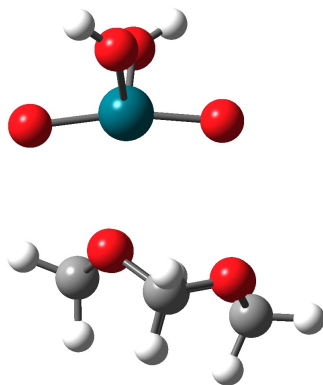


Figure 5.10:  $\text{UO}_2(\text{OH})_2$  8C4 complex ((a)) in its excited state geometry, showing that the uranyl unit bends towards the crown ether macrocycle.

Table 5.25: Comparison of the O-U-O bond angle and excitation energy ( $\Delta E$ ) for the  $\sigma_u \rightarrow \delta_u$  triplet excitation at the ground and excited state geometries

Complex	Ground State Geometry		Excited State Geometry	
	Angle ( $^\circ$ )	$\Delta E$ (eV)	Angle ( $^\circ$ )	$\Delta E$ (eV)
(a) 8C4	179.8	2.52	168.1*	2.13
(b) 12C4	169.7	2.60	178.0	2.31
(d) Porph	99.9	3.35	109.6	2.17
(e) Phthalo	105.1	3.27	135.4	2.10

\* O-U-O angle bent towards 8C4

At the excited state geometries; the  $\text{U-O}_{y1}$ , U-P and U-M bond lengths increase and the  $\text{U-O}_{\text{lig}}$  decrease. In the previous section, it was seen that in complex (ii) the distance between the uranium and macrocyclic ligand decreased, thus increasing steric interactions and enhancing the bending of the uranyl unit. In these complexes, however, the U-M distance increases and thus there is less steric interaction and thus a plausible explanation for the decrease in O-U-O bending.

In comparison to the ground state geometries, complex (d) has uneven U-M bond lengths (see Table 5.26) as the uranyl unit has moved closer to one set of nitrogens when looking from an aerial view and this also results in asymmetric  $\text{U-O}_{\text{lig}}$  bond lengths. As was the case at the ground state, complex (a) has two different

U-M bond lengths and it is likely that only the two with the shorter distance are interacting with the crown ether macrocycle and this is again evidenced in the QTAIM data.

Table 5.26: Important bond lengths ( $\text{\AA}$ ) in the excited state complexes: uranium to macrocycle O/N (U-M), distance of the uranyl unit above the macrocycle plane ( $\text{UO}_2\text{-P}$ ), uranium to ligand ( $\text{U-O}_{\text{lig}}$ ) and the U-O bond length in uranyl ( $\text{U-O}_{\text{yl}}$ )

Complex	U-M	$\text{UO}_2\text{-P}$	$\text{U-O}_{\text{lig}}$	$\text{U-O}_{\text{yl}}$
(a) 8C4	2.87/3.92	2.96	2.12	1.82
(b) 12C4	3.10	2.40	2.14	1.82
(d) Porph	2.42/2.63	1.44	2.60/2.72	1.90
(e) Phthalo	2.54	1.57	2.60	1.84

Tables 5.27 and 5.28 give the QTAIM metrics of the excited state electronic structures at the excited state geometries of the complexes. As mentioned previously, the complex (d) has uneven  $\text{U-O}_{\text{lig}}$  and U-M bond lengths and so there are two values for these metrics in Tables 5.27 and 5.28. As was the case in the ground state geometry, the data for complex (a) corresponds to the smaller of the U-M distances, and there are also two different values for the  $\text{O}_{\text{yl}}$  metric, although there is no geometric reason for why this would be. It is worth noting that for all metrics with multiple values quoted, the metric associated with the smallest U-atom distance is given first.

In comparison to the ground state geometries, the topological metrics for:  $\text{U-O}_{\text{yl}}$  decreases across all complexes, except (e); U-M increases in (a) and the smaller U-M distance in (d) and decrease elsewhere; and the U-L metrics are unchanged. At the excited state geometries, the covalency in the uranyl unit decreases for all complexes, except (e), which is likely due to the large increase in the O-U-O angle.

The integrated QTAIM metrics have similar trends to at ground geometries:  $q_{\text{O}_{\text{yl}}}$  is more negative in the complexes with porphyrinoid macrocycles ((d) & (e)) than those with crown ethers macrocycles ((a) & (b));  $\delta_{\text{U-L}}$  is larger in complexes (a) & (b); and  $\delta_{\text{U-M}}$  larger in complexes (d) & (e).

At the excited state geometry of (a):  $q_{\text{U}}$ ,  $\lambda_{\text{U}}$ ,  $q_{\text{UO}_2}$ ,  $\delta_{\text{U-L}}$  and  $\delta_{\text{U-M}}$  increase;  $q_{\text{O}_{\text{yl}}}$  becomes less negative and;  $\lambda_{\text{O}_{\text{yl}}}$ ,  $\lambda_{\text{UO}_2}$  and  $\delta_{\text{U-O}_{\text{yl}}}$  decrease. Complex (b) has similar trends to the (a), except  $\delta_{\text{U-M}}$  decreases and  $\lambda_{\text{U}}$  remains unchanged. For complex (d), only the metrics associated with the smaller U-L and U-M distances are considered for the comparison to the ground state geometry as those with larger bond lengths have the opposite trends. In (d):  $q_{\text{U}}$  and  $\delta_{\text{U-O}_{\text{yl}}}$  decrease at the excited state geometry, while all other metrics increase. As expected from the topological

Table 5.27:  $\rho_{\text{BCP}}$ ,  $\nabla^2\rho_{\text{BCP}}$  and  $H_{\text{BCP}}$  QTAIM metrics at the uranium-oxygen (U-O<sub>yl</sub>), uranium-ligand (U-L) and uranium-macrocycle (U-M) BCPs at the excited state electronic structures of the fully coordinated complexes at the excited state geometries.

Complex/ Bond	Metric	(a) 8C4 (T <sub>1</sub> )	(b) 12C4 (T <sub>1</sub> )	(d) Porph (T <sub>32</sub> )	(e) Phthalo (T <sub>32</sub> )
U-O <sub>yl</sub>	$\rho_{\text{BCP}}$	0.254	0.250	0.213	0.255
	$\nabla^2\rho_{\text{BCP}}$	0.383	0.398	0.493	0.381
	$H_{\text{BCP}}$	-0.200	-0.193	-0.134	-0.197
U-L	$\rho_{\text{BCP}}$	0.116	0.115	0.039/0.031	0.039
	$\nabla^2\rho_{\text{BCP}}$	0.464	0.429	0.145/0.111	0.156
	$H_{\text{BCP}}$	-0.027	-0.026	0.0002/0.00001	0.001
U-M	$\rho_{\text{BCP}}$	0.022	0.014	0.070/0.045	0.054
	$\nabla^2\rho_{\text{BCP}}$	0.080	0.050	0.210/0.139	0.170
	$H_{\text{BCP}}$	0.001	0.0005	-0.009/-0.002	-0.003

Table 5.28:  $q$ ,  $\lambda$  and  $\delta$  QTAIM metrics at the uranium (U), uranyl oxygens (O<sub>yl</sub>), ligand (L) and macrocycle (M) critical points at the excited state electronic structures of the fully coordinated complexes at the excited state geometries.

Complex/ Bond	Metric	(a) 8C4 (T <sub>1</sub> )	(b) 12C4 (T <sub>1</sub> )	(d) Porph (T <sub>32</sub> )	(e) Phthalo (T <sub>32</sub> )
U	$q$	2.751	2.772	2.626	2.756
	$\lambda$	86.718	86.625	86.047	87.250
O <sub>yl</sub>	$q$	-0.872/-0.843	-0.852	-1.055	-0.939
	$\lambda$	7.793/7.761	7.732	8.034	7.805
	$\delta$	1.675/1.715	1.664	1.503	1.845
UO <sub>2</sub>	$q$	1.036	1.068	0.517	0.878
	$\lambda$	105.846	105.612	106.164	105.580
L	$\delta$	0.867	0.853	0.224/0.168	0.228
M	$\delta$	0.122	0.066	0.383/0.256	0.327

results,  $\delta_{\text{U-O}_{yl}}$  increases in (e) along with  $\delta_{\text{U-L}}$  and  $q_{\text{U}}$ ; the other metrics all decrease at the excited state geometry, with the exception of  $\delta_{\text{U-M}}$  which remains unchanged.

Comparing the excited state geometry QTAIM metrics to those obtained in

Section 5.3.2.2 for complex (ii), it can be clearly seen that this complex (ii) bridges the gap between the complexes with porphyrinoid macrocycles ((d) & (e)) and those with crown ether macrocycles ((a) & (b)). When comparing the trends in the (d) & (e) to those in complex (ii), it was found that the trends oppose each other and this favours the enhanced bending of complexes (d) & (e) over complex (ii). For example, complexes (d) & (e) have an increased interaction between the uranium and macrocyclic ligand ( $\delta_{U-M}$ ) and a decrease between the uranium and coordinated oxygen ligands  $\delta_{U-L}$  and the reverse is true for complex (ii)). This trend can be largely explained by the bond lengths; the U-M bond length is shorter than the U-O<sub>lig</sub> in the porphyrinoid complexes and the reverse is true in complex (ii). The increased interaction between the uranium and the macrocycle is likely to be the primary cause in the increased bending of the uranyl unit. It is also worth noting that at the excited state geometries, the U-M distance decreases in complex (ii) and this causes an increase in U-M interaction and results in an enhancement of the bending in the uranyl unit; the reverse is true at the excited state geometries for the porphyrinoid complexes.

## 5.4 Conclusions

In this chapter, three different studies were carried out. Firstly free uranyl was distorted from 180° - 150° with CASPT2 and spin-orbit coupled calculations to investigate the effect of bending on the excitation energy and oscillator strengths of the  $\sigma_u \rightarrow \delta_u$  excitation. It was found that as the uranyl unit deviated from linear, the  $\sigma_u \rightarrow \delta_u$  excitation became more optically accessible and the excitation energy decreased. The red shift in excitation energy can be attributed to the destabilisation of the hole MO ( $\sigma_u$ ) as the uranyl unit is distorted. As the  $\sigma_u \rightarrow \delta_u$  triplet excitation is still optically accessible at smaller O-U-O angles, experimentally bent complexes were then studied with DFT.

Three synthetically realised complexes, which had some of the smallest O-U-O angles in the literature, were then studied with DFT and QTAIM methods. These complexes had similar results to the linear complexes studied in Chapter 4 and thus suggest that the bending in the uranyl unit is due to steric and not electronic interactions.

Finally, enhanced bending of the uranyl unit was achieved by complexing with porphyrinoid macrocyclic ligands (complexes (d) & (e)). Due to the flexibility of the crown ether macrocycles (complexes (a) & (b)), only small deviations in the uranyl unit were achieved  $\sim 170^\circ$ . Comparing the complexes with porphyrinoid macrocycles to complex (ii) it was found that there was increased interaction between the uranium and the macrocyclic nitrogens and a decrease in between the uranium oxygen ligands. This is likely due to the fact that in complex (ii) the macrocycle is neutral and the ligands negative, while the reverse is true in complexes (d) & (e).

It is also worth noting that the increased bending results in a decrease in the uranyl covalency in complexes (d) & (e) in comparison to both the linear and experimentally bent complexes. There is sufficient evidence that the bending in complexes (d) & (e) does have some electronic origins but is also likely to have increased steric interactions too due to the inflexibility of the porphyrinoid rings.

From both Sections 5.3.2 and 5.3.3 it is clear that largely the cause of bending is likely due to steric interactions, both at the ground and excited state geometries. This is made clear by comparison of the complexes with porphyrinoid macrocycles ((d) & (e)) and complex (ii). At the ground state geometries, the macrocycle in complexes (d) & (e) has a greater interaction with uranium in comparison to complex (ii), with complexes (d) & (e) complexes having the shorter U-M distance. At the excited state geometries, the U-M distance increases in complexes (d) & (e) and decreases in complex (ii), resulting in an increase and decrease in the O-U-O angle respectively. These trends are clearly linked with the proximity of the macrocyclic ligand and hence the bending in the O-U-O unit is dominated by unfavourable steric interactions. It is also worth noting that there could also be electronic origins in complexes (d) & (e) which could add to the distortion of the uranyl unit; these would likely be a result from the coordinating macrocyclic ligand being negatively charged and hence having a stronger interaction with the uranium shown in the QTAIM analysis.

From this investigation, in order to continue the search for significant bend uranyl complexes it is suggested that the following design suggestions should be taken into account. Firstly a small rigid macrocycle should be used to coordinate the uranyl, with a small pore-size to ensure side-on coordination is preferred. Second, negatively charged macrocycles should be utilised to enhance electronic effects towards the bending. Finally in this chapter both oxygen and nitrogen coordination was investigated, while it appears that nitrogen is superior in causing deviation in the uranyl unit, this may be due to overall rigidity and negatively charged attributes of the ligand and not the coordinating atom species. Although hard donors (oxygen/nitrogen) would be recommended for future investigations of bent uranyl complexes.

# References

- [1] S. Schöne, T. Radoske, J. März, T. Stumpf, M. Patzschke, A. Ikeda-Ohno, *Chem. Eur. J.* **2017**, *23*, 13574–13578.
- [2] S. T. Liddle, *Angew. Chem. Int. Ed.* **2015**, *54*, 8604–8641.
- [3] M. B. Jones, A. J. Gaunt, *Chem. Rev.* **2013**, *113*, 1137–1198.
- [4] R. J. Baker, *Chem. Eur. J.* **2012**, *18*, 16259–16271.
- [5] E. S. Ilton, A. Haiduc, C. L. Cahill, A. R. Felmyt, *Inorg. Chem.* **2005**, *44*, 2986–2988.
- [6] B. Gu, W. M. Wu, M. A. Ginder-Vogel, H. Yan, M. W. Fields, J. Zhou, S. Fendorf, C. S. Criddle, P. M. Jardine, *Environ. Sci. Technol.* **2005**, *39*, 4841–4847.
- [7] J. C. Renshaw, L. J. Butchins, F. R. Livens, I. May, J. M. Charnock, J. R. Lloyd, *Environ. Sci. Technol.* **2005**, *39*, 5657–5660.
- [8] W. M. Wu, J. Carley, T. Gentry, M. A. Ginder-Vogel, M. Fienen, T. Mehlhorn, H. Yan, S. Carroll, M. N. Pace, J. Nyman, J. Luo, M. E. Gentile, M. W. Fields, R. F. Hickey, B. Gu, D. Watson, O. A. Cirpka, J. Zhou, S. Fendorf, P. K. Kitanidis, P. M. Jardine, C. S. Criddle, *Environ. Sci. Technol.* **2006**, *40*, 3986–3995.
- [9] W. M. Wu, J. Carley, M. Fienen, T. Mehlhorn, K. Lowe, J. Nyman, J. Luo, M. E. Gentile, R. Rajan, D. Wagner, R. F. Hickey, B. Gu, D. Watson, O. A. Cirpka, P. K. Kitanidis, P. M. Jardine, C. S. Criddle, *Environ. Sci. Technol.* **2006**, *40*, 3978–3985.
- [10] E. A. Pedrick, J. W. Schultz, G. Wu, L. M. Mirica, T. W. Hayton, *Inorg. Chem.* **2016**, *55*, 5693–5701.
- [11] Y. Wang, Z. Liu, Y. Li, Z. Bai, W. Liu, Y. Wang, X. Xu, C. Xiao, D. Sheng, J. Diwu, J. Su, Z. Chai, T. E. Albrecht-Schmitt, S. Wang, *J. Am. Chem. Soc.* **2015**, *137*, 6144–6147.
- [12] S. Wu, P. M. Kowalski, N. Yu, T. Malcherek, W. Depmeier, D. Bosbach, S. Wang, E. V. Suleimanov, T. E. Albrecht-Schmitt, E. V. Alekseev, *Inorg. Chem.* **2014**, *53*, 7650–7660.

- [13] J. L. Sessler, D. Seidel, A. E. Vivian, V. Lynch, B. L. Scott, D. W. Keogh, *Angew. Chem. Int. Ed.* **2001**, *40*, 591–594.
- [14] P. L. Arnold, D. Patel, C. Wilson, J. B. Love, *Nature* **2008**, *451*, 315–317.
- [15] G. Szigethy, K. N. Raymond, *J. Am. Chem. Soc.* **2011**, *133*, 7942–7956.
- [16] T. W. Hayton, *Dalton Trans.* **2018**, *47*, 1003–1009.
- [17] E. Lu, O. J. Cooper, J. McMaster, F. Tuna, E. J. L. McInnes, W. Lewis, A. J. Blake, S. T. Liddle, *Angew. Chem. Int. Ed.* **2014**, *53*, 6696–6700.
- [18] J. C. Tourneux, J. C. Berthet, T. Cantat, P. Thuéry, N. Mézailles, M. Ephritikhine, *J. Am. Chem. Soc.* **2011**, *133*, 6162–6165.
- [19] L. A. Borkowski, C. L. Cahill, *Cryst. Growth Des.* **2006**, *6*, 2248–2259.
- [20] J. C. Berthet, P. Thuéry, M. R. S. Foreman, M. Ephritikhine, *Radiochim. Acta.* **2008**, *96*, 189.
- [21] J. C. Berthet, P. Thuéry, M. R. S. Foreman, M. Ephritikhine, *Eur. J. Inorg. Chem.* **2000**, 1969–1973.
- [22] D. S. Arney, C. J. Burns, *J. Am. Chem. Soc.* **1995**, *117*, 9448–9460.
- [23] P. B. Duval, C. J. Burns, W. E. Buschmann, D. L. Clark, D. E. Morris, B. L. Scott, *Inorg. Chem.* **2001**, *40*, 5491–5496.
- [24] C. Villiers, P. Thuéry, M. Ephritikhine, *Angew. Chem. Int. Ed.* **2008**, *47*, 5892–5893.
- [25] A. E. Vaughn, C. L. Barnes, P. B. Duval, *Angew. Chem. Int. Ed.* **2007**, *46*, 6622–6625.
- [26] Cambridge Structural Database, version 5.38, **2016**.
- [27] G. W. Gokel, W. M. Leevy, M. E. Weber, *Chem. Rev.* **2004**, *104*, 2723–2750.
- [28] C. J. Pedersen, H. K. Frensdor, *Angew. Chem. Int. Ed.* **1972**, 16–25.
- [29] T. E. Cooper, D. R. Carl, J. Oomens, J. D. Steill, P. B. Armentrout, *J. Phys. Chem. A.* **2011**, *115*, 5408–5422.
- [30] C. Görrler-Walrand, S. De Houwer, L. Fluyt, K. Binnemans, *Phys. Chem. Chem. Phys.* **2004**, *6*, 3292–3298.
- [31] J. Lagrange, J. P. Metabanzoulou, P. Fux, P. Lagrange, *Polyhedron* **1989**, *8*, 2251.
- [32] A. Dejean, P. Charpin, G. Folcher, P. Rigny, *Polyhedron* **1987**, *6*, 189.
- [33] R. D. Rogers, L. K. Kurihara, M. M. Benning, *J. Inclus. Phenom.* **1987**, *5*, 645.
- [34] A. Navaza, F. Villain, P. Charpin, *Polyhedron* **1984**, *3*, 143.
- [35] Y. Gong, J. K. Gibson, *Inorg. Chem.* **2014**, *53*, 5839–5844.

- [36] J. Jian, S. X. Hu, W. L. Li, M. J. An Stipdonk, J. Martens, G. Berden, J. Oomens, J. Li, J. K. Gibson, *Inorg. Chem.* **2018**, *57*, 4125–4134.
- [37] J. T. Brewster, H. Zafar, H. D. Root, G. D. Thiabaud, J. L. Sessler, *Inorg. Chem.* **2020**, *59*, 32–47.
- [38] I. T. Ho, Z. Zhang, M. Ishida, V. M. Lynch, W. Y. Cha, Y. M. Sung, D. Kim, J. L. Sessler, *J. Am. Chem. Soc.* **2014**, *136*, 4281–4286.
- [39] P. J. Melfi, K. K. Sung, T. L. Jeong, F. Bolze, D. Seidel, V. M. Lynch, J. M. Veauthier, A. J. Gaunt, M. P. Neu, Z. Ou, K. M. Kadish, S. Fukuzumi, K. Ohkubo, J. L. Sessler, *Inorg. Chem.* **2007**, *46*, 5143–5145.
- [40] J. T. Brewster, H. D. Root, D. Mangel, A. Samia, H. Zafar, A. C. Sedgwick, V. M. Lynch, J. L. Sessler, *Chem. Sci.* **2019**, *10*, 5596–5602.
- [41] J. T. Brewster, Q. He, G. Anguera, M. D. Moore, X. S. Ke, V. M. Lynch, J. L. Sessler, *Chem. Commun.* **2017**, *53*, 4981–4984.
- [42] J. T. Brewster, A. Aguilar, G. Anguera, H. Zafar, M. D. Moore, J. L. Sessler, *J. Coord. Chem.* **2018**, *71*, 1808–1813.
- [43] A. K. Burrell, G. Hemmi, V. Lynch, J. L. Sessler, *J. Am. Chem. Soc.* **1991**, *113*, 4690–4692.
- [44] J. L. Sessler, A. Gebauer, M. C. Hoehner, V. Lynch, *Chem. Commun.* **1998**, 1835–1836.
- [45] A. K. Burrell, M. J. Cyr, V. Lynch, J. L. Sessler, *J. Chem. Soc. Chem. Commun.* **1991**, 1710–1713.
- [46] J. L. Sessler, A. E. Gorden, D. Seidel, S. Hannah, V. Lynch, P. L. Gordon, R. J. Donohoe, C. D. Tait, D. W. Keogh, *Inorg. Chim. Acta.* **2002**, *341*, 54–70.
- [47] R. Espinozaa, V. Lynch, J. L. Sessler, T. D. Modyb, M. T. Dulay, *Inorg. Chim. Acta.* **1996**, *246*, 23–30.
- [48] M. P. Wilkerson, C. J. Burns, D. E. Morris, R. T. Paine, B. L. Scott, *Inorg. Chem.* **2002**, *41*, 3110–3120.
- [49] M. Staudinger, M. Lüthy, *Helv. Chim. Acta* **1925**, *8*, 65–67.
- [50] D. Cram, *Science* **1988**, *240*, 760–767.
- [51] I. Hataue, Y. Oishi, M. Kubota, H. Fujimoto, *Tetrahedron* **1991**, *47*, 9317–9328.
- [52] A. van der Ham, T. Hansen, G. Lodder, J. D. Codée, T. A. Hamlin, D. V. Filippov, *Chem. Phys. Chem* **2019**, *20*, 2103–2109.

- [53] F. Aquilante, J. Autschbach, A. Baiardi, S. Battaglia, V. A. Borin, L. F. Chibotaru, I. Conti, L. De Vico, M. Delcey, I. F. Galván, N. Ferré, L. Freitag, M. Garavelli, X. Gong, S. Knecht, E. D. Larsson, R. Lindh, M. Lundberg, P. Å. Malmqvist, A. Nenov, J. Norell, M. Odelius, M. Olivucci, T. B. Pedersen, L. Pedraza-González, Q. M. Phung, K. Pierloot, M. Reiher, I. Schapiro, J. Segarra-Martí, F. Segatta, L. Seijo, S. Sen, D. C. Sergentu, C. J. Stein, L. Ungur, M. Vacher, A. Valentini, V. Veryazov, *J. Chem. Phys.* **2020**, *152*.
- [54] I. Fdez. Galván, M. Vacher, A. Alavi, C. Angeli, F. Aquilante, J. Autschbach, J. J. Bao, S. I. Bokarev, N. A. Bogdanov, R. K. Carlson, L. F. Chibotaru, J. Creutzberg, N. Dattani, M. G. Delcey, S. S. Dong, A. Dreuw, L. Freitag, L. M. Frutos, L. Gagliardi, F. Gendron, A. Giussani, L. González, G. Grell, M. Guo, C. E. Hoyer, M. Johansson, S. Keller, S. Knecht, G. Kovačević, E. Källman, G. Li Manni, M. Lundberg, Y. Ma, S. Mai, J. P. Malhado, P. Å. Malmqvist, P. Marquetand, S. A. Mewes, J. Norell, M. Olivucci, M. Oppel, Q. M. Phung, K. Pierloot, F. Plasser, M. Reiher, A. M. Sand, I. Schapiro, P. Sharma, C. J. Stein, L. K. Sørensen, D. G. Truhlar, M. Ugandi, L. Ungur, A. Valentini, S. Vancoillie, V. Veryazov, O. Weser, T. A. Wesolowski, P. O. Widmark, S. Wouters, A. Zech, J. P. Zobel, R. Lindh, *J. Chem. Theory Comput.* **2019**, *15*, 5925–5964.
- [55] D. Feller, *J. Comput. Chem.* **1996**, *17*, 1571–1586.
- [56] B. P. Pritchard, D. Altarawy, B. Didier, T. D. Gibson, T. L. Windus, *J. Chem. Inf. Model.* **2019**, *59*, 4814–4820.
- [57] K. L. Schuchardt, B. T. Didier, T. Elsethagen, L. Sun, V. Gurumoorthi, J. Chase, J. Li, T. L. Windus, *J. Chem. Inf. Model.* **2007**, *47*, 1045–1052.
- [58] B. O. Roos, R. Lindh, P. Å. Malmqvist, V. Veryazov, P. O. Widmark, *J. Phys. Chem. A* **2004**, *108*, 2851–2858.
- [59] B. O. Roos, R. Lindh, P. Å. Malmqvist, V. Veryazov, P. O. Widmark, *Chem. Phys. Lett.* **2005**, *409*, 295–299.
- [60] T. H. Dunning Jr., *J. Chem. Phys.* **1989**, *90*, 1007–1023.
- [61] R. A. Kendall, T. H. J. Dunning, R. J. Harrison, *J. Chem. Phys.* **1992**, *96*, 6796–6806.
- [62] K. Pierloot, E. Van Besien, *J. Chem. Phys.* **2005**, *123*.
- [63] K. Pierloot, E. Van Besien, E. Van Lenthe, E. J. Baerends, *J. Chem. Phys.* **2007**, *126*.
- [64] F. Wei, G. Wu, W. H. Schwarz, J. Li, *Theor. Chem. Acc.* **2011**, *129*, 467–481.
- [65] J. P. Zobel, J. J. Nogueira, L. González, *Chem. Sci.* **2017**, *8*, 1482–1499.
- [66] B. Miehlich, A. Savin, H. Stoll, H. Preuss, *Chem. Phys. Lett.* **1989**, *157*, 200–206.

- [67] C. Lee, W. Yang, R. G. Parr, *Phys. Rev. B.* **1988**, *37*, 785–789.
- [68] A. D. Becke, *J. Chem. Phys.* **1993**, *98*, 1372–1377.
- [69] A. D. Becke, *Phys. Rev. A.* **1988**, *38*, 3098–3100.
- [70] R. Krishnan, J. S. Binkley, R. Seeger, J. A. Pople, *J. Chem. Phys.* **1980**, *72*, 650–654.
- [71] M. J. Frisch, G. W. Trucks, H. B. Schlegel, G. E. S. an M. A. Robb, J. R. Cheeseman, J. A. J. Montgomery, T. Vreven, K. N. Kudin, J. C. Burant, J. M. Millam, S. S. Iyengar, J. Tomasi, V. Barone, B. Mennucci, M. Cossi, G. Scalmani, N. Rega, G. A. Petersson, H. Nakatsuji, M. Hada, M. Ehara, K. Toyota, R. Fukuda, J. Hasegawa, M. Ishida, T. Nakajima, Y. Honda, O. Kitao, H. Nakai, M. Klene, X. Li, J. E. Knox, H. P. Hratchian, J. B. Cross, V. Bakken, C. Adamo, J. Jaramillo, R. Gomperts, R. E. Stratmann, O. Yazyez, A. J. Austin, R. Cammi, C. Pomelli, J. W. Ochterski, P. Y. Ayala, K. Morokuma, G. A. Voth, P. Salvador, J. J. Dannenberg, V. G. Zakrzewski, S. Dapprich, A. D. Daniels, M. C. Strain, O. Farkas, D. K. Malick, A. D. Rabuck, K. Raghavachari, J. B. Foresmann, J. V. Ortiz, Q. Cui, A. G. Baboul, S. Clifford, J. Cioslowski, B. B. Stefanov, G. Liu, A. Liashenko, P. Piskorz, I. Komaromi, R. L. Martin, D. J. Fox, T. Keith, M. A. Al.Laham, C. Y. Peng, A. Nanayakkara, M. Challacombe, P. M. W. Gill, B. Johnson, W. Chen, M. W. Wong, C. Gonzalez, J. A. Pople, *Gaussian 09. 2015 Gaussian Inc. Wallingford CT.*
- [72] X. Cao, M. Dolg, H. Stoll, *J. Chem. Phys.* **2003**, *118*, 487–496.
- [73] X. Cao, M. Dolg, *J. Mol. Struc-THEOCHEM* **2004**, *673*, 203–209.
- [74] W. Küchle, M. Dolg, H. Stoll, H. Preuss, *J. Chem. Phys.* **1994**, *100*, 7535–7542.
- [75] A. K. Wilson, T. Van Mourik, T. H. J. Dunning, *J. Mol. Struct.: THEOCHEM* **1996**, *388*, 339–349.
- [76] S. Hirata, M. Head-Gordon, *Chem. Phys. Lett.* **1999**, *314*, 291–299.
- [77] T. A. Keith, AIMAll, **2014**.
- [78] T. Lu, F. Chen, *J. Comput. Chem.* **2012**, *33*, 580–592.
- [79] D. E. Woon, T. H. J. Dunning, *J. Chem. Phys.* **1993**, *98*, 1358–1371.
- [80] R. Ahlrichs, M. Bär, M. Häser, H. Horn, C. Kölmel, *Chem. Phys. Lett.* **1989**, *162*, 165–169.
- [81] A. Klamt, G. Schüürmann, *J. Chem. Soc., Perkin Trans. 2* **1993**, 799–805.
- [82] S. Matsika, R. M. Pitzer, *J. Phys. Chem. A.* **2001**, *105*, 637–645.
- [83] R. G. Denning in *Electronic Structure and Bonding in Actinyl Ions*, **1992**, pp. 217–276.

- [84] Z. Zhang, R. M. Pitzer, *J. Phys. Chem. A* **1999**, *103*, 6880–6886.
- [85] N. Kaltsoyannis, *Inorg. Chem.* **2000**, *39*, 6009–6017.
- [86] N. Kaltsoyannis, *Chem. Soc. Rev.* **2003**, *32*, 9–16.
- [87] R. G. Denning, J. C. Green, T. E. Hutchings, C. Dallera, A. Tagliaferri, K. Giarda, N. B. Brookes, L. Braicovich, *J. Chem. Phys.* **2002**, *117*, 8008–8020.
- [88] R. L. Dekock, E. J. Baerends, P. M. Boerrigter, J. G. Snijders, *Chem. Phys. Lett.* **1984**, *105*, 308–316.
- [89] P. Di Pietro, A. Kerridge, *Inorg. Chem.* **2016**, *55*, 573–583.
- [90] D. L. Clark, S. D. Conradson, R. J. Donohoe, D. W. Keogh, D. E. Morris, P. D. Palmer, R. D. Rogers, C. D. Tait, *Inorg. Chem.* **1999**, *38*, 1456–1466.
- [91] P. G. Allen, J. J. Bucher, D. L. Clark, N. M. Edelstein, S. A. Ekberg, J. W. Gohdes, E. A. Hudson, N. Kaltsoyannis, W. W. Lukens, M. P. Neu, P. D. Palmer, T. Reich, D. K. Shuh, C. D. Tait, B. D. Zwick, *Inorg. Chem* **1995**, *34*, 4797–4807.
- [92] L. H. Jones, *Spectrochim. Acta.* **1958**, *10*, 395–403.
- [93] L. H. Jones, *Spectrochim. Acta.* **1959**, *15*, 409–411.
- [94] K. I. Ingram, L. J. L. Häller, N. Kaltsoyannis, *Dalton Trans.* **2006**, *2*, 2403–2414.

## Chapter 6

# Investigation of a *trans* - *cis* isomerism in uranyl hydroxide analogues via intramolecular proton transfer

*Within this chapter an intramolecular proton transfer from a hydroxide ligand to a uranyl oxygen is investigated on both the ground and excited state potential energy surfaces on a variety of different complexes. This reaction results in a trans to cis isomerisation of the uranyl unit and hence is an alternative way to create a bend in the uranyl unit in comparison to Chapter 5. The activation energy for both the forward (*trans*→TS) and the reverse (*cis*→TS) reactions as well as the relative stabilisation of the trans conformer compared to the cis are investigated while varying one/two of the equatorial ligands from the benchmark uranyl hydroxide ( $[UO_2(OH)_4]^{2-}$ ) complex. The aim of this chapter is to primarily decrease the activation energy of the forward reaction ( $E_a T^\ddagger$ ) and secondly to increase the stability of the cis conformer, which will be indicated by an increase in the activation energy of the reverse reaction ( $E_a C^\ddagger$ ) as well as a decrease in the trans stabilisation energy ( $\Delta^{TC}$ ). Throughout this chapter numerous investigations were conducted, changing the chemical structure of the benchmark complex in order investigate the effect of these changes on  $E_a T^\ddagger/E_a C^\ddagger$  and  $\Delta^{TC}$ . Firstly, the effect of excitation (at the ground state geometry) into the optically accessible  $\sigma_u \rightarrow \delta_u$  state on  $E_a T^\ddagger/E_a C^\ddagger$  and  $\Delta^{TC}$  was established. Upon excitation of the benchmark complex,  $E_a T^\ddagger$  and  $\Delta^{TC}$  decreased, while  $E_a C^\ddagger$  increased indicating the relative stabilisation of the cis conformer in the excited state. Therefore for each subsequent complex studied both  $E_a T^\ddagger/E_a C^\ddagger$  and  $\Delta^{TC}$  was calculated at both the ground and excited state electronic structures at the ground state geometry. The effect of overall charge, electronegativity and bite angle were also investigated, using different ligand types, in three separate studies with: neutral ligands, halogens and negatively charge oxygen coordinating bidentate ligands respectively.*

## 6.1 Introduction

In Chapter 5, the uranyl unit was distorted via complexation with ligands which resulted in unfavourable steric interactions. A number of different bulky ligands were investigated and it was concluded that porphyrinoid-type ligands (complexes (d) and (e) in Section 5.3.3 of Chapter 5), with a small pore size, rigid structure and negative charge gave the largest deviation from 180°, resulting in an O-U-O angle of 100°. This angle is close to a *cis* arrangement of the uranyl unit, however thermochemical calculations showed that these porphyrinoid complexes were unlikely to be synthetically viable. An alternative method of arriving at the *cis* conformation of uranyl is via an intramolecular reaction.

Clark *et. al* investigated uranyl hydroxide ( $[\text{UO}_2(\text{OH})_4]^{2-}$ ) in highly alkaline conditions in order to simulate the waste tanks within the Department of Energy (DOE) complex. [1] Their studies showed a rapid ligand exchange between axial and equatorial oxygens in which they explained via a concerted mechanism (Figure 6.1) involving the movement of two hydrogens. Later Schreckenbach *et. al* [2] investigated this mechanism computationally and found that a large activation energy (245.18 kJ mol<sup>-1</sup>) was required. This led them to propose a non-aqueous intramolecular proton exchange of a single proton, between a OH equatorial ligand and the uranyl unit. Their mechanism involves a stable intermediate with a bent uranyl unit, *cis*-uranyl. The first half of their proposed mechanism is shown via an energy profile in Figure 6.2, the second half of the mechanism is simply another proton transfer, involving the second uranyl oxygen and another hydroxide ligand resulting in the final product in Figure 6.1. During their investigation they also found several different stable *cis* isomers of  $[\text{UO}_2(\text{OH})_4]^{2-}$  with O-U-O angles as low as 113° and an energy difference between the *trans* and *cis* conformers ( $\Delta^{\text{TC}}$ ) as 75.3 kJ mol<sup>-1</sup>. It is worth noting that later Schreckenbach *et. al* lowered the activation energy by 25.52 kJ mol<sup>-1</sup> via inclusion of a water molecule into the proton shuttle, which was further lowered by 21 kJ mol<sup>-1</sup> by use of a continuum solvent. [3] However, they concluded that these activation energies did not readily explain the rapid exchange between the axial and equatorial oxygens. Bühl and Schreckenbach proposed that the issue with their suggested mechanism was down to the *cis* uranyl intermediate, which requires the system to sacrifice the energetic advantage of remaining in its *trans* or linear arrangement. To which they proposed a mechanism which allows uranyl to retain its linearity. [4]

Herein, the proposed mechanism involving an intramolecular proton exchange between a OH equatorial ligand and the uranyl unit suggested by Schreckenbach *et. al* [2] (Figure 6.2) is utilised as an alternative method of obtaining *cis* uranyl. In this chapter, the energetics for the intramolecular proton exchange between a OH equatorial ligand and the uranyl oxygen with a variety of other ligand types is investigated, with the primary aim of decreasing  $E_a\text{T}^\ddagger$  from that of  $[\text{UO}_2(\text{OH})_4]^{2-}$ .

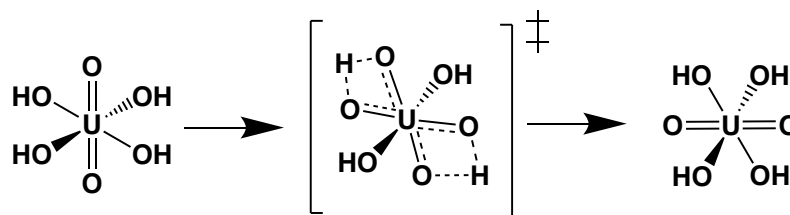


Figure 6.1: Concerted mechanism proposed by Clark *et. al* explaining the rapid ligand exchange between axial and equatorial oxygens. [1, 3]

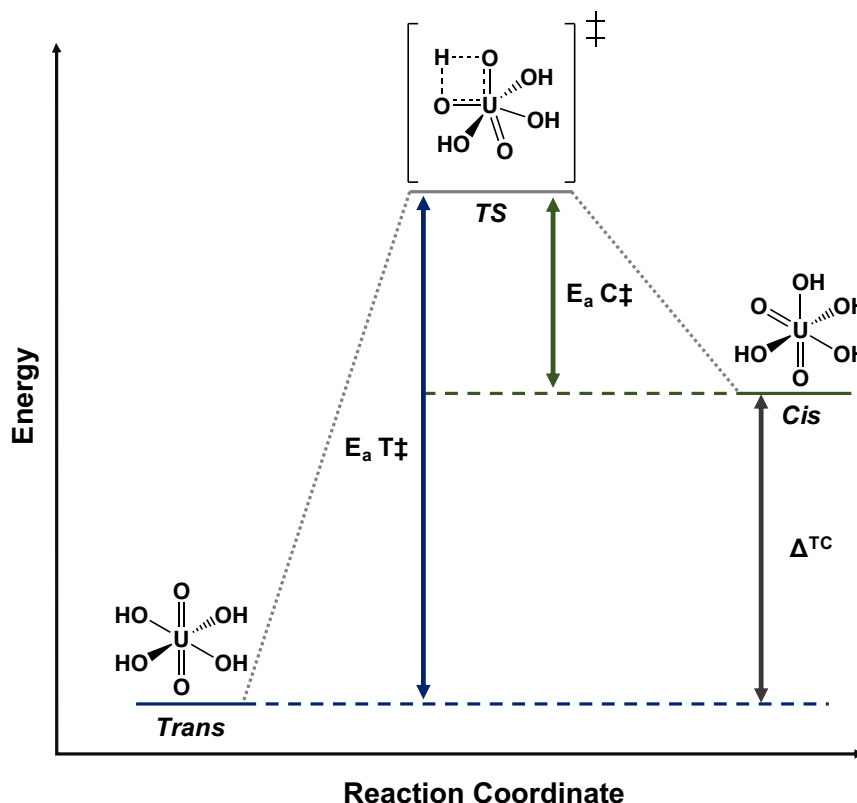


Figure 6.2: Energy profile for a proton transfer from an equatorial hydroxide ligand to a uranyl oxygen as proposed by Schreckenbach *et. al* [2]. The activation energy for the forward reaction (*trans* → *Transition State* (*TS*)) and the reverse (*cis* → *TS*) are represented by  $E_a T^\ddagger$  and  $E_a C^\ddagger$  respectively, while the relative stabilisation of the *trans* isomer with respect to the *cis* is denoted  $\Delta^{TC}$ .

The energy profile representing the intramolecular proton transfer investigated in this chapter is given in Figure 6.2. The *trans* conformer of the  $[UO_2(OH)_4]^{2-}$  complex is the global minimum, the *transition state* (*TS*) shows a hydrogen equidistant between two neighbouring oxygens with the activation energy required to go between the two labelled as  $E_a T^\ddagger$ . The *cis* conformation is higher in energy than the *trans* conformer and the relative stabilisation of the *trans* isomer relative to the *cis* isomer is denoted  $\Delta^{TC}$  and the activation energy of the reverse reaction is given by  $E_a C^\ddagger$ .

It was thought that conducting this intramolecular reaction in the excited state

may also decrease the energy barriers and so vertical excitation energies for the optically accessible  $\sigma_u \rightarrow \delta_u$  excitation, previously studied in Chapters 3, 4 and 5, were utilised to examine the barriers in the excited state. It was seen in Chapter 5 Section 5.3.2 that at the excited state geometries the uranyl angle, already significantly bent, further decreased and hence it was thought that this excitation would lower  $E_a T_{\ddagger}$ . As well as decreasing  $E_a T_{\ddagger}$ , a secondary objective was to stabilise the *cis* conformation and this would be indicated by the increase in  $E_a C_{\ddagger}$  and decrease in  $\Delta^{\text{TC}}$  in comparison to  $[\text{UO}_2(\text{OH})_4]^{2-}$ . Out of the two metrics,  $E_a C_{\ddagger}$  is the more relevant as this indicates the kinetic stability of the *cis* conformer, in contrast  $\Delta^{\text{TC}}$  indicates the thermodynamic stability and out of the two conformers the *trans* will always be the more thermodynamically stable.

After the preliminary study of the benchmark complex -  $[\text{UO}_2(\text{OH})_4]^{2-}$  [2] (complexes (a) and (b)), in both the ground and excited states, three other sets of ligand types were investigated. The ligands were chosen in order to vary the chemical system by changing: the overall charge of the complex (Section 6.3.1, complexes (i) - (vi)), the electronegativity of the ligands (Section 6.3.2, complexes (A) - (I)) and the coordination type from monodentate to bidentate (Section 6.3.3, complexes (1) - (5)). Each ligand replaced up to two of the equatorial OH ligands, resulting in three different structures for each ligand investigated (Figure 6.7): 1 coordinating ligand and two different conformations with 2 non-hydroxide ligand coordination; where the non-hydroxide ligands are  $90^\circ$  and  $180^\circ$  to each other. The first investigation involved neutral  $\text{H}_2\text{O}$  and  $\text{NH}_2\text{Me}$  ligands ((i) - (vi)) in order to investigate the effect of the overall charge of the complex on the energetics. Second, halogen ligands: F, Cl and Br ((A) - (I)) were utilised to explore the effect of ligand electronegativity and lastly, bidentate ligands: Catechol, Oxalate and Biphenolate, ((1) - (5)) were utilised to investigate the effect of the bite angle.

## 6.2 Computational Details

All simulations were performed at the hybrid DFT level, using the B3LYP [5–9] exchange–correlation functional in the Gaussian09 (Revision E.01) programme. [10] The Stuttgart RSC 1997 [11–13] basis set and associated small effective core potential (60 electrons), acquired from the basis-set exchange [14–16] was used for uranium while the correlation consistent aug-cc-pVDZ [17–19] Dunning basis set was implemented for the light elements (H, C, N, O, P, S, Cl). Geometry optimisations for the *cis* and *trans* isomers were characterised as minima by vibrational frequency analysis, while the optimised transition state (*TS*) geometries were characterised by having a single large imaginary mode indicating a proton transfer from the hydroxide equatorial ligand to the uranyl oxygen. The Tamm–Dancoff Approximation (TDA) [20] to Time Dependent-DFT (TD-DFT) [21, 22] was used to calculate vertical excitations at the optimised *TS*, *cis* and *trans* geometries.

In order to isolate the correct *TS* firstly an approximate geometry was constructed and vibrational analysis was conducted. Once the highest imaginary mode depicted proton transfer a *TS*-optimisation calculation was conducted and characterised via vibrational analysis. From the isolated *TS*, an IRC (Intrinsic Reaction Coordinate) calculation with 30 steps was conducted in order to simulate the reaction path from the *TS* in both directions. The resultant ‘ends’ of the IRC curve gave approximate *trans* and *cis* geometries, which were then optimised to minima.

### 6.3 Results and Discussion

The optimised ground state geometry of complex (2) from Chapter 4 was used as a starting point and a proposed *TS* geometry for a proton transfer from an equatorial hydroxide ligand to a uranyl hydroxide was estimated. Vibrational analysis indicated that the highest imaginary mode depicted a proton transfer and thus a transition state optimisation was conducted from this starting point.

The global minima structure of the hydroxide complex, as found by Ingram *et al.* [23] and studied in Chapter 4 has hydroxide ligands which are 180° to each other aligned parallel and those 90° to each other aligned antiparallel. Therefore, the *TS*, from this global minima has two possible orientations of the hydroxide groups; where the hydroxide ligands are aligned parallel or antiparallel to the oxygen accepting the proton, complexes (b) and (a) respectively, as shown in Figure 6.3.

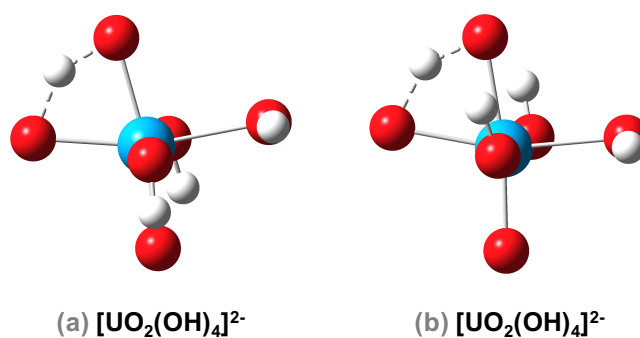


Figure 6.3: Two possible orientations for the equatorial hydroxide ligand at the *TS* optimised geometries

Upon optimising the *TS* structures for both complexes,  $E_a T^\ddagger$  values were calculated as: 158.205 kJ mol<sup>-1</sup> and 157.788 kJ mol<sup>-1</sup> for complexes (a) and (b) respectively. Complex (b) (hydroxides pointing up) had the smaller  $E_a T^\ddagger$  and was the lower energy of the two *TS* geometries and hence was used for the remainder of the study.

An IRC calculation using *TS* (b) as the starting geometry was then conducted. This calculation generates a reaction path from the *TS* in both directions with the resultant ‘ends’ of the IRC curve giving approximate *cis* and *trans* geometries. The IRC plot for hydroxide is given in figure 6.4; from left to right the curve represents

the *cis* isomer, the *TS* and then the *trans* isomer at the lowest energy.

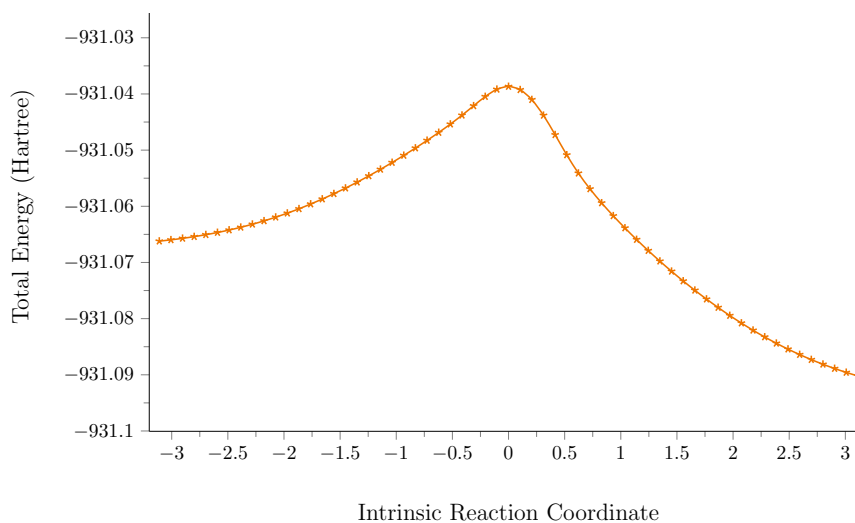


Figure 6.4: IRC reaction path for complex (b); the stages of the curve, from left to right, represent the *cis* isomer, the *TS* and then the *trans* isomer at the lowest energy

Using the ‘end points’ (intrinsic reaction coordinates 3 and -3) from the IRC curve as starting points, the *cis* and *trans* isomers were optimised and the resultant energy barriers were calculated as:  $E_a T^\ddagger = 157.788 \text{ kJ mol}^{-1}$ ,  $E_a C^\ddagger = 74.909 \text{ kJ mol}^{-1}$  and  $\Delta^{\text{TC}} = 82.879 \text{ kJ mol}^{-1}$ .  $E_a T^\ddagger$  and  $\Delta^{\text{TC}}$  are in excellent agreement with that calculated by Schreckenbach *et. al* [2];  $161.92 \text{ kJ mol}^{-1}$  and  $75.3 \text{ kJ mol}^{-1}$ , respectively.

In order to calculate whether these energy barriers increase or decrease in the excited state, vertical excitations were conducted at each geometry. As was the case in Chapters 4 and 5 the optically accessible  $\sigma_u \rightarrow \delta_u$  excitation is the state of interest. For simplicity, only the lowest energy  $\sigma_u \rightarrow \delta_u$  excitation is used in the calculation of the excited state barriers. Excited state geometry optimisations were not conducted as obtaining an electronically excited *TS* structure is very challenging and computationally expensive. It was deemed that the total energies of the vertical excitations at the ground state geometry would indicate if there were significant changes in the energetics at the excited state.

The  $\sigma_u$  and  $\delta_u$  MOs for each conformation are given in Figure 6.5 and the lowest energy  $\sigma_u \rightarrow \delta_u$  excitation energies are summarised in Table 6.1. These MOs show clear  $\sigma_u$  and  $\delta_u$  nature and as was seen in Chapter 4 there is mixing between the uranium 5f and all oxygen 2p AOs which causes bonding interactions in the *trans* conformer and antibonding interactions in both the *cis* and *TS* conformers. The lowest energy  $\sigma_u \rightarrow \delta_u$  excitations given in Table 6.1 all involve excitations to the more stable (and more localised) particle MO (left hand  $\delta_u$  MO in Figure 6.5).

In order to obtain the energy barriers in the excited state, the excitation energy is added to the total energy of the conformer. The resultant excited state energy

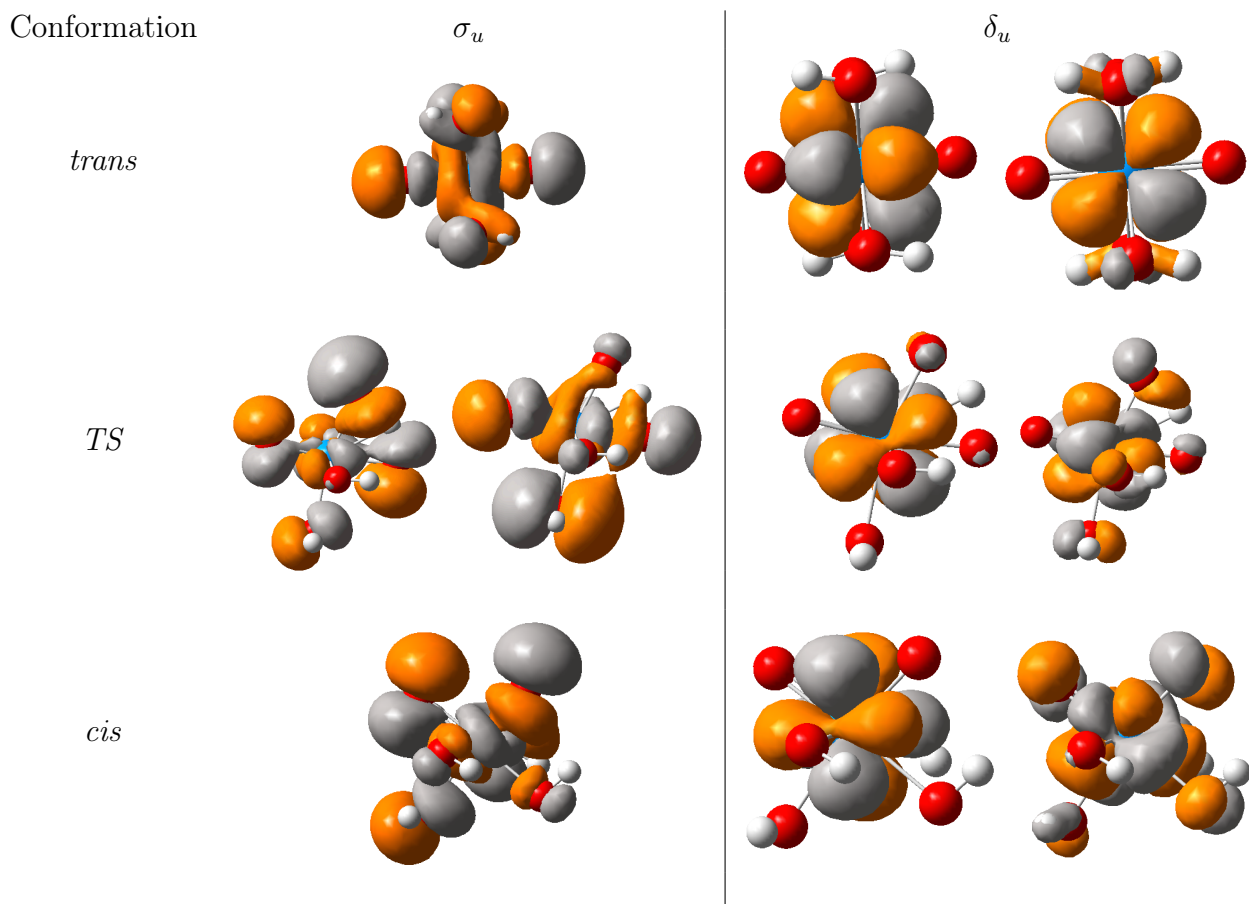


Figure 6.5: MOs with  $\sigma_u$  and  $\delta_u$  nature for each conformer of  $[\text{UO}_2(\text{OH})_4]^{2-}$

Table 6.1: Lowest energy  $\sigma_u \rightarrow \delta_u$  excitation energy ( $\Delta E$ ) and overall contribution from the transition of interest for the conformers of  $[\text{UO}_2(\text{OH})_4]^{2-}$

Conformer	State	$\Delta E$ (eV)	Contribution (%)
<i>trans</i>	T <sub>56</sub>	2.72	92
<i>TS</i>	T <sub>49</sub>	2.50	85
<i>cis</i>	T <sub>44</sub>	2.47	87

barriers were calculated as:  $E_a\text{T}\ddagger = 137.217 \text{ kJ mol}^{-1}$ ,  $E_a\text{C}\ddagger = 77.572 \text{ kJ mol}^{-1}$  and  $\Delta^{\text{TC}} = 59.646 \text{ kJ mol}^{-1}$ .

Energy diagrams at both the ground (GS) and excited states (ES) are given in Figure 6.6. In comparison to the ground state,  $E_a\text{T}\ddagger$  and  $\Delta^{\text{TC}}$  have significantly decreased while  $E_a\text{C}\ddagger$  increased slightly in the excited state; indicating that the *cis* conformation becomes more stable in the excited state in comparison to the ground state.

The rest of this chapter involves investigating the effects of different ligand types on the activation energies and the *trans* stabilisation, using the *TS* geometry of

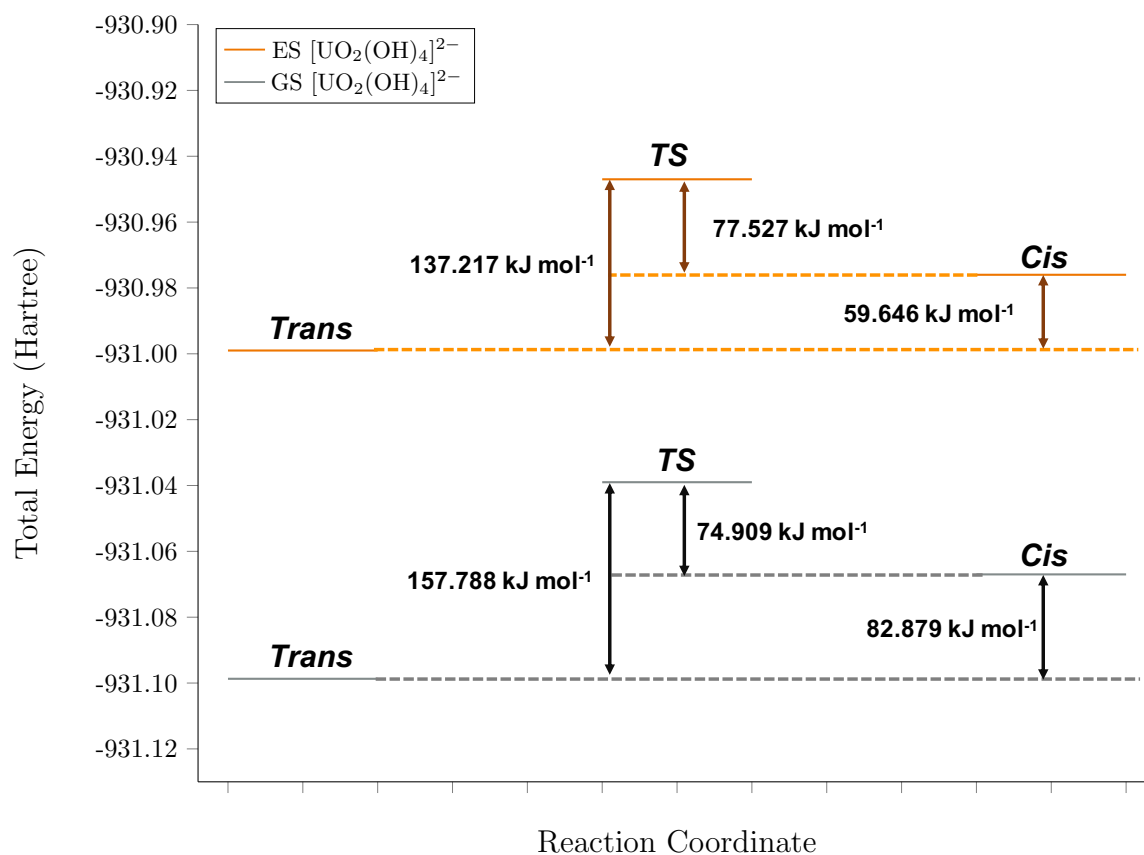


Figure 6.6: Energy diagrams at both the ground and excited states of complex (b)

complex (b) as a starting point and replacing up to two of the equatorial hydroxide ligands. For each ligand investigated, three structures were generated as shown in Figure 6.7.

### 6.3.1 Effect of overall charge

In this section both H<sub>2</sub>O and NH<sub>2</sub>Me neutral ligands were investigated, complexes (i) - (vi) depicted in Figure 6.7, in order to assess the effect on  $E_a T^\ddagger$ ,  $E_a C^\ddagger$  and  $\Delta^{TC}$  when the overall charge of the complex is changed. Complexes (i) and (iv) replace an equatorial OH ligand from (b) with a H<sub>2</sub>O or NH<sub>2</sub>Me ligand, respectively, resulting in a -1 charge on the complex. The remaining complexes replace two OH ligands with H<sub>2</sub>O/NH<sub>2</sub>Me and are neutral. In the two H<sub>2</sub>O/NH<sub>2</sub>Me coordinate complexes there are two arrangements of these ligands, one where the neutral ligands are either 90° ((ii) and (v)) or 180° to each other ((iii) and (vi)) and the other. The optimised *TS* geometries are shown in Figure 6.7.

IRC calculations were run on each *TS* geometry and the ‘end points’ were used as starting geometries for the *cis* and *trans* geometry optimisations. However, the optimisation calculations of the *cis* conformations of (i) and (ii) optimised to the *trans* arrangement of the uranyl unit. The optimisation pathway for complex (i)

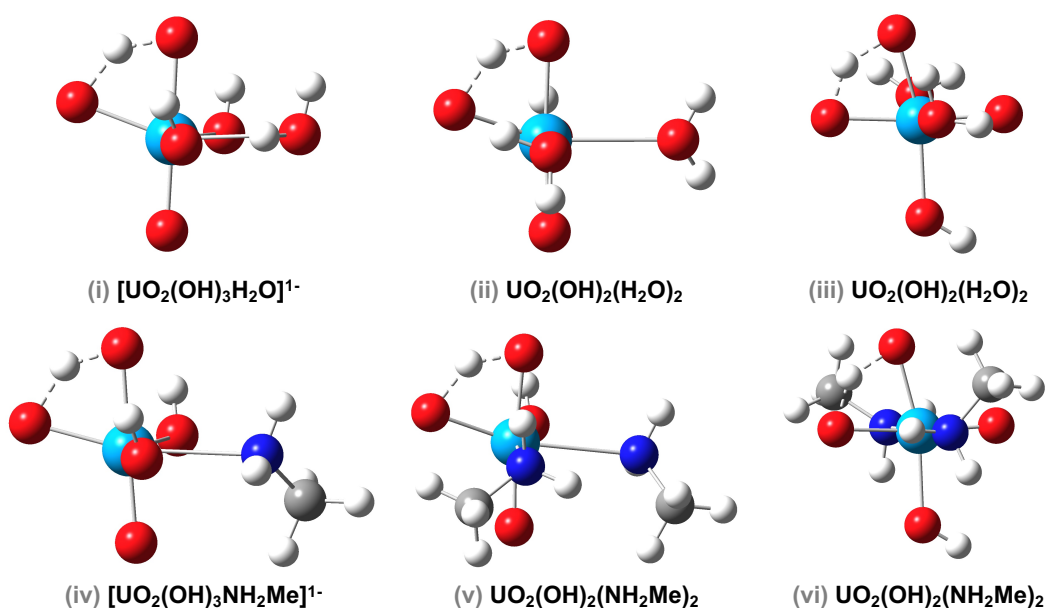


Figure 6.7: Optimised *TS* geometries for the neutral ligand ( $\text{H}_2\text{O}$  and  $\text{NH}_2\text{Me}$ ) complexes investigated

Table 6.2: Comparison of the activation energies for the forward and reverse reaction ( $E_a\text{T}^\ddagger/E_a\text{C}^\ddagger$ ) and the *trans* stabilisation ( $\Delta^{\text{TC}}$ ) energy for complexes (i) - (vi) at the optimised geometries.

Complex	$E_a\text{T}^\ddagger$ (kJ mol <sup>-1</sup> )	$E_a\text{C}^\ddagger$ (kJ mol <sup>-1</sup> )	$\Delta^{\text{TC}}$ (kJ mol <sup>-1</sup> )
(b) $(\text{UO}_2(\text{OH})_4)^{2-}$	157.788	74.909	82.879
(i) $[\text{UO}_2(\text{OH})_2(\text{H}_2\text{O})]^{1-}$	180.351	80.911*	99.440*
(ii) $\text{UO}_2(\text{OH})_2(\text{H}_2\text{O})_2$	194.795	97.139*	97.656*
(iii) $\text{UO}_2(\text{OH})_2(\text{H}_2\text{O})_2$	170.754	107.497	63.256
(iv) $[\text{UO}_2(\text{OH})_2(\text{NH}_2\text{Me})]^{1-}$	178.604	81.071*	97.533*
(v) $\text{UO}_2(\text{OH})_2(\text{NH}_2\text{Me})_2$	189.470	97.317*	92.153*
(vi) $\text{UO}_2(\text{OH})_2(\text{NH}_2\text{Me})_2$	167.365	105.079	62.286

\* Energies taken using IRC calculation

shows the uranyl unit straightening and the ligands moving around the complex to make room resulting in the water dissociating, while in complex (ii), the *cis* conformer simply optimised to the *trans* arrangement of the uranyl unit and both waters remained coordinated. The latter optimisation pathway was also experienced in the corresponding  $\text{NH}_2\text{Me}$  complexes ((iv) and (v)) again highlighting the simi-

larities between the two complexes. Multiple attempts were made to obtain the *cis* conformations of these complexes but with no success.

Table 6.2 summaries  $E_a T_{\ddagger}^{\ddagger}$ ,  $E_a C_{\ddagger}^{\ddagger}$  and  $\Delta^{TC}$  for complexes (i) - (vi). The missing *cis* conformation energies are substituted with the data from the *cis* 'end point' of the IRC calculation and are indicated with \*. All the energy barriers are larger than in complex (b), which indicates that the *TS* structure is more destabilised. Complexes with the same structure but different ligands *i.e.* (i) and (iv) have similar energy barriers, with the complex containing  $NH_2Me$  ligands being between 2-5  $\text{kJ mol}^{-1}$  lower. The data in Table 6.2 indicates that decreasing the overall charge of the complex results in an increase in both  $E_a T_{\ddagger}^{\ddagger}$  and  $E_a C_{\ddagger}^{\ddagger}$  and a decrease in  $\Delta^{TC}$ , which indicates that the *cis* conformer becomes more stabilised. Complexes (iii) and (vi) are more stable than the corresponding complexes with the ligands at  $90^\circ$  to each other and represent the best alternative to complex (b). These complexes have the lowest  $E_a T_{\ddagger}^{\ddagger}$  and  $\Delta^{TC}$  and largest  $E_a C_{\ddagger}^{\ddagger}$ , corresponding to the most stabilised *cis* conformer in complexes (i) - (vi).

Table 6.3: Lowest energy  $\sigma_u \rightarrow \delta_u$  excitation energy ( $\Delta E$ ) and overall contribution from the transition of interest for the minimum and *TS* geometries of complexes (i) - (vi) .

Complex	Conformer	State	$\Delta E$ (eV)	Contribution (%)
(i) $(UO_2(OH)_3H_2O)^{1-}$	<i>trans</i>	$T_1$	2.60	70
	<i>TS</i>	$T_1$	2.37	75
(ii) $UO_2(OH)_2(H_2O)_2$	<i>trans</i>	$T_1$	2.45	91
	<i>TS</i>	$T_1$	2.26	80
(iii) $UO_2(OH)_2(H_2O)_2$	<i>trans</i>	$T_1$	2.53	95
	<i>TS</i>	$T_1$	2.31	67
	<i>cis</i>	$T_1$	2.38	96
(iv) $(UO_2(OH)_3NH_2Me)^{1-}$	<i>trans</i>	$T_1$	2.63	74
	<i>TS</i>	$T_1$	2.38	76
(v) $UO_2(OH)_2(NH_2Me)_2$	<i>trans</i>	$T_1$	2.50	86
	<i>TS</i>	$T_1$	2.27	82
(vi) $UO_2(OH)_2(NH_2Me)_2$	<i>trans</i>	$T_1$	2.58	97
	<i>TS</i>	$T_1$	2.35	69
	<i>cis</i>	$T_1$	2.41	97

Excitations for (b): *trans*  $T_{56} = 2.72$  eV, *TS*  $T_{49} = 2.50$  eV, *cis*  $T_{44} = 2.47$  eV

Vertical excitation calculations were performed on all minima and *TS* geometries and the lowest-lying  $\sigma_u \rightarrow \delta_u$  excitation for each structure is summarised in Table 6.3.

While the resultant MOs of interest have similar overall natures to those shown in Figure 6.5, the overall density is more complex due to the extra contributions from the electron density in the ligands.

$E_a T^\ddagger$ ,  $E_a C^\ddagger$  and  $\Delta^{TC}$  in the excited state of complexes (i) - (vi) are summarised in Table 6.4. As was the case in complex (b),  $E_a T^\ddagger$  and  $\Delta^{TC}$  are all lowered in the excited state. In contrast to (b) however,  $E_a C^\ddagger$  in complexes (iii) and (vi) decreases in the excited state; as  $\Delta^{TC}$  decreases in these complexes, the decrease in  $E_a C^\ddagger$  is consistent with the stabilisation of the *TS* in the excited state. The trends between the complexes remain unchanged in the excited state, with just the magnitudes of the energetics decreasing and hence the analysis remains the same.

Table 6.4: Comparison of the activation energies for the forward and reverse reaction ( $E_a T^\ddagger/E_a C^\ddagger$ ) and the *trans* stabilisation ( $\Delta^{TC}$ ) energy in the excited states of complexes (i) - (vi) .

Complex	$E_a T^\ddagger$ (kJ mol <sup>-1</sup> )	$E_a C^\ddagger$ (kJ mol <sup>-1</sup> )	$\Delta^{TC}$ (kJ mol <sup>-1</sup> )
(b) $(UO_2(OH)_4)^{2-}$	137.217	77.572	59.646
(i) $[UO_2(OH)_2(H_2O)]^{1-}$	158.034	/	/
(ii) $UO_2(OH)_2(H_2O)_2$	176.270	/	/
(iii) $UO_2(OH)_2(H_2O)_2$	149.430	101.274	48.156
(iv) $[UO_2(OH)_2(NH_2Me)]^{1-}$	153.904	/	/
(v) $UO_2(OH)_2(NH_2Me)_2$	167.067	/	/
(vi) $UO_2(OH)_2(NH_2Me)_2$	145.028	98.961	46.067

Out of the neutral complexes studied in this section, (iii) and (vi) are the most promising. Although  $E_a T^\ddagger$  is larger in these neutral complexes ((iii)/(vi)) when compared to (b), the *cis* conformation is more stabilised as indicated by the larger  $E_a C^\ddagger$  and smaller  $\Delta^{TC}$  energies.

Figure 6.8 compares the energy diagrams of complexes (b) ( $[UO_2(OH)_4]^{2-}$ ) and (iii) ( $UO_2(OH)_2(H_2O)_2$ ) at both the ground (GS) and excited states (ES). As both neutral ligands investigated gave similar barrier heights throughout this section, only one is compared to (b) for simplicity.

Figure 6.8 clearly shows the relative stabilisation of the *cis* conformer in the neutral (iii)  $UO_2(OH)_2(H_2O)_2$  complex as well as the large increase in the activation energy of the backward reaction in comparison to (b)  $[UO_2(OH)_4]^{2-}$ .

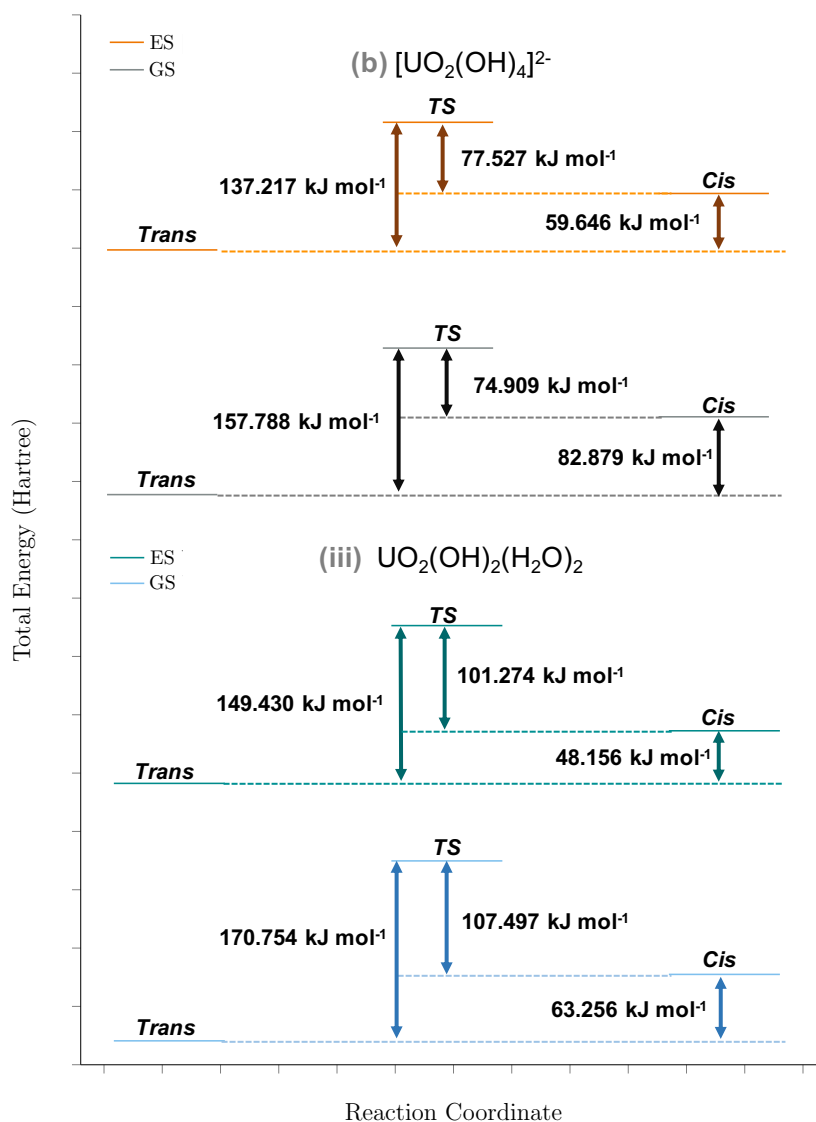


Figure 6.8: Energy diagrams for complexes (b) and (iii) at both the ground (GS) and excited states (ES).

In summary, decreasing the overall charge of the complex increases both  $E_a T^\ddagger$  and  $E_a C^\ddagger$  and stabilises the *cis* conformation. Therefore, the rest of the ligands studied in this section will ensure an overall -2 charge on the complex in order to attempt to keep  $E_a T^\ddagger$  lower than in these neutral complexes.

### 6.3.2 Replacing hydroxide with a halogen

In this section the effect of halogen coordination on  $E_a T^\ddagger$ ,  $E_a C^\ddagger$  and  $\Delta^{TC}$  is investigated. F, Cl and Br ligands were chosen as they are a monoatomic ligands of -1 charge, which ensures the total charge of -2 and keeps the system simple to avoid additional computational expense. These ligands allow exploration of the effect of electronegativity on the energy barriers to be investigated. The complexes with F ligands ((A) - (C)) are the most electronegative, followed by the benchmark

complex (b), which is more electronegative than the Cl complexes ((D) - (F)) and finally the Br complexes are the least electronegative ((G) - (I)). Investigating ligands within the same group also allows for trends to be highlighted within the halogen group in addition to the decreasing electronegativity down the group.

As in the previous section, the *TS* geometry of complex (b) was used as a starting point for the *TS* geometries of the halogen complexes ((A) - (I)), of which the optimised *TS* geometries are shown in Figure 6.9.

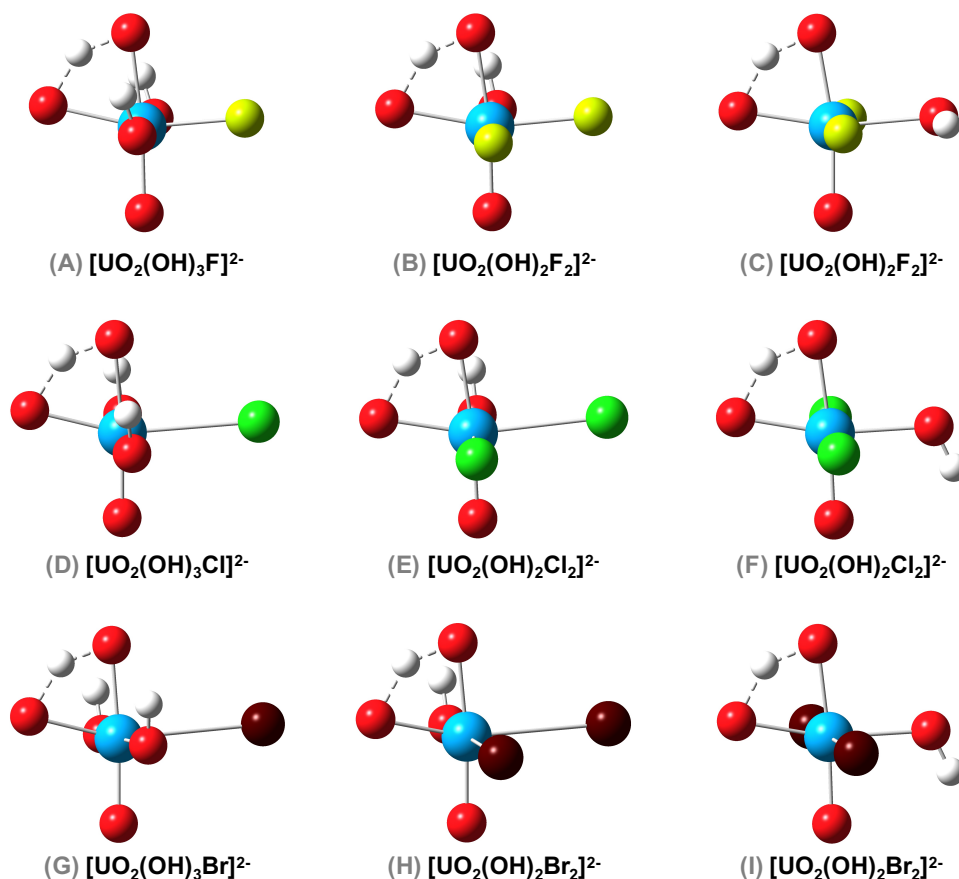


Figure 6.9: Optimised *TS* geometries for the halogen ligands (F, Cl and Br) complexes investigated

From these optimised *TS* geometries, IRC calculations were run followed by optimisations of the *cis* and *trans* geometries starting from the ends of the IRC curves. In contrast to the neutral  $\text{H}_2\text{O}$  and  $\text{NH}_2\text{Me}$  ligand complexes ((i) - (vi)) all of the *cis* conformations for the halogen complexes resulted in minima *cis* conformers.  $E_a\text{T}^\ddagger$ ,  $E_a\text{C}^\ddagger$  and  $\Delta^{\text{TC}}$  for complexes (A) - (I) are summarised in Table 6.5.

Comparison of complex (b) with the fluorine complexes ((A) - (C)) give very similar energetic results with only a small decrease in  $E_a\text{T}^\ddagger$  and  $\Delta^{\text{TC}}$  and a small increase in  $E_a\text{C}^\ddagger$ . This indicates that the *cis* conformation becomes more stabilised when the electronegativity of the ligand increases.

Moving down the halogen group to the chlorine complexes, ((D) - (F)), results in all energies increasing, with the exception of  $E_a\text{C}^\ddagger$  in (D) and  $\Delta^{\text{TC}}$  in (F). Hence in the chloride complexes, both the *trans* and *cis* conformers are stabilised but the

Table 6.5: Comparison of the activation energies for the forward and reverse reaction ( $E_a T^\ddagger/E_a C^\ddagger$ ) and the *trans* stabilisation ( $\Delta^{TC}$ ) energy of complexes (A) - (I).

Complex	$E_a T^\ddagger$ (kJ mol <sup>-1</sup> )	$E_a C^\ddagger$ (kJ mol <sup>-1</sup> )	$\Delta^{TC}$ (kJ mol <sup>-1</sup> )
(b) [UO <sub>2</sub> (OH) <sub>4</sub> ] <sup>2-</sup>	157.788	74.909	82.879
(A) [UO <sub>2</sub> (OH) <sub>3</sub> F] <sup>2-</sup>	154.421	76.691	77.730
(B) [UO <sub>2</sub> (OH) <sub>2</sub> F <sub>2</sub> ] <sup>2-</sup>	154.913	77.997	76.915
(C) [UO <sub>2</sub> (OH) <sub>2</sub> F <sub>2</sub> ] <sup>2-</sup>	157.908	88.167	69.741
(D) [UO <sub>2</sub> (OH) <sub>3</sub> Cl] <sup>2-</sup>	166.370	67.668	98.702
(E) [UO <sub>2</sub> (OH) <sub>2</sub> Cl <sub>2</sub> ] <sup>2-</sup>	169.588	77.881	91.707
(F) [UO <sub>2</sub> (OH) <sub>2</sub> Cl <sub>2</sub> ] <sup>2-</sup>	159.149	92.640	66.509
(G) [UO <sub>2</sub> (OH) <sub>3</sub> Br] <sup>2-</sup>	168.367	67.855	100.512
(H) [UO <sub>2</sub> (OH) <sub>2</sub> Br <sub>2</sub> ] <sup>2-</sup>	172.177	79.294	92.883
(I) [UO <sub>2</sub> (OH) <sub>2</sub> Br <sub>2</sub> ] <sup>2-</sup>	160.175	94.425	65.751

*trans* stabilisation is more significant indicated by the increase  $\Delta^{TC}$  and/or the *TS* becomes more destabilised.

The bromide complexes ((G) - (I)), result in  $E_a T^\ddagger$  and  $E_a C^\ddagger$  increasing and  $\Delta^{TC}$  decreasing, with the exception of  $E_a C^\ddagger$  in (G) and  $\Delta^{TC}$  in (I). This overall trend is shows that both the *trans* and *cis* conformers are stabilised, with the *cis* having the more significant relative stabilisation in order to decrease  $\Delta^{TC}$  and/or the *TS* becoming more destabilised.

From the energetic data in Table 6.5, the complexes which have the two halogen ligands at 180° to each other ((C), (F) and (I)) are the most promising. These complexes have the most stable *cis* conformer, indicated by the smallest  $\Delta^{TC}$  and largest  $E_a C^\ddagger$  values, and the smallest  $E_a T^\ddagger$ , within the complexes of the same ligand. These findings were also established with the neutral complexes but unconfirmed as the *cis* conformations for all other complexes except where the ligands were 180° to each other ((iii) and (iv)) were unobtainable, although that in itself highlighted that the *cis* conformations in the other complexes were unstable. Energy diagrams for the comparison of these three halogen complexes, (C), (F) and (I) are given in Figure 6.10.

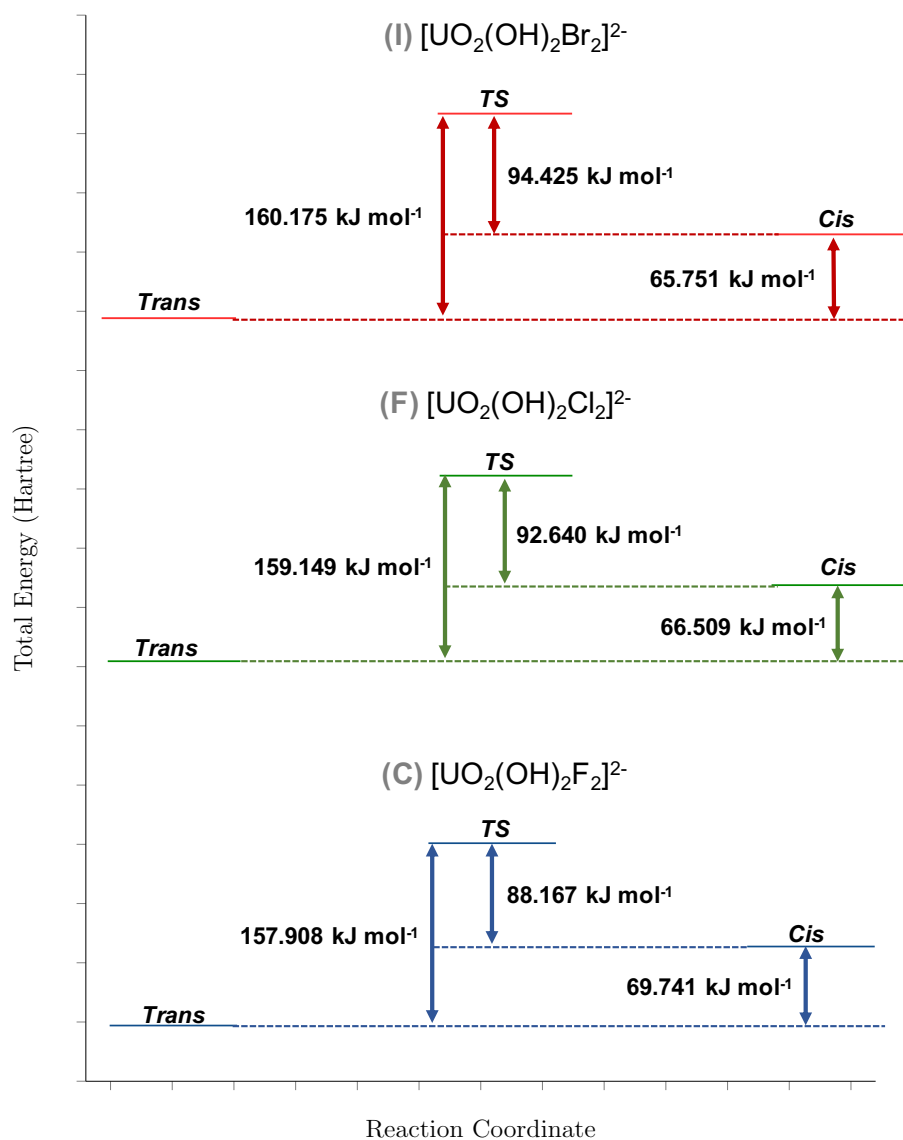


Figure 6.10: Ground state energy diagrams for the complexes which have two halogen ligands  $180^\circ$  to each other ((C), (F) and (I)).

The energy diagrams for complexes (C), (F) and (I) show an anti correlation between  $E_a\text{T}^\ddagger/E_a\text{C}^\ddagger$  and the electronegativity, in contrast to the positive correlation between  $\Delta^{\text{TC}}$  and electronegativity. These observations indicate that the *cis* conformer becomes more stabilised and the *TS* more destabilised as electronegativity decreases and the ligands become larger.

Vertical excitations were conducted on the optimised geometries of complexes (A) - (I) and the lowest energy  $\sigma_u \rightarrow \delta_u$  excitation for each conformer are given in Table 6.6. As was established in Chapter 4, the electron density on the halogen 2p AOs interacts with the U5f  $\sigma_u$  MO resulting in bonding and antibonding interaction between the  $\sigma_u$  on the uranyl unit and the halogen 2p AOs. Therefore, the halogen MOs are more complex than the neutral ligand counterparts, however, the overall nature is the same between all the complexes.

Table 6.6: Lowest energy  $\sigma_u \rightarrow \delta_u$  excitation energies ( $\Delta E$ ) and overall contribution from the transition of interest for the optimised geometries of complexes (A) - (I).

Complex	Conformation	State	$\Delta E$ (eV)	Contribution (%)
(b) (UO <sub>2</sub> (OH) <sub>4</sub> ) <sup>2-</sup>	<i>trans</i>	T <sub>56</sub>	2.72	92
	<i>TS</i>	T <sub>49</sub>	2.50	85
	<i>cis</i>	T <sub>44</sub>	2.47	87
(A) (UO <sub>2</sub> (OH) <sub>3</sub> F) <sup>2-</sup>	<i>trans</i>	T <sub>41</sub>	2.65	59
	<i>TS</i>	T <sub>40</sub>	2.50	82
	<i>cis</i>	T <sub>55</sub>	2.86	68
(B) (UO <sub>2</sub> (OH) <sub>2</sub> F <sub>2</sub> ) <sup>2-</sup>	<i>trans</i>	T <sub>26</sub>	2.59	90
	<i>TS</i>	T <sub>27</sub>	2.46	85
	<i>cis</i>	T <sub>32</sub>	2.52	83
(C) (UO <sub>2</sub> (OH) <sub>2</sub> F <sub>2</sub> ) <sup>2-</sup>	<i>trans</i>	T <sub>23</sub>	2.57	96
	<i>TS</i>	T <sub>31</sub>	2.42	77
	<i>cis</i>	T <sub>22</sub>	2.46	97
(D) (UO <sub>2</sub> (OH) <sub>3</sub> Cl) <sup>2-</sup>	<i>trans</i>	T <sub>32</sub>	2.67	54
	<i>TS</i>	T <sub>23</sub>	2.47	75
	<i>cis</i>	T <sub>31</sub>	2.56	95
(E) (UO <sub>2</sub> (OH) <sub>2</sub> Cl <sub>2</sub> ) <sup>2-</sup>	<i>trans</i>	T <sub>3</sub>	2.61	69
	<i>TS</i>	T <sub>1</sub>	2.43	76
	<i>cis</i>	T <sub>25</sub>	2.87	58
(F) (UO <sub>2</sub> (OH) <sub>2</sub> Cl <sub>2</sub> ) <sup>2-</sup>	<i>trans</i>	T <sub>2</sub>	2.62	82
	<i>TS</i>	T <sub>1</sub>	2.39	71
	<i>cis</i>	T <sub>1</sub>	2.44	83
(G) (UO <sub>2</sub> (OH) <sub>3</sub> Br) <sup>2-</sup>	<i>trans</i>	T <sub>30</sub>	2.67	69
	<i>TS</i>	T <sub>28</sub>	2.45	73
	<i>cis</i>	T <sub>31</sub>	2.54	82
(H) (UO <sub>2</sub> (OH) <sub>2</sub> Br <sub>2</sub> ) <sup>2-</sup>	<i>trans</i>	T <sub>10</sub>	2.60	56
	<i>TS</i>	T <sub>1</sub>	2.40	68
	<i>cis</i>	T <sub>31</sub>	2.84	55
(I) (UO <sub>2</sub> (OH) <sub>2</sub> Br <sub>2</sub> ) <sup>2-</sup>	<i>trans</i>	T <sub>3</sub>	2.61	95
	<i>TS</i>	T <sub>1</sub>	2.38	95
	<i>cis</i>	T <sub>1</sub>	2.43	96

The excitation energy of the  $\sigma_u \rightarrow \delta_u$  state is largest in the *trans* conformers and smallest in the *TS* structures across all complexes. This is consistent with the stabilisation/destabilisation of the hole MO ( $\sigma_u$ ) in the *trans* and *TS* conformers respectively. The particle MO ( $\delta_u$ ) is largely non-bonding and therefore should be unaffected by the positioning of the ligands, this is highlighted by Figure 6.5 which shows the  $\delta_u$  MOs being very similar across the conformers of complex (b), it is worth noting that the  $\delta_u$  MOs in the halogen complexes are extremely similar.

Table 6.7: Comparison of the activation energies for the forward and reverse reaction ( $E_a T^\ddagger/E_a C^\ddagger$ ) and the *trans* stabilisation ( $\Delta^{TC}$ ) energy of complexes (A) - (I) in the excited state (ES).

Complex	$E_a T^\ddagger$ (kJ mol <sup>-1</sup> )	$E_a C^\ddagger$ (kJ mol <sup>-1</sup> )	$\Delta^{TC}$ (kJ mol <sup>-1</sup> )
(b) [UO <sub>2</sub> (OH) <sub>4</sub> ] <sup>2-</sup>	137.217	77.572	59.646
(A) [UO <sub>2</sub> (OH) <sub>3</sub> F] <sup>2-</sup>	140.807	42.391	98.416
(B) [UO <sub>2</sub> (OH) <sub>2</sub> F <sub>2</sub> ] <sup>2-</sup>	142.399	71.629	70.769
(C) [UO <sub>2</sub> (OH) <sub>2</sub> F <sub>2</sub> ] <sup>2-</sup>	143.648	85.021	58.626
(D) [UO <sub>2</sub> (OH) <sub>3</sub> Cl] <sup>2-</sup>	146.812	58.666	88.147
(E) [UO <sub>2</sub> (OH) <sub>2</sub> Cl <sub>2</sub> ] <sup>2-</sup>	151.459	34.878	116.581
(F) [UO <sub>2</sub> (OH) <sub>2</sub> Cl <sub>2</sub> ] <sup>2-</sup>	137.566	87.623	49.943
(G) [UO <sub>2</sub> (OH) <sub>3</sub> Br] <sup>2-</sup>	147.970	59.239	88.731
(H) [UO <sub>2</sub> (OH) <sub>2</sub> Br <sub>2</sub> ] <sup>2-</sup>	153.304	36.667	116.638
(I) [UO <sub>2</sub> (OH) <sub>2</sub> Br <sub>2</sub> ] <sup>2-</sup>	138.283	89.504	48.779

The energetic data at the excited state of complexes (A)- (I) is given in Table 6.7. In the excited state all the barriers ( $E_a T^\ddagger$ ,  $E_a C^\ddagger$  and  $\Delta^{TC}$ ) decrease, with the exception of  $\Delta^{TC}$  in complexes (A), (E) and (H). These exceptions indicate a destabilisation of the *cis* conformer which is also highlighted by the significant decrease in  $E_a C^\ddagger$  in these complexes.

Overall, replacing the hydroxide ligands with the more electronegative fluorine ligands results in a small decrease in  $E_a T^\ddagger$  and  $\Delta^{TC}$  and a small increase in  $E_a C^\ddagger$ . These results are promising at the ground state electronic structures, showing a smaller  $E_a T^\ddagger$  and a more stabilised *cis* conformation, however at the excited state, the energies barriers were not lowered as effectively as in complex (b). The chloride

ligands in contrast have in a slight increase in  $E_a T_{\ddagger}^{\dagger}$  for all three structures, with complex (F) only having a slight increase when compared to (b). In contrast to (b), the *cis* conformation in complex (F) is more stable indicated by the larger  $E_a C_{\ddagger}^{\dagger}$  and smaller  $\Delta^{TC}$  values. These promising results were replicated in the excited state electronic structures, which suggests that complex (F) is the ‘best’ complex (besides (b)) investigated thus far, due to the low  $E_a T_{\ddagger}^{\dagger}$  and  $\Delta^{TC}$  energies and the larger  $E_a C_{\ddagger}^{\dagger}$  value.

### 6.3.3 Effect of bite angle: investigation of bidentate ligands

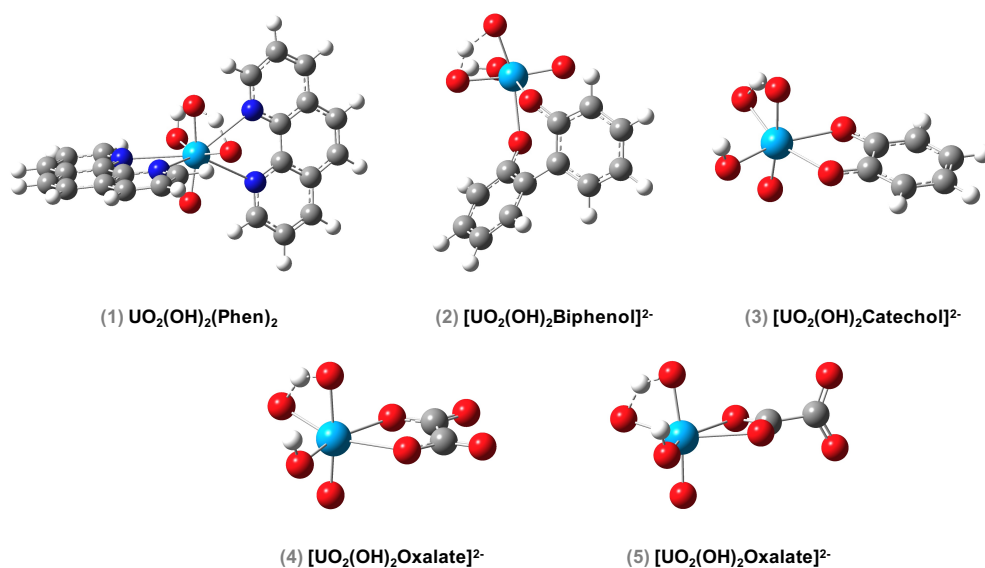


Figure 6.11: Optimised *TS* geometries for the bidentate complexes

Thus far only simple monodentate ligands have been considered. In this section, three different bidentate ligands with oxygen coordination and a -2 charge (biphenol ((2)), catechol ((3)) and oxalate ((4) & (5))) are investigated along with a variation of complex (i) studied in Section 5.3.2 of Chapter 5 (with OH replacing the Cl ligands, now labelled complex (1) as shown by Figure 6.11) which has a bent uranyl unit and has been studied experimentally by Schöne *et.al.* [24] This complex is included to investigate the effect of an already bent uranyl unit and it is worth noting that complex (1) is neutral in contrast to the -2 charge for all other complexes in this section. Attempts were made to optimise a similar system with a -2 charge; in this instance one of the phenanthroline ligands was replaced with two chloride ligands, however an optimised *trans* geometry was unobtainable as the during the optimisation calculation, the remaining phenanthroline (phen) ligand dissociated from the rest of the complex. These issues were rationalised by unfavourable steric interactions as the other -2 complexes were only 6 coordinate.

The optimised *TS* geometries for each of the bidentate complexes are given in Figure 6.11; there are two different binding modes for the oxalate ligand (complexes (4) and (5)), both were studied to extend the investigation of the bite angle on the energy barriers.

In complexes containing a bidentate ligand, the bite angle is defined as the ligand–metal–ligand bond angle between the bidentate ligand and the metal. [25] In this section, the bite angle can be used in order to compare the bidentate ligands to each other and the effect of the bite angle on the activation energies and *trans* stabilisation energy is therefore investigated throughout this section. The bite angle of the bidentate complexes are summarised in Table 6.8; the two phen bidentate ligands in complex (1) have different bite angles and so the average of the two is given in the table.

Table 6.8: Bite angles of the bidentate complexes shown in Figure 6.11.

Complex	Bite Angle (°)
(1) $\text{UO}_2(\text{OH})_2(\text{Phen})_2$	57.7*
(2) $[\text{UO}_2(\text{OH})_2 \text{Biphenol}]^{2-}$	74.0
(3) $[\text{UO}_2(\text{OH})_2 \text{Catechol}]^{2-}$	68.0
(4) $[\text{UO}_2(\text{OH})_2 \text{Oxalate}]^{2-}$	66.5
(5) $[\text{UO}_2(\text{OH})_2 \text{Oxalate}]^{2-}$	53.7

\*average value

*Cis* and *trans* conformers were optimised for complexes (1) - (5) and a summary of the energy barriers are given in Table 6.9. In comparison to complex (b)  $\Delta^{\text{TC}}$  increases for all complexes with the exception of (1). This is perhaps unsurprising given that the uranyl unit is already distorted in this complex and therefore the *cis* conformation would be comparably more stable. Similarly to complexes (iii) and (vi) and the chloride complexes ((D) - (F)) studied previously,  $E_a\text{T}^\ddagger$  increases by roughly  $10 \text{ kJ mol}^{-1}$  in all the negatively charged complexes, again (1) is an exemption, where  $E_a\text{T}^\ddagger$  and  $E_a\text{C}^\ddagger$  are significantly larger in comparison to the other complexes.

Table 6.9: Comparison of the activation energies for the forward and reverse reaction ( $E_a T^\ddagger/E_a C^\ddagger$ ) and the *trans* stabilisation ( $\Delta^{TC}$ ) energy of complexes (1) - (5) in the ground state.

Complex	$E_a T^\ddagger$ (kJ mol <sup>-1</sup> )	$E_a C^\ddagger$ (kJ mol <sup>-1</sup> )	$\Delta^{TC}$ (kJ mol <sup>-1</sup> )
(b) [UO <sub>2</sub> (OH) <sub>4</sub> ] <sup>2-</sup>	157.788	74.909	82.879
(1) UO <sub>2</sub> (OH) <sub>2</sub> (Phen) <sub>2</sub>	389.902	322.572	67.329
(2) [UO <sub>2</sub> (OH) <sub>2</sub> Biphenol] <sup>2-</sup>	168.420	77.096	91.324
(3) [UO <sub>2</sub> (OH) <sub>2</sub> Catechol] <sup>2-</sup>	161.994	78.297	83.697
(4) [UO <sub>2</sub> (OH) <sub>2</sub> Oxalate] <sup>2-</sup>	167.241	77.075	90.166
(5) [UO <sub>2</sub> (OH) <sub>2</sub> Oxalate] <sup>2-</sup>	170.519	77.852	92.667

The data in Table 6.9 shows that there is no direct correlation between bite angle and the energy barriers. Comparing complexes (2) and (3), shows  $E_a T^\ddagger$  and  $\Delta^{TC}$  increasing and  $E_a C^\ddagger$  decreasing when the bite angle decreases. However, further reduction in the bite angle *i.e.* from complex (3) - (4) / (5) these trends are reversed. Hence no overall correlation between the energy barriers and bite angle is established. Based on the ground state data, complex (3) is the most promising complex due to having the lowest  $E_a T^\ddagger$  and  $\Delta^{TC}$  and the largest  $E_a C^\ddagger$  indicating the most stable *cis* conformation out of the bidentate ligands studied. It is worth noting that both complexes (b) and (F) are more promising, however final conclusions are delayed until after the excited state analysis.

The energy diagrams of complexes (b), (3) and (1) are compared in Figure 6.12; showing the similar nature of (b) and (3) and the comparatively different nature exhibited in complex (1). As complexes (2) - (5) have comparatively similar behaviours, the best complex ((3)) was chosen as a comparison to the benchmark complex ((b)). Alternatively complex (1) exhibits vastly different behaviour and thus is shown as a contrast.

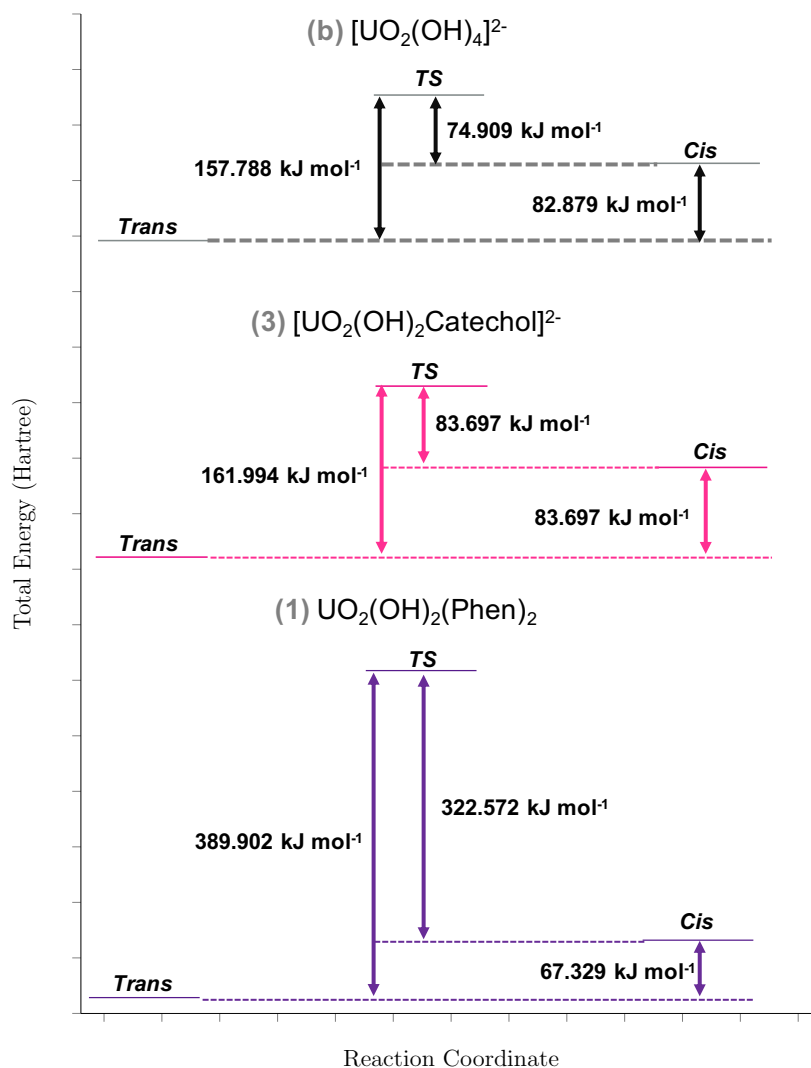


Figure 6.12: Ground state energy diagrams for complexes (b), (3) and (1).

Vertical excitations for all optimised geometries were analysed in order to assess how  $E_a T_{\ddagger}^{\dagger}$ ,  $E_a C_{\ddagger}^{\dagger}$  and  $\Delta^{\text{TC}}$  change in the excited state. The lowest energy  $\sigma_u \rightarrow \delta_u$  excitation energy and overall  $\sigma_u \rightarrow \delta_u$  contributions are summarised in Table 6.10.

In comparison to the complexes studied in the previous sections, the overall contribution of  $\sigma_u \rightarrow \delta_u$  character is much lower in the bidentate complexes. This is primarily due to increased bonding/antibonding interactions between the oxygen 2p equatorial ligands with the uranyl 5f orbitals, as described in the previous Section 6.3.2. This increase in bonding/antibonding interactions results in several MOs with  $\sigma_u$  nature, similar to what was seen in Chapter 4. As well as the increase in  $\sigma_u$  type MOs, there are also several MOs which have density solely on the ligands but make up minor transitions in the overall excitation. These two factors contribute to the lower contribution to the  $\sigma_u \rightarrow \delta_u$  excitation in contrast to the simpler complexes studied previously.

Table 6.10: Lowest energy  $\sigma_u \rightarrow \delta_u$  excitation energy ( $\Delta E$ ) and overall contribution from the transition of interest for the optimised geometries for complexes (1) - (5).

Complex	Conformation	State	$\Delta E$ (eV)	Contribution (%)
(b) (UO <sub>2</sub> (OH) <sub>4</sub> ) <sup>2-</sup>	<i>trans</i>	T <sub>56</sub>	2.72	92
	<i>TS</i>	T <sub>49</sub>	2.50	85
	<i>cis</i>	T <sub>44</sub>	2.47	87
(1) UO <sub>2</sub> (OH) <sub>2</sub> (Phen) <sub>2</sub>	<i>trans</i>	T <sub>1</sub>	2.64	94
	<i>TS</i>	T <sub>1</sub>	2.47	74
	<i>cis</i>	T <sub>1</sub>	2.40	92
(2) (UO <sub>2</sub> (OH) <sub>2</sub> Biphenol) <sup>2-</sup>	<i>trans</i>	T <sub>17</sub>	2.60	28
	<i>TS</i>	T <sub>12</sub>	2.42	48
	<i>cis</i>	T <sub>23</sub>	2.76	53
(3) (UO <sub>2</sub> (OH) <sub>2</sub> Catechol) <sup>2-</sup>	<i>trans</i>	T <sub>34</sub>	2.80	69
	<i>TS</i>	T <sub>48</sub>	2.84	30
	<i>cis</i>	T <sub>26</sub>	2.49	57
(4) (UO <sub>2</sub> (OH) <sub>2</sub> Oxalate) <sup>2-</sup>	<i>trans</i>	T <sub>9</sub>	2.63	96
	<i>TS</i>	T <sub>1</sub>	2.45	80
	<i>cis</i>	T <sub>3</sub>	2.48	72
(5) (UO <sub>2</sub> (OH) <sub>2</sub> Oxalate) <sup>2-</sup>	<i>trans</i>	T <sub>24</sub>	2.66	64
	<i>TS</i>	T <sub>15</sub>	2.53	40
	<i>cis</i>	T <sub>28</sub>	2.86	45

$E_a T_{\ddagger}^{\dagger}$ ,  $E_a C_{\ddagger}^{\dagger}$  and  $\Delta^{\text{TC}}$  energies in the excited state of complexes (1) - (5) are summarised in Table 6.11. In the excited state, only complex (1) exhibits the same behaviour as the benchmark complex with decreasing  $E_a T_{\ddagger}^{\dagger}$  and  $\Delta^{\text{TC}}$  energies and increasing  $E_a C_{\ddagger}^{\dagger}$ , however  $E_a T_{\ddagger}^{\dagger}/E_a C_{\ddagger}^{\dagger}$  are still over double any other complex studied in this chapter. Complexes (2) and (5) show a decrease in both  $E_a T_{\ddagger}^{\dagger}$  and  $E_a C_{\ddagger}^{\dagger}$  and an increase in  $\Delta^{\text{TC}}$ ; which indicates destabilisation of the *cis* isomer and stabilisation of the *TS* upon excitation. In the excited state of complex (4)  $E_a T_{\ddagger}^{\dagger}$ ,  $E_a C_{\ddagger}^{\dagger}$  and  $\Delta^{\text{TC}}$  decrease indicating stabilisation of the *cis* and *TS* conformers and/or destabilisation of the *trans* conformer. Finally complex (3), which was the most promising in the the ground state, results in  $E_a T_{\ddagger}^{\dagger}$  and  $E_a C_{\ddagger}^{\dagger}$  increasing and  $\Delta^{\text{TC}}$  decreasing in the excited state; corresponding to the *cis* conformer becoming more stabilised and the *TS* conformer more destabilised.

Table 6.11: Comparison of the activation energies for the forward and reverse reaction ( $E_a T^\ddagger/E_a C^\ddagger$ ) and the *trans* stabilisation ( $\Delta^{TC}$ ) energy of complexes (1) - (5) in the excited state (ES).

Complex	$E_a T^\ddagger$ (kJ mol <sup>-1</sup> )	$E_a C^\ddagger$ (kJ mol <sup>-1</sup> )	$\Delta^{TC}$ (kJ mol <sup>-1</sup> )
(b) [UO <sub>2</sub> (OH) <sub>4</sub> ] <sup>2-</sup>	137.217	77.572	59.646
(1) UO <sub>2</sub> (OH) <sub>2</sub> (Phen) <sub>2</sub>	373.104	328.747	44.356
(2) [UO <sub>2</sub> (OH) <sub>2</sub> Biphenol] <sup>2-</sup>	151.429	44.320	107.109
(3) [UO <sub>2</sub> (OH) <sub>2</sub> Catechol] <sup>2-</sup>	166.047	111.777	54.269
(4) [UO <sub>2</sub> (OH) <sub>2</sub> Oxalate] <sup>2-</sup>	149.767	73.833	75.935
(5) [UO <sub>2</sub> (OH) <sub>2</sub> Oxalate] <sup>2-</sup>	158.295	46.002	112.292

In the excited states, complex (3) has the largest  $E_a T^\ddagger$  (with the exception of (1)) and it is the only complex in which this increases in the excited state and hence can no longer be considered as the most promising complex for the bidentate complexes. Taking into consideration both the ground and excited state  $E_a T^\ddagger$ ,  $E_a C^\ddagger$  and  $\Delta^{TC}$  energies it can be concluded that complex (4) is the most promising complex as it is the most consistent with the benchmark complex when considering the bidentate complexes studied in this section.

### 6.3.4 Summary

$E_a T^\ddagger$ ,  $E_a C^\ddagger$  and  $\Delta^{TC}$  for all complexes studied are summarised in Table 6.12. Overall, these complexes exhibit similar behaviour and energies to the benchmark complex (b) ([UO<sub>2</sub>(OH)<sub>4</sub>]<sup>2-</sup>), with the exception of complex (1), which has significantly larger  $E_a T^\ddagger$  and  $E_a C^\ddagger$  energies. Complexes which replace 2 OH ligands with monodentate ligands 180° from each other ((iii), (vi), (C), (F) and (I)) were found to be the most stable within their ligand type, and hence resulted in them having lowest  $E_a T^\ddagger$  and  $\Delta^{TC}$  energies and the largest  $E_a C^\ddagger$  energy.

In the ground state the  $E_a T^\ddagger$  was only lowered upon complexation with the more electronegative fluorine ligand (complexes (A), (B) and (C)). However, upon excitation the barriers for the fluorine complexes did not decrease as significantly as in (b), although these complexes still have some significantly low  $E_a T^\ddagger$  values in the excited state.

Complexes (F) and (I) have a greater decrease in  $E_a T^\ddagger$  upon excitation than in (b), however the overall barriers are still slightly larger than in the benchmark

complex. In contrast to (b) however, both complexes (F) and (I) have larger  $E_a C\ddagger$  and smaller  $\Delta^{TC}$  in both the ground and excited states which indicates that the *cis* isomer is more stabilised. It is worth noting that this result was also achieved by complexes (iii) and (vi), although not to the same extent. It is this property which makes these complexes the most promising out of all the monodentate ligands studied.

Equivalent lowering of  $E_a T\ddagger$  in the excited state was also achieved in complex (4), however the stabilisation of the *cis* complex is not as significant as in the complexes discussed previously, although in the ground state it is comparable to that in complex (b).

Table 6.12: Comparison of the activation energies [ $\text{kJ mol}^{-1}$ ] ( $E_a T\ddagger/E_a C\ddagger$ ) and the *trans* stabilisation energies ( $\Delta^{TC}$ ) [ $\text{kJ mol}^{-1}$ ] for all complexes studied in this chapter at both the ground (GS) and excited states (ES).

Complex	$E_a T\ddagger$ ( $\text{kJ mol}^{-1}$ )		$E_a C\ddagger$ ( $\text{kJ mol}^{-1}$ )		$\Delta^{TC}$ ( $\text{kJ mol}^{-1}$ )	
	GS	ES	GS	ES	GS	ES
(b) $[\text{UO}_2(\text{OH})_4]^{2-}$	157.788	137.217	74.909	77.572	82.879	59.646
(i) $[\text{UO}_2(\text{OH})_3\text{H}_2\text{O}]^{1-}$	180.351	158.034	80.911	/	99.440	/
(ii) $\text{UO}_2(\text{OH})_2(\text{H}_2\text{O})_2$	194.795	176.270	97.139	/	97.656	/
(iii) $\text{UO}_2(\text{OH})_2(\text{H}_2\text{O})_2$	170.754	149.430	107.497	101.274	63.256	48.156
(iv) $[\text{UO}_2(\text{OH})_3\text{NH}_2\text{Me}]^{1-}$	178.604	153.904	81.071	/	97.533	/
(v) $\text{UO}_2(\text{OH})_2(\text{NH}_2\text{Me})_2$	189.470	167.047	97.317	/	92.153	/
(vi) $\text{UO}_2(\text{OH})_2(\text{NH}_2\text{Me})_2$	167.365	145.028	105.079	98.961	62.286	46.067
(A) $[\text{UO}_2(\text{OH})_3\text{F}]^{2-}$	154.421	140.807	76.691	42.391	77.730	98.416
(B) $[\text{UO}_2(\text{OH})_2\text{F}_2]^{2-}$	154.913	142.399	77.997	71.629	76.915	70.769
(C) $[\text{UO}_2(\text{OH})_2\text{F}_2]^{2-}$	157.908	143.648	88.167	85.021	69.741	58.626
(D) $[\text{UO}_2(\text{OH})_3\text{Cl}]^{2-}$	166.370	146.812	67.668	58.666	98.702	88.147
(E) $[\text{UO}_2(\text{OH})_2\text{Cl}_2]^{2-}$	169.588	151.459	77.881	34.878	91.707	116.581
(F) $[\text{UO}_2(\text{OH})_2\text{Cl}_2]^{2-}$	159.149	137.566	92.640	87.623	66.509	49.943
(G) $[\text{UO}_2(\text{OH})_3\text{Br}]^{2-}$	168.367	147.970	67.855	59.239	100.512	88.731
(H) $[\text{UO}_2(\text{OH})_2\text{Br}_2]^{2-}$	172.177	153.304	79.294	36.667	92.883	116.638
(I) $[\text{UO}_2(\text{OH})_2\text{Br}_2]^{2-}$	160.175	138.283	94.425	89.504	65.751	48.779
(1) $\text{UO}_2(\text{OH})_2(\text{Phen})_2$	389.902	373.104	322.572	328.747	67.329	44.356
(2) $[\text{UO}_2(\text{OH})_2 \text{Biphenol}]^{2-}$	168.420	151.429	77.096	44.320	91.324	107.109
(3) $[\text{UO}_2(\text{OH})_2 \text{Catechol}]^{2-}$	161.994	166.047	78.297	111.777	83.697	54.269
(4) $[\text{UO}_2(\text{OH})_2 \text{Oxalate}]^{2-}$	167.241	149.767	77.075	73.833	90.166	75.935
(5) $[\text{UO}_2(\text{OH})_2 \text{Oxalate}]^{2-}$	170.519	158.295	77.852	46.002	92.667	112.292

Figure 6.13 compares the energy diagrams of the ‘best’ complexes from each of the three studies to the benchmark complex as discussed above. It is worth noting that  $E_a T^\ddagger$ ,  $E_a C^\ddagger$  and  $\Delta^{TC}$  are very similar for complexes (iii) & (vi) and (F) & (I) and hence are not shown in the energy diagram.

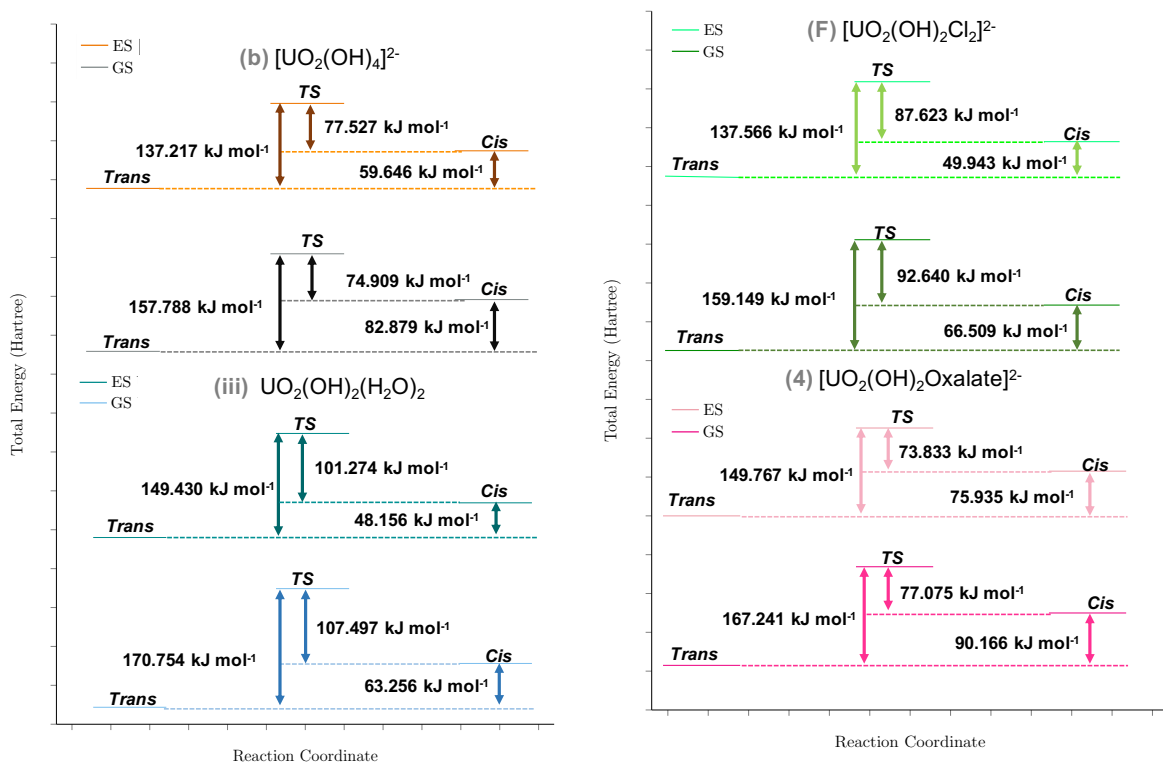


Figure 6.13: Energy diagrams comparing the best complex from every section to the benchmark complex

Despite these complexes exhibiting promising  $E_a T^\ddagger$ ,  $E_a C^\ddagger$  and  $\Delta^{TC}$  energies it is worth highlighting that none of the complexes studied in this chapter have profoundly better characteristics than the benchmark complex and therefore they are likely to behave quite similarly from an experimental perspective.

## 6.4 Conclusions and future work

Throughout this chapter the intramolecular proton transfer from an OH ligand to a uranyl oxygen was investigated at both the ground and excited state electronic structures on a number of different complexes. The effect of replacing one/two of the equatorial ligands on  $E_a T^\ddagger$ ,  $E_a C^\ddagger$  and  $\Delta^{TC}$  was investigated with the aim of finding a complex which decreased the  $E_a T^\ddagger$  and stabilised the *cis* conformer, which would be indicated by an increase in  $E_a C^\ddagger$  and decrease in  $\Delta^{TC}$ .

The [UO<sub>2</sub>(OH)<sub>4</sub>]<sup>2-</sup> complex ((b)) studied computationally by Schreckenbach *et al* [2] provided the inspiration and a benchmark complex for this work. The results of complex (b) were in excellent agreement with the literature and hence consolidating the accuracy of the model chemistry utilised.

Following the benchmark complex, the effect of overall charge of the complex was investigated by replacing one or two of the OH ligands with neutral H<sub>2</sub>O or NH<sub>2</sub>Me ligands. The *cis* conformations for all complexes except when the two neutral ligands were 180° to each other were unobtainable and hence considered to be more unstable than the benchmark complex. For the two complexes where all optimised conformers were obtained, despite having a larger E<sub>a</sub>T‡ were still promising as E<sub>a</sub>T‡ decreased by a similar amount to (b) in the excited state and Δ<sup>TC</sup> decreased in these complexes hence suggesting that the *cis* conformer is more stabilised. Despite these promising results, it was concluded that having an overall -2 charge resulted in the lower E<sub>a</sub>T‡ energy.

Next the effect of electronegativity on the ligands was investigated via coordination of the halogens. E<sub>a</sub>T‡ was lowered by complexation with the more electronegative fluorine complexes however, E<sub>a</sub>T‡ was not lowered as significantly as in (b) in the excited state. Complexation with less electronegative Cl and Br ligands, coordinated 180° to each other resulted similar results to the neutral ligands discussed above with similar Δ<sup>TC</sup> energies and lower E<sub>a</sub>T‡ energies and hence these complexes are more promising than the equivalent neutral complexes. The halogen complex results also indicated that while decreasing the electronegativity does generally increase E<sub>a</sub>T‡, the effect is not very significant, highlighted by the similar E<sub>a</sub>T‡ values between the Cl and Br ligands.

Finally the effect of bidentate ligands was investigated. In the ground state complex (3) appeared to be the best choice, upon excitation however, it was the only complex to increase in E<sub>a</sub>T‡. Therefore, complex (4) was deemed the most promising, due to having similar properties to both the neutral and halogen complex discussed above. Interestingly a variation of complex (1) studied in Chapter 5 in which the uranyl unit was already bent resulted in much larger E<sub>a</sub>T‡ and E<sub>a</sub>C‡ values than all other complexes. Although the large E<sub>a</sub>T‡ energy makes this complex unsuitable, it is worth noting that out of all the complexes, the *cis* conformation in complex (1) was the most stable. In the future it would be worth investigating complexes with a similarly distorted uranyl unit but with an overall negative charge to see if the E<sub>a</sub>T‡ can be lowered while keeping the increased stabilisation of the *cis* conformer.

From this chapter it can be concluded that while [UO<sub>2</sub>(OH)<sub>4</sub>]<sup>2-</sup> still has the lowest E<sub>a</sub>T‡, complexes with two less electronegative ligands positioned 180° to each other are similarly promising as they result in similarly low E<sub>a</sub>T‡ but with the corresponding *cis* conformer will become more stable.

In the future, this investigation can be extended to include full excited state geometries for the σ<sub>u</sub>→δ<sub>u</sub> excitation to investigate whether the barriers still decrease at relaxed excited state geometries. However, obtaining an optimised excited state geometry for the *TS* will be very challenging. It would also be worthwhile investi-

gating a greater range of more complex equatorial ligands in order to increase the steric interaction between the uranyl oxygens and the equatorial ligands resulting in the *cis* conformation being more favourable and hence reducing  $E_a T^\ddagger$ . Finally further investigation into the total charge of the complex on the energy barriers could be conducted as in this study the optimised *cis* conformers were not obtained. This could be achieved with the investigation of neutral bidentate ligands as the *cis* conformer was isolated in (1).

# References

- [1] D. L. Clark, S. D. Conradson, R. J. Donohoe, D. W. Keogh, D. E. Morris, P. D. Palmer, R. D. Rogers, C. D. Tait, *Inorg. Chem.* **1999**, *38*, 1456–1466.
- [2] G. Schreckenbach, P. J. Hay, R. L. Martin, *Inorg. Chem.* **1998**, *37*, 4442–4451.
- [3] G. Schreckenbach, G. A. Shamov, *Acc. Chem. Res.* **2010**, *43*, 19–29.
- [4] M. Bühl, G. Schreckenbach, *Inorg. Chem.* **2010**, *49*, 3821–3827.
- [5] B. Miehlich, A. Savin, H. Stoll, H. Preuss, *Chem. Phys. Lett.* **1989**, *157*, 200–206.
- [6] C. Lee, W. Yang, R. G. Parr, *Phys. Rev. B.* **1988**, *37*, 785–789.
- [7] A. D. Becke, *J. Chem. Phys.* **1993**, *98*, 1372–1377.
- [8] A. D. Becke, *Phys. Rev. A.* **1988**, *38*, 3098–3100.
- [9] R. Krishnan, J. S. Binkley, R. Seeger, J. A. Pople, *J. Chem. Phys.* **1980**, *72*, 650–654.
- [10] M. J. Frisch, G. W. Trucks, H. B. Schlegel, G. E. S. an M. A. Robb, J. R. Cheeseman, J. A. J. Montgomery, T. Vreven, K. N. Kudin, J. C. Burant, J. M. Millam, S. S. Iyengar, J. Tomasi, V. Barone, B. Mennucci, M. Cossi, G. Scalmani, N. Rega, G. A. Petersson, H. Nakatsuji, M. Hada, M. Ehara, K. Toyota, R. Fukuda, J. Hasegawa, M. Ishida, T. Nakajima, Y. Honda, O. Kitao, H. Nakai, M. Klene, X. Li, J. E. Knox, H. P. Hratchian, J. B. Cross, V. Bakken, C. Adamo, J. Jaramillo, R. Gomperts, R. E. Stratmann, O. Yazyez, A. J. Austin, R. Cammi, C. Pomelli, J. W. Ochterski, P. Y. Ayala, K. Morokuma, G. A. Voth, P. Salvador, J. J. Dannenberg, V. G. Zakrzewski, S. Dapprich, A. D. Daniels, M. C. Strain, O. Farkas, D. K. Malick, A. D. Rabuck, K. Raghavachari, J. B. Foresmann, J. V. Ortiz, Q. Cui, A. G. Baboul, S. Clifford, J. Cioslowski, B. B. Stefanov, G. Liu, A. Liashenko, P. Piskorz, I. Komaromi, R. L. Martin, D. J. Fox, T. Keith, M. A. Al.Laham, C. Y. Peng, A. Nanayakkara, M. Challacombe, P. M. W. Gill, B. Johnson, W. Chen, M. W. Wong, C. Gonzalez, J. A. Pople, *Gaussian 09. 2015 Gaussian Inc. Wallingford CT.*
- [11] W. Küchle, M. Dolg, H. Stoll, H. Preuss, *J. Chem. Phys.* **1994**, *100*, 7535–7542.

- [12] X. Cao, M. Dolg, H. Stoll, *J. Chem. Phys.* **2003**, *118*, 487–496.
- [13] X. Cao, M. Dolg, *J. Mol. Struc-THEOCHEM* **2004**, *673*, 203–209.
- [14] D. Feller, *J. Comput. Chem.* **1996**, *17*, 1571–1586.
- [15] B. P. Pritchard, D. Altarawy, B. Didier, T. D. Gibson, T. L. Windus, *J. Chem. Inf. Model.* **2019**, *59*, 4814–4820.
- [16] K. L. Schuchardt, B. T. Didier, T. Elsethagen, L. Sun, V. Gurumoorthi, J. Chase, J. Li, T. L. Windus, *J. Chem. Inf. Model.* **2007**, *47*, 1045–1052.
- [17] T. H. J. Dunning, *J. Chem. Phys.* **1989**, *90*, 1007–1023.
- [18] R. A. Kendall, T. H. J. Dunning, R. J. Harrison, *J. Chem. Phys.* **1992**, *96*, 6796–6806.
- [19] D. E. Woon, T. H. J. Dunning, *J. Chem. Phys.* **1993**, *98*, 1358–1371.
- [20] S. Hirata, M. Head-Gordon, *Chem. Phys. Lett.* **1999**, *314*, 291–299.
- [21] E. Runge, E. K. U. Gross, *Phys. Rev. Lett.* **1984**, *53*, 997–1000.
- [22] E. K. U. Gross, W. Kohn in *Density Functional Theory of many-fermion systems*, (Ed.: P.-O. Löwdin), **1990**, pp. 255–291.
- [23] K. I. Ingram, L. J. L. Häller, N. Kaltsoyannis, *Dalton Trans.* **2006**, *2*, 2403–2414.
- [24] S. Schöne, T. Radoske, J. März, T. Stumpf, M. Patzschke, A. Ikeda-Ohno, *Chem. Eur. J.* **2017**, *23*, 13574–13578.
- [25] P. Dierkes, P. W. N. M. van Leeuwen, *J. Chem. Soc., Dalton Trans.* **1999**, 1519–1530.

# Chapter 7

## Conclusions and Outlook

The aim of this thesis was to investigate the covalency of uranyl and its complexes by considering both the ground and electronically excited state structures. Herein, QTAIM analysis has been applied for the first time to investigate the excited state electronic structures of f-element complexes. Throughout this work the excitation of interest has been the optically accessible  $\sigma_u \rightarrow \delta_u$  triplet excitation, which is allowed via spin-orbit coupling.

In Chapter 3 an in-depth analysis of the covalency in uranyl via symmetry-preserving excited states was conducted. Vertical excitations demonstrated an inverse relationship between the orbital mixing coefficient,  $\Lambda$ , and the excitation energy. In excitations involving orbitals with U 5f character (*e.g.*  $\sigma_u$  and  $\pi_u$ )  $\Lambda$  was more dependent on the metal-ligand Hamiltonian matrix element,  $H_{ML}$ , whereas for excitations involving orbitals with U 6d character (*e.g.*  $\sigma_g$  and  $\pi_g$ )  $\Lambda$  became increasingly dependent on the difference in fragment orbital energy levels,  $\Delta E_{ML}$ . These trends were further enhanced in electronically excited state geometries, with a relationship between excitation energy and bond length. Enhanced charge transfer character in the  $\pi_g \rightarrow \pi_g^*$  state was established in the excited state, which would not have been concluded based on the ground state data alone.

In Chapters 4 and 5, equatorial complexation resulted in the U-O bond length increasing and the excitation energy of the  $\sigma_u \rightarrow \delta_u$  excitation was blue-shifted. QTAIM analysis indicated movement of charge from the U-O<sub>yl</sub> bonding region to the uranyl oxygens resulting in an increase in the ionic nature of the U-O<sub>yl</sub> bond. It was also concluded that the excitation energies of the complexes could be rationalised by the relative stabilisation/destabilisation of the hole/particle MOs within the ligand set. At the electronic excited state geometries, the bond lengths increased, and the excitation energy was red-shifted commensurate with the trends observed in free uranyl.

In Chapter 4, while clear trends between the complexes were observed in the ground state, in the electronic excited state trends in the QTAIM data were difficult to correlate. The lack of correlation between the increase/decrease in  $\delta_{U-O_{yl}}$  and  $\delta_{U-L}$  was surprising, although trends in the QTAIM data were rationalised it was on an

individual excitation basis.

The synthetically realised bent complexes studied in Chapter 5 resulted in comparable QTAIM metrics to those linear complexes studied in Chapter 4. This highlighted that the origin of the distortion of the uranyl unit was a result of steric interactions as there was no significant differences in the electronic structures. The QTAIM analysis allowed for the design of novel theoretical complexes, which were found to significantly enhance the bending in the uranyl unit. From these results design criteria for bent uranyl complexes were established.

Due to the novel theoretical complexes studied in Chapter 5 being synthetically unviable, an alternative method of obtaining *cis* uranyl was studied. In Chapter 6 an intramolecular proton transfer was investigated on uranyl hydroxide analogues. Exchanging one or two hydroxide ligands with a variety of small equatorial ligands enabled the effects of different coordination environments to be studied: overall charge of the complex, electronegativity of the ligands and bidentate ligand coordination. It was found that although changing the equatorial ligands increased the barrier energy, in some complexes the stability of the *cis* conformation was enhanced. Complexes which exchanged two OH ligands with two less electronegative ligands 180° to each other (Cl and Br in this case) resulted in a slight increase in the barrier energy but the corresponding *cis* conformer was more stable. Finally, these intramolecular reactions were also considered in the excited state, although only vertical excitations were considered, excitation into the  $\sigma_u \rightarrow \delta_u$  state lowered energy barrier in the majority of the complexes.

Throughout this thesis the significance of probing excited state structures is established. Despite small deviations in the geometric values, QTAIM analysis at the excited state geometries often highlighted interesting properties which were not established in the ground state. Although this was present throughout all four investigations, this was particularly prominent in Chapter 4. Chapter 6 highlighted that reaction barriers for an intramolecular proton transfer could be lowered in the excited state, indicating a potential new way to synthesis *cis* uranyl, which is yet to be synthesised so far in the literature.

In order to improve the assessment of the covalency in uranyl complexes, higher energy excitations, such as those studied in Chapter 3 could be utilised and the dependence of  $\Lambda$  could be established in the complexes studied in Chapters 4 and 5. Also a wider range of ligands can be investigated in order to fully rationalise trends between hard/soft donor atoms established in Chapter 4. Investigation of complexes which bend the uranyl unit through electronic origins would make an interesting comparison to those in Chapter 5 in order to see if there are any discernible differences within the QTAIM metrics. It would also be worthwhile investigating a greater range of more complex equatorial ligation in both Chapters 4 and 6, with investigation into increased steric interactions on the energy barrier in the intramolecular

proton transfer reaction being more extensively studied in Chapter 6.

Finally, this work could provide a promising starting point for investigation of covalency in other actinide complexes. Minor actinides (Am, Cm) are of particular relevance to the nuclear industry as they contribute to the high radiotoxicity of spent nuclear fuel. Understanding the covalency in Am and Cm complexes could aid in selective complexation methods, which coordinate the minor actinides over the lanthanides in spent nuclear fuel.